Proceedings of:

Precision Mechanical Design and Mechatronics for Sub-50nm Semiconductor Equipment

2008 Spring Topical Meeting

April 7 and 8, 2008

Lawrence Berkeley National Laboratory
Berkeley, California

The American Society for Precision Engineering (ASPE) is a multidisciplinary professional and technical society concerned with research and development, design, manufacture and measurement of high accuracy components and systems. ASPE activities encompass relevant aspects of mechanical, electronic, optical and production engineering, physics, chemistry, and computer and materials science. Membership is open to anyone interested in any aspect of precision engineering.

Founded in 1986, ASPE provides a new focus for a diverse but important community. Other professional organizations have covered aspects of precision engineering, always as a sideline to their principal goals. ASPE is based on the core of generic concepts necessary to achieve precision in any application; independent of discipline, ASPE intends to be the focus for precision technology, and to represent all facets from research to application.

ASPE — The American Society for Precision Engineering
301 Glenwood Avenue, Suite 205, Raleigh, NC 27603
P.O. Box 10826, Raleigh, NC 27605
Telephone: (919) 839-8444 Fax (919) 839-8039
http://www.aspe.net

Preface

This book comprises the proceedings of the 2008 Spring Topical Meeting. The contributions reflect the authors' opinions and are published as presented to ASPE, without change. Their inclusion in this publication does not necessarily constitute endorsement by the ASPE, or its editorial staff.

Individual readers of this book and nonprofit libraries acting for them are permitted to make fair use of the material contained in this book to be used in teaching or research; provided they copy said paper in total, as written by the author. Permission is granted to quote excerpts from the scientific or technical works in this book with proper acknowledgment of the source to include: The author's name, the book name, and the ASPE tag line. Reproduction of figures and tables is likewise permitted from the contents of this book, provided that the same acknowledgment of the same source and content is permitted.

Any other type reproduction, systematic copying or multiple reproduction of any material in this book is expressly prohibited except with the written permission of the ASPE editorial staff, addressed to the Society's headquarters.

ISBN 978-1-887706-46-9

2008

American Society for Precision Engineering
301 Glenwood Avenue, Suite 205
Raleigh, NC 27603

Printed in the United States of America

2008 Spring Topical Meeting

Contents

Preface . . . . . *ii*

Contents . . . . . *iii*

Program . . . . . *iv*

Foreword . . . . . *v*

Technical Paper Index . . . . . *vi*

Technical Papers *3-138*

Author Index *139*

2008 Spring Topical Meeting

Meeting Schedule

	Monday, April 7	Tuesday, April 8
7:30	Registration and Continental Breakfast	
8:15	WELCOME REMARKS	
8:30 10:00	TECHNICAL SESSION I	TECHNICAL SESSION V
	Coffee Break	
10:30 12:00	TECHNICAL SESSION II	TECHNICAL SESSION VI
	Lunch	
1:00	POSTER SESSION	
1:30 3:00	TECHNICAL SESSION III	TECHNICAL SESSION VII
	Refreshment Break	
3:30 5:00	TECHNICAL SESSION IV	TECHNICAL SESSION VIII
	FREE TIME	
6:00	Depart for Dinner	
6:30 8:30	DINNER AT RESTAURANT	

Foreword

The system error budgets for controlling critical dimensions (CD) and overlay during semiconductor processing lead to astonishingly small numbers for individual elemental errors including stages, alignment, long- and short-term stability, servo-control, and thermal management. The 3-sigma sum of numerous error terms for placing a pattern onto a wafer is typically a small fraction of the nominal critical dimension. As the lithography and related industries move to CD's less than 50 nm, it is important to assess the precision engineering community's ability to meet these increasingly stringent requirements.

The objective of this meeting is to enable a technical dialogue between engineers directly supporting the semiconductor industry and the broader field of precision engineering. The focus of this meeting will be on issues regarding precision mechanics and control, recognizing that detailed issues of lithographic processing, such as resist development, are well-represented in other venues. The intended semiconductor technology audience includes current lithograph tool makers, and also related processing requirements, such as mask writing, opto-mechanics, mask distortion, and future technologies such as EUV, maskless, and nano-imprint lithographies.

2008 Spring Topical Meeting Program Committee:

Meeting Co-Chairmen:

John S. Taylor
Lawrence Livermore National Laboratory
Jan van Eijk
Technical University of Delft / MICE, bv

Technical Organizing Committee:

Chris J. Evans, Zygo Corporation
Pete Fitsos, Lawrence Livermore National Lab.
Stephen J. Ludwick, Aerotech, Inc.
Robert-Han Munnig Schmidt, Delft Univ. of Technology
Senajith B. Rekawa, Lawrence Berkeley National Lab.
Marcel J. M. Renkens, Philips Applied Technologies
Jeffrey W. Roblee, AMETEK - Precitech, Inc.
Marek Zywno, KLA-Tencor

Technical Sessions

Introduction

Monday, April 7, 2008, 8:15 am - 8:30 am

1. ***Welcome and Introductory Remarks***
   John S. Taylor (Lawrence Livermore National Laboratory); and Jan van Eijk (Technical University of Delft / MICE, bv)

Session I
Overview, Systems

Monday, April 7, 2008, 8:30 am - 10:00 am

1. ***Controlling Lithography Variability: It's No Longer a Question of Nanometers (They Are Too Big)***
   Lercel, M. (SEMATECH) 3
2. ***A Perspective on Stage Dynamics and Control***
   Butler, H. (ASML Netherlands B.V.) 7
3. ***Double Patterning Requirements for Optical Lithography and Prospects for Optical Extension Without Double Patterning***
   Hazelton, A. J.; Wakamoto, S.; Hirukawa, S.; Magome, N.; Ishikawa, J. (Nikon Corporation); Binnard, M. (Nikon Research Corporation of America); McCallum, M. (Nikon Precision Europe GmbH); and Lapeyre, C.; Guilmeau, I.; Barnola, S.; Gaugiran, S. (CEA/LETI) 10

Session II
Mechatronics for Advanced Lithography

Monday, April 7, 2008, 10:30 am - 12:00 pm

1. ***Metrology and Motion***
   van Eijk, J. (Technical University of Delft / MICE, bv) 16
2. ***A High-bandwidth, High-precision, Two-axis Steering Mirror***
   Kluk, D. J.; Trumper, D. L. (Massachusetts Institute of Technology) 19
3. ***Active Magnetic Bearing — Controls Strategy and Calibrations***
   Norg, M. L. (Norg Consulting); Tousain, R. (Philips Applied Technologies), and van Eijk, J. (Technical University of Delft / MICE, bv) 25

Poster Session

Monday, April 7, and Tuesday, April 8, 2008 -1:00 pm - 1:20 pm

1. ***Six Degrees of Freedom Magnetic Levitation Stage Using New Active Magnetic Bearings***
   Choi, Y.-M.; Gweon, D.-G. (Korea Advanced Institute of Science & Technology (KAIST)); Jeong, J. (Korea University); and Kim, D.-M. (Samsung Electronics) 31
2. ***Practical Control Method for Nano Positioning Using a Langevin Ultrasonic Motor in Vacuum Environment***
   Kim, W. S.; Lee, S.-K. (Gwangju Institute of Science and Technology (GIST)); and Yun, C. H. (Korea Institute of Industrial Technology) 35
3. ***Novel Stage With Voice Coil Motor for Laser Beam Direct Writing***
   Hwang, D.-H.; Kim, J.-Y.; Lee, M.-G.; (Ajou University); and Kim, H.-S. (Institute of Advanced Engineering (IAE)) 39

Session III
Precision Positioning Systems
Monday, April 7, 2008, 1:30 pm - 3:00 pm

1. ***Describing Nanometer-level Errors in Precision Motion Control Stages***
   Ludwick, S. J. (Aerotech, Inc.) 44
2. ***Sub Nanometer Precision Hybrid Positioning Systems for Vertical Inspection Tools***
   Glöss, R. (Physik Instrumente (PI) GmbH & Co. KG) 48
3. ***Experiences With Opto-mechanical Systems That Affect Optical Surfaces at the Sub-nanometer Level***
   Hale, L. C. (Innovative Machine Solutions, LLC); and Taylor, J. S. (Lawrence Livermore National Laboratory) 52

Session IV
Advanced Control Strategies
Monday, April 7, 2008, 3:30 pm - 5:00 pm

1. ***Feedforward Tuning Methods for Wafer Scanning Systems***
   Stearns, H.; Yu, S.; Mishra, S.; Tomizuka, M. (University of California at Berkeley) 58
2. ***Motion Control for Nano Lithography***
   Ruben, S. D.; Tsao, T.-C. (University of California at Los Angeles) 64
3. ***Damping and Homing in a Nanoimprinting Machine***
   Ozturk, O.; Brien, J. F.; Hocken, R. J. (University of North Carolina at Charlotte) 70

Session V
Advanced Lithographic Systems
Tuesday, April 8, 2008, 8:30 am - 10:00 am

1. ***Providing Precision Mechatronic Solutions for the Challenges of EUV-Lithography***
   Renkens, M. J. M.; Tabor, R.; Ruijl, T. A. M. (Philips Applied Technologies) 74
2. ***Critical Dimension Control, Overlay and Throughput Budgets in UV Nanoimprint Stepper Technology***
   Sreenivasan, S. V. (The University of Texas at Austin / Molecular Imprints); and Schumaker, P. D.; Choi, B. J. (Molecular Imprints, Inc.) 78
3. ***Overcoming Overlay Challenges in Nanoimprint by Wafer/Mask Bending***
   Walmsley, R. G.; Wu, W.; Tong, W. M.; Bartman, J.; Chen, Y.; Yu, Z.; Stewart, D.; Park, I.; Picciotto, C.; Gao, J.; Williams, R. S. (Hewlett-Packard Company) 93

Session VI
Reticle Chucking and Distortion
Tuesday, April 8, 2008, 10:30 am - 12:00 pm

1. ***Controlling Image Placement Errors During the Fabrication of EUVL Masks***
   Engelstad, R. L.; Buttala, V. S. R.; Vukkadala, P. Mikkelson, A. R.; Nataraju, M.; Turner, K. T. (University of Wisconsin - Madison) 97
2. ***Analysis of Coulomb and Johnsen-Rahbek Electrostatic Chuck Performance for EUV Lithography***
   Sogard, M. R. (Nikon Research Corporation of America); Mikkelson, A. R.; Turner, K. T.; Engelstad, R. L. (University of Wisconsin - Madison); and Nataraju, M. (Intel Corporation) 103
3. ***Chuck Induced Deformations in EUV Mask Substrate Metrology***
   Evans, C. J.; Truax, B.; Smith, C. (Zygo Corporation) 108

Session VII
Motion Control for Novel Lithography
Tuesday, April 8, 2008, 1:30 pm - 3:00 pm

1. ***Displacement Measurement Interferometer Error Correction Techniques***
   Mielke, S. L.; Demarest, F. C. (Zygo Corporation) 113
2. ***Design of an Interferometer for EUV Interference Lithography at the NIST SURF III Synchrotron***
   Cole, K.; Vallance, R. R. (The George Washington University); and Lucatorto, T. (National Institute of Standards and Technology) 117
3. ***Electron Beam Pattern Generation System Design***
   Hartley, J. G. (SUNY at Albany) 123

Session VIII
Advanced Actuation
Tuesday, April 8, 2008, 3:30 pm - 5:00 pm

1. ***System Design Based on "Dynamic Error Budgeting" ****
   van Eijk, J. (Technical University Delft / MICE bv); Trumper, D. L. (Massachusetts Institute of Technology); and Jabben, L. (Vision Dynamics) 127
2. ***Nanotube Micro-opto-mechanical Systems***
   Panchapakesan, B. (University of Delaware) 128
3. ***From Desperate to Disparate: Broad Array of Centimeter Travel, Picometer Resolution, High Stiffness Piezomechanisms Suddenly Enables a Wealth of Next-Generation Tools***
   Jordan, S. C. (PI (Physik Instrumente) L.P.) 133

* *No extended abstract available at press time*

Technical Papers

CONTROLLING LITHOGRAPHY VARIABILITY: IT'S NO LONGER A QUESTION OF NANOMETERS (THEY ARE TOO BIG)

Michael Lercel, SEMATECH, Albany, NY

ABSTRACT

Although most of the focus on the semiconductor lithography roadmap is in trying to image smaller features, one of the most critical concerns is being able to do the imaging with precision and accuracy. Semiconductor lithography is the ultimate in precision manufacturing. Each wafer must be printed with small features, with well defined control of size and position, and at speeds of more than 100 wafers per hour per tool. With an roadmap that predicts 32nm half-pitch devices in manufacturing before 2012, the size and placement of each feature must be controlled within a few nanometers. And with double exposure techniques become more likely for manufacturing, precision is insufficient – now accuracy from one exposure to another becomes critical. The process to image the device features requires multiple components – each of which contributes to the overall error budget. This fact makes the tools, the photomasks, and the process control very challenging for the industry. In this talk, the ITRS lithography roadmap requirements for future device nodes will be discussed with a particular emphasis on the demanding specifications for variability control. The differing requirements of several lithography technologies; such as EUVL, double patterning, and nanoimprint; will be compared.

INTRODUCTION

Producing smaller semiconductor devices requires an extreme test of precision manufacturing. Smaller devices must be fabricated and at ever tighter tolerances. The requirements for future lithography are outlined in the International Technology Roadmap for Semiconductors (ITRS), which is an unique set of requirements determined by consensus building in the semiconductor industry. Although not every company implements the ITRS requirements directly, the ITRS provides a general guide for the industry stretching from general system performance to device and transistor requirements, and finally to unit process requirements like for lithography. The performance requirements can then be used as guidelines for error budgets by integrated circuit and production tool requirements.

The roadmap generally shows that meeting future requirements requires some level of innovation, and it is this level of innovation that drives the semiconductor industry on an aggressive performance and density scaling.

LITHOGRAPHY ROADMAP

Dimensional scaling is driven mostly by device requirements for increased performance and density. For the past two decades, the industry has relied on optical lithography in the deep ultraviolet to pattern the most critical levels. Smaller features have been printed by decreasing the wavelength (from 248nm to 193nm) and by increasing the numerical aperture (NA) of the lens. The numerical aperture change from 0.6 to 0.93 in air was enabled by improved lens polishing technology. Now up to 1.35NA is possible due to further lens improvements and the use of water as the medium between the lens and wafer. It may be possible to increase the NA beyond 1.55 with the use of high index fluids and lens material. Smaller dimensions can also be achieved through double patterning where two lithography steps are used to define a single device level. However, the aggressive scaling roadmap may allow for the introduction of a new lithography technique such as extreme ultraviolet lithography (EUVL). By operating in the soft-x-ray spectrum, EUVL provides much lower diffraction limited resolution, but requires significantly different infrastructure than optical lithography. Another novel technique, nanoimprint lithography, provides for a mechanical pattern transfer by molding. Both EUVL and nanoimprint have been shown to be capable of patterning 22nm half-pitch features, but the challenge is enabling a cost-effective infrastructure compared to the already well-established optical lithography techniques.

Not just resolution, but also tolerances become more difficult with each technology node. Figure 1 shows the dimensional and tolerance requirements over time that indicate that tolerance is tightening even faster than pure scaling. For device performance reasons, gate size and contact size scaling is not keeping pace with the rest of the roadmap. This has driven increased tolerance requirements on overlay and CD uniformity, as indicated in Table 1.

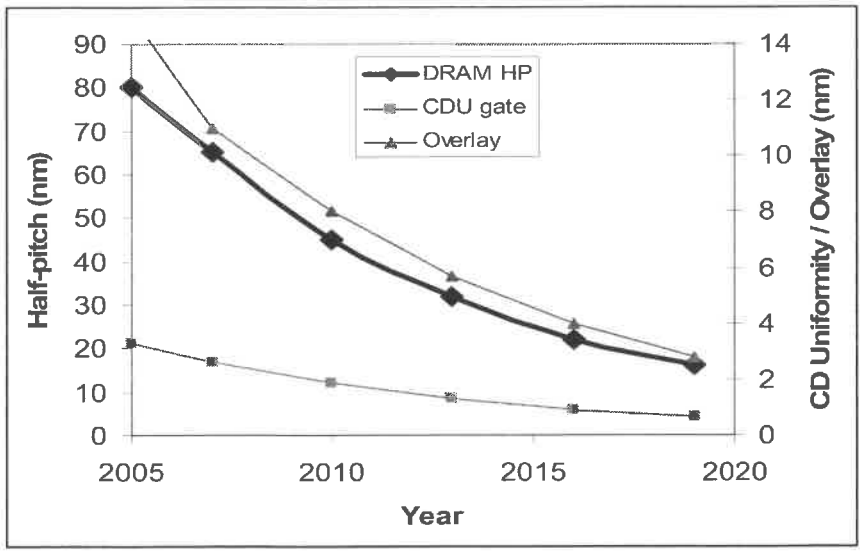

FIGURE 1. Half-pitch scaling for DRAM (left axis) and corresponding variability numbers for CD uniformity and overlay (right axis).

Memory technologies, such as DRAM and Flash, have very aggressive density scaling roadmaps, as reflected by the tight Flash half-pitch in Table 1 where the half-pitch is expected to be under 18nm in high-volume manufacturing in less than 10 years. However, other technologies, such as microprocessors, can have tighter variability requirements. The MPU gate CD control is the tightest CD uniformity requirement as this is driven by being 12% of the physical gate size (and allowing for some contribution from the gate etch). The 12% tolerance value is determined by clock speed and power dissipation requirements of the device. Most of the other CD uniformity and overlay values are determined by statistical partitioning of error budgets. For example, the CD uniformity of contact holes and contact-hole-to-gate overlay are set to prevent shorting between the contacts and gates, and to allow a minimum contact hole area for resistance.

In addition to the basic lithography requirements, severe demands are placed upon the components that make up the overall error budget. Even though it is a reduction technology, photomask requirements, for example, can be as tight as the lithography requirements. In optical lithography, some printing errors are magnified. This is called the Mask Error Enhancement Factor (MEEF). If the magnification ratio is 4X from mask to wafer, and the MEEF is 4, then the photomask CD uniformity requirement is identical to the allowed CD uniformity component on the wafer. Future lithography technologies may reduce the severe photomask tolerances by having a smaller effective MEEF. EUVL has a lower effective MEEF due to not being as close to the diffraction limit of the optics as with immersion lithography. Even nanoimprint lithography can have less critical CD uniformity requirements compared to optical lithography because it has a MEEF of one (but is also 1X reduction).

TABLE 1. ITRS device requirements for the major technology nodes (from the 2007 ITRS update). Even in 2007, meeting the gate CD control requirement can only be met with workarounds.

Year of Production	2007	2010	2013	2016	2019	2022
DRAM ½ pitch (nm) (contacted)	65	45	32	22	16	11
DRAM and Flash						
DRAM ½ pitch (nm)	65	45	32	23	16	11
Flash ½ pitch (nm) (un-contacted poly)	54	36	25	18	13	9
Contact in resist (nm)	70	50	35	25	18	12.4
Contact after etch (nm)	64	45	32	23	16	11.3
Overlay [A] (3 sigma) (nm)	13	9.0	6.4	4.5	3.2	2.3
CD control (3 sigma) (nm) [B]	6.8	4.7	3.3	2.3	1.7	1.2
MPU						
MPU/ASIC Metal 1 (M1) ½ pitch (nm)	68	45	32	23	16	11
MPU gate in resist (nm)	42	30	21	15	11	8
MPU physical gate length (nm) *	25	18	13	9	6	4
Contact in resist (nm)	84	56	39	28	20	14
Contact after etch (nm)	77	51	36	25	18	13
Gate CD control (3 sigma) (nm) [B] **	2.6	1.9	1.3	0.9	0.7	0.5

The very tight variability requirements translate into very tight tolerances on the manufacturing equipment error budgets. The resolution and CD uniformity drive lens polishing tolerances to reduce lens aberrations and flare. For EUVL, the contribution from diffraction limited imaging is reduced, but with a much shorter wavelength, polishing requirements on the optics become even more tight. For EUVL optics, the total allowed wavefront error must be <0.27nm rms, and the tolerance on each mirror must be much tighter than this. The advanced optical lithography techniques also often have a small depth-of-focus which requires precise control of wafer to lens spacing. Today, depth-of-focus less than 100nm is common, and the total error budget includes mask and wafer flatness in addition to the tool positioning precision and height measurement error.

The overlay of one layer to another requires precise mechanical control of the lithography patterning tool. The overlay error budget includes stage positioning on the tool, mask contributions (from both levels), lens distortion, and alignment detector performance. Stage positioning for both the mask and wafer stages must be a small fraction of the total overlay target – which is only 6.4nm for the 32nm half-pitch node. The use of double patterning actually drives even tighter overlay requirements because now two (or more) wafer passes define a single device level (which must be, in principle, identical to one defined by a single exposure).

An added challenge for the equipment is the need to perform this level of variability control at very high productivity. State-of-the-art lithography exposure tools are >$30M so to be cost-effective, they operate at >120 wafers/hour (300mm). Typical stage speeds are >500 mm/sec for the wafer and >2000 mm/sec for the reticle stages to meet this throughput.

The ability to produce the tight variability performance requires measurement at even tighter tolerances. Ideally, metrology tools operate at a precision-to-tolerance level of 10%, but the very difficult semiconductor requirements mean that many metrology tools operate at 20%. Nevertheless, this still requires that the metrology tool measure five times better than the original process tool. So overlay tool precision must be close to 1nm and CD uniformity needs to be measured to about half a nanometer for the 32nm half-pitch node.

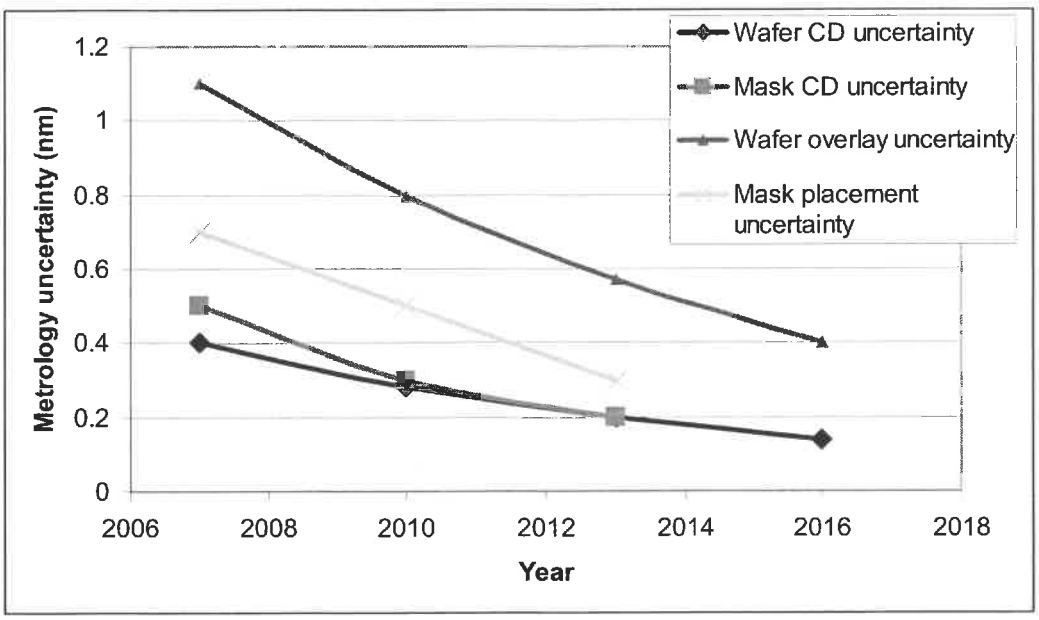

FIGURE 2. Comparison of metrology uncertainty requirements for wafer and mask.

As noted above, the mask requirements can often be as tight (or even tighter) than the wafer requirements. However, mask tools run at much lower throughputs and some requirements (such as overlay) benefit from the reduction ratio. Also, the most common technique of writing masks, e-beam lithography, has less severe requirements on depth-of-focus and lens errors than optical lithography. The exception for mask tools is the metrology tools required to characterize the masks. The mask pattern placement, a component of overlay, is actually much more difficult to measure than overlay on the wafer. The pattern location must be measured in absolute terms across the entire six inch square photomask. This requires absolute measurement capability of about 10 parts-per-billion across the six inch surface.

SUMMARY

The lithography roadmap places very tight requirements on patterning resolution and variability control. These requirements are driven by the economics of device scaling, and the technical requirements for device performance and thermal management. The incredible variability requirements are now measured in nanometers for current and near-future technologies. This requires error budget components for equipment and metrology tools that are now reaching sub-nanometer levels. So when it comes to variability control, it is no longer nanotechnology, it will soon be picotechnology.

A PERSPECTIVE ON STAGE DYNAMICS AND CONTROL

Hans Butler
Mechatronic Systems Development
ASML, Veldhoven, The Netherlands
e-mail: hans.butler@asml.com

ABSTRACT
In the semiconductor industry, a wafer stepper is used to expose the pattern on a mask ('reticle') onto a wafer. Accurate positioning of the reticle and the wafer is of crucial importance for creating a working IC. This paper reflects on the stage dynamics and control design in Stepper technology, introduces the modifications needed to successfully implement Scanner technology, and shows the further improvements in dual-stage TWINSCAN™ systems.

1 THE STEPPER

Originally, each exposure ('die') was created by illuminating the reticle for a certain time period, after which the light source was switched off and the wafer was moved ('stepped') to a next die location. After the stepping movement, the system was allowed to settle, and when the position accuracy had reached a certain level the light source was switched on again. The wafer stage consisted of a foot floating on a granite stone by means of an air bearing, and connected to a wafer table ('mirror block'). Horizontal motion was created by an H-type linear motor that was fixed to the stone by means of dampers. The table also had vertical movement directions for the purpose of focussing the wafer in the image plane of the lens, requiring a measurement of the distance of the wafer to the lens by means of a level sensor system. The horizontal stage position was measured by an interferometer system. The stage was guided by means of mechanical bearings 'rolling' over the motor beams. With regard to controlling the stage, the horizontal controllers (3-DOF) acted independently from the vertical directions (also 3-DOF). Figure 1 shows the basic layout.

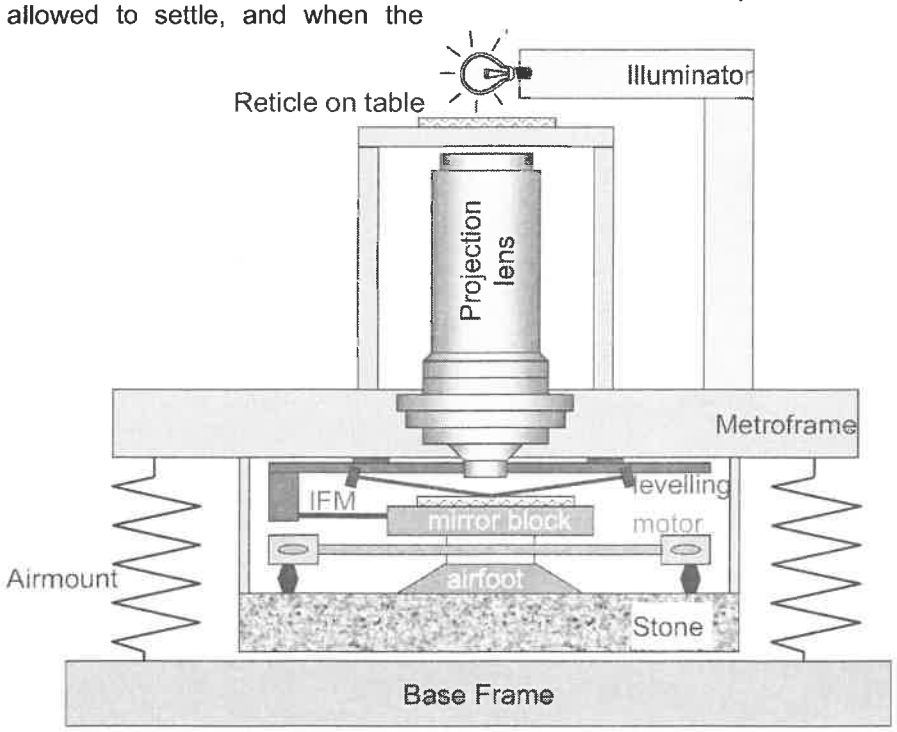

FIGURE 1. Basic layout of the stepper

The main characteristics of this architecture are:

- The stage design mainly concentrated on actuation in its center of mass, to avoid torques acting on the airfoot or mirror block.
- Horizontal reaction forces of the stage were exerted on the stone through a mechanical low-pass filter (the dampers). These reaction forces introduced considerable metroframe movements, which was however of limited importance because it was allowed to wait for settling before exposure. In addition, frame-motion compensators were introduced that substantially cancelled these motions.
- Stage dynamics were dominated by stiffness in mechanical bearings, and frame dynamics excited by stage reaction forces.

2 THE SCANNER

At some point in time, the scanning principle replaced the stepping method. In a scanner, the die is exposed in a scanning fashion, while illuminating only a thin slit of light. The wafer stage and reticle stage then move in opposite directions during exposure, with a ratio defined by the projection lens magnification. The main advantage lies in the optics: only a small part of the lens is used, allowing lens optimisation for this smaller area. In addition, the die size can be extended without building a larger, more expensive, lens. Figure 2 shows the basic scanner principle.

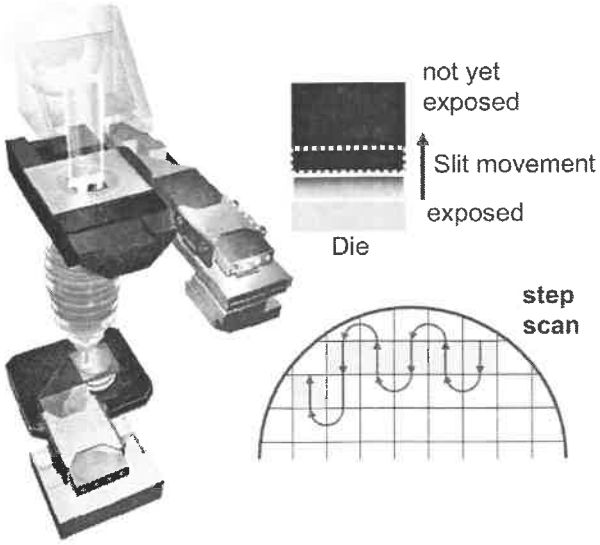

FIGURE 2. The scanning principle

For the stage, the scanning principle has some major consequences:

- Not only the wafer, also the reticle has to move, and both have to reach high accuracy during a scanning motion, both horizontally and vertically (on-line wafer levelling).
- Wafer and reticle motions have to be synchronised with the light source control.

To make this possible, several concept changes were introduced that distinguish a scanner from a stepper. First, the reaction forces are no longer exerted on the metroframe, by mounting the long-stroke motors on the baseframe. Second, to avoid vibrations of the baseframe from entering the accurate stage, a Lorentz short-stroke motor is connected between the long-stroke motor and the stage. For the vertical directions, no change is introduced: reaction forces are still exerted on the stone, and hence guided to the metrology frame. Third, the control scheme is extended with a 'slight' coupling between the vertical and horizontal controllers. The reason for this lies in the scanning levelling: when the stage has to tilt around a horizontal axis to keep the wafer in focus, the stage tends to rotate around its center of mass, introducing a horizontal shift on wafer level. This effect is cancelled by introducing coupling between the horizontal and vertical controllers, as shown in Figure 3.

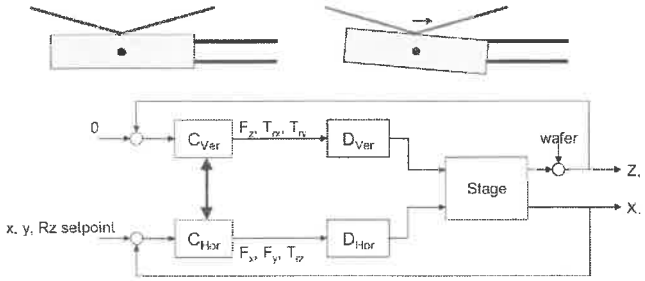

Figure 3. When tilting the stage, a horizontal motion has to be created as well.

The position of the image on the wafer is now determined by both the wafer stage and the reticle stage. Positioning errors of the wafer stage can be corrected by adjusting the reticle stage position, in order to improve the image positioning on the wafer (Figure 4). Of course, correction in the other direction is also possible.

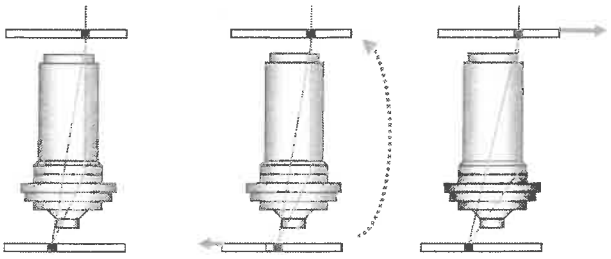

Figure 4. Wafer stage position errors are compensated by reticle stage.

3 TWINSCAN™

When the industry shifted from 200 mm to 300 mm wafers, TWINSCAN™ was introduced, with the aim of compensating the lost throughput due to the larger wafer size by introducing two wafer stages. While one stage exposes a wafer, the other stage measures the horizontal wafer position on the stage, in addition to the wafer height map. The wafer height map is then used for feedforward levelling of the stage during expose. Throughput was increased further by increasing stage accelerations and velocities.

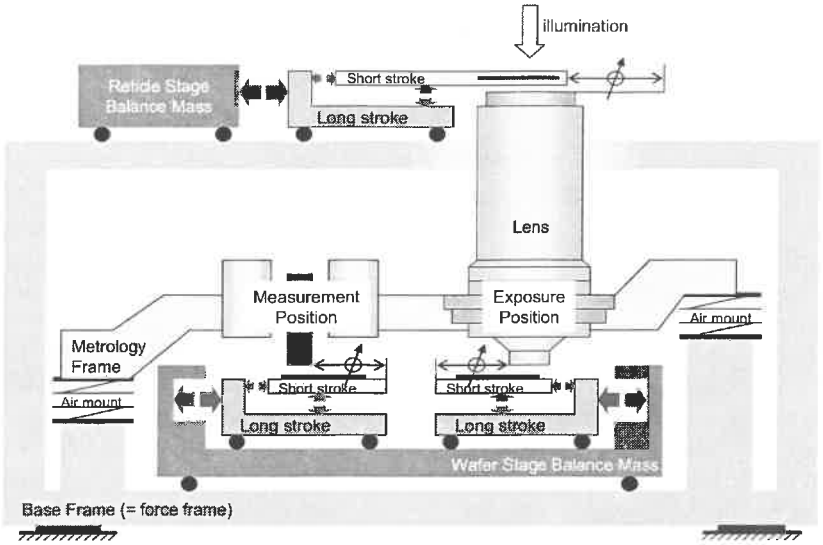

Figure 5. TWINSCAN™ dynamic architecture

Some main contributors to the TWINSCAN™ improvements are (see Figure 5):

- Dynamic architecture: horizontal forces are exerted on balance masses, to further decrease reaction forces from entering the metrology frame. The balance masses have motion freedom in horizontal directions by means of airbearings, which guide them over the baseframe. They absorb the horizontal motor forces by moving in the oppositie direction as the stage itself, keeping the motion distance small by their large mass.
- The vertical forces are exerted on the long-stroke motors, which are mounted to the balance masses. This implies that vertical forces are now guided to the baseframe, because in vertical direction the balance masses are stiffly coupled to the baseframe by means of the airbearings. The usage of vertical Lorentz actuators ensures isolation from vertical baseframe vibrations.
- All stages are equipped with 6-DOF Lorentz actuators and full 6-DOF decoupled control. Any coupling between motion directions can therefore be compensated, and potential vibrations are isolated.
- With increasing scanspeeds, it becomes harder to keep the wafer in the focal plane of the lens using on-line levelling, requiring high bandwidths and complicated look-ahead strategies. Instead, TWINSCAN™ maps the wafer height surface before exposure. The gathered height information is translated into vertical setpoint profiles that are tracked by the stage at exposure.

4 CONCLUSIONS

In the transition from steppers to scanners, the main changes relate to the dynamic architecture, actuator principles, and stage control. In TWINSCAN™, a further perfection in the basic design was made by using balance masses, full 6-DOF Lorentz actuators and 6-DOF stage control, in addition to off-line levelling. Future tools will build on extending and perfectioning the existing architecture.

DOUBLE PATTERNING REQUIREMENTS FOR OPTICAL LITHOGRAPHY AND PROSPECTS FOR OPTICAL EXTENSION WITHOUT DOUBLE PATTERNING

Andrew J. Hazelton[2], Shinji Wakamoto[2], Mike Binnard[1], Shigeru Hirukawa[2], Martin McCallum[3], Nobutaka Magome[2], Jun Ishikawa[2], Céline Lapeyre[4], Isabelle Guilmeau[4], Sébastien Barnola[4], Stéphanie Gaugiran[4]
[1]Nikon Research Corp. of America
Belmont, CA
[2]Nikon Corporation
Tokyo, Japan
[3]Nikon Precision Europe GmbH
West Lothian, United Kingdom
[3]CEA/LETI
Grenoble, France

ABSTRACT

Double patterning (DP) has become part of the development roadmaps of many device manufacturers for half pitches of 32 nm and beyond. Depending on the device layer, many types of DP and double exposure (DE) are being considered. This paper explores requirements of the most complex DP methods: pitch splitting, where line density is doubled through two exposures, and sidewall processes, where a deposition process is used to make the final pattern. Budgets for Critical Dimension (CD) uniformity and overlay are presented with tool and process requirements to achieve these budgets. Experimental results showing 45 nm lines using dry ArF lithography with a k1 factor of 0.20 are presented to highlight some of the challenges.

INTRODUCTION

The resolution of microlithography processes is given by the Rayleigh criterion,

$$R = k1 * \frac{\lambda}{NA}$$

where λ is the wavelength, NA is the numerical aperture of the projection lens, and $k1$ is a factor related to illumination and other effects. Leading edge lithography systems are now using ArF excimer lasers with λ=193 nm, off-axis illumination to provide k1 between 0.25 (the theoretical minimum for a single exposure) and 0.4, and water immersion for NA=1.3~1.35, providing a resolution around 45 nm.

To reach 32 nm resolution, several approaches are under consideration in the industry. EUV lithography (reducing λ to 13 nm) continues to be hampered by development challenges. Extending ArF technology using high index fluids and glasses (increasing NA to 1.5 or more) is appealing, but suitable materials do not yet exist. The only mainstream technology that can be ready for the beginning of 32 nm production is double patterning (reducing k1 below 0.25). These processes, where two separate patterning processes are combined to create the final pattern, face challenges due to significant increases in process cost and technical requirements for the exposure tools to achieve the required accuracy of the final pattern.

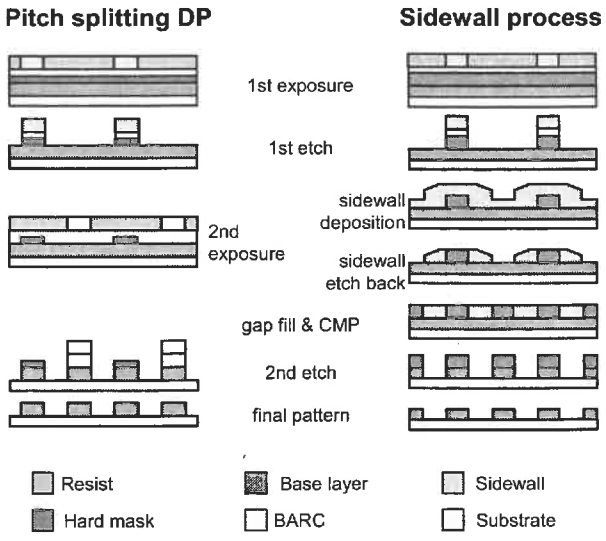

FIGURE 1. Double Patterning process flow.

The appropriate double patterning process depends on the type of pattern being imaged. In addition, requirements for memory circuits and logic circuits are also different. Because of these different requirements, many double exposure and patterning processes have been proposed.[1][2][3][4] This paper explores two of the processes most likely to be used for 32nm production: pitch-splitting double patterning, and sidewall processing.

In pitch-splitting double patterning (DP), after the first exposure, the wafer is developed and some form of processing is performed to maintain the integrity of the first exposure. The wafer is then recoated with photoresist and the second pattern is exposed and developed. Finally, the combined pattern is transferred into the underlying layer. For these processes, either lines or trenches can be printed.[5][6][7]

In sidewall processing, the wafer is exposed only once. After developing and etching, sidewalls are conformally deposited on all sides of the pattern. These sidewalls can then be used as a mask (or spacers for another mask material) for subsequent etching.[8] Because the sidewalls are deposited with nominally constant width, and uniformly on all sides of the exposed pattern, there are limitations on the final patterns that can be generated with this process. In addition, trim exposures may be required to eliminate undesired sidewall patterns.

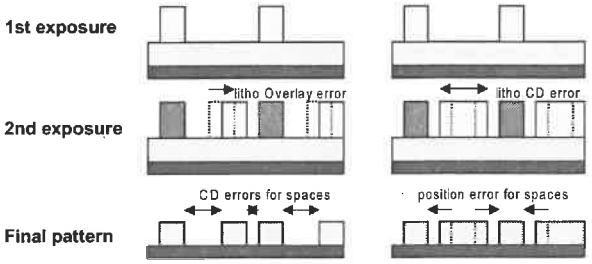

FIGURE 2. Overlay influence on CDU (left) and CD effect on overlay (right)

Two of the critical measures of lithography performance are Critical Dimension Uniformity (CDU) and Overlay. CDU is a measure of the variation (within a chip, across a wafer, or throughout a lot of wafers) of the most critical (typically the smallest) features. Overlay is a measure of the alignment accuracy between the current layer and previous layers. Double patterning is a challenge because CDU and overlay requirements are tighter, and because the effects become intertwined. (Fig 2)

CRITICAL DIMENSION UNIFORMITY

For pitch splitting processes, the final pattern CD uniformity is not the same as the CD uniformity of a single exposure. Assuming a DP process for printing lines, the final CD uniformity of the lines is a combination of the CD uniformities of the two exposures. For the spaces, any overlay error between the exposures will result in a CD error as shown in the left of Fig 2, and any CD error will result in an overlay error of the two patterns as described below (Fig. 2, right). Trench DP processes have corresponding phenomena, but the affected patterns are the lines.

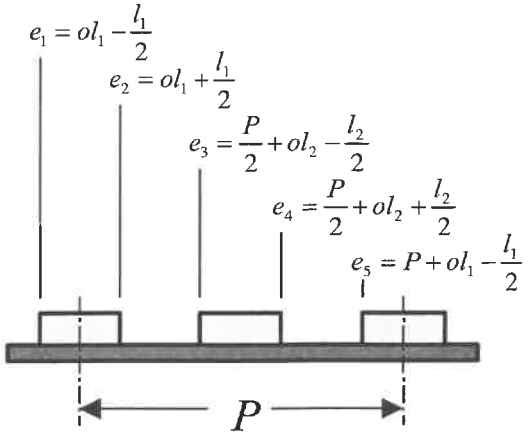

FIGURE 3. Definition of variables for pitch splitting DP.

To understand the lithography requirements to achieve the final CD uniformity target, these effects need to be quantified. Consider two exposures with the following characteristics:

pattern 1 line width: l_1 (mean $\overline{L_1}$; 3σ ΔCD_1)
pattern 2 line width: l_2 (mean $\overline{L_2}$, 3σ ΔCD_2)
pattern 1 pos. offset: ol_1 (mean $\overline{m_1}$, 3σ ΔOL_1)
pattern 2 pos. offset: ol_2 (mean $\overline{m_2}$; 3σ ΔOL_2)

The position offset is the shift between the actual position of the pattern from the ideal position. This offset does not include the repeatable grid and distortion error of the tool. Using these definitions, the tool-to-itself overlay (SO, also called single machine overlay) of the lithography tool can be expressed as:

$$\overline{m_{SO}} = \overline{m_2} - \overline{m_1} \quad (1)$$

$$\Delta OL_{SO} = \sqrt{\Delta OL_2^{\,2} + \Delta OL_1^{\,2}} = \sqrt{2}\Delta OL \quad (2)$$

where the variation of overlay error is assumed to be equal for the two exposures, i.e. $\Delta OL = \Delta OL_1 = \Delta OL_2$.

The position of the line edges can be calculated and are shown in Fig. 3, where *P* is the desired pitch.

CD uniformity for lines

Focusing first on the lines, the width of the lines is simply:

$$\begin{aligned} L_1 &= e_2 - e_1 = l_1 \\ L_2 &= e_4 - e_3 = l_2 \end{aligned} \tag{3}$$

In this case there are two populations of lines with potentially different mean values. The general expression for the pooled variance with individual mean values (μ_1 , μ_2) and standard deviations (σ_1 , σ_2) is:

$$\sigma_p = \sqrt{\frac{\sigma_1^2}{2} + \frac{\sigma_2^2}{2} + \left[\frac{3}{2}(\mu_1 - \mu_2)\right]^2} \tag{4}$$

Assuming the CD uniformity is the same for the two exposures:

$$\Delta CD_{Line} = \sqrt{\Delta CD^2 + \left[\frac{3}{2}\left(\overline{L_1} - \overline{L_2}\right)\right]^2} \tag{5}$$

where $\Delta CD = \Delta CD_1 = \Delta CD_2$.

CD uniformity for spaces

For the spaces, the width of each space is expressed as:

$$\begin{aligned} S_1 &= e_3 - e_2 = \frac{P}{2} + ol_2 - ol_1 - \frac{l_1}{2} - \frac{l_2}{2} \\ S_2 &= e_5 - e_4 = \frac{P}{2} - ol_2 + ol_1 - \frac{l_1}{2} - \frac{l_2}{2} \end{aligned} \tag{6}$$

Assuming the CD uniformity and the standard deviation of the overlay is the same for each exposure, and also noting the difference between the width of the spaces is:

$$S_1 - S_2 = 2ol_2 - 2ol_1 \tag{7}$$

The resultant CD uniformity of the two exposures is:

$$\begin{aligned} \Delta CD_{space} &= \sqrt{\frac{\Delta CD^2}{2} + 2\Delta OL^2 + \left[3\left(\overline{m_1} - \overline{m_2}\right)\right]^2} \\ &= \sqrt{\frac{\Delta CD^2}{2} + \Delta OL_{SO}^2 + \left[3\left(\overline{m_1} - \overline{m_2}\right)\right]^2} \end{aligned} \tag{8}$$

Since single machine overlay does not include the overlay error contributed by reticle matching and intermediate processes, as described later, this expression should be replaced by a more general expression for the overlay in double patterning, resulting in:

$$\Delta CD_{space} = \sqrt{\frac{\Delta CD^2}{2} + \Delta OL_{Line}^2 + \left[3\left(\overline{m_1} - \overline{m_2}\right)\right]^2} \tag{9}$$

CD uniformity for Sidewall Process

For the sidewall process, the calculation is somewhat different. In this case, the final pattern is formed with one exposure process and one deposition process. Similar to the pitch splitting process, consider an exposure and deposition process with the following characteristics:

pattern line width: l_{litho} (mean $\overline{L_1}$; 3σ ΔCD_1)
pattern pos. offset: ol_{litho} (mean $\overline{L_1}$; 3σ ΔOL_{litho})
sidewall width: l_{depo} (mean $\overline{L_1}$; 3σ ΔCD_{depo})

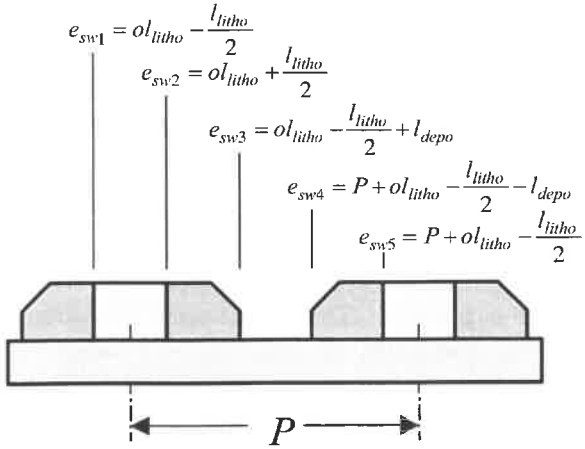
$e_{sw1} = ol_{litho} - \frac{l_{litho}}{2}$
$e_{sw2} = ol_{litho} + \frac{l_{litho}}{2}$
$e_{sw3} = ol_{litho} - \frac{l_{litho}}{2} + l_{depo}$
$e_{sw4} = P + ol_{litho} - \frac{l_{litho}}{2} - l_{depo}$
$e_{sw5} = P + ol_{litho} - \frac{l_{litho}}{2}$
P

FIGURE 4. Definition of variables for Sidewall Process

The line edge positions are calculated and shown in Fig. 4. For a process where spaces between the sidewalls define the final pattern:

$$\begin{aligned} S_{sw1} &= e_{sw2} - e_{sw1} = l_{litho} \\ S_{sw2} &= e_{sw4} - e_{sw3} = P - l_{litho} - 2l_{depo} \end{aligned} \tag{10}$$

In this case, the CD uniformity of the first set of lines is simply ΔCD_{litho} , but the second set of lines includes the additional nonuniformity of the deposited sidewall, with:

$$\Delta CD_{sw2} = \sqrt{\Delta CD_{litho}^2 + 4\Delta CD_{depo}^2} \tag{11}$$

Defining $L_{lithonominal}$ and $L_{deponominal}$ as the respective desired values of L_{litho} and L_{depo} we can define the mean linewidth errors as

$$\begin{aligned} \Delta L_{litho} &= L_{lithonominal} - \overline{L_{litho}} \\ \Delta L_{depo} &= L_{deponominal} - \overline{L_{depo}} \end{aligned} \tag{12}$$

Using equation (4) and noting that

$$P = 2\left(L_{lithonominal} + L_{deponominal}\right) \tag{13}$$

we find the overall CDU of a sidewall process is:

$$\Delta CD_{swGap} = \sqrt{\Delta CD_{litho}{}^2 + 2\Delta CD_{depo}{}^2 + \left[\frac{3}{2}\left(P - 2\left(\overline{L_{litho}} + \overline{L_{depo}}\right)\right)\right]^2} \quad (14)$$

$$= \sqrt{\Delta CD_{litho}{}^2 + 2\Delta CD_{depo}{}^2 + \left[3\left(\Delta L_{litho} + \Delta L_{depo}\right)\right]^2} \quad (15)$$

Investigating the term in parentheses above, we can see that if a positive mean error of the printed line CD is offset by a corresponding negative mean error of the deposited layer, it will not contribute to the CD nonuniformity of the final pattern.

In the case where the final pattern is defined by the sidewalls themselves, the final CDU only depends on the sidewall uniformity, and not on the lithography CDU and overlay, i.e.:

$$\Delta CD_{swWall} = \Delta CD_{depo} \quad (16)$$

OVERLAY

The overlay of the final pattern, similarly, is not the same as the overlay of a single exposure. In the case of lines, the final overlay is a combination of the overlays of the 2 exposures, errors between the mask patterns for the two exposures, and errors introduced by the processing between the two exposures.

Overlay for lines

To calculate the overlay budget for a pitch splitting process, an extension of the typical single patterning process overlay budget will be used. In addition to the tool overlay contribution, a reticle term is required because the exposure of two different patterns requires two separate reticles with potentially two separate illumination conditions. Also, a process term is included because the wafer is removed from the exposure tool and processed between the two exposures. This results in:

$$\Delta OL_{Line} = \sqrt{\Delta OL_{SO}{}^2 + \Delta OL_{reticle}{}^2 + \Delta OL_{process}{}^2} \quad (17)$$

Where $\Delta OL_{reticle}$ is the 3σ matching error between the two reticles and $\Delta OL_{process}$ is the 3σ overlay offset induced by processing between the two exposures.

CD nonuniformity effect on spaces

As shown in the right side of Fig. 2, in the case of spaces, any CD nonuniformity will affect the position of the spaces and result in additional overlay error. The position of each space as a function of the CD is expressed as:

$$\Delta_{S1} = \frac{e_3 + e_2}{2} = \frac{P}{4} + \frac{l_1}{4} - \frac{l_2}{4}$$
$$\Delta_{S2} = \frac{e_5 + e_4}{2} = \frac{3P}{4} - \frac{l_1}{4} + \frac{l_2}{4} \quad (18)$$

noting that the difference between the position of the spaces is:

$$\Delta_{S1} - \Delta_{S2} = -\frac{P}{2} + \frac{l_1}{2} - \frac{l_2}{2} \quad (19)$$

The CDU-induced overlay error of the two exposures is:

$$\Delta OL_{CD-space} = \sqrt{\frac{\Delta CD^2}{8} + \left[\frac{3}{4}\left(\overline{L_1} - \overline{L_2}\right)\right]^2} \quad (20)$$

This contribution can be added to the overlay expression above for the Line DP case resulting in:

$$\Delta OL_{space} = \sqrt{\Delta OL_{SO}{}^2 + \Delta OL_{reticle}{}^2 + \Delta OL_{process}{}^2 + \frac{\Delta CD^2}{8} + \left[\frac{3}{4}\left(\overline{L_1} - \overline{L_2}\right)\right]^2} \quad (21)$$

Overlay for Sidewall Process

In the case of sidewall processes, since there is only a single exposure, the requirements for overlay are not as severe as for pitch splitting. In this case, we can assume the overlay requirement is the same as for a single exposure process at the same node.

TABLE 1. CD Budget for Pitch Splitting, determined by the requirement of 3.3 nm for Space CDU. Only the first two terms contribute to CDU for lines.

	Budget	Space CDU	Line CDU
$\overline{L_1} - \overline{L_2}$	0.5 nm	3.3 nm	2.6 nm
ΔCD	2.5 nm		
$\overline{m_{SO}}$	0.5 nm		
ΔOL_{Line}	2.3 nm		

32 NM NODE REQUIREMENTS AND EXPOSURE TOOL BUDGET

For the 32 nm node, the 2007 version of the ITRS specifies CDU of 3.3 nm, with a significantly tighter specification for transistor gates of 1.3 nm. Since pitch splitting technology is expected to be used for metal layers, we assume a requirement of 3.3 nm for double patterning CDU. Similarly, the ITRS specifies overlay of 6.4 nm. In a single exposure process, the tool-to-itself overlay occupies about 70% of this budget, so a reasonable assumption for the

lithography portion of the overlay budget in a pitch splitting process is 4.5 nm.

CD uniformity budget

Starting with the CDU requirement of 3.3 nm for Spaces (because fewer factors contribute to Line CDU), we determine the budget components shown in Table 1. As explained above, the effects of overlay must be included in the CDU budget for spaces.

The CDU values in this budget include contributions from the etching process as well as from lithography. As etching is a multiple step process (resist trimming, BARC open, hard mask open), each step must be carefully tuned to minimize its added nonuniformity. For this purpose, multiple adjustments (RF power, Temperature, gas flow, etc.) are available on recent etch tools that allow step by step tuning of the etch uniformity. Recently, CDUs of approximately 1 nm have been reported for leading edge lithography tools [9], so it should be possible to achieve these CDU targets. The difference in average CD between the two exposures can be influenced by topography changes and different etch biases for the two exposures.

However, the overlay mean and 3σ budget terms shown in Table 1 are significantly tighter than those of current exposure tools. Achieving these target will require special measures.

TABLE 2. CD Budget for Sidewall Process, determined by 3.3 nm allowance for Gap CDU.

	Budget	Gap CDU	Wall CDU
Δ CD litho	2.5 nm	3.3 nm	
Δ CD deposition	1.1 nm		1.1 nm
adjustment error $\Delta L_{litho} + \Delta L_{depo}$	0.5 nm		

The lithography budget for Sidewall Processing (Table 2) is the same as for pitch splitting processes. The requirements for deposition and adjustment error are fairly tight and more investigation is required to ascertain the feasibility of these values.

Overlay budget

As shown in equation (17), the overlay budget has contributions from the exposure tool, reticle matching, and the intermediate processing. Based on these three elements, the following overlay budget is specified for the pitch splitting process. The mean plus 3σ overlay target is chosen to be the same as required for the CDU.

TABLE 3. Overlay Budget

	Budget	ΔOL_{line}
Overlay mean	0.5 nm	
Overlay 3σ	1.8 nm	2.3 nm
Reticle matching	1.0 nm	
Process factors	1.0 nm	
DP overlay mean+3σ	2.8 nm	

As the current generation of exposure tools have overlay specifications of around 6.5 nm, the requirement of 0.5 nm + 1.8 nm = 2.3 nm for the 32 nm node is a significant reduction. This requires a detailed review and careful adjustment of the overlay error sources. Three particular areas are targeted:

1. Air fluctuations of the interferometer measurements of the wafer and reticle stage positions. Thermal fluctuations of the air inside the exposure tool change the refractive index along the beam path. Countermeasures include significantly reducing the thermal fluctuations and significantly reducing the length of the beam path.
2. Thermal drift of machine components affecting intra- and inter-lot stability. Frequent calibration of the system through use of the Tandem Stage technology on Nikon's latest exposure tools can significantly reduce these errors.
3. High-order grid and shot shape correction. Lower order grid order correction is commonly applied, but higher order grid corrections will be required. In addition, shot shape errors caused by reticle distortion will also be necessary.

Achieving the matching specifications for the reticle will also be a challenge. For example, reticle writing error should be reduced from current levels of 1.0~1.5 nm to 0.5 nm or less. Further studies are required to confirm the reticle budget, but it seems likely a single mask writer will be required for each pair of masks.

EXPERIMENTAL RESULTS

Experiments were performed on a Nikon S307E dry ArF scanner (NA 0.85) connected to a Sokudo RF^3 track, and a Lam Versys etching tool. The targeted imaging is similar to an immersion process, however, where 32 nm features imaged at 1.30 NA have a k1 of 0.22, the 45 nm features targeted on the 0.85 NA system have a k1 of 0.20. Reducing k1 to this level while maintaining sufficient process window is a challenge.

A critical part of the process is ensuring that the profile of the first hardmask is not overly compromised by the second etch step. An example of this can be seen in Fig. 2 where during transfer into the second hardmask, the first feature is compromised. Further work is required, but this shows etching is not a trivial part of the double patterning process.

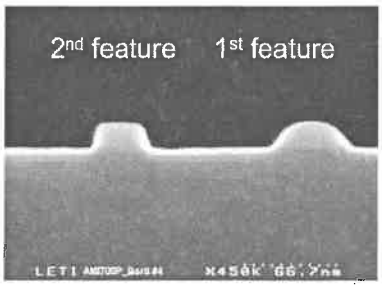

FIGURE 5. SEM images of initial DP etched patterns.

SEM images of etched 45 nm line/space patterns, a k1 of 0.20, can be seen in Fig. 3. The CDU of the (dark) lines is good, but due to some slight pattern misalignment, the (light) space CDU is not as good. Further optimization of the process is required.

CONCLUSIONS

To meet the requirements for 32 nm processes, several types of double patterning have been proposed. Pitch splitting has the most severe requirements for lithographic processing with overlay accuracy < 3 nm, Δ CD 2.5 nm, reticle matching 1 nm, and process-induced overlay error 1 nm required. These can be achieved in time, but will be very challenging. To delay the need for adopting these technologies, several alternative processing methods are expected to be employed for the 32 nm node including: sidewall processing for memory, pattern layout simplification for logic, further improvements in k1 factors, and novel double exposure techniques for logic manufacturing.

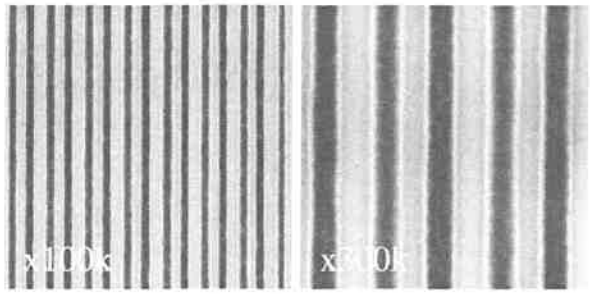

FIGURE 6. Etched 45 nm line/space patterns with k1=0.20

REFERENCES

[1] M. Burkhardt, et al., "Dark Field Double Dipole Lithography (DDL) for Back-End-of-Line Processes," Proc. of SPIE Vol. 6520, 65200K (2007).

[2] H. Nakamura, et al., "Ultra-low k1 oxide contact hole formation and metal filling using resist contact hole pattern by Double L&S Formation Method." Proc. of SPIE Vol. 6520, 65201E (2007).

[3] Y. Trouiller, et al., "32 nm SOC printing with double patterning, regular design, and 1.2 NA immersion scanner." Proc. of SPIE Vol. 6520, 65201D (2007).

[4] H. Ohki, et al., "Experimental study on non-linear multiple exposure method." Proc. of SPIE Vol. 3051, pp. 85-93 (1997)

[5] C. Lim, et al., "Positive and Negative Tone Double Patterning Lithography." Proc. of SPIE Vol. 6154, 615410 (2006).

[6] R-H. Kim, et al., "Double Exposure Using 193nm Negative Tone Photoresist." Proc. of SPIE Vol. 6520, 65202M (2007).

[7] RHEM private communication.

[8] W. Jung et al., "Patterning with amorphous carbon spacer for expanding the resolution limit of current lithography tool." Proc. of SPIE Vol. 6520, 65201C (2007).

[9] K. Goto, et al., "Adapting Non Topcoat Process to High Volume Manufacturing." 4th Symposium on Immersion Lithography, PR-02 (2007).

[10] A.J. Toprac, "AMD's Advanced Control of Poly-gate Critical Dimension," Process, Equipment, and Materials Control in IC Manufacturing V, A.J. Toprac and Kim Dang (editors), Proceedings of SPIE, 3882, 62 (1999).

METROLOGY AND MOTION

Prof. Dr. Ir. Jan van Eijk
Advanced Mechatronics
Technical University of Delft / MICE bv
The Netherlands

SUMMARY
In next-generation semiconductor equipment positioning performance in the order of one nanometer and better will be required. Achieving such performance creates novel challenges for the sensor systems and disturbance levels in equipment. Over the past 25 years a number of system concepts have been developed. Most recent breakthrough has been obtained with the rigorous separation of metrology and functional parts from the moving elements. Bringing the low-frequency acceleration levels down from about 10 mm/s^2 to less than 0.1 mm/s^2. Enabling this is the class of "Floating Carpet" 6DOF motion concepts. The Delft University has demonstrated such a device and achieved sub-nanometer performance.

CHALLENGES IN SEMICONDUCTOR TOOLS
In semicon patterning and inspection the following main developments can be observed;

1. The size of wafers has grown to 300 mm and a next step in size is considered.
2. The allowable motion errors must be made ever smaller and as a result the allowable dynamic servo errors must be less than 1 nanometer.
3. To achieve affordable manufacturing the productivity must grow and therefore the speed and acceleration of wafer stages is rising. Where 5 m/s^2 was acceptable for a long time the desired accelerations of wafer stages are growing to 20 m/s^2 and beyond.

The combined influence of these developments calls for new concepts in machine design.

LARGE SIZE SUBSTRATES
When the growing size of tools is analyzed it is seen that extreme performance is achieved in tools with limited size, such as AFM and miniature SEM systems. Due to the limited size the natural frequencies of mechanics or control can be relatively high. These frequencies have a linear relation with the inverse of the typical dimension. Thus at the 10 mm scale of an optical disc actuator a frequency of control around 5 kHz is achieved. Even with disc accelerations of 0.5 m/s^2 dynamic following errors of about 0.5 nm can be achieved.
In contrast the wafer size of 300 mm will lead to typical frequencies 30 times lower, leading to about 150 Hz. To achieve a dynamic error below 0.5 nm in this case requires the disturbances in the target accelerations to be less than 0.5 mm/s^2. In real machines achieving such performance is not easy. With the step to 450 mm wafers requirements become again about twice as demanding.

HIGHER ACCELERATIONS
It is obvious that the mass of wafer carriers is growing with wafer size. Typical systems have a mass between 10 and 20 kg. When such a mass is accelerated with 20 m/s^2 reaction forces up to 400 N are needed. With a frame mass of about 2000 kg such a driving force initiates a frame acceleration of 200 mm/s^2. It will be obvious that it is not an option to wait for the frame to settle to a level about 400 times smaller. Steps must be taken to avoid the occurrence of large frame accelerations.

CONCEPTUAL SOLUTIONS
The following list gives an overview of some solutions;

1. Frame motion compensation. Here an external motor applies a force on the frame that is equal but in opposite direction of the reaction force in the machine.
2. Active Isolators that measure the frame acceleration and generate an external restoring force. Of course this can be combined with a feed-forward correction as in 1.
3. Driving the stage from outside the frame on the vibration isolators. Thus a reaction force is directly applied to the external world. In figure 1. a sketch of such a concept is shown. Here a voice coil actuator drives the

stage while its "stationary" part is driven from a linear motor mounted outside the machine frame.

4. Balancing masses can be used to avoid reaction forces in the frame. With the "stationary part" of the linear motor connected to a 200 kg frame sitting on air bearings the inertial stroke of the stator would be about 30 mm for a 300 mm wafer move. Such a solution will effectively reduce the frame accelerations.
5. Mounting the stage drive motors outside the machine frame and following the frame in all 6 Degrees of Freedom (DOFs). Using a stage suspended in 6 DOF's, driven from the fixed world and following the frame through active control. Such systems are called "Floating Carpets". In this solutions no changing forces are applied on the frame of the machine, in this way the frame is considered to be a "Metrology Frame".

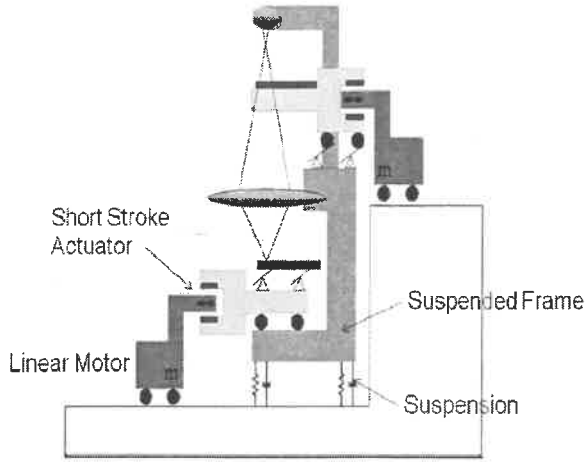

FIGURE 1. Schematic Concept for a scanning Litho tool with driving forces on the Wafer stage generated with a Lorentz Short Stroke Actuator connected to a Linear Motor. The Linear Motor is mounted outside the suspended Frame.

FLOATING CARPET AND METROLOGY FRAME

In a research program of the Delft University the combination of a metrology frame and a 6DOF manipulator based on reluctance type actuators. The intended application is the mastering of Blu Ray optical discs, possibly using E-beam exposure in a vacuum environment. Here the typical dimension is about 150 mm. No large accelerations are applied in this system but it demonstrates some of the typical challenges of designing Floating Carpet manipulators.

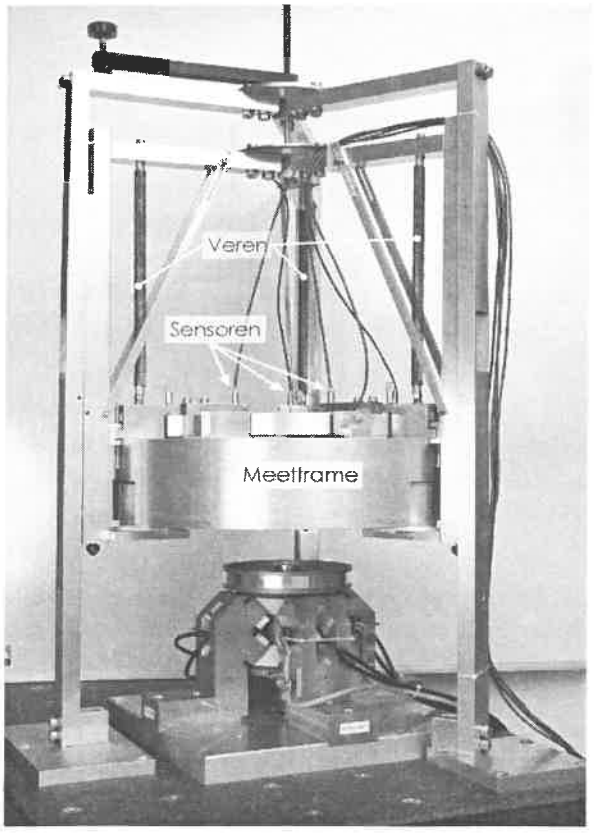

FIGURE 2. Overview of the total set-up with the Rotor at the bottom and the Metrology Frame suspended over it. The Metrology frame is raised to obtain visibility for the Rotor.

In figure 2 the total set-up of the system is shown. Simple suspension is used for the vibration isolation of the frame. Capacitive sensors are mounted in the metrology frame measuring the position of the rotor. In fig. 3 a drawing of the rotor manipulator is shown. Eight reluctance actuators are used to control the 5 degrees of freedom. The rotation is driven by a separate motor. The gravity compensator is responsible for generating the lift force without creating position dependence. The goal is to control the position of rotor relative to the frame and to avoid vibrations from the floor to excite the rotor through "magnetic stiffness" effects. In the specific laboratory conditions the low frequency acceleration of the floor is about 50 mm/s2 and the acceleration of the suspended

frame is about 8 mm/s^2. The final performance obtained, with a non spinning rotor, was an accuracy better than 1.5 nm. (Lit. 1)

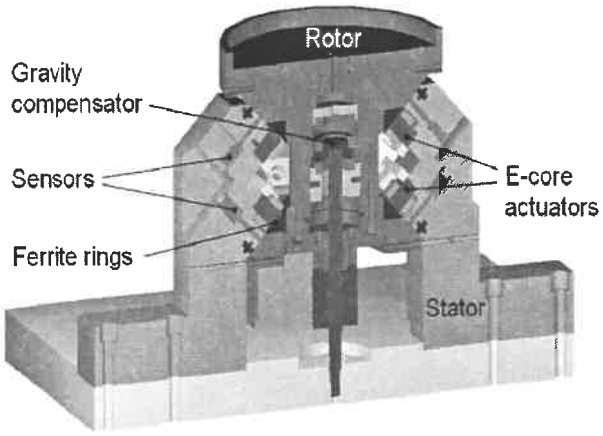

FIGURE 3. Schematic of the design of the Rotor system with the Reluctance Actuators and the Gravity Compensator.

In this example the potential of 6DOF "Floating Carpet" concepts can be clearly demonstrated. The same concept is used in the Lithography tools of ASML in the Netherlands.

REFERENCES

[1] Jabben, I. Mechatronic Design of a Magnetically Suspended Rotating Platform. PhD thesis Technical University Delft, 2007 ISBN 978-90-9022523-4.

A HIGH-BANDWIDTH, HIGH-PRECISION, TWO-AXIS STEERING MIRROR

Daniel J. Kluk, David L. Trumper
Mechanical Engineering Department
Massachusetts Institute of Technology
Cambridge, MA

INTRODUCTION

This paper focuses on the design, fabrication, assembly, and testing of a high bandwidth two-axis mirror positioner for precision optical platforms, which we refer to as the Advanced Fast Steering Mirror (AFSM). This novel positioner consists of a platform driven in two rotational axes by flux-steering electromagnetic actuators, and controlled via position feedback loops. The AFSM is designed for beam stabilization tasks in lithography, laser communication, lidar, and similar optical applications. We have experimentally demonstrated small-signal system bandwidth of 10 kHz using optical quad-cell feedback and a two-channel analog control architecture. The AFSM has a travel range of ± 3.5 mrad, and a measured angular acceleration of 10^5 rad/sec^2.

The work presented here grew out of the Mars Lasercomm demonstration program of 2005, in which MIT Lincoln Labs played a major development role. Fast steering mirrors (FSMs) are a critical component for optical communication technology [1]. Their purpose is to accurately track a desired position, and sufficiently reject disturbances such that beam pointing errors are small enough to allow acquisition and tracking of optical signals over long distances. In the case of the Mars Lasercomm program, a laser beam originating from a Mars-orbiting satellite must be pointed within 400 nanoradians RMS error in order to allow communication with an earth-based detector array [2].

A picture of the AFSM is shown in Figure 1. The mirror to be steered is attached to the square platform at the center. The two actuated degrees of freedom, θ_x and θ_z, lie in the plane of this mirror platform. Four permanent magnet biased flux steering actuators apply forces to magnetic armatures bonded to the edges of the mirror platform. Each actuator applies a force to the armatures in either the positive or negative direction normal to the mirror surface, thereby developing torques which rotate the mirror in the actuated DOFs. The actuators are rigidly mounted to the base, while the mirror platform is suspended relative to the base by a set of flexures. The flexures include an axial rod to restrain mirror-normal motions, and a set of captured rubber sheets within the actuators to restrain the lateral degrees of freedom.

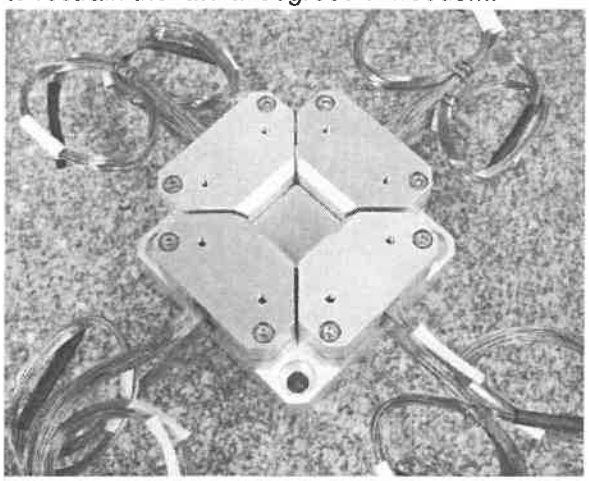

FIGURE 1. Photograph of the Advanced Fast Steering Mirror (AFSM). The actuator wires are coiled in this picture.

A CAD rendering of the final AFSM design iteration is shown in Figure 2. The mirror which comprises the heart of the optical system is located in the center, and is drawn in red. The two principal actuated degrees of freedom, θ_x and θ_z, are indicated by the dashed lines running through the mirror center.

Figure 3 illustrates the AFSM hardware in cross-section. This view is obtained by conceptually slicing Figure 2 vertically through either the θ_x or θ_z axis. There are two types of flexures, which in concert constrain the four non-actuated DOFs. The metallic axial flexure constrains the mirror in the Y translation DOF, while the four elastomeric flexures constrain X and Z translation and θ_y rotation (note that two of the four elastomeric flexures are out-of-plane and are therefore not shown).

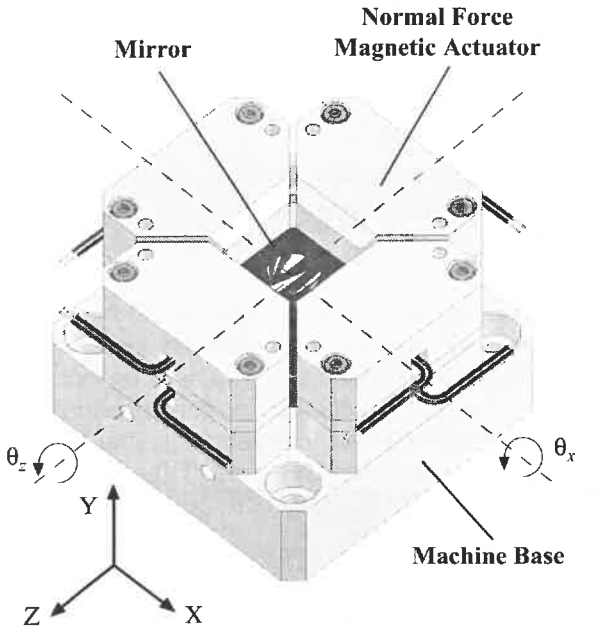

FIGURE 2. Isometric CAD rendering of the Advanced Fast Steering Mirror (AFSM).

Also illustrated are the capacitance probes that measure the mirror displacements relative to the housing, and the associated clamping mechanism that holds them in place.

DISCUSSION OF PRIOR ART

Fast steering mirror technology has existed in various stages of sophistication for many years. The most common approach is to use a pair of single axis mirrors optically linked so as to provide two-axis steering of a beam of light. These single axis devices are typically driven by a galvanometer and are still widely used in many scientific and industrial machines, such as bar code scanners, high speed product printing, medical imaging devices, and laser light show entertainment displays [3].

Piezoelectric designs, such as those marketed commercially by Physik Instrumente Corporation (PI), allow higher stiffness and bandwidth, and a simple mechanical configuration; however, they suffer from limited angular travel, higher hysteresis losses, and require relatively expensive high voltage drive amplifiers[4].

Several fast steering mirrors for space applications have been developed in the past two decades, and a few designs have seen flight service. Over the past several decades, Ball

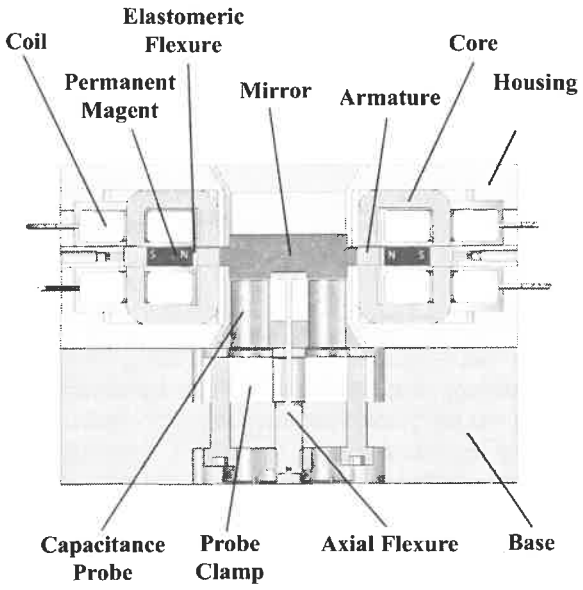

FIGURE 3. Cross-sectional view of the AFSM showing the mirror, flexure supports, capacitance probes, and actuators.

Aerospace Corporation has produced a wide range of devices for air and space flight service [5]. The Ball designs typically employ electromagnetic actuation via Lorentz-force (voice coil) drives. Mirror sizes are on the order of tens of millimeters, and typical published bandwidths range from 250 to 1000 Hz, with 1.5 kHz as the highest advertised bandwidth. Other published designs include a two-axis conical scanner driven at resonant frequency [6] and a fully-suspended six DOF mirror operated using MIMO control [7].

Lincoln Laboratory has also developed fast steering mirrors over the last two decades. Lincoln's current suite of fast steering mirrors, several of which have seen flight service, are based on development work in the early 1990s by Loney [1]. This mirror design has been dubbed the High-Bandwidth Steering Mirror (HBSM); he current variant is the HBSM-D. Loney's design demonstrates a bandwidth of 10 kHz and an angular range of ± 13 mrad, for mirror apertures of 10 and 16 mm.

AFSM KEY TECHNOLOGIES

Two key novel technologies are adopted in the AFSM described here. First, as part of his PhD thesis, Xiaodong Lu developed a normal-force, flux steering actuator configuration that he successfully employed in a single degree-of-freedom fast tool servo system [8]. The actuator relies on

normal force principles similar to a solenoid, but has the advantage of being nearly linear in both current and stroke, thus making it easy to control. Theoretically, it is capable of accelerations of up to 4000g, which is 100 times that of a voice coil constructed from copper wire (40g).

The second technology ([9], [10]) uses viscoelastic materials (specifically, elastomers such as neoprene and silicone) as kinematic bearings in place of traditional metallic flexures. Elastomeric bearings are advantageous because they impart natural, frequency-dependent damping properties to the dynamic structure, are compact, and have low mass. Moreover, when configured in the proper geometry, such bearings provide stiff kinematic constraint of non-actuated DOFs, yet are compliant in the actuated DOFs.

AFSM MECHANICAL DESIGN

The moving mirror platform and its supporting flexures is shown in Figure 4, In this view, the mirror, armatures, and kinematic supports (axial flexure and rubber bearings) are shown. The basic mirror envelope is 30x30x10 mm in the X, Z, and Y axes, respectively. The 30 mm lateral dimensions allow for a large optical beam aperture, and the 10 mm normal dimension imparts required structural stiffness.

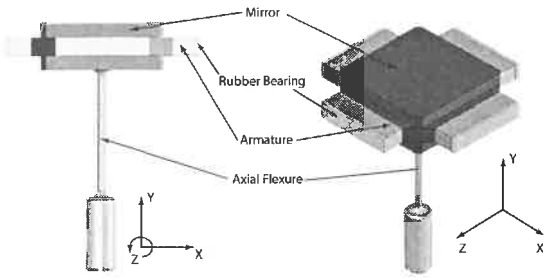

FIGURE 4. CAD rendering of the AFSM moving mirror and armature design, along with its flexure supports..

Elastomeric Bearing Design

Although commonly in use for decades in bridge bearings, automobile suspensions, and the like, the use of elastomers in precision machine applications is a relatively recent development. In their theses, Cuff [10] and Barton [9] provide detailed treatments of the history, properties, and the precision engineering applications associated with elastomer flexures and bearings.

As explained in Lindley [11], the design equations for elastomeric flexure supports are nearly identical to those derived from the theory of elasticity for metallic flexures; however, the effective compression modulus must be modified to account for the near-incompressibility of the material. Iterating through the stiffness calculations for various elastomer hardness material thickness values, we arrived at the bearing design given in Table 1, below.

Property	Value
Length l	20 mm
Width w	4 mm
Thickness t	1 mm
Hardness	70 Shore A
Eff. Compression Modulus E_c	30 MPa
Shear Modulus G	1.7 MPa
Shape Factor S_{rect}	1.66
Shear Strain at Full Deflection	20%
Compressive Stiffness k_c	2.4 N/μm
Shear Stiffness k_s	0.136 N/μm
Torsional Stiffness k_{tor}	4.7 N-m/rad

TABLE 1. Elastomer Flexure Design Values

ACTUATOR ELECTROMAGNETIC DESIGN

The architecture of one of the AFSM actuators is displayed in Figure 5. The actuator consists of two symmetric halves, upper and lower, each of which contain an electrical coil wrapped around a magnetically permeable core. Each coil and core is rigidly potted in place to the actuator housing, which is displayed in green in the figure.

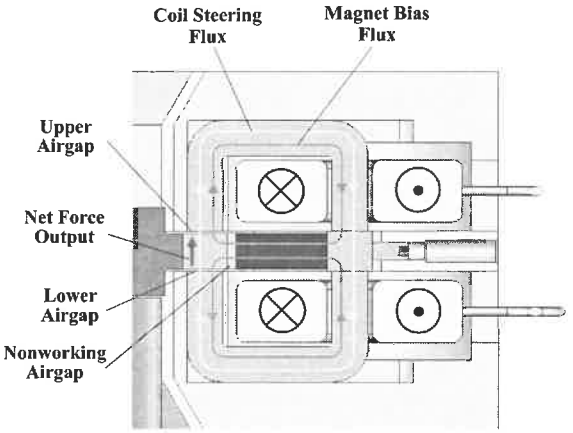

FIGURE 5. Flux-steering actuator principle of operation.

At the heart of the actuator is a permanent magnet, which generates a DC biasing flux that

passes through the armature and returns through the upper and lower core halves. This flux is indicated by the magenta-colored arrows in Figure 5. The amount of flux passing through one core half or another is determined by the position of the armature, as well as any steering flux from the coils. With the armature in the neutral position and no coil current, the magnet flux is evenly divided between the upper and lower core halves, and thus there is no net force on the armature.

The two actuator coils are wired in series, and thus behave as if they were one coil. Applying a positive-valued current produces a magnetic flux pointing upward at the working airgaps, as indicated by the yellow arrows in Figure 5. The flux differential between the two working airgaps in this case causes a net upward force on the armature. Reversing the current direction reverses the steering flux, and thus produces a net downward force on the armature.

The above description is confirmed as follows via flux analysis of the actuator magnetic circuit. For the analysis we neglect leakage and fringing losses, and assume the magnetic core and armature materials to have infinite permeability. The magnet permeability is assumed to be equal to air. Using these assumptions, we obtain the magnetic circuit layout depicted in Figure 6.

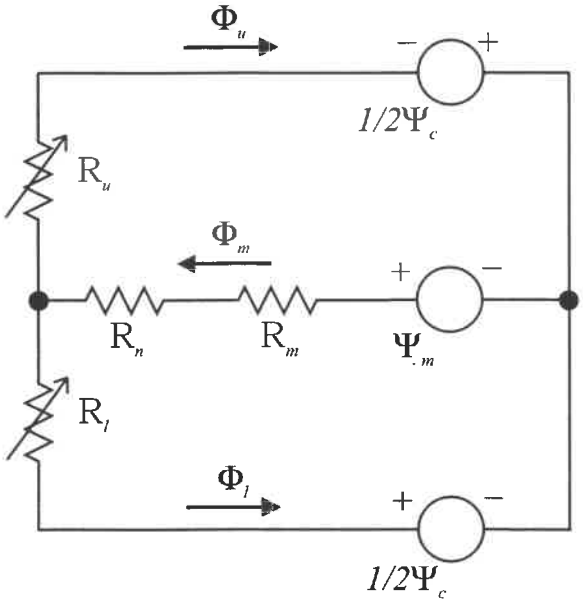

FIGURE 6. The AFSM actuator magnetic circuit used for flux analysis.

We determine the unknown fluxes in terms of the known airgap reluctances and magnetomotive forces from the coils and permanent magnet as follows:

$$\Phi_m = \frac{1/2\Psi_c(\mathcal{R}_l - \mathcal{R}_u) + \Psi_m(\mathcal{R}_l + \mathcal{R}_u)}{\mathcal{R}_{mag}(\mathcal{R}_l + \mathcal{R}_u) + \mathcal{R}_l\mathcal{R}_u} \quad (1)$$

$$\Phi_u = \frac{\Psi_c(\mathcal{R}_{mag} + 1/2\mathcal{R}_l) + \Psi_m\mathcal{R}_l}{\mathcal{R}_{mag}(\mathcal{R}_l + \mathcal{R}_u) + \mathcal{R}_l\mathcal{R}_u} \quad (2)$$

$$\Phi_l = \frac{-\Psi_c(\mathcal{R}_{mag} + 1/2\mathcal{R}_u) + \Psi_m\mathcal{R}_u}{\mathcal{R}_{mag}(\mathcal{R}_l + \mathcal{R}_u) + \mathcal{R}_l\mathcal{R}_u}. \quad (3)$$

Next, we normalize the armature displacements about the null position, denoting the upper and lower actuator airgaps g_u and g_l as

$$g_u = x_o - x \quad (4)$$

$$g_l = x_o + x, \quad (5)$$

where x_o is the airgap length with the actuator in the null position, and x is the armature displacement relative to this position. With this definition, we obtain the magnetic circuit reluctances as

$$\mathcal{R}_{mag} = \frac{l_m + g_n}{\mu_o a_p} \quad (6)$$

$$\mathcal{R}_u = \frac{x_o - x}{\mu_o a_p} \quad (7)$$

$$\mathcal{R}_l = \frac{x_o + x}{\mu_o a_p} \quad (8)$$

$$\Psi_m = M_o l_m \quad (9)$$

$$1/2\Psi_c = Ni_c \quad (10)$$

where $l_m + g_n$ is the combined length of the magnet and nonworking airgap, μ_o is the permeability of vacuum, a_p is the working and nonworking airgap pole area, and M_o is the permanent magnet magnetization.

With the circuit fluxes known, the force on the armature in the working direction is given, via the normal component of the Maxwell stress tensor as

$$F_{act} = \frac{\Phi_u^2 - \Phi_l^2}{2\mu_o a_p} \qquad (11)$$

Of course, a lateral force is also present (in the nonworking direction) due to the permanent magnet flux on this surface, but this force is supported by the elastomeric bearing, and is ignored in the analyses herein.

Examining Equations 11, 2, 3, 7, and 8, it is evident that the actuator force output is nearly linear. This is because even though the individual upper and lower gap forces vary in a nonlinear manner, the *difference* between the squares of the upper an lower gap fluxes is nearly constant, regardless of the coil current or armature position. This difference is established by the biasing effect of the permanent magnet, and as such, it is primarily the magnet properties that determine the force sensitivity of the actuator.

The nonlinearity in the actuator force profile arises from the $\mathcal{R}_l\mathcal{R}_u$ term in the denominator of Equations 2 and 3. However, if the upper and lower gap reluctances are kept small, the $\mathcal{R}_{mag}$ term will dominate, resulting in an essentially linear force profile. For our design values, the actuator has a peak force output of 36 N, and an equivalent magnetic stiffness of -0.1246 N/μm. Note that this negative stiffness tends to destabilize the static equilibrium. In our design it is countered by the larger positive stiffness of the elastomeric bearings.

SYSTEM IDENTIFICATION AND COMPENSATOR DESIGN

We have tested the AFSM using both the capacitive sensors local to AFSM, and with an external optical quad cell measuring the spot location of a laser beam reflected off the AFSM mirror. Due to space limitations, only the optical feedback based testing is described herein. The plant dynamics using optical feedback are shown in Figure 7. Here, the first few structural modes of the AFSM mirror are revealed. The first one appears at about 23 kHz, which agrees very well with the first two modes at 22 kHz predicted by finite element analysis. An additional group of modes is visible at 35 kHz and the 40 to 50 kHz band, which is also consistent with the FEA predictions of the higher modes. For this plant, the transfer

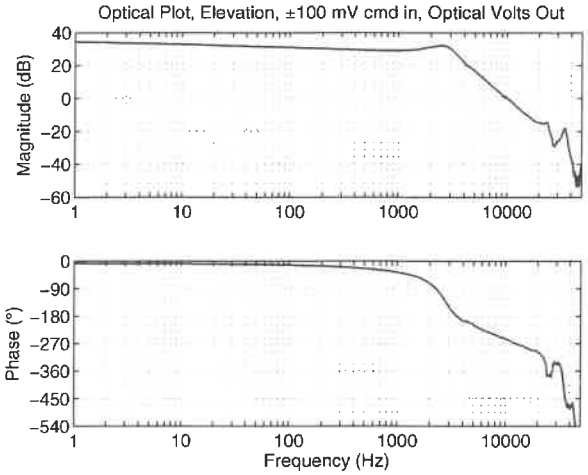

FIGURE 7. Measured AFSM elevation axis frequency response using optical quad cell feedback.

function of the controller is:

$$G_c(s) = 2\frac{\left(\frac{s}{2\pi(3000)} + 1\right)^3}{\left(\frac{s}{2\pi(50)} + 1\right)\left(\frac{s}{2\pi(30000)} + 1\right)^2} \qquad (12)$$

For this controller, the gain and phase margins are 11 dB and 40 degrees, respectively, as shown in the plots in Figure 8.

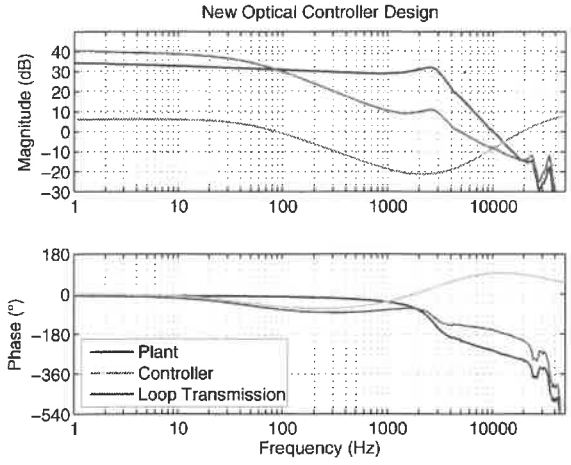

FIGURE 8. Second optical controller design (green) with measured plant dynamics (blue) and resulting loop transmission (red).

The closed-loop frequency response of the system using optical feedback has a 10 kHz, -3 dB bandwidth. The closed-loop step response is

plotted in Figure 9. The response has a rise time of about 40 microseconds, a settling time of 400 microseconds, and overshoot of 25%.

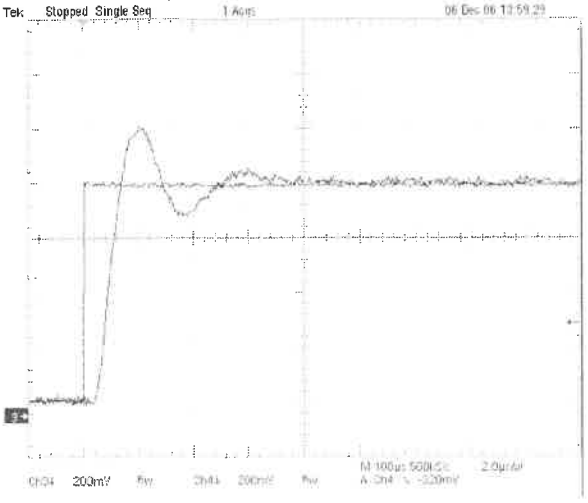

FIGURE 9. Closed-loop 800-millivolt (20 μrad) step response using optical feedback.

The high performance demonstrated with our AFSM prototype indicates that this is a promising approach for beam steering mirrors for ground and airborne applications.

ACKNOWLEDGMENTS

This work was accomplished at the MIT Lincoln Laboratory. A significant component of the research was funded through the Lincoln Laboratory Advanced Concepts Committee program. This work forms part of the first author's Master of Science thesis submitted to the Mechanical Engineering Department at the Massachusetts Institute of Technology[12]. We thank Fred Sommerhalter for his considerable skills in fabricating the actuators for the AFSM.

REFERENCES

[1] Loney, Gregory C. *High Bandwidth Steering Mirror Research.* Project Report IRP-15, MIT Lincoln Laboratory, 1992.

[2] Hawe, Larry Edward II. *Control of a Fast Steering Mirror for Laser-Based Satellite Communication.* M.S. Thesis, Massachusetts Institute of Technology, 2006.

[3] Cambridge Technology. *How to Choose a Closed Loop Galvanometer Based Scanner.* http://www.cambridgetechnology.com/news/Choosing_A_Galvanometer.html.

[4] Physik Instrumente GmbH. *Fast Steering Mirros with Piezoelectric Drives.* http://www.physikinstrumente.com/en/products/steering_mirror/index.php.

[5] Ball Aerospace Corporation. *Custom Fast Steering Mirrors.* http://www.ballaerospace.com/fsm_precision.html. Accessed November 2005.

[6] Hardy, Bruce and Paul Hauser. *Scanning Apparatus and Method That Avoids Unwanted Reactions.* U.S. Patent No. 6,612,192, September 2003.

[7] Medbery, James and Avanindra Gupta. *Stable Controller Design of a Six Degree-of-Freedom Magnetically Suspended Fine Steering Mirror (MSFSM).* SPIE Active and Adaptive Optical Components, Volume 1543, 1991.

[8] Lu, Xiaodong. *Electromagnetically-Driven Ultra-Fast Tool Servos for Diamond Turning.* Ph.D. Thesis, Massachusetts Institute of Technology, 2005.

[9] Barton Martinelli, Augusto E. *Rubber Bearings for Precision Positioning Systems.* M.S. Thesis, Massachusetts Institute of Technology, 2005.

[10] Cuff, David P. *Electromagnetic Nanopositioner.* M.S. Thesis, Massachusetts Institute of Technology, 2007.

[11] Lindley, P. B. *Engineering Design With Natural Rubber.* The Malaysian Rubber Producers' Research Association, Brikendonbury, England, 1974.

[12] Kluk, Daniel J. *An Advanced Fast Steering Mirror for Optical Communication.* M.S. Thesis, Massachusetts Institute of Technology, 2007.

Active Magnetic Bearing
Controls Strategy and Calibrations

Meindert L. Norg*[1], Rob Tousain*[2], and Jan van Eijk*[3]

***Philips Applied Technologies**
Eindhoven, the Netherlands
www.apptech.philips.com

INTRODUCTION

Guide-ways in positioning systems (stages) for semiconductor applications are often realized by air bearings and roller bearings. For X-Y stages, a so-called H-bridge design is often utilized (see *FIGURE 1*): an X-stage-module stacked on top of a Y-stage-module. Although these bearing systems are passive, and therefore seemingly rather cost-effective compared to active systems, the motion performance is limited. Moreover, active bearing systems have the advantage that additional motion degrees of freedom are automatically obtained

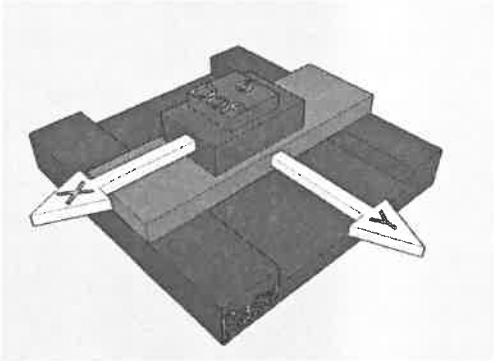

FIGURE 1. Standard High Precision Stage. The X- and Y-modules form the long stroke X-Y stage. The top module is a 6 DoF short stroke module. This article describes the integration of the 6-DoF module with the X-module.

Until now, nm-level motion performance in 6 degrees of freedom (DoF) has been realized only through the application of a hybrid stage concept, i.e. by stacking an active 6-DoF short stroke stage-module providing fine adjustments (e.g. horizontal and vertical) on top of a passive long stroke X-Y stage-system, as depicted by the top module in *FIGURE 1* (see also [1]).

In our work we successfully integrated the X-module and 6-DoF-module functions by using Active Magnetic Bearing (AMB) technology. The result is a full 6 DoF active positioning system with nm-level motion performance in one single module. It allows for a much simpler stage design that can be reproduced at low cost, suitable for next generation semiconductor applications.

Motivation

Applying AMB technology combining long stroke and 6-DoF functions in one single module yields significant advantages, compared to stages with conventional passive bearings, as is highlighted in [2], [3].Specific advantages are:

- Full 6-DoF motion capability (eliminating the need for stacking modules)
- Ultra-low contamination (no contact, no lubrication, enabling vacuum applications)
- Infinite static stiffness, enabled by the active position feedback control-loop.
- Applicability in machine architectures with isolated metrology frames, enabled by force-type actuators.

Contents

This article concentrates on the basic design of an Active Magnetic Bearing stage. After describing the basic building blocks, and the controller schematics, three examples of calibrations are presented:

- AMB non linearity compensation;
- Linear Motor Gain Calibration and the
- Static Force Compensation.

---

[1] Meindert Norg is now with Norg Consulting *"Applied Controls Engineering"*, Canonsburg, PA, USA, Meindert@NorgConsulting.com
[2] Rob Tousain is a Senior Technologist at Philips Applied Technologies, Mechatronics Program. High Tech Campus 7, Eindhoven, The Netherlands, Rob.Tousain@philips.com
[3] Jan van Eijk is now with MICE BV, Eindhoven, the Netherlands, Jan@MiceBV.nl

BASIC DESIGN

Philips Applied Technologies has designed and built several motion platforms utilizing AMBs. This section describes some of the building principles of a one-long-stroke, 6-DoF stage.

Active Magnetic Bearing Element

Basically, an AMB can be comprised of an E-shaped piece of SiFe transformer laminations, equipped with a coil around the center leg (see *FIGURE 2*). In order to compensate for gravity, and to ensure a more linear operating behavior, a permanent magnet is added to the center leg. A typical magnet would be 1 mm thick NdFeB with a residual flux density of 1.4 Tesla. A counter material, called 'the bridge', is placed opposite to the AMB legs. The total flux generated by permanent magnet and coil generates an attracting force between the AMB legs and the bridge. The current through the coils is used to control this force and, as a result, the position of the stage.

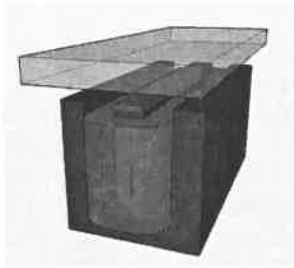

FIGURE 2. AMB element.

Stage Actuators

A theoretical minimum of 6 actuators is required in order to actively move a stage in 6 degrees of freedom (DoF). For reasons of symmetry, guided by design principles and additional requirements a combination of 6 AMBs and 2 linear motors was used to build a 6 DoF stage; a total of 8 motors, enabling actuation of one long- and 5 short-stroke movements.

The long stroke X-axis is guided (that is: stage movements are constrained) in vertical direction (Z, Rx and Ry) by four vertical AMBs (see *FIGURE 3*). Simultaneously, these AMBs are used as short stroke actuators in Z, Rx and Ry directions, enabling stage excursions up to 1 mm and 1 mrad. As mentioned before, AMBs are equipped with permanent magnets, each compensating 25% of the stage mass. As a result, the coils only need to offset the magnet force when moving away from the nominal position, resulting in a very energy efficient floating mechanism.

For movements in horizontal Y direction, the stage is equipped with two opposing AMBs, allowing for up to 1 mm stroke.

Finally, two standard off-the-shelf brushless linear motors are used as X- and Rz-axis actuators, one on each side of the stage.

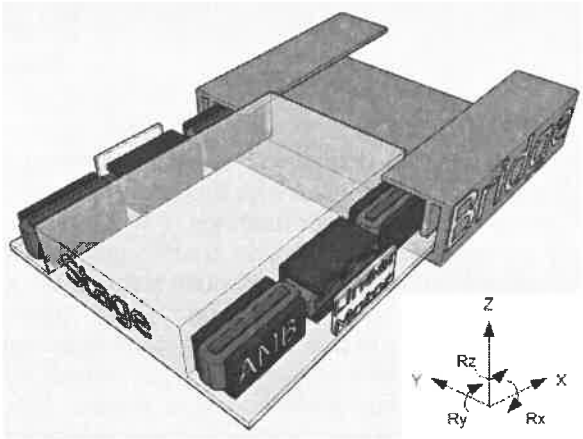

FIGURE 3. AMB Stage. The AMBs and the Linear Motor Coils are connected to the 'Stage'. The stationary part serves as the 'bridge' and holds the linear motor magnets.

Position Sensors

To measure the stage position, a combination of 8 displacement sensors is used: 6 short-stroke probes, and two encoders. The probes measure the stage's Z, Rx, Ry and Y location; the linear encoders measure the X long stroke position and the Rz orientation of the stage. The signals of these sensors are fused to calculate the 6 DoF stage position (also called the 'logical position'). A 6 DoF Laser Interferometer (IFM) measurement system is installed in addition to above mentioned sensors to achieve the accuracies required for semiconductor applications.

Imprint Lithography Prototype

As part of the US Navy and SPAWAR project "NanoImprint lithography at Manufacturing Scale" (NIMS, contract#: N66001-06-C-2003) a prototype AMB high precision stage has been designed and built for an Imprint Lithography application (see [4] and *FIGURE 4*).

In this application, the substrate on the stage is positioned underneath and moved up against a template (not shown). The negative image of the template features is transferred onto the substrate. Some of the design characteristics of the stage are: 30 kg moving mass; 0.4 m X-range; 1 m/s max velocity and 2.5 m/s^2 acc.

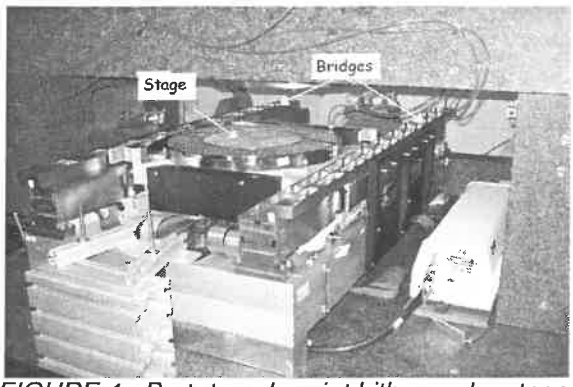

FIGURE 4. Prototype Imprint Lithography stage.

Slow stictionless move

In today's leading edge lithography applications, the ratio between the wafer size (300 mm) and smallest feature size (50 nm) is significant; it is therefore important to combine the ability of high velocities and accurate positioning. To demonstrate the absence of stiction and friction (which often prohibit accurate positioning) a 0.5 nm/s move in X-direction was performed (see *FIGURE 5* and [5]). With a maximum velocity of 1 m/s, this design supports an impressive dynamic range for the velocity of over 9 orders.

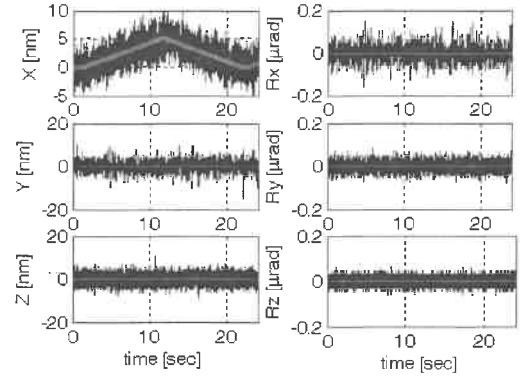

FIGURE 5. 6-DOF stage position, during 0.5 nm/s move (b-) with setpoint (g-). Notice the absence of cross talk from X to the other axes.

Summary

In this section the basic building blocks and architecture of an AMB stage are described.
Four Z-AMBs enable movement and guidance in Z, Rx, Ry, and two Y-AMBs move and guide the stage in the Y direction. The X- and Rz-directions are actuated by the two linear motors.
Six inductive probes and two encoders measure the location and orientation of the stage, which is calculated in the controller. An Interferometer system can be installed for increased accuracy.

CONTROLER SCHEMATICS

This section describes some aspects of the controller implementation. First a short description of the controller hardware is presented. Then, the sensor- and actuator transformations and the AMB non linearity compensation methodology are discussed.

Controller Hardware

The servo controller is implemented on proprietary controller hardware and software developed at Philips Applied Technologies.
The controller schematics are designed and implemented in Simulink, and the C-code, generated using MathWorks' Real Time Workshop is downloaded and executed on an industrial PC running VxWorks. Commercially available IO-cards (some with application specific firmware) are used to interface with sensors and actuators. This platform is capable of controlling multiple axes, allowing for a stacked X-Y stage configuration. The flexibility of Simulink allows for complex interactions between individual axes, such as cross axes Feed Forward, and the implementation of sensor fusion and actuator non-linearity compensation. The complete controller design, comprising of approximately 150 filter orders and several 100s of parameters, offers the capability of tracing 15 parallel signals at sampling frequency and executes at a rate of up to 5 kHz.

A higher level software layer governs the start-up-and shut-down procedures, setpoint generation and measurement system switching.

Sensor Transformation

In many multi-DoF industrial control solutions, kinematics relations are used to decouple the motion system into rigid body modes to facilitate decoupled controller design (see "Sensor Transform." block in *FIGURE 6*). This decoupling transforms sensor readings into logical positions and orientations (X, Y, Z, Rx, Ry and Rz) by means of the Sensor Transformation. For an optimal decoupling, this logical position represents the location and orientation of the Center of Gravity (CoG) of the stage.

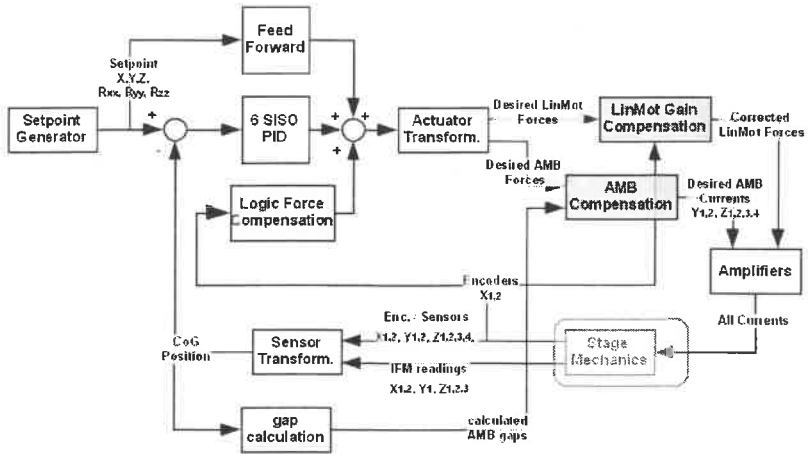

FIGURE 6. Basic control scheme: PID feedback and feed-forward with setpoint generator, geometric decoupling matrices and actuator linearization algorithm.

Actuator Transformation

On the controller's actuator side, controller forces and torques are distributed over 8 available actuators, by means of an Actuator Transformation. The Actuator Transformation (AT) is basically the (pseudo) inverse of the relation between the set of actuator forces and their resulting logical Forces and Torques:

$\vec{M} = AT^{-1} \cdot \vec{F}$ where:

- $\vec{M}$ is a vector containing the logical Forces and Torques: $[F_x \quad F_y \quad F_z \quad T_x \quad T_y \quad T_z]^T$
- AT represents the Actuator Transformation
- $\vec{F}$ is a vector with individual actuator forces: $[F_{X1} \quad F_{X2} \quad F_Y \quad F_{Z1} \quad F_{Z2} \quad F_{Z3} \quad F_{Z4}]^T$

AT^{-1} is constructed using the actuators-orientations and -positions relative to the CoG.

AMB Non linearity Compensation

Since the AMBs are reluctance actuators, the *Current-Force* relationship is non-linear, and inversely related to the *Gap* between AMB and counter material. In some AMB applications (for example AMB systems that operate at a fixed position, like rotary applications) this non-linear relationship is dealt with by introducing sufficient controller robustness. The instability introduced by the non-linearity of the AMBs is stabilized by the controller, which is acceptable at bandwidths of more than a few 100 Hz.

When a relatively large range of motion is desired (> 400 μm), the non-linearity of the AMBs is thought to be too large (in combination with relatively low 50 Hz bandwidth), to be compensated for by the controller. Therefore, in the presented application, in order to achieve the highest possible performance, the AMB's non linearity is compensated by means of parametric functions calculating the required *Current* based on desired *Force* and a calculated air-*Gap* for each individual AMB. The *Force-Current-Gap* relationship is obtained through linear regression using an e.g. 5-parameter polynomial function and a data set obtained through off-line actuator identification (see [6] for more details).

Summary

In this section the controller hardware was presented. Further, the Coordinate Transformation, Actuator Transformations and AMB's Nonlinearity Compensation were described.

CALIBRATIONS

This section describes some of the calibrations methods that were developed and implemented in order to optimize the stage's servo performance of stage. The calibrations relate to the controller components that are indicated by the dark grey blocks in *FIGURE 6*. First an in-situ identification of the AMB characteristics is presented, where a sinusoidal disturbance is injected while the AMBs response is measured. Secondly, a similar identification of the Linear Motor Gain is described. Finally, the static force correction is described, revealing the AMB's magnetic hysteresis.

AMB Calibration

The off-line measured *Force-Current-Gap* relationship is an approximation of the real AMB's behavior in the stage. Factors like mounting errors and amplifier gain variations will contribute to a discrepancy between model and actual relationship. Especially for applications where an exact knowledge of the stage-forces interacting with the process-forces is important (for example in the Imprint Lithography application this stage

was designed for) having a proper AMB model is beneficial. In order to improve the static model of the actual AMB characteristics, an in-situ calibration is executed.

In order to find the real force, generated by each of the AMB's at any given location for any given current, a calibration is implemented where a sinusoidal disturbance is injected in the servo loop. The forced stage movements and motor currents are used to identify the AMB model. With the real current and the real position known (through separate calibrations of the amplifiers and the measurement system), the only unknown is the real force generated by the AMBs. These forces are estimated by using the stage's position and the already discussed AT.

FIGURE 7 shows the result of one AMB calibration. In this case, a 10 kg mass was added to the stage in order to perform a second measurement at a higher force level.

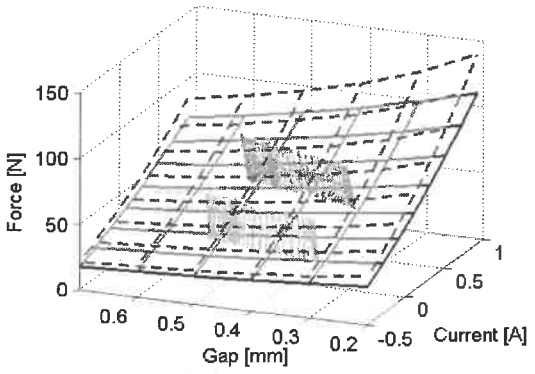

FIGURE 7. In-situ calibration results of one of the Z- AMB. Original model (dashed) and new model (solid). Note that the two data-sets are located on the (solid) plane.

One of the flaws of this calibration is that there is no guarantee that diagonally opposing AMB's are not 'fighting' each other during the acceleration and deceleration phases. This is undesirable from both a calibration and an energy dissipation viewpoint. A separate calibration could, still under floating conditions, search for a minimal RMS value of the four real AMB currents, minimizing this 'fighting' behavior.

Linear Motor Calibration

The accuracy of the acceleration feed forward has a significant impact on the settling time. In our application, a linear motor gain variation of 10 % was observed, likely caused by the non-optimal location of the linear motor coil assembly in the magnet track, and the HALL-effect sensor based commutation. This section describes the linear motor gain calibration.

The contents of the "LinMot Gain Compensation" block from *FIGURE 6* are detailed in *FIGURE 8*.

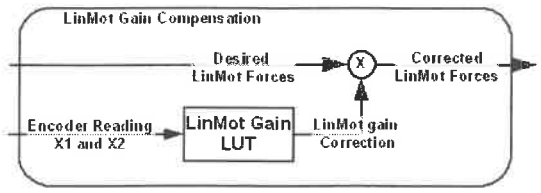

FIGURE 8. Implementation of LinMot Gain Compensation.

The goal of this calibration is to determine the linear motor gain as function of the stage position. Again, a sinusoidal disturbance is injected into the servo loop, this time forcing the stage to 'shake' in the X-direction and, due to the difference in motor gain between motor 1 and 2, also in Rz. The data is traced, analyzed and translated into lookup tables for the actuator K-factors.

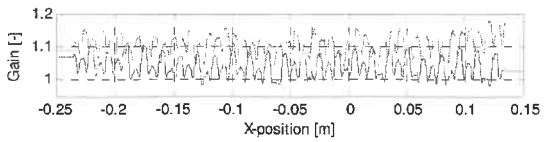

FIGURE 9. Result of LinMot Gain calibration for Linear motor 1 (solid) and 2 (dashed).

FIGURE 9 shows the results of one of these calibrations. In this case, the average real linear motor gain is slightly smaller than designed, resulting in a larger than 1 compensation gain. The spatial frequency content of the gain correction indicates that most of the gain error is present at the 4th harmonic of the 30 mm linear motor magnet pitch.

Static Forces Calibration

During slow movements in the long stroke X direction, disturbance forces from cables, cogging forces and other position dependent factors are evident from observing the controller's integrators. A fairly straightforward correction is to measure these forces and torques during a slow move back and forth covering the X-axis stroke, as a function of stage position, and adding them to the controller output. The upper plot in *FIGURE 10* shows the result of the calibration measurement (solid) and the calculated correction (dashed).

The lower plot in *FIGURE 10* shows the effectiveness of activating the generated Static Force Calibration. Most observable in this plot is the residual hysteresis force in the X-direction.

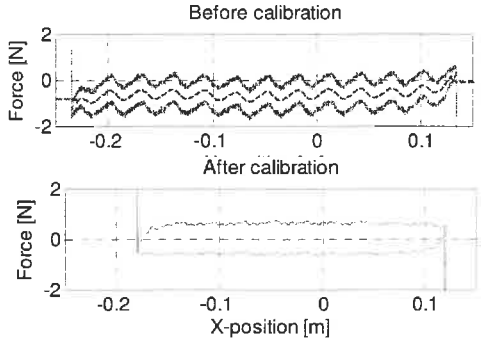

FIGURE 10. Static Force Calibration measurement (UPPER) with measurement (solid) and resulting calibration table contents (dashed), and the result after calibration (LOWER).

In Active Magnetic Bearings, hysteresis is generally observed during movements in both the direction of the magnetic force (e.g. Z and Y) and perpendicular to this magnetic force (X); and indeed both are observed in our application and influence the accuracy of force generation of AMBs.

The observed hysteresis force is approximately ± 0.6 N while moving in the X direction and ± 0.05 N during a ± 100 µm move in Z direction with a note that increasing the range of the Z-move also increases the measured hysteresis.

Summary

In this section, three examples of calibrations as applied to the Active Magnetic Bearing stage are described:

1. In-situ calibration of the AMB behavior,
2. Linear Motor Gain calibration and
3. Static Force Compensation.

From the third calibration magnetic hysteresis became evident.

CONCLUSION

In this article, a description of a high precision Active Magnetic Bearing stage is given. Using a combination of Active Magnetic Bearings and linear motors as actuators, a full 6 DoF free floating stage was designed and built.

The position feedback controller is described, including the Sensor- and Actuator-Transformation that deal. A measurement of a slow 0.5 nm/s move was shown demonstrating the frictionless design characteristic.

Several calibrations that aim to improve the overall performance in general and the accuracy of force generation in particular, are described:

- AMB non linearity compensation;
- Linear Motor Gain Calibration and the
- Static Force Compensation.

The last compensation revealed the hysteretic characteristic of Active Magnetic Bearings.

REFERENCES

[1] M. van de Wal, G. van Baars, F. Sperling, O. Bosgra *Multivariable H∞/µ feedback control design for high-precision wafer stage motion* - Control Engineering Practice, 2002

[2] A.T.A. Peijnenburg et. al., *in Proceedings of the 31st International Conference on Micro- and Nano-Engineering, Vienna, Austria*, 2005, pp 1372-1375

[3] A.C.P. de Klerk, et al. *Design of a next generation 6DoF stage for scanning applications in vacuum with nanometer accuracy and mGauss magnetic stray field*; Proc. of the 19th ASPE Annual Meeting, Orlando, Florida, October 24-29 2004, pp 60-63

[4] J.P.M. Vermeulen, et al. *'Active magnetic bearing technology suitable for nanoimprint lithography applications*, Proc. of the Nanoimprint and Nanoprint Technology 2006 (NNT2006) in San Francisco, CA, November 15-17, 2006

[5] M.L.Norg, et al. Active Magnetic Bearing Technology applied in High Precision Application. Magnetics Magazine, FALL 2007.

[6] M.L.Norg, et al. Active Magnetic Bearing Technology applied in High Precision Application. 2007 Magnetics Conference, April 3-5 2007, Chicago, IL, USA

SIX DEGREES OF FREEDOM MAGNETIC LEVITATION STAGE USING NEW ACTIVE MAGNETIC BEARINGS

Young-Man Choi[1], Jaehwa Jeong[2], Dae-Gab Gweon[1], and Dongmin Kim[3]
[1]Department of mechanical engineering
KAIST
Daejeon, Korea
[2]Department of control and instrumentation engineering
Korea University
Youngi-Gun, Chungnam, Korea
[3]Mechatronics center
Samsung Electronics
Suwon, Gyeonggi-do, Korea

INSTRUCTIONS

A magnetic levitation (Maglev) stage is one of the solutions for positioning mechanism in the high vacuum environment because of its non-contact nature. It does not need any fluid supply and exhaust which lower the degree of vacuum. Frictionless movement gives excellent scanning performance. Another advantage of a maglev stage is high control bandwidth which works to reduce settling time and improve disturbance rejection. Because a maglev stage inherently has six degrees of freedom(DOF) motion ability, it can control vertical level (Z) and two tilt (Θ_x and Θ_y) of a target specimen as well as positions in XY Θ_z. A conventional stage using mechanical guides is quite weak at ground vibration whereas a maglev stage possesses good performance in vibration isolation because it can actively control the transmissibility. At the same time, it can make infinite quasi-static stiffness using integral control [1].

On the other hand, there are some difficulties to implement magnetic levitation. Consuming power to compensate the gravity, it generates heat which deforms mechanical structures and changes properties of actuators or sensors. And often it requires a nonlinear control algorithm to compensate nonlinear behavior of levitating mechanism. Basically, more than six high precision sensors are needed because maglev stage should be controlled in six degrees-of-freedom.

In order to levitate a moving platform precisely, electromagnetic actuators have been widely used. However, an electromagnetic actuator should consume power continuously to suspend the weight of the moving platform. In this case, heat generated by coil current deforms the mechanical structures and deteriorates system accuracy. Thus, we need gravity compensating mechanism in addition to electromagnetic actuator.

Hol proposed a gravity compensator using permanent magnets and a coil [2]. Because it had an axis-symmetric structure, large static force and small force variation could be achieved.

In this paper, we propose a new active magnetic bearing using Halbach magnet arrays [3] and Lorentz coils for a magnetic levitation stage. Because the Halbach magnet array can confine magnetic flux density, the proposed magnetic bearing exerts larger levitation force than the conventional one. The repulsion and attraction between Halbach magnet arrays and a target magnet are main sources of levitation, which doesn't generate any heat when compensating the gravity. Also, the Lorentz coil can make dynamic force in the same direction of the static levitation force using the confined magnetic field by the Halbach magnet arrays.

This active magnetic bearing is named a Halbach linear active magnetic bearing (HLAMB). Due to its large force capacity and embodied Lorentz coils, the HLAMB has a compact size. Moreover, the HLAMB is optimally designed to have near-zero stiffness within its workspace.

Using the proposed HLAMB, a maglev dual-servo stage is designed. A dual-servo stage uses a coarse stage for long strokes and a fine stage for high precision positioning. The coarse stage is an H-type gantry stage consisting of three linear motors and conventional linear guides, which moves x and y direction in plane with 300mm × 300mm travel range. The fine stage is levitated by four HLAMB upon the

coarse stage. The position of the fine stage is measured by three laser interferometers and three capacitive sensors. Because both the voice coil motor and the HLAMB have linear characteristics and no mechanical connection, six degrees of freedom levitation is obtained.

HALBACH LINEAR ACTIVE MAGNETIC BEARING

Conceptual design

Figure 1 shows the concept of the HLAMB. To levitate the target magnet, Halbach magnet arrays are used. Each Halbach magnet array has three segments of permanent magnet. The upper and the lower magnets are magnetized horizontally whereas the middle magnets are magnetized vertically. The target magnet is magnetized horizontally. The upper magnets attract the target magnet and the lower magnets repulse it. Thus, the net static force is almost doubled and its direction becomes vertical.
Due to the confined magnetic field, a Lorentz coil can be embodied compactly in the Halbach magnetic bearing.

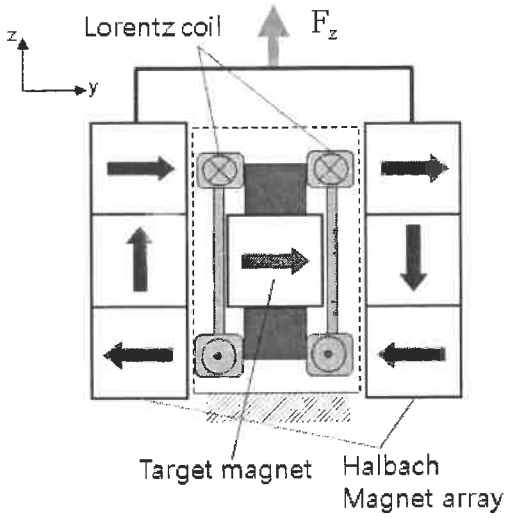

FIGURE 1. Halbach linear magnetic bearing

For high dynamic force, Lorentz coil should be located at the point where the magnetic field density is high. As shown in Fig. 2, the magnetic field in the middle of the Halbach magnet arrays is not strong enough. Because of symmetric magnet location, the magnetic field is also symmetric. Near the Halbach magnet array magnetic field density is strong but the direction is not exactly horizontal. Thus, we used two coils which are located symmetrically near the Halbach magnet arrays. Their resultant force has only z-directional component and resultant moment becomes zero. The two Lorentz coils and the target magnet are fixed together on ground (actually, on the coarse stage) and the two Halbach magnet arrays are fixed on the moving platform (actually, on the fine stage).
However, there is a problem with the Halbach magnetic bearing. Due to the non-uniform magnetic field, the target magnet cannot have uniform levitating force when the position of the target magnet is changed from the nominal position. Simultaneously, there comes large parasitic force in y-direction. Thus, we optimized the dimensions of the Halbach magnetic arrays and the locations of the magnets in order to make the system have small Z stiffness and Y force. The Lorentz coils are located to achieve maximum dynamic force.

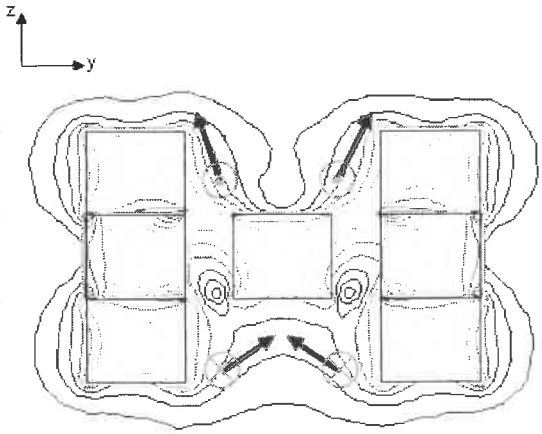

FIGURE 2. Magnetic field of HLAMB

TABLE 1. Design specifications of the HLAMB

	Spec.	Unit
Total size	40×40×42	mm^3
Static Z force	24.45	N
Dynamic Z force	6.53	N/A
Max. Z stiffness	11.2	N/m
Max. Y force	0.024	N
Max. Torque about x-axis	0.025	Nm
Power @ continuous 20N dynamic force	28.2	W
Natural frequency of internal mode	0.34	Hz

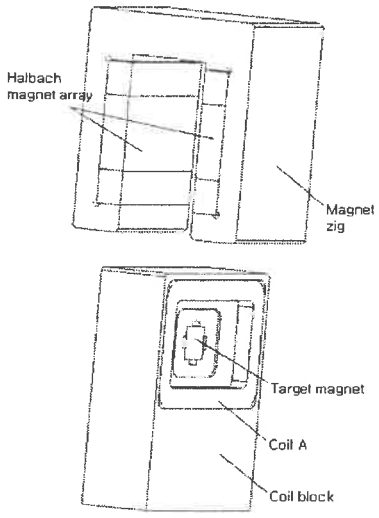

FIGURE 3. 3D model of the HLAMB

Final design

The result of the design optimization is presented in Table 1. Fig. 3 shows the 3D modeling of the finally designed HLAMB. The middle magnet becomes longer to decrease Z stiffness and parasitic forces. The maximum Z stiffness is about 11.2N/m which results the natural frequency of 0.34Hz. The Y force and torque about x-axis are very small enough to be ignored. For fabrication, Halbach magnet arrays are assembled in the magnet jig. The magnet jig is made of aluminum alloy. Two coils and one target magnet are assembled in a monolithic coil block. To eliminate eddy current, the coil block is made of polycarbonate. The total size of the HLAMB is about 40mm×55mm×65mm.

6-DOF DUAL-SERVO STAGE

In this section, a 6-DOF dual servo stage is designed. The coarse stage to carry the 6-DOF maglev fine stage is designed. And the fine stage is configured using the HLAMBs and voice coil motors.

The coarse stage is an H-type XY stage shown in Fig. 4 The Y platform moves in the y-direction on the Y1 and Y2 mechanical guide by two linear motors. Two linear scales measure each position of both ends of the Y platform. From the readings of the two linear scales, we can know the translation in the y-direction and the rotation about z-axis of the coarse stage. On the Y platform, the X platform moves in x-direction by the X motor. The position of the X platform is measured also by a linear scale (not shown here). Each linear motor has the continuous force of 139N and the peak force of 695N.

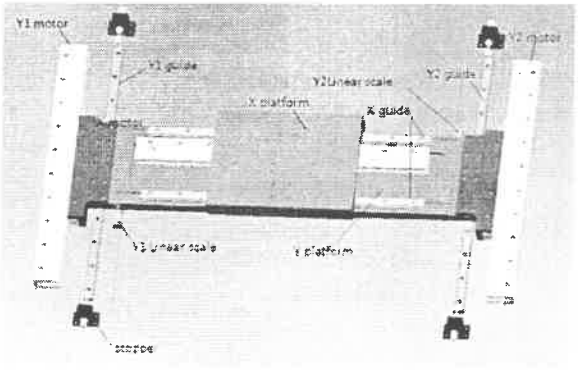

FIGURE 4. Coarse stage

The fine stage is installed on the X platform of the coarse stage. To achieve 6-DOF positioning ability, four HLAMB and four voice coil motors (VCM) are used. The HLAMBs controls 3-DOF including Z, Θ_x and Θ_y. The VCMs controls 3-DOF including X, Y and Θ_z. As shown in Fig. 5, the HLAMBs and the VCMs are symmetrically placed on the X platform. All coils are fixed to the X platform while all magnet assemblies are fixed to the moving platform of the fine stage. In this case, we can prevent heat generated by the coils from transferring to the plane mirrors. Also, it does not have any wiring or connection from the coarse stage. The in-plane components of the position of the moving platform are measured by laser interferometers using the two plane mirrors. The out-of-plane components are measured by three capacitive sensors.

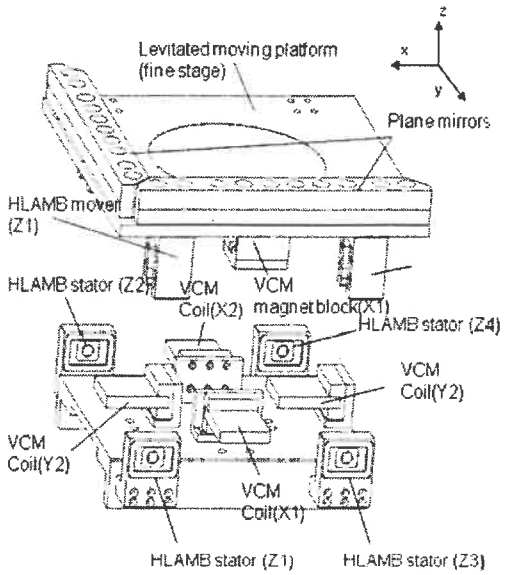

FIGURE 5. Fine stage

The fabricated system is shown in Fig. 6. The coarse stage is fixed on the top of the granite base. The passive isolator supporting the granite base suppresses the ground vibrations.

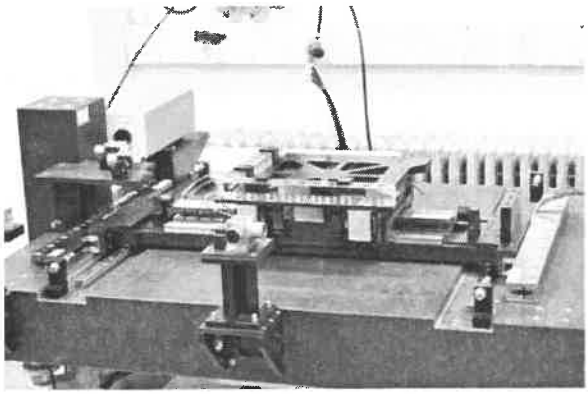

FIGURE 6. Picture of the total system

CONCLUSIONS AND FUTURE WORKS

In this paper, a 6-DOF dual-servo stage was proposed. The moving platform is suspended by new Halbach linear active magnetic bearings. Because the HLAMB has zero-stiffness in static and large dynamic force, it is quite advantageous to levitate the fine stage with active vibration isolation. In future, the performance of the 6-DOF positioning stage will be evaluated.

REFERENCES

[1] A.T.A. Peijnenburg, J.P.M. Vermeulen and J. Van Eijk, Magnetic levitation systems compared to conventional bearing systems. Microelectronic engineering. 2006; 82: 1372-1375

[2] S.A.J. Hol, E. Lomonova, A.J.A. Vandenput Design of a magnetic gravity compensation system. Precision Engineering. 2006; 30: 265–273

[3] K. Halbach Design of permanent multipole magnets with oriented rare earth cobalt material. Nuclear Instruments and Methods. 1980; 169 : 1-10

PRACTICAL CONTROL METHOD FOR NANO POSITIONING USING A LANGEVIN ULTRASONIC MOTOR IN VACUUM ENVIRONMENT

Wan Soo Kim[1], Cheol Ho Yun[2] and Sun Kyu Lee[1]
[1]Department of Mechatronics
Gwangju Institute of Science and Technology
Gwangju, Republic of Korea
[2] Lightweight Components Team
Korea Institute of Industrial Technology Gwangju R&D center
Gwangju, Republic of Korea

ABSTRACT

This paper presents an investigation about the practical control method of noble linear positioning stage for the vacuum environment use. The stage is driven by the hybrid bolt clamped Langivin (BCL) type ultrasonic linear motor which is excited with its different modes of natural frequencies in both lateral and longitudinal directions. This stage system has various variables to drive such as driving frequency, magnitude of preload, phase difference of each mode, and exciting voltage and current etc. In this paper, to obtain the robust driving condition of the motor, the parameters of motor are designed by using Taguchi method.

In addition, because the accurate model of motor in vacuum environment is hard to find, nominal characteristic trajectory following (NCTF) control method was adopted. To achieve the fine control performance in vacuum environment the feedback control parameters were also optimized by Taguchi method. Finally the stage is operated in high vacuum condition, and the operating performances are investigated comparing with air environment. As a result, the robustness of point to point (PTP) positioning was accomplished in high vacuum condition with nanometer level accuracy.

INTRODUCTION

Recently, great attention has been shown to the utilization of an ultrasonic linear motor to achieve a high positioning accuracy and a high driving force in the semiconductor and optical industry [1]. Especially, compared with many kinds of magnetic linear motors, ultrasonic linear motors have several advantages, including a simple structure, quick response, ability to maintain position without energy consumption, and electromagnetic immunity [2, 3]. Such characteristics of ultrasonic motors can resolve complicated problems about precise positioning over long strokes and holding position at any given point in vacuum environment [4-8]. However, to drive the ultrasonic linear motor, it requires the control of several electro-mechanical parameters such as driving frequency, voltage, current, phase difference of each mode, and mechanical preload etc. Because of above problem, the control of ultrasonic motor based on mathematical modeling is not efficient.

In this study, to guarantee the robustness of motor system for vacuum environment the parameter design was considered. Since electro-mechanical parameters are hard to control in vacuum environment, the robustness of system must be required. To obtain the robustness, parameters of motor are designed by using Taguchi method. Moreover, to achieve the fine control performance in vacuum environment, nominal characteristic trajectory following (NCTF) control method with Taguchi method was adopted. Finally the stage is operated in high vacuum condition. As a result, the robustness of positioning was accomplished in high vacuum condition with nanometer level accuracy.

MOTOR DESIGN

Figure1 shows the configuration of the ultrasonic linear motor which consists of a bolt-clamped Langevin-type longitudinal and bending hybrid transducer. The vibrator was designed for the 3rd longitudinal and 6th bending modes, and three nodes were common to two vibrations.

The stator has two types of piezoelectric elements (PZTs) to excite the two different vibrations, which are sandwiched in aluminum blocks with a bolt. The elliptic motion of points at the tips of the vibrator is generated by combining the two modes which are excited with a phase difference of 90 degrees; the vibrator is pressed against the slider by means of the proper support

mechanisms and slider moves one direction in one direction with frictional force in the contact points. And then slider moves opposite direction by changing phase of vibrations.

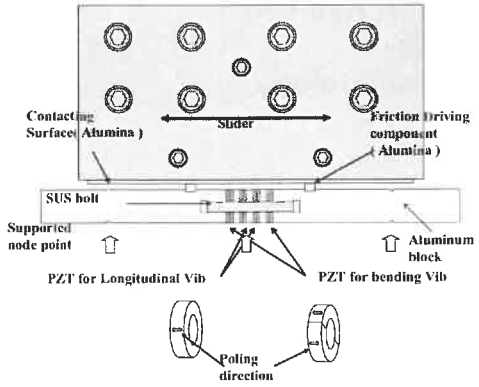

FIGURE 1. The figure identification

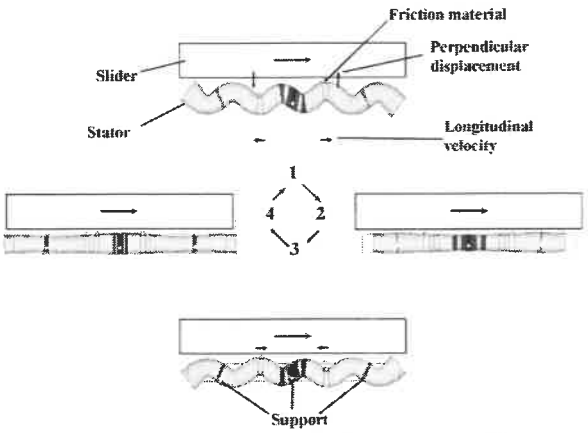

FIGURE 2. Operation sequence of the ultrasonic linear motor

PARAMETER DESIGN

The optimal design of parameter is completed by Taguchi method, which is an effective analysis technique. In practical situation, there exist many parameters for motor driving. Among these parameters, the driving frequency (F variable), inductance of system (I variable), input voltage of longitudinal mode (VL variable), input voltage of bending mode (VB variable) set as control parameters. (*Table 1*)

TABLE 1. The control parameters and level selected for the ultrasonic motor

Parameters	Level 1	Level 2	Level 3
F	30.71 kHz	30.81 kHz	30.91 kHz
I	2.75 mH	2.98 mH	3.34 mH
VL	90 V_{rms}	110 V_{rms}	130 V_{rms}
VB	130 V_{rms}	150 V_{rms}	170 V_{rms}

Taguchi method creates a standard orthogonal array, and reduced L18 array was employed. [9] The output velocity is the target to be studied. We define the object function is the higher velocity the better. Both directional velocity of forward (N1) and backward (N2) was set as noise factors.

TABLE 2. The experimental results using the reduced L18 orthogonal array and SN ratio. (output dimension: mm/sec)

No	F	I	VL	VB	N1	N2	S/N
1	1	1	1	1	42.9	29.1	107.1224
2	2	2	2	2	58.65	67.35	112.4028
3	3	3	3	3	56.85	75.15	112.6178
4	1	2	3	3	72.9	57.6	112.5903
5	2	3	1	1	55.65	49.2	110.8196
6	3	1	2	2	49.2	38.85	109.1717
7	2	3	2	3	73.2	83.7	114.3116
8	3	1	3	1	52.8	40.95	109.6883
9	1	2	1	2	61.5	43.5	110.4965
10	3	2	2	1	52.95	43.5	110.0183
11	1	3	3	2	85.05	87.6	115.1981
12	2	1	1	3	52.65	45.15	110.1877
13	2	1	3	2	60.9	48	111.0149
14	3	2	1	3	49.8	55.05	110.8363
15	1	3	2	1	72.75	52.35	112.0546
16	3	3	1	2	49.8	60.45	111.1834
17	1	1	2	3	67.65	50.7	111.6527
18	2	2	3	1	62.4	45.6	110.8095

Based on obtained S/N ratio value, the optimal parameters were found. (*FIGURE 3.*) As a result, 30.81 kHz driving frequency, 3.34 mH inductance of system, 130 V_{rms} input voltage of longitudinal mode and 170 V_{rms} bending mode were chosen. In this condition, 73.05 mm/sec velocity output of forward direction, 71.85 mm/sec of backward direction were obtained.

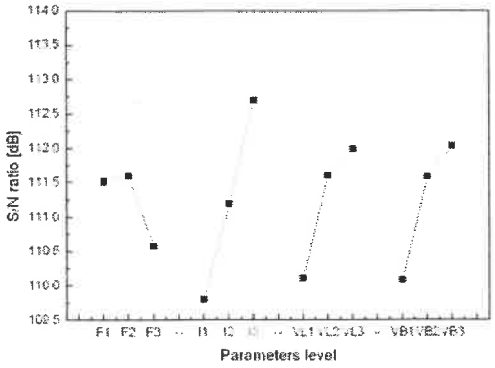

FIGURE 3. The S/N ratio response of each parameter

NCTF CONTROL WITH TAGUCHI METHOD

After the parameters design, a feedback system was constructed, as shown in *Fig. 4*. The control system used an optical linear encoder to detect the position of the slider with a resolution of 15 nm. The position signal from the encoder was fed back to a controller (Delta Tau U-MAC). The signal from the controller was modulated with the signal of driving frequency through the analogue multiplier (AD633). As shown in *Fig. 4*, the modulated signal was amplified by the power amplifier to excite the longitudinal mode, while another signal excites the bending mode after phase shift. Each vibration produces a micro-elliptic motion at the driving points. This elliptic motion generates the driving force.

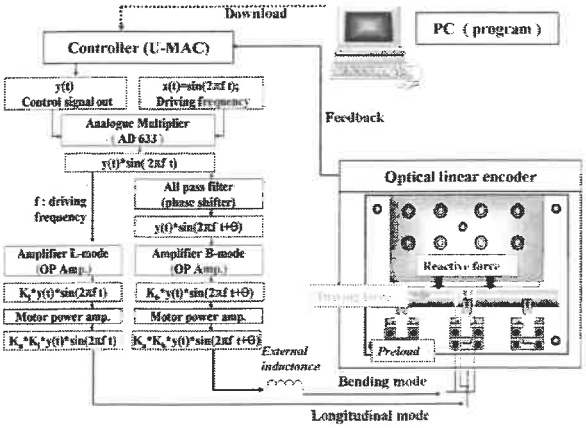

FIGURE 4. Total system construction with feedback control

It is hard to find the mathematical model of ultrasonic motor in vacuum environment. In order to control the ultrasonic motor in vacuum environment, the nominal characteristic trajectory following (NCTF) control method was adopted, because the NCTF control doesn't require the model [10]. The controller consists of the nominal characteristic trajectory (NCT) and PI compensator. The objective of the PI compensator is to make the mechanism motion follow the NCT, finishing at the origin of the phase plane. The signal output of the NCT is the u_p, which is the difference between the actual error rate of the mechanism and error rate of the NCT. *(Fig. 5)*

Figure 6 shows the NCT curve of the ultrasonic motor. We could observe the every covertures follow same trajectory. And these covertures represent the system characteristics. Based on obtained NCT curve, the NCTF controller was designed. In addition, to guarantee the robustness all parameters are designed with Taguchi method.

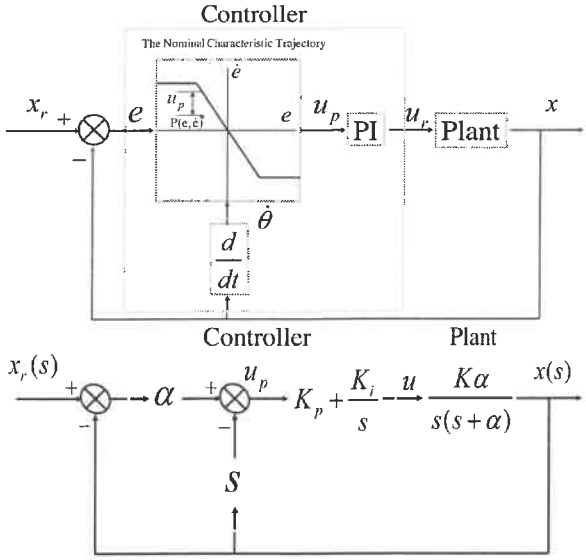

FIGURE 5. Structure of NCTF control system

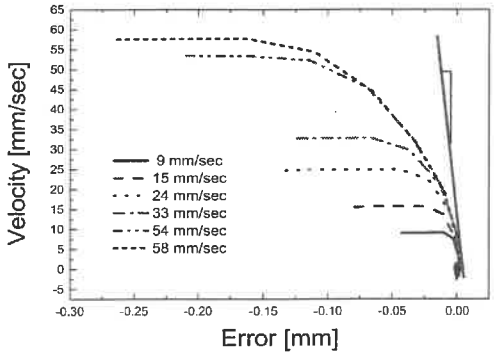

FIGURE 6. NCT curve of ultrasonic motor

In this case, α , K_p and K_i are set as control parameters, and the reduced L9 array was employed. The steady state error is the target to be studied. We define the object function is that the zero value is the best. Both directional error of forward (N1) and backward (N2) was set as noise factors. Based on obtained S/N ratio value, the optimal parameters were found. *(FIGURE 7.)* As a result, when 30 mm long stroke positioning was tested, the fine control was achieved with 20 nm positioning error. *(FIGURE 8.)*

TABLE 3. The experimental results using the reduced L9 orthogonal array and SN ratio. (output dimension: nm)

No.	α	K_p	K_i		N1	N2	S/N
1	1	1	1		117.19	-92.18	-43.40
2	1	2	2		64.06	-107.81	-41.69

3	1	3	3		12.50	−67.19	−35.01
4	2	1	2		103.13	−104.69	−43.34
5	2	2	3		142.19	−70.32	−43.53
6	2	3	1		68.75	−45.31	−38.13
7	3	1	3		68.75	−45.31	−38.13
8	3	2	1		165.63	−48.44	−43.60
9	3	3	2		220.31	−39.06	−45.26

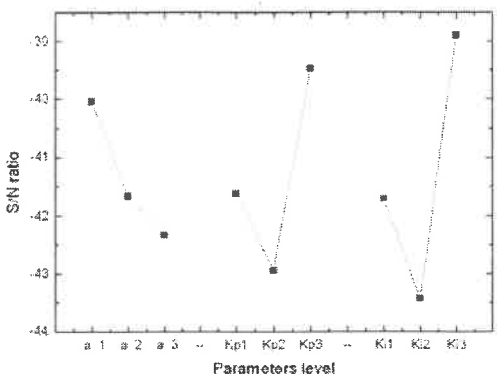

FIGURE 7. The S/N ratio response of each parameter

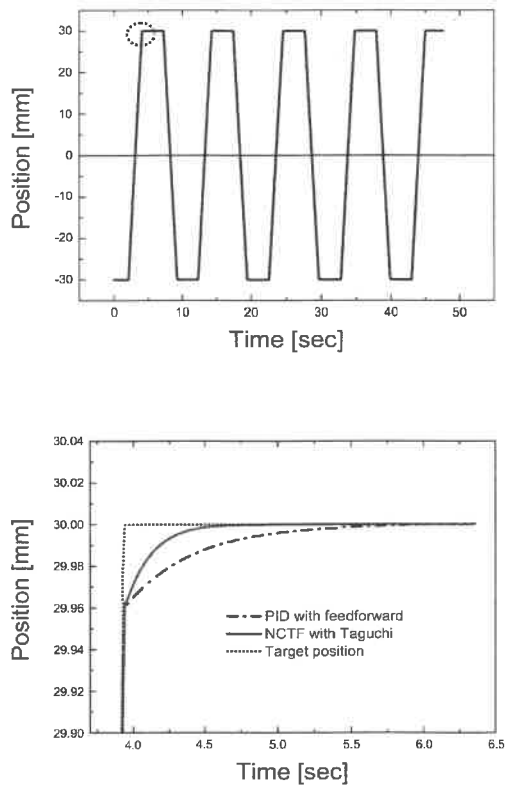

FIGURE 8. The positioning result by NCTF control with Taguchi method

CONCLUSION

High power and high precision Langevin ultrasonic actuator is developed. The parameters design was completed by Taguchi method. Finally, the stable positioning of long stroke with 20 nm final positioning error was achieved by NCTF control with Taguchi method in the vacuum environment.

REFERENCES

[1] Chang-Kyu Song, Young-Jae Shin, Hu-sang Lee, Performance assessment of an ultraprecision machine tool positioning system with a friction drive, Int. J. PRECISION ENGINEERING AND MANUFACTURING Vol.6 No.3 :pp. 8-12 (2005)

[2] T. Hemsel, J. Wallaschek, IEEE Ultrasonics Symp. , pp. 663 (2000)

[3] Nobuhiko Henmi, Michihiko Tanaka, An Open-Loop Method for Point-to-Point Positioning of a Piezoelectric Actuator, Int. J. PRECISION ENGINEERING AND MANUFACTURING Vol.8 No.2 pp. 9-13 (2007)

[4] Y. Tomikawa, T. Ogasawara, T. Takano, Ferroelectrics Vol. 91:163 (1989)

[5] M. Kurosawa, H. Yamada, S. Ueha, Proc. 9th Symp. Ultrasonics, Sendai, Jpn. J. Appl. Phys. Vol. 28-1:158 (1988)

[6] B. Zhai, S-P. Lim, K-H. Lee, S. Dong, P. Lu, Sensors & Actuat. Vol. 86:154 (2000)

[7] J. Zumeris, U. S. Patent 5453653 (1995)

[8] Maik Mracek, Tobias Hemsel, Synergetic driving concepts for bundled miniature ultrasonic linear motors, Ultrasonics, Vol 44, pp. 597-e602 (2006)

[9] Yuin Wu, Alan Wu, Taguchi Methods for Robust design, ASME press (2000)

[10] Sato K, Wahyudi, Shimokohbe A, "Design and characteristics of practical control system for PTP positioning (in Japanese)," Trans Jpn Soc Mech Eng (series C) 2001; 67(664):222-8

NOVEL STAGE WITH VOICE COIL MOTOR FOR LASER BEAM DIRECT WRITING

Donghyun Hwang[1], Jin-Young Kim[1], Ho-Sang Kim[2] and Moon G. Lee[1]
[1]Division of Mechanical Engineering
Ajou University
Suwon-si, Gyeonggi-do, R.O. Korea
[2]Center for Robot Technology & Manufacturing
Institute of Advanced Engineering
Yongin-si, Gyeonggi-do, R.O. Korea

ABSTRACT
Laser beam direct writing (LBDW) technology has potential to be applied to semiconductor and FPD (flat panel display) industry. In order to transfer and then wirte micro and nano pattern for semiconductor and FPD device such as PDP and LCD, the equipments should be able to carry large sized work-piece and have high productivity and high accuracy. We proposed a novel XY-stage mechanism which is compact and fast with long range of motion. The stage actuated by four voice coil motors (VCMs) which are composed of coil windings, yoke and magnets. Two VCM's are for X-directional motion and the other two VCM's are for Y-direction. The stage moves over 20 mm × 20 mm in XY-range with maximum acceleration of 1.2g and bandwidth of 20 Hz. Magnetics of the VCM is analyzed and designed with using a finite element method. The laser writing system with the stage is applied to position work-piece or laser head.

INTRODUCTION
Laser beam direct writing (LBDW) technology has potential to be applied to semiconductor and FPD (flat panel display such as PDP and LCD) industry. It is proposed to write directly on resist materials coated on quartz, silicon substrate or glass, by laser beam, to enable cost effective mask-less exposure. If the technology is applied to semiconductor or FPD process, high cost masks are not necessary because the laser beam writes micro/nano pattern directly on the substrates. Also if it is used to fabricate mask, expensive focused ion beam or electron beam equipments are not needed any more. High power laser and scanning optics are usually incorporated into the LBDW equipment's rigid body, and spot dancing should be minimized for accurate writing. Long life time and compact laser beam writing is capable by the system.

In order to pattern micro and nano pattern for FPD device in Fig. 1, the equipments should be able to carry large sized work-piece mother glass and have high productivity and accuracy. To meet the requirements of next generation FPD, the equipment should travel long range with higher speed and higher precision than the conventional.

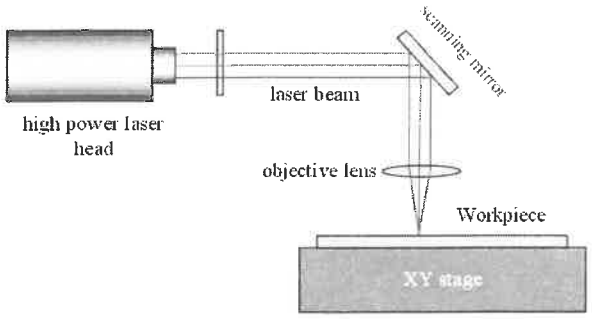

FIGURE 1. Working principle of a laser direct writing equipment

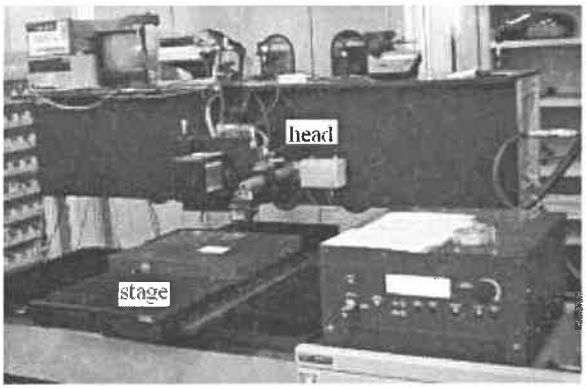

FIGURE 2. An example of laser direct writing system

A pilot LBDW equipment is presented by Jeon et al in Fig. 2. It has XY stage and laser optics. The laser direct writing method was studied to manufacture waveguide. An experiment was

done using UV laser polymerization method for a basic test as shown in Fig. 3. [1]

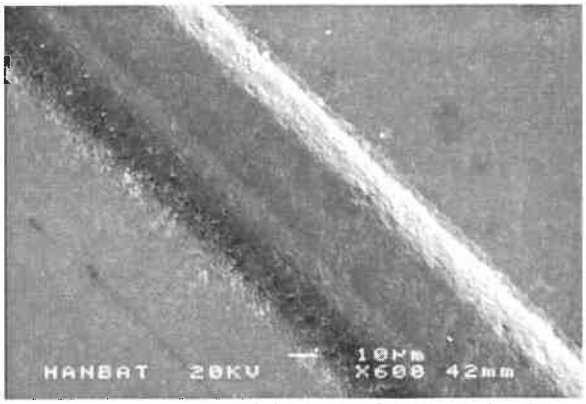

FIGURE 3. An SEM image of pattern by laser direct writing

A NOVEL VCM STAGE

We proposed a novel xy-stage mechanism which is compact and fast with long range of motion as depicted in Fig. 4.

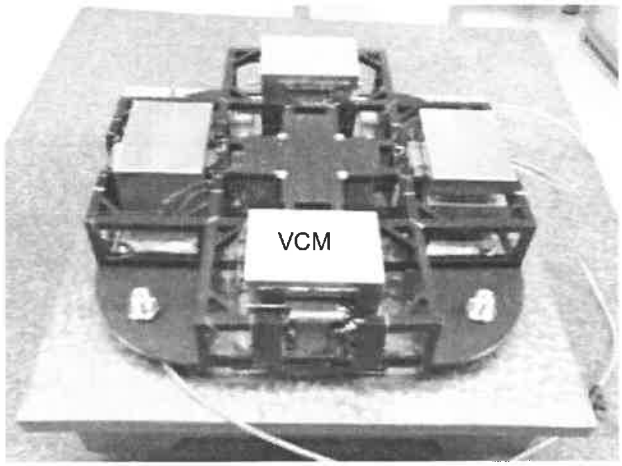

FIGURE 4. Proposed XY stage for laser direct writing

The stage actuated by voice coil motors (VCMs) which are composed of coil windings, yoke and magnets as presented in Fig. 5. The yokes are fixed on ground and magnets are attached to the yokes. The coil moves in an air-gap between two magnets. The magnets and yoke generate magnetic flux in the gap. The VCM has double sided structure which has double sided yoke and magnets. This structure enables the effective length of coil so long and magnetic flux so dense that makes the actuating force higher and the bandwidth of system wide.

The stage is mounted on air bearings presented in Fig. 6 and connected to four coil blocks of four VCMs, therefore the coil's motion is delivered to the stage. The coil windings move when they are energized by current according to Lorenz force. The coil's motion is perpendicular to winding direction, i.e. current direction.

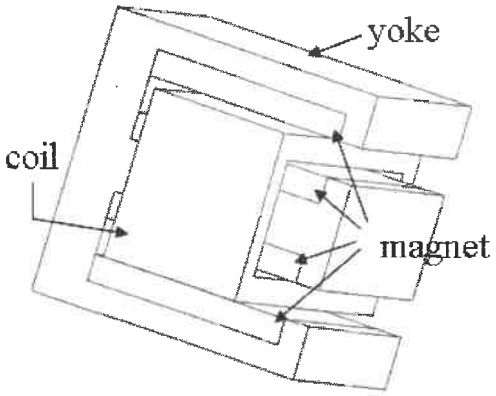

FIGURE 5. Proposed VCM: assembled view

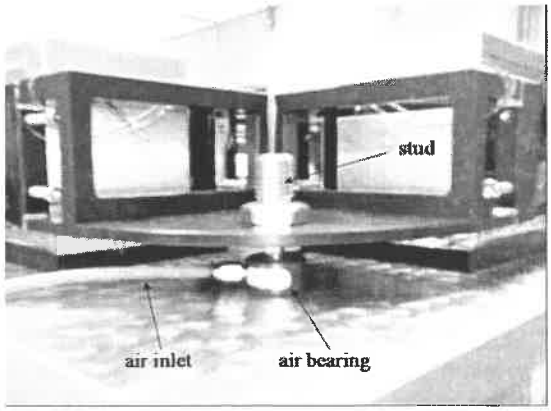

FIGURE 6. Air bearings are used for supporting and floating the stage on granite surface.

In this case it is necessary to control the minor angular motion with respect to the z-axis, as well as the X- and Y-axes motion. The actuator is under over constraints with four of them. Nevertheless, the designed system is symmetrically laid out, and is quite resilient and sturdy against environmental disturbances. The four coils are connected by a coil jig, and thus move together as one body. On this coil jig is laid the stage carrying a work-piece to be fabricated.

The coil jig and the connecting part were attached using ES-2 from EPONS Co., which is resistance to heat and environmental effects. An assembly jig was used to ensure accurate assembly of the system. This assembly jig makes sure that the assembled parts are accurate in the height, parallelism, and perpendicularity before the adhesive material is

applied to be solidified. The magnet is of NdFeB family (H_c=923 kA/m, B_r=1.25 T). This magnet is known to have the highest flux density per unit volume. The magnets were attached using an aluminum adhesive material called Devcon, 10610/10621, which was designed for cementing metal pieces together, and is of a non-magnetic substance unaffected by magnetism. A assembly jig was used when the magnets and the yokes were assembled. Each yoke was grabbed by the jig while the adhesive material is applied on its surface, and each magnet was let slip into the recess, thus avoiding any accidents while improving the assembly accuracy.

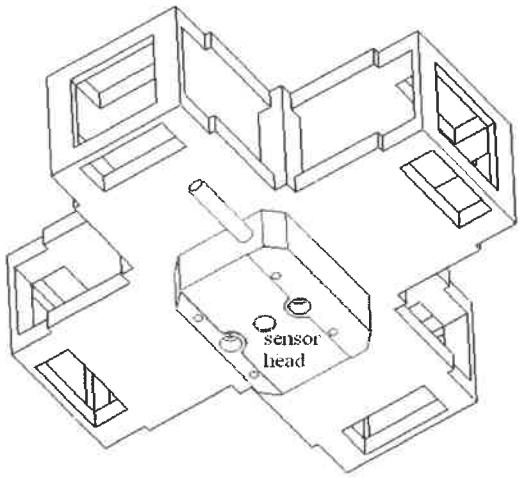

(a) Sensor head is fixed under the stage

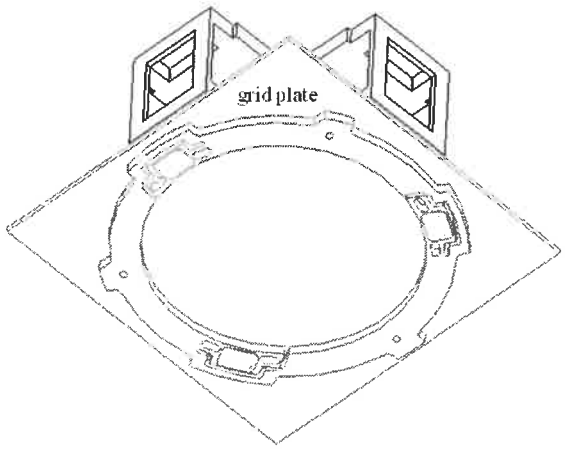

(b) Between sensor head and granite surface, grid plate is mounted.

FIGURE 7. Grid sensor head and plate are mounted under XY-stage.

A position sensor is needed for the expected control operation. Fig. 7 shows a grid sensor mounted at the center. The sensor comprises a head and a grid, and the grid is attached on 정반 while the stage is moving about, and the head should be installed in parallel while maintaining a minute gap on the grid surface. XY positions may be measured using this grid sensor.

The moving mass of each VCM is lighter than the mass of moving magnet type because magnet is generally heavier than coil block. The smaller mass enables the stage with higher speed. However, the actuating force of stage exerts on non-fixed point of coil which causes difficulty of control. Using the moving magnet type VCM, the stage is controlled with narrow bandwidth which is not for high speed and high throughput. This mechanism is more compact and light-weighted than the triangular structure proposed by former researchers. [2] However, there is control burden for the stage inevitably has redundant actuator.

VCM DESIGN: MAGNETICS

In this work, design specifications and object of the stage are as follows: moving range should cover over 20 × 20 mm^2, size of the stage must be smaller than 550 × 550 × 110 mm^3, and bandwidth of control be maximized under design limitation. Abbott et al design a similar system with 15 mm of moving range and bandwidth of 35Hz. [3]

There are so many design constraints such as size limit of stage, temperature rising of the coil, temperature rising of magnets, saturation of yoke, voltage and current limit of amplifier, power limit of amplifier and etc.

Design variables of VCM are diameter of coil, number of turns of coil, air-gap between magnets, air-gap between coil and magnet, size of magnet, size of yoke, and size of coil block.

From the variables, back electro-motive force constant, motor constant, resistance, power and temperature rising of coil, and driving voltage and current are determined. Length and width of magnet is set to be equal. Considering the winding process of coil, manufacturing tolerance of coil block is about 2mm, therefore, the air-gap between coil block and magnet is set to be 2mm because smaller gap results in large actuating force.

To make moving mass light, the stage is assumed to be manufactured using engineering plastic, Bakelite width high stiffness compare to its weight. The yoke is aluminum-coated S40C, and coil is enameled self-boned copper wire.

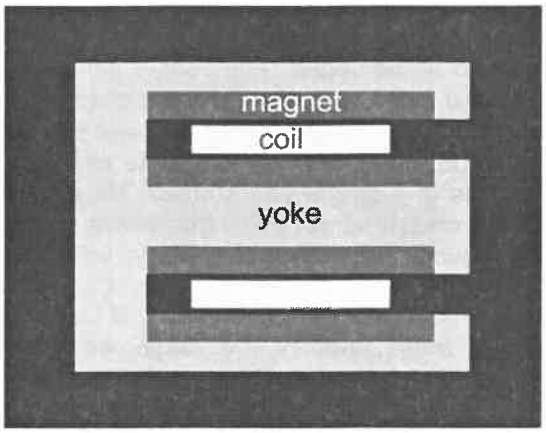

FIGURE 8. Analysis model of finite element method for VCM

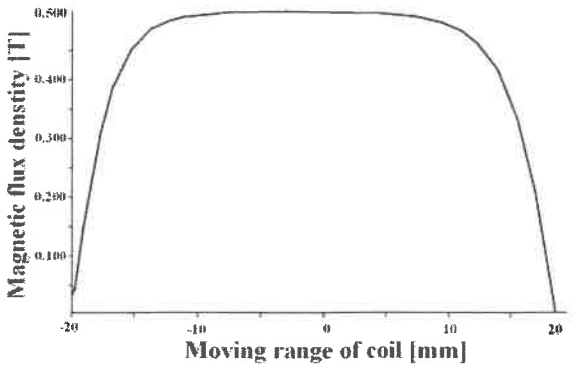

FIGURE 9. Magnetic flux density in air gap between magnets

In order to calculate air-gap flux density, we use a commercial finite analysis software, Flux2D. The analysis model is presented in Fig. 8. After the calculation, magnetic flux density on coil is obtained as shown in Fig. 9. In motion range of coil, maximum flux density is 0.516T and average density is 0.433T. The average value will be used in the following design.

The results of magnetic design of VCM are depicted in Table 1. The magnetic flux is closely uniform in stage's moving range, 20 × 20 mm^2 as shown in Fig. 6. The size limitation of overall stage system is satisfied by the results.

VCM DESIGN: CONTROLLER

Because the air bearings have no friction and their air supply tube is very flexible, the moving mass can be assumed as a mass without spring and friction. To design control characteristics of the system, we use PI controller and then we obtained bandwidth of the system. If inductance of coil is negligible and back-emf constant is similar to motor constant, there is the following relation, Eq. (1).

$$G_p(s) = \frac{X(s)}{V(s)} = \frac{k_b}{mRs^2 + k_b^2 s} \quad (1)$$

TABLE 1 Design variable of VCM

Design variables	Dimensions
Dia. of coil	0.6 mm
No. of coil turns	1403
Air gap	2.0mm
Size of magnet	80×80×10 mm^3
Size of yoke	110×80×108 mm^3
Size of stage	530×530×108 mm^3

In the equations, v(t) is input voltage, R is resistance, k_b is the back-emf constant of VCM, m is the mass, and x(t) is position of the coil. $G_p(s)$ is transfer function of plant, VCM.

The maximum tracking frequency, ω_{max} is determined using Routh-Hurwitz stability criteria with phase margin 50deg. [6] Via commercial software, Matlab and its Simulink, the controller is modeled as shown in Fig. 10 and the maximum voltage and current are estimated. The amplifier of VCM should be selected to cover this value. System parameters and calculated maximum voltage and current are presented in Table 2.

TABLE 2 System parameter of VCM

Design variables	Dimensions
Back-emf constant	97.3 Vs/m
Moving mass	7.00 kg
Proportional constant	11.959 ×10^3
Integral constant	1.4052 ×10^3
Maximum voltage	238 V
Maximum current	9.73 A

From the Matlab simulation, the resonant frequency of VCM is 13.8 Hz and bandwidth is 24.1 Hz in Fig. 10. Considering long moving range and multi-axis motion of the stage, this controller characteristic is safisfiable compare to Abbott's research.

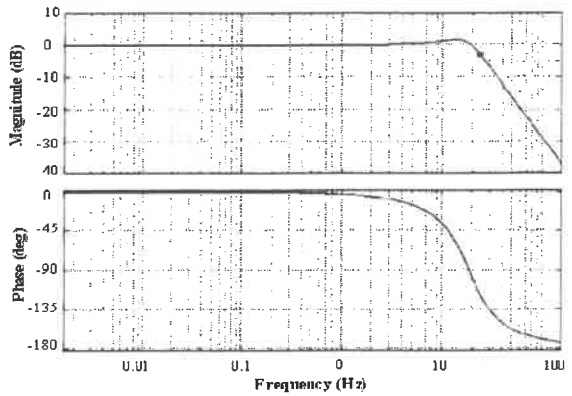

FIGURE 10. Frequency response of VCM stage

CONCLUSION

The present study reported design, construction, and validation of an actuator based on voice coil motors for high-speed long-stroke translational movement in the application field of advanced laser fabrication. A conceptual form of the voice coil motor was determined so as to satisfy the intended travel range, and to realize the maximum bandwidth, and the average magnetic flux density was determined through a simulated experiment, and the actuator was constructed using the values determined by the design.

Also, the optimal parameters for the VCM were selected to control intended XY-axis linear movements. PI controller was designed to present the maximum bandwidth, and the response of the simulated experiment frequency of the actuator control was confirmed using a commercial program, Matlab.

Air bearings were selected so as to minimize the friction and wearing and to optimize the floating force, and its use allows diverse weights for the work-pieces to be fabricated.

The constructed actuator based on the VCM is currently undergoing various characteristic tests, and its performance as a high-speed, long-stroke translational actuator for laser writing applications is being further studied. Especially, velocity profile tracking performance should be also enhanced to be applied to LBDW.

REFERENCES

[1] Shin B.-S. Kim J.-G. Chan W.-S. Yang S.-B. and Jeon B. H. Development of Direct Writing Technology using VU Laser. Proceedings of Workshop on High Performance Micro Optics and Fluidics Technology, 11 April 2002, R. O. Korea. 2001; 1-5.

[2] Kim D. M. The Design and Control of XYθ Fine Stage using VCM for Wafer Stage. M. D. Thesis, Dept. of Mech. Eng. KAIST. 2002.

[3] Abbott R. Allott B. Bann K. Boehlen M. Gower P. Rumsby I. S. and Sykes N. New Techniques for Laser Micormachining MEMS Devices, Proceedings of SPIE; 2000; 4760; 281-288.

[4] Phillips C. L. Harbor R. D. Feedback Control Systems 4th ed. Prentice Hall International. 2000; 388-390.

DESCRIBING NANOMETER-LEVEL ERRORS IN PRECISION MOTION CONTROL STAGES

Stephen J. Ludwick
Aerotech, Inc.
Pittsburgh, PA, USA

INTRODUCTION

Error budgets for high-precision semiconductor equipment allocate a certain portion of the overall error to the motion control system. In many cases, the allocation is just a few nanometers. The type of commanded motion can coarsely be categorized in two ways, as either a scanning or step-and-settle problem. In this paper, we will focus on scanning operation, where the goal is constant velocity with minimal deviation from a straight line in space while the axes are moving. Simultaneous motion with two axes is usually needed to follow wafer features that are never exactly aligned with any individual mechanical axis. Single-valued specifications are not adequate to describe the motion control requirements. In this paper we will review the types of errors motion seen with staging used in semiconductor processing equipment, and present alternate ways of writing specifications and acceptance test procedures to determine suitability in given applications. Our study will focus on linear motion stage systems built around rolling-element bearings.

TYPICAL SYSTEM DESCRIPTION

The data presented in this paper is from a system that is fairly representative of those used in high-precision semiconductor processing equipment. A pair of mechanical bearing stages with linear motor drives and non-contact optical encoders are arranged in a stacked configuration, and mounted inside a vacuum chamber that is itself on an active vibration isolation platform. Air bearing systems can provide much smoother motion than can rolling-element mechanical bearings, but we find that size and budget constraints rarely allow the use of the differential pumping mechanism that permits air bearings to be operated in vacuum environments where many of the semiconductor processing operations occur.

On top of the linear stages, we install a pair of orthogonal stick mirrors and some type of a wafer chuck. A servo controller and linear power amplifiers (parts of the "Aerotech A3200" family) implement discrete-time closed-loop control using feedback from the stage-mounted encoders. A typical position loop crossover frequency (roughly corresponding to "bandwidth") will be about 50-100 Hz. We quantify the servo performance with a software-based frequency response analyzer, and use a bank of second-order discrete-time filters to shape the complete open-loop response.

There is usually a significant offset of several hundred millimeters between the location of the encoders, and the location of the point of interest on the wafer. Competing design requirements; namely small footprint, cost-effective manufacturability, and serviceability, often force a non-ideal sensor location.

A two-axis laser interferometer system aligned with the point of interest on the wafer measures the location of the stages near the work point. This greatly reduces Abbe errors, but they are nearly impossible to eliminate entirely in most designs with nanometer-level error budgets. The interferometers may or may not be used as position feedback sensors in the servo control loop, depending on the particular system architecture.

CONSTANT VELOCITY SCANNING

Scanning stages are those that operate in a "constant velocity" mode, where the stage moves the wafer under a tool at a nominally fixed rate. Many of the motion control requirements that we receive express this specification as a percentage (e.g. stage velocity error <0.1% at 10 mm/s). On further examination, we usually find that position error, or dynamic accuracy during the scan, is the real underlying requirement.

Most motion control systems are sampled in time, with quantized position feedback. The backward-difference expression for velocity is

$$v[t] = \frac{x[t] - x[t-T]}{T}, \quad (1)$$

which has a smallest non-zero value of

$$\Delta v_{\min} = \frac{\Delta x_{\min}}{T}. \quad (2)$$

The variable T represents the sampling time, and $\Delta x_{\min}$ is the least count of the position feedback sensor. Smaller position quanta improve the velocity resolution, but smaller sampling times make it appear that the velocity stability is worse in a simple plot of first-order velocity versus time.

The underlying issue is that most sensors used in linear feedback loops measure position directly, and derive velocity information from them. Direct velocity sensors of comparable resolution are not readily available. Velocity can be derived from position with slightly more sophisticated signal processing techniques, but this generally requires some agreement between the parties as to what filtering methods to use, and also requires some underlying assumptions about the ability of the motion control systems to react to different frequency bands.

Expressing a "velocity stability" specification in terms of a position error eliminates the problems related to discrete-time sampling. Instead we express the deviation from perfect motion in the native units (position) of the sensor used to verify it. Figure 1 shows an example of the stage error in the scanning direction as it moves at a nominal velocity of 10 mm/s. In this case, the servo loop used feedback from the stage-mounted position encoder while the plotted data is from an independent laser interferometer located at approximately the work height.

Quantifying absolute accuracy requires significant bookkeeping and attention to details of beam dead path, sine and cosine errors, and thermal stability among others. The Zygo Corporation details some aspects of these error sources [1]. In many cases absolute accuracy is not required, and instead short-term repeatability and in situ calibration are all that is needed. The data shown in Figure 1 has already been scaled as would be typical of operation where the system finds reference marks on a wafer and adjusts the linear scale factor on the measured position accordingly.

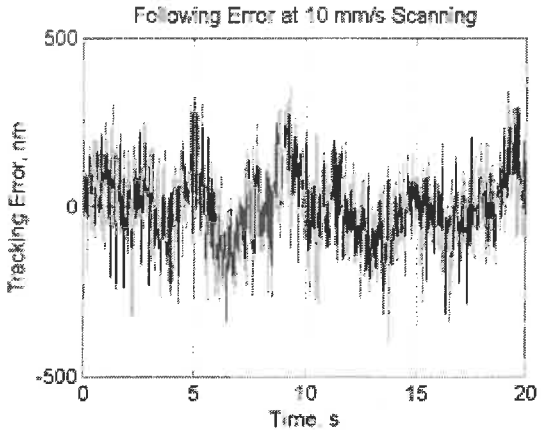

FIGURE 1. The tracking error, or dynamic accuracy of a linear stage when scanned at 10 mm/s velocity shows apparent randomness as well as components at relative low and high frequencies.

The error remaining after the simple scaling can be expressed in terms similar to the surface metrology characteristics of waviness and roughness. The exact frequency or period of the division is application dependent, but we view the lower-frequency portion (waviness) of the error as the component that can be corrected with either a calibration map on the stage, or in customer image processing or beam steering software. The residual higher-frequency error (roughness) is not as straightforward to correct, and often is the limiting bound on dynamic position resolution. The plot in Figure 2 shows the low-frequency portion of the error, and that in Figure 3 shows the high-frequency portion.

The preferred method for specifying dynamic tracking error therefore identifies both the allowable error magnitude as well as the frequency bands over which the specification must be met. The same is true for any dynamic error (straightness, vertical straightness, or angular error). The most rigorous expression of the specification is in terms of a power spectral density with units of nm^2/Hz, or equivalent. However, some customers prefer third-octave or other analyses where the specification is in units of root-mean-square nanometers over specified frequency bands.

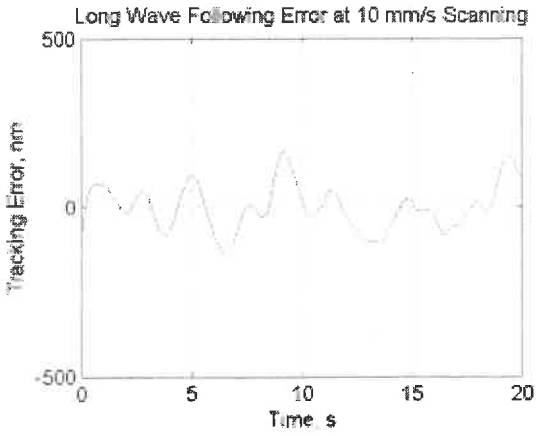

FIGURE 2. The low-frequency portion of the tracking error is analogous to waviness in surface metrology, and is often corrected by means of software calibration. This figure shows the components of the error with a period greater than 10 mm.

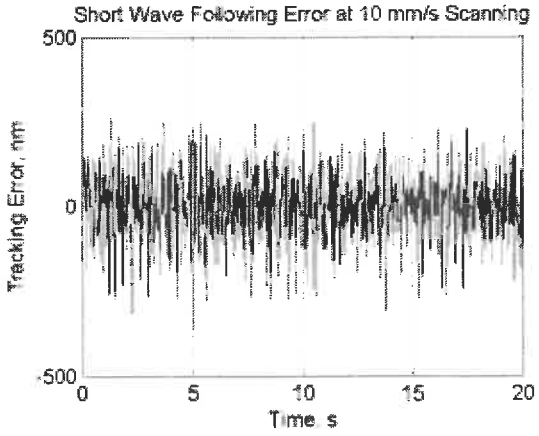

FIGURE 3. The high-frequency portion of the tracking error is analogous to roughness in surface metrology, and is often corrected by means of software calibration. This figure shows the components of the error with a period of less than 10 mm.

The higher-frequency error motions are not as random as they first appear. The traces in Figure 4 shows the data from five sequential scans. Between each of these data sets, the stage scanned 300 mm in the forward direction, came to a stop, scanned back to the starting direction, and stepped over in the lateral direction and began a new scan to simulate the eventual processing of an entire wafer. There is a high-degree of correlation between runs, suggesting that very deterministic phenomena such as mechanical tolerances on the bearing rails and rollers dominate even the "jitter" in the error motion. This phenomena is similar to an observation by Mr. Jim Bryan [2] that the asynchronous error motion in mechanical bearing spindles often "unwraps" itself when the system runs first in the forward, and then in the reverse directions.

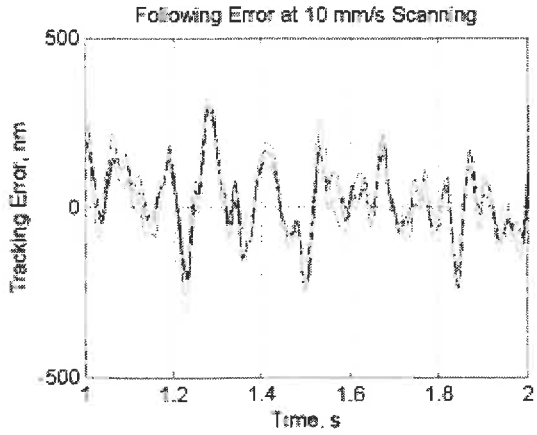

FIGURE 4. The apparent randomness on the stage following error is seen to be quite repeatable over multiple runs (five successive data sets on this example).

The degree of correlation is best over a limited range of travel in both the linear and rotary cases, but after longer travels (where "longer" is system dependent) the degree of correlation drops. The trace in Figure 5 shows the expected result that correlation is best between successive runs, and generally becomes worse with each additional run as the total distance traveled increases. We postulate that this is due to small but accumulating levels of slipping in the bearings, but have not tested this experimentally.

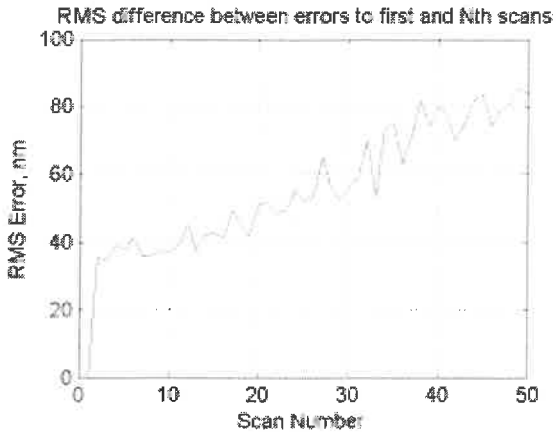

FIGURE 5. The difference between the error trace in the first scan and successive scans increases with the total distance traveled. Continually-updated error maps are needed to compensate.

Fixed error maps for correcting these errors are not successful due to their changing nature, as well as due to present-time computational limits on our ability to generate and process very fine-scale error maps. However, in future work it is entirely feasible to use the error data from a previous scan to modify the next position command and build a self-correcting error map with an iterative learning control scheme.

CONCLUSIONS

Simple single-valued expressions of stage error motions are generally inadequate for expressing either stage scanning or step-and-settle operation. Dynamic error motions while scanning are best expressed as a power spectral density, or at least as allowable stage errors within different frequency bands. Higher-frequency error motions can have very good short-term repeatability, and this characteristic should be used in reducing error motions for next-generation semiconductor processing equipment.

REFERENCES

[1] Zygo Corporation [homepage on the Internet]. A Primer on Displacement Measuring Interferometers [updated 1999 Jan; cited 2008 Mar 24]. Available from: http://www.zygo.com/products/zmi/dmiprim.pdf.

[2] Bryan JB, Personal Communication.

SUB NANOMETER PRECISION HYBRID POSITIONING SYSTEMS FOR VERTICAL INSPECTION TOOLS

Rainer Gloess
Advance Mechatronics
Physik Instrumente(PI) GmbH & Co. KG
Karlsruhe, GERMANY

INTRODUCTION

Improvement in the accuracy of motion control tools for nanotechnology can be achieved with adaptronic design principals and integration of piezo technology in the system design. Two new concepts for high linear accuracy and large travel ranges, were developed. The first one is based on a piezo actuator based walking drive mechanism and the second one uses the mechatronic combination of piezoelectric and motorized drives controlled by a common incremental sensor loop. [1]

Test equipment for semiconductor technology requires horizontal and vertical positioning stages for sensors and optics. [2] This paper describes a new adaptronic product design, specially prepared for vertical motion of optics for inspection or profiling systems. Simultaneous control of piezo flexure actuators and motorized drives provides inches of travel with nanometer to subnanometer resolution.

PIEZO WALK DRIVES AND STACKED HYBRID SYSTEMS

Piezo walk drive technology provides advantages in systems, where high stiffness, compactness but low speed are required. The new NEXLINE piezowalk drive technology is a piezoelectric hybrid system which combines the d33 longitudinal piezo effect with d15 deformation – the shear effect. These drives require high resolution sensors and a controller for step and analog control of the hybrid piezo stacks.

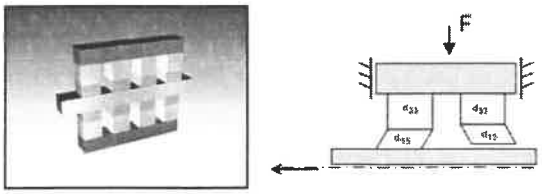

FIGURE 1. NEXLINE® piezo walk drive structure, Four stacks with d33 and d15 piezo material are preloaded from both sides onto a moving runner

A different approach to long travel with high resolution is the combination of piezo ultrasonic motors with piezo flexure actuated stages. Piezo ultrasonic systems can achieve high dynamic performance and very smooth motion. Additionally, when the ultrasonic system is switched off, the self-locking effect is very benefitial for long-term stability and a prerequisite for high system accuracy using the fine adjustment range of the piezo flexure stage.

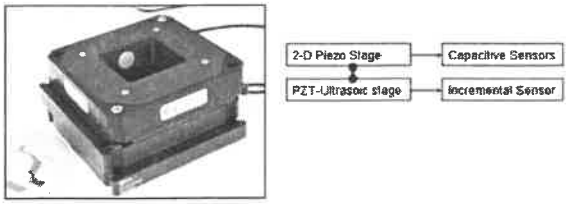

FIGURE 2. *Example of a stacked hybrid system: High-speed coarse positioning over large range: 25 x 25 mm in x and y with ultrasonic drives. Piezo flexure stage for fine positioning: Up to 6 axes, down to sub-nm resolution.*

This type of stacked (independent) hybrid motion system provides subnanometer resolution but the absolute accuracy at the platform is limited to the accuracy of the coarse (fast) piezo ultrasonic stage. The system requires two sensors and two controllers- one for the piezo ultrasonic system and the second for the multi axis piezo stage.

NEW CHALLENGE WITH SINGLE SENSOR HYBRID STAGE DESIGN

The Hybrid Multi Actuator Principle

To overcome the limitations of the independent stacked design, the new hybrid system is the integration of one extremely high resolution incremental sensor into a stage driven by both – a short range piezo stack actuator and a long range servo motor (or piezo-ultrasonic) actuator at the same time.

With the proposed design, the stage motion is measured directly by the incremental sensor. This sensor can be an optical incremental sensor, an interferometer or a magnetic incremental sensor type. Because of the long stroke motion and limited space, an incremental sensor seems to be the best solution.
Which type of main (long travel) actuator is chosen depends on the application. For small volume and high static forces (high loads in vertical direction) servo motor–leadscrew systems provide advantages. For horizontal motion, systems with air bearings, and electromagnetic linear motors could be a good choice. In high vacuum applications piezo ultrasonic drives can be benefitial.

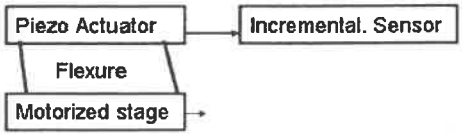

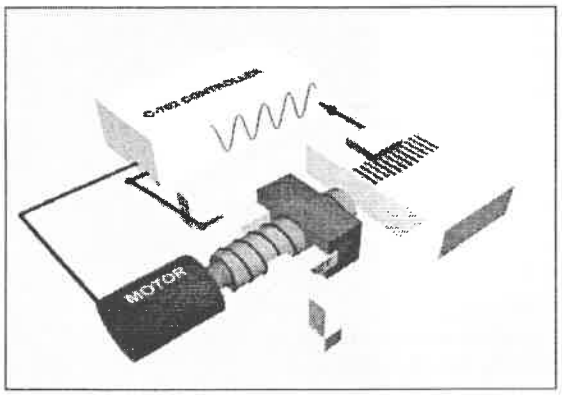

FIGURE 3. Function principle of hybrid system: A high resolution optical incremental sensor with interpolation unit and controller running both the servo motor-ballscrew drive and the piezo stack actuators.

The integrated piezo stack actuators are used to overcome the friction effects, eliminate the ballscrew hysteresis and to improve the dynamic behavior (somewhat similar to an active damper). They can be implemented in a direct drive or flexure arrangement. This design prevents additional hysteresis effects.
The hybrid controller structure controls both- the coarse, main (electromagnetic or ultrasonic) actuator and the fine drive piezo actuator simultaneously. The loop is closed via the incremental sensor- placed at the carrier platform. In the M-714.HD stage a Heidenhain sensor and a special interpolator is used to provide noise free 2nm incremental steps.

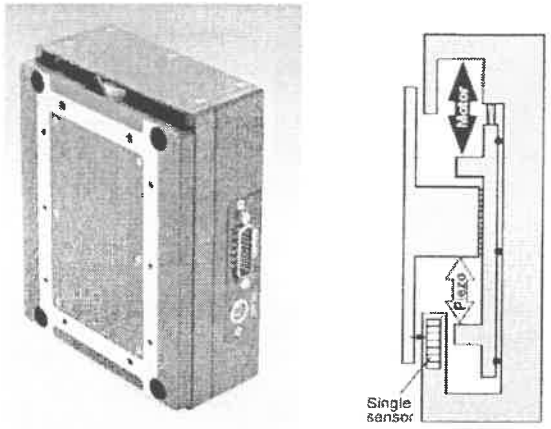

FIGURE 4. M-714.HD hybrid translation stage optimized for vertical applications

Embeded Controller Design for Hybrid Stages

The hybrid controller runs on an embedded PC based on the OnTime real-time operating system, with hardware-clock-buffered sensor inputs and a synchronized output buffer. The servo motor is driven by a PWM signal and the piezo amplifier is driven by 24bit D/A converter. The sampling rate can be set between 1kHz and 200kHz, with 10kHz used for initial testing.

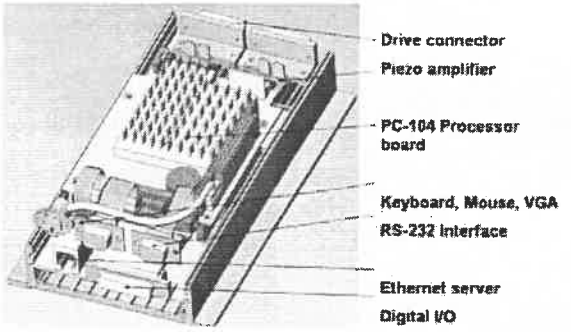

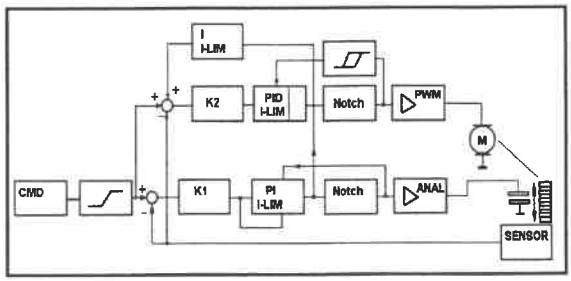

FIGURE 5. Hybrid controller hardware and main control structure (one channel)

The OnTime real time operating system has a very short interrupt latency time of less than 1.5µs. Since both actuators–piezo and servo motor–are acting on the same moving platform, it is necessary to separate the control frequencies for both drives in the controller. The piezo is operated in a higher bandwidth than the servo motor The tests show that the frequency separation should be larger than a factor of two.
The structure of the current controller has another feature: there is an integral term added between the piezo and the motor path. This term minimizes the piezo drive voltage in long term operation to increase the lifetime.

Control Strategy for Hybrid Systems

Figure 5 shows the structure of the digital control algorithm. A PID filter is used for the servo motor. With additional notch filters the resonant frequencies can be canceled. In our controller 2 notch filters for each motor path are used.
The basic control function of a piezo actuator is more simple than that of a servo motor, because of the constant transfer function up to the resonance peak.
The linearized transfer function of a piezo actuator can be approximated as follows:

$$T_z(p) = \frac{K_p}{1 + 2D\frac{1}{\omega_0}p + \left(\frac{p}{\omega_0}\right)^2} \qquad (1)$$

K_p *Gain*
D *Damping coefficient*
ω_0 *Resonant Frequency*

With the Nyquist criterion it can be shown that a simple PI controller function may be stable but can not provide very high bandwidth.. At least a notch filter should be added into the control path, to cancel the resonant frequency peak and improve the stability. [3]

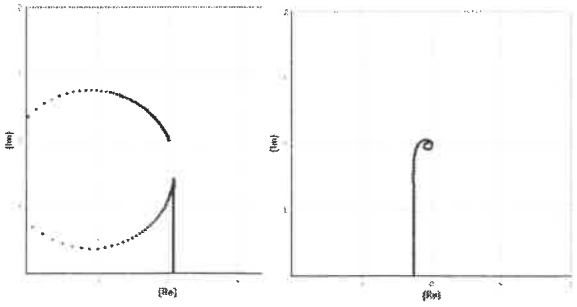

FIGURE 6. Z-plane of the open loop transfer function a) without notch filter b) with notch filter

$T_l(p)$ is the open loop transfer function defined as:

$$T_L(p) = T_C(p)*T_N(p)*T_A(p)*T_Z(p)*T_S(p) \qquad (2)$$

To further improve the performance,, various methods were developed at PI to overcome non-linearity (hysteresis) and creep effects of piezo ceramics.

$$T_N(p) = \frac{1 + \left(\frac{p}{\omega_n}\right)^2}{1 + \frac{p}{D_n\omega_n} + \left(\frac{p}{\omega_n}\right)^2} \qquad (3)$$

The notch filter frequency in (3) is set to the system resonant frequency to avoid controller instability at this point. $\omega_n = \omega_o$
The transfer function of the PI (proportional/integral) term can be set to:

$$T_c(p) = \frac{K_p \cdot \left(T_i \cdot p + T_i T_g \cdot p^2\right)}{T_i p + T_i T_g \cdot p^2} \qquad (4)$$

Tg Smoothing term time constant

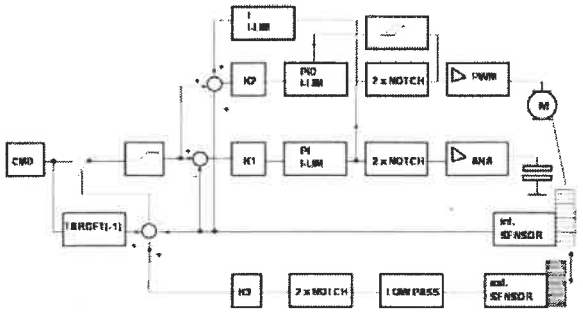

FIGURE 7. Hybrid controller structure with internal and external sensor

The controller can be hardware synchronized via a second interface. The interpolator unit (factor 1000) of the internal sensor is integrated in the stage to reduce the signal noise level. A serial bus is designed to transmit the sensor data in each servo loop cycle.
Figure 7 describes the configuration of the internal and external sensor setup. The external sensor input moves the target position for the trajectory generator so that the main control loop is not destabilized. The design provides stability also under conditions where highly resonant equipment is placed on the stage. Using a programmable interface with an external

incremental sensor, the stage can be operated parallax-free without Abbe error misalignment. The controller firmware is open for implementation of forward looking algorithms.

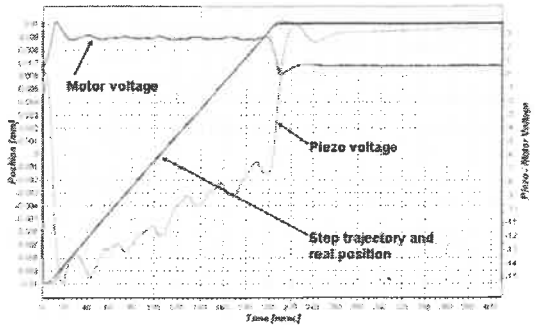

FIGURE 8. Step size of 20µm with small overshoot

Figure 8 shows the hybrid setup with a small overshoot to show the continuosly driven mode of both actuators. The servo motor and the piezo are actuated at all time. The piezo voltage is controlled within a range of +/- 10 V for the final position (+/- 36 V maximum).

Test Results of the Hybrid Stage

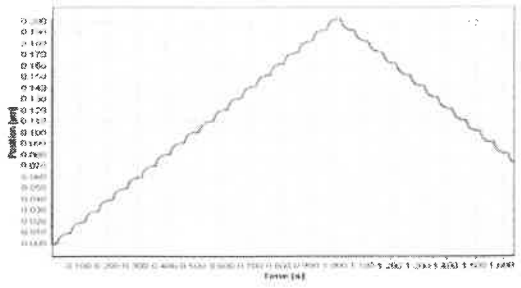

FIGURE 9. Sequence of 10nm steps forward and backward measured with laser interferometer

The hybrid system shows no significant hysteresis at the stage platform.

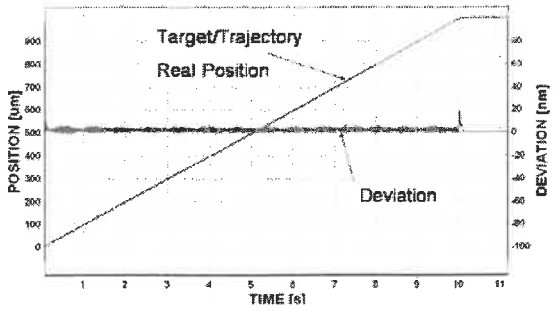

FIGURE 10 Linear travel of 1mm

For longer moves the tracking error can be reduced to less than 10nm deviation from the target trajectory.

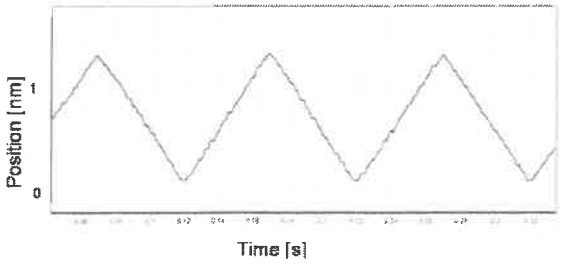

FIGURE 11. 1.2nm (peak to peak) test triangle signal measured with Sony BH20 optical linear encoder (16384 interpolation factor)

Internal and external sensors with resolution significantly better than 1 Nanometer can be used in the hybrid system. The 24 bit D/A structure provides piezo resolution in the picometer range.

SUMMARY

New system designs show that hybrid nanopositioning stages based on electromagnetic and piezo electrical actuators together with high resolution incremental sensors provide a very flexible technology. For maximum performance the piezo part should be separated via a flexure guidance and be controlled by the same position sensor used for the coarse drive. A new type of embedded controller and a two path control algorithm shows promising results for extremely small steps, high repeatability and good linearity over long travel ranges.

REFERENCES

[1] R.Gloess, H.Marth. Adjusting Device with Piezo Drive, US-Patent 5 424 597

[2] Zygo, High Performance 3D Optical Profiler, brochure, Zygo cooperation, Laurel Brook Road, Middlefield, Connecticut 06455

[3] R.Gloess. Systeme zur Nanopositionierung, Teil 2 ,F&M, Jahrg. 108 (2000) Carl Hanser Verlag Muenchen, S.72-78

EXPERIENCES WITH OPTO-MECHANICAL SYSTEMS THAT AFFECT OPTICAL SURFACES AT THE SUB-NANOMETER LEVEL

Layton C. Hale[1] and John S. Taylor[2]
[1]Innovative Machine Solutions, Brentwood, CA, USA
[2]Lawrence Livermore National Laboratory, Livermore, CA, USA

INTRODUCTION

Projection optical systems built for Extreme Ultraviolet Lithography (EUVL) demonstrated the ability to produce, support and position reflective optical surfaces for achieving transmitted wavefront errors of 1 nm or less. Principal challenges included optical interferometry, optical manufacturing processes, multi-layer coating technology and opto mechanics. Our group was responsible for designing, building and aligning two different projection optical systems: a full-field, 0.1 NA, four-mirror system for 70 nm features and a small-field, 0.3 NA, two-mirror system for 30 nm features. Other than physical size and configuration, the two systems were very similar in the way they were designed, built and aligned. A key difference exists in the optic mounts, driven primarily by constraints from the metrology equipment used by different optics manufacturers. As mechanical stability and deterministic position control of optics will continue to play an essential role in future systems, we focus our discussion on opto-mechanics and primarily the optic mounts.

BACKGROUND

A major next-generation lithography program, involving three national laboratories and members of an industrial consortium of microelectronics manufacturers, organized in 1997 to develop enabling technologies for Extreme Ultraviolet Lithography (EUVL). A main objective was realized with the construction of a prototype tool called the Engineering Test Stand (ETS), which as shown in FIGURE 1, was configured as a full-field, step-and-scan lithography tool [1, 2]. Using four mirrors with a modest 0.1 numerical aperture (NA), the system was capable of printing 70 nm features.

Within our program, a complementary project sponsored by Sematech developed a small-field, 0.3 NA, two-mirror projection optic designed to print 30 nm features. Several systems were built by us and Zeiss to be used in Micro-Exposure Tools (MET) such as that shown in FIGURE 2 [3, 4]. These development tools enabled high-resolution printing several years before high-NA, pre-production (or beta) tools were to become available from commercial suppliers.

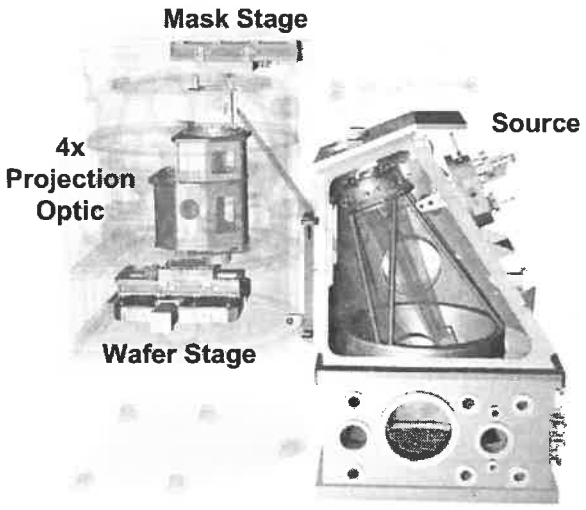

FIGURE 1. Solid model of the ETS.

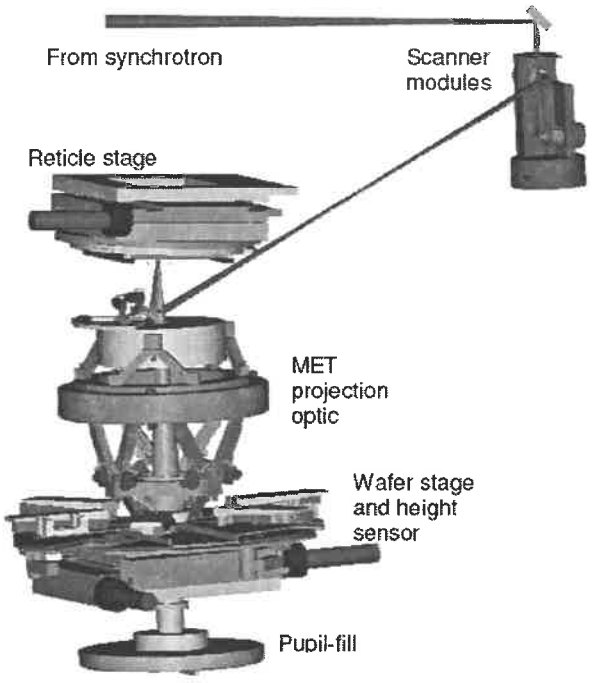

FIGURE 2. Solid model of the Microfield Exposure Station located at the Advanced Light Source, Lawrence Berkeley National Laboratory.

Design features of the ETS projection optic

The four mirrors in the ETS projection optic are identified in the order that light reflects through the system as FIGURE 3 shows. The system has eight actuated degrees of freedom (or compensators) to facilitate fine alignment using optical interferometry as feedback. The compensators are: tip-tilt-piston actuation for both M2 and M4, and X-Y actuation for M3, where Z is vertical along the optical axis. Mechanical adjustments are provided for all the mirrors through the use of fitting spacers and clearance holes at bolted interfaces. M1, M2 and M4 are mild off-axis aspheres and are adjustable in five degrees of freedom, while the spherical M3 requires only three. All optical surfaces are axisymmetric about the optical axis, which passes through M3. The image ring field is 3 x 26 mm and concentric with the optical axis. The object ring field is 4x larger and lies on the opposite side of the optical axis. The system can be adjusted telecentric at the image plane using X-Y actuators on the aperture stop located just above M3.

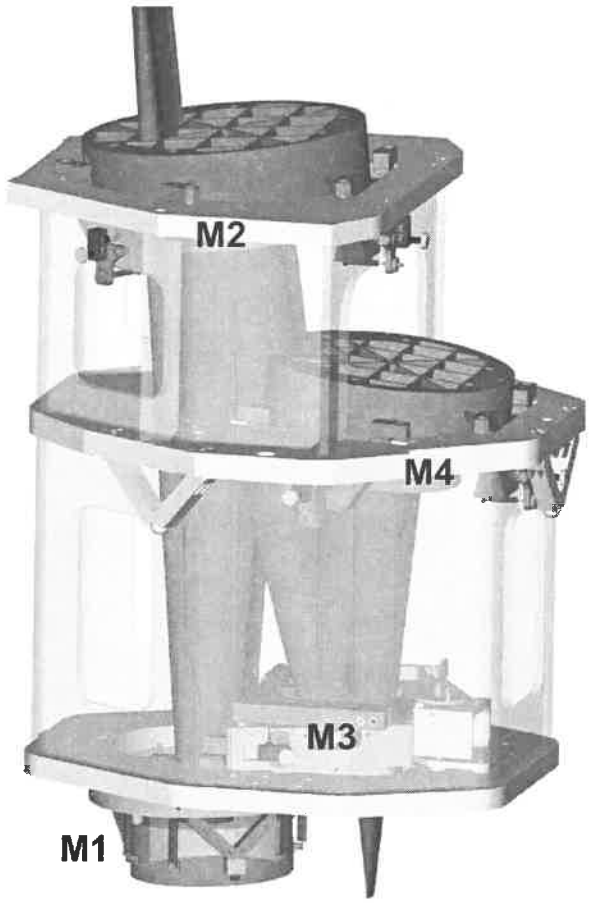

FIGURE 3. Solid model of the four-mirror ETS projection optic with 4x magnification. The size is 514 x 550 x 1075 mm (wafer to mask).

Design features of the MET projection optic

Again identified in the order that light reflects through the system, M1 and M2 are both mild on-axis aspheres with holes cut in their centers for ray clearance. As FIGURE 4 shows, M1 is suspended from a six-degree-of-freedom hexapod, where all motions except Z rotation act as compensators for fine alignment using optical interferometry as feedback. A manual Z rotational axis allows large-angle clocking of M2 relative to M1, which may be used to cancel any astigmatism the mirrors have in common. Mechanical adjustments are provided using clearance holes and fitting spacers at the hexapod legs and clearance holes where the optic mounting flexures bolt to structures.

The image and object planes are tilted 0.8° and 4°, respectively, in order for light to enter the system off a reflective mask. The fields are rectangular, 0.2 x 0.6 mm at the wafer and 5x larger at the mask, to limit the design wavefront error to 0.42 nm RMS and the distortion to 242 nm peak. For non tilted planes over a 0.6 mm diameter image field, the design wavefront error is 0.28 nm RMS and the distortion is 2.42 nm peak.

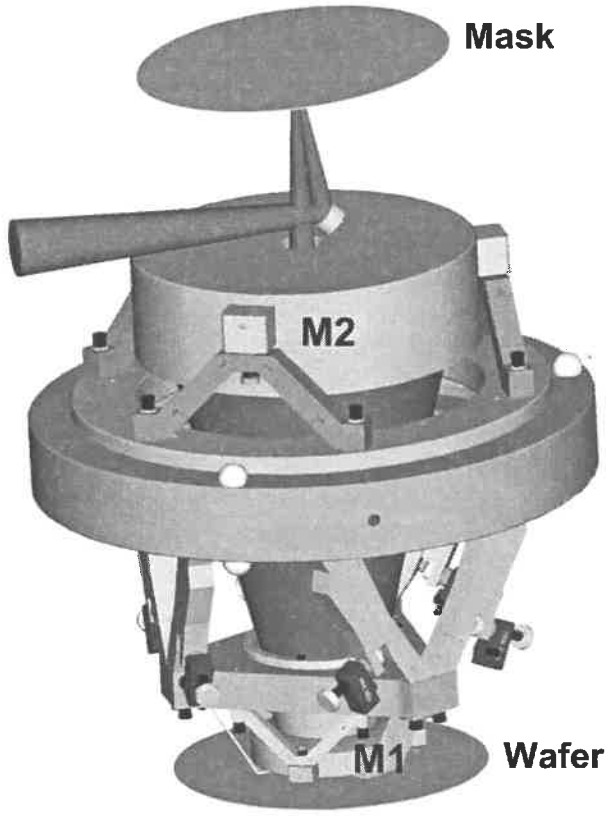

FIGURE 4. Solid model of the two-mirror MET projection optic with 5x magnification. The size is Ø360 x 474 mm (wafer to mask).

Design features in common

Both ETS and MET projection optical systems were constructed principally from materials having low coefficients of thermal expansion (CTE) such as Zerodur for the mirrors and Super Invar for the structural components. In most cases, threaded fasteners consisted of Invar-36 threaded studs and steel nuts and washers, usually Allen nuts unless the smaller height of a hex nut was advantageous. A practical advantage of studs and nuts over cap screws is the additional freedom within the thread clearances for the nut to square itself to the surface being clamped. Particularly for the single-fastener joints prevalent in our designs, we found that tightening cap screws would at times cause the joint to move (shift and/or rotate) but not so with studs. As a rule, all these joints had shallow counterbores on either surface to relieve the bulge area around threads and to concentrate the area of contact to a larger mean radius.

Exact-constraint design principles were employed throughout these systems, including the optic mounts, the actuation stages and the interface between the projection optic and the tool. Since the total figure error allowed over the clear aperture of a mounted optic was 0.25 nm RMS and we typically allowed less than 10% of this in total to the optic mounts, this dictated a very repeatable state of stress in the optic from fabrication metrology through mounting and use. In addition, the relative positions of optics must remain very stable through final alignment and use.

The optic mounts for the ETS and MET projection optics are similar in the use of six flexural links between the mirror and a robust structure called a cell. Often referred to as bipod flexures [5], the links are arranged as three vees that connect to the mirror at three vertices and to the cell at six ends. FIGURE 5 shows a typical bipod for an ETS optic and FIGURE 6 shows a complete ETS optic mount. However the ETS and MET optic mounts differ in how the connect-disconnect functionality is implemented. The following section explains the two approaches and the rational for each [6].

Alignment actuation was achieved on both systems using flexure stages driven by commercial piezo-screw actuators [7]. The stage configurations differed depending on the degrees of freedom required for compensation, but all incorporated mechanical advantage to increase the available force and decrease both least increment of motion and effective CTE [8, 9]. These actuators do not provide consistent step size so position feedback was provided separately using either capacitance gauges to directly sense motion on the ETS optic cells or LVDTs embedded in the actuation flexures of the MET hexapod.

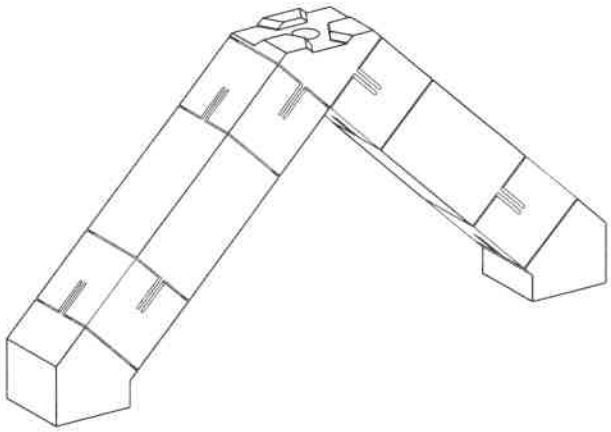

FIGURE 5. The bipod flexure used on ETS optics has a six-constraint interface to the optic.

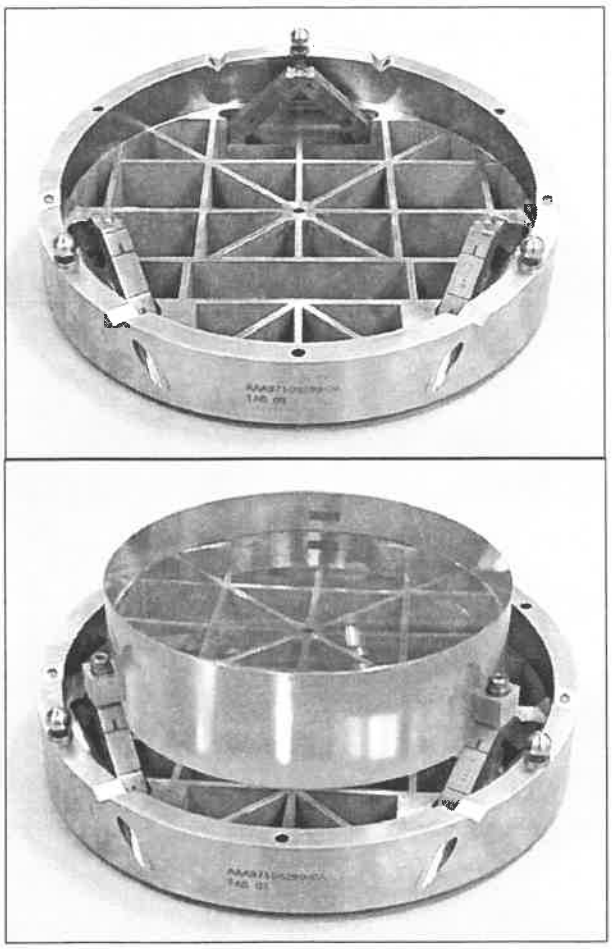

FIGURE 6. M2 optic mount with surrogate optic installed (below). The actual M2 optic has a large cutout to clear the ray bundle.

While both systems used a kinematic interface between the projection optic and the tool (or alignment interferometer), the substantial mass difference led to different design solutions. At 35 kg, the MET projection optic could reasonably interface using a classic three-vee kinematic coupling, with both contact stress and friction force being acceptable. Referring to FIGURE 4, three balls attach through conical seats in both the upper and lower surfaces of the ring-shaped housing. The tool would present three vees (or equivalent constraints) to the lower set of balls while the upper set is available for other equipment to stack on top.

With a mass of over 200 kg, the ETS projection optic presented three, flexure-mounted cones (equivalent to vees) that rested on three balls in the tool. This kept the contact stress low enough to use an unhardened material (Super Invar) and it reduced the friction force. A damping treatment was applied in parallel with the flexures to reduce amplification of the suspension modes of the system [10].

OPTIC MOUNTS

The main functional requirements of the optic mounts are: 1) to enable reproducible fabrication metrology, 2) to preserve the optical figure achieved in manufacturing through use in the system, and 3) to hold its position stable within the system. The optical fabrication process is iterative between metrology and material removal, and for several practical reasons, we chose not to subject the optic mount to the material removal process. This choice required the optic mount to have connect-disconnect functionality. Further it would be impractical to coat the optic in the mount.

Another choice driven by schedule and the desire to keep the optics as simple as possible was to bond mounting features to the optic with epoxy. We used Super Invar blocks bonded to the outer cylinder of the optic with a nominal bond line of 0.1 mm. Concern for stability in this joint over time motivated experiments to quantify the creep rate of several candidate epoxies from which the time to drift out of alignment could be inferred [11]. We estimated 6 to 12 months and experience has shown it to be at least this long.

Designers of production tools will confront tighter surface figure and positioning tolerances, need for longer term stability and significantly higher levels of fluence. The ETS optics were measurably heated, > 1° C for M1 then progressively less in sequence, but not so much as to require cooling measures beyond radiation in the vacuum. For production-tool optic mounts, we would expect to see mounting features produced directly in the optic substrate and some means of active cooling.

ETS optic mounts

The ETS optics were manufacture by Tinsley (now ASML Optics) using the PSDI Interferometer for figure metrology [12,13]. Interferometers for M2, M3 and M4 were constructed with vertical axes to test the optics in their use orientation. This allowed the more conservative strategy of using the same mounts for fabrication metrology as used in the system. As long as the mounts generate a very repeatable elastic strain within the optic, the optical fabrication process will produce the desired shape as mounted.

Gravity-induced strain is huge when the figure error budget is sub-nanometer. This requires the position and orientation of the flexure constraints to be very repeatable. A second source of strain comes from disturbance loads. Each bipod flexure has nonzero compliance in four unconstrained degrees of freedom, which can generate three moments, M_r, M_t, M_z, and a force, F_r, where for example, an optic is usually most sensitive to M_r (a moment about a radial axis from the optic centerline through the vertex of the bipod). Disturbance loads can arise from non repeatable coupling to the optic, differential thermal expansion and plastic deformation of the flexures, say, from accidental damage.

For the ETS optic mounts (see FIGURE 5, FIGURE 6 and FIGURE 7) a three-tooth kinematic coupling was used at each bipod to provide the requisite, highly repeatable, connect-disconnect functionality [14]. The contacting surfaces were cut into the Super Invar parts using wire EDM. Tests on this coupling showed it to be repeatable to within 1 μm in position and 10 μr in angle, which was well within the error budget. However over untold number of engagements, debris would accumulate in the contact area and cause non repeatability visible to the interferometer. A simple cleaning would fix the problem. We believe the debris came from wearing in of the EDM surfaces, but it also could have come from the preload spring, a design that looked simple on paper but turned out to be flawed. The spring was compressed a set distance using a shoulder screw threaded into the flexure. After repeated use, the solid lubricant (Dichronite®) would wear from the threads and cause high friction or galling. Applying too much torque to the screw caused the coupling

to disengage (as a torque-limiting slip coupling), dangerously twisting the flexure. Technicians compensated for the bad design by replacing components when the friction became high.

The flexures were manufactured with travel stops designed to guard against over deflection from simple bending but they still were vulnerable to other modes such as twisting. We required a credible means of recovering from flexure damage that might occur late in fabrication or during assembly into the system. The process of bonding the blocks to the optic was done in the optic mount with the flexures nearly in a relaxed state, that is, with minimum disturbance loads. The best way to return to this state is to repeat the bonding process. However, there is a small risk that the flexure was also damaged earlier in fabrication but went unnoticed, meaning the optic was produced correctly with a nonzero, unknown disturbance. This could be detected by observing motion of the flexures between connect and disconnect states, but we did not instigate this level of quality control.

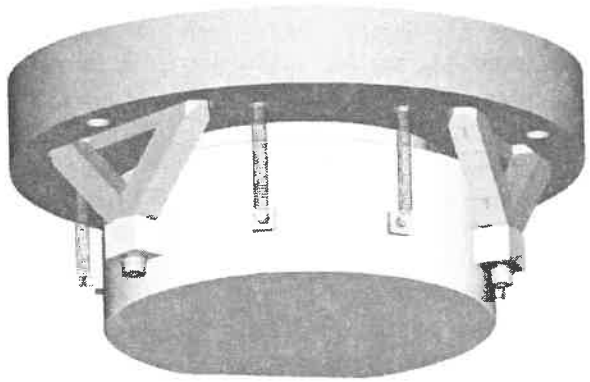

FIGURE 7. M1 optic mount with three bipod flexure constraints and six weight-relief springs.

M1 posed new challenges having a convex radius of curvature over 3 m. It was deemed more practical to build the M1 interferometer with a horizontal axis and to contend with the consequences by using more elaborate optic mounts. It was decided for non technical reasons to use separate mounts for fabrication metrology (with a horizontal axis) and for use in the system (with a vertical axis). A typical approach that proved satisfactory for the horizontal-axis mount is a simple band. The wrap angle was optimized using finite element analysis (FEA) to minimize non spherical deformation over the clear aperture. FIGURE 7 shows the vertical-axis mount, which supports the optic rigidly with three bipod flexures and compliantly with six additional weight-relief springs around the perimeter. This produced primarily spherical deformation, which may be absorbed into the radius tolerance. The resulting non spherical deformation was sufficiently small with nine support points. The tension in each spring was set to one-ninth the weight of the optic using a simple apparatus with a force transducer and a positioning stage.

MET optic mounts

The MET optics were produced by Zeiss using there own interferometers. The very short cavity length between the optic under test and the reference optic prevented us from using the same bipod-style mount for both fabrication metrology and use in the projection optic. Fortunately the interferometers could be set up with vertical axes to test the optics in their use orientation. Then the gravity-induced strain that is polished out of the optic in the metrology mount will be correct for the projection optic mount if both provide constraints in the same positions and orientations. This is demonstrated in FIGURE 8 and FIGURE 9. Strain from disturbance loads is best matched by driving them sufficiently toward zero for both mounts. This was analyzed in the design process using an error budget, which later became a control model for the assembly process.

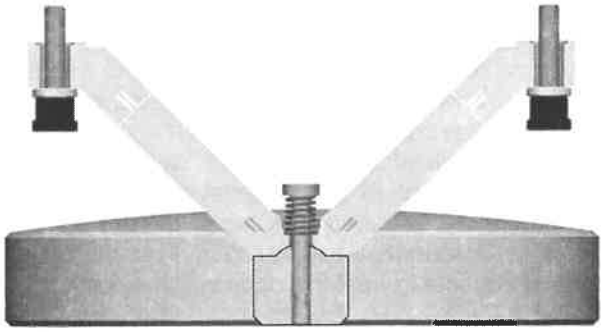

FIGURE 8. M1 projection optic mount showing a cross section through the bipod and cone-sphere interface to the optic.

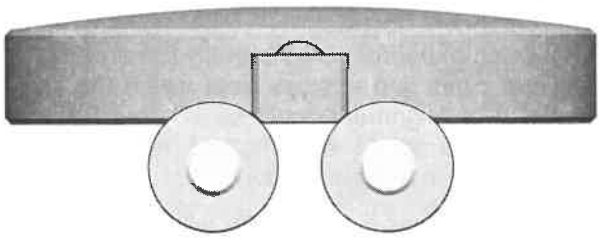

FIGURE 9. M1 fabrication metrology mount showing equivalent constraints provided by anti-friction bearings.

For both M1 and M2 metrology mounts, three pairs of anti-friction bearings were used to act as a low-friction, 3-V kinematic coupling. The rollers contact spherical surfaces machined into the three blocks bonded to each optic. This metrology mount performs well and is very quick and easy to use. For both M1 and M2 projection optic mounts, three bipod flexures provide constraint through the same points and in the same planes as the metrology mounts, within manufacturing tolerances. The bipods have conical sockets that interface with spheres on the bonded blocks. Referring to the figures for M1, the upper sphere that mates to the bipod is concentric with the partial spheres that contact the rollers. The downward-facing spheres for M2 serve both purposes.

Disturbance loads are minimized at assembly first by positioning the bipods so that the conical sockets match the positions of the spheres, which minimizes F_r. We used a coordinate measuring machine (CMM) for this and subsequent steps. In theory, the angular degrees of freedom at the cone-sphere interface allow M_r, M_t and M_z to be minimized; however in practice, this can be very tedious. We used the CMM to measure the bipods before and after mounting the optic. Then we used this information to deduce the disturbance loads sprung into the flexures. Our technique to lower the optic gently onto the mount would often yield one or two disturbance loads out of bounds. At times we would resort to tapping the flexure to bring it in bounds. The joint was then preloaded with a spring to keep it in place; however, we found that friction was insufficient to prevent rotation in the joint due to normal handling. Adding a drop of epoxy would wick into the joint and prevent this rotation, yet the joint is fragile enough to separate if needed.

ACKNOWLEGEMENTS

This work was performed under the auspices of the U.S. Department of Energy by Lawrence Livermore National Laboratory in part under Contract W-7405-Eng-48 and in part under Contract DE-AC52-07NA27344.

REFERENCES

[1] Tichenor, Daniel A., et al., "EUV Engineering Test Stand," SPIE Emerging Lithographic Technologies IV, 2000, **3997** https://e-reports-ext.llnl.gov/pdf/237705.pdf

[2] Tichenor, Daniel A., et al., "System Integration and Performance of the EUV Engineering Test Stand," SPIE Emerging Lithographic Technologies V, 2001, **4343** https://e-reports-ext.llnl.gov/pdf/239913.pdf

[3] Naulleau, Patrick P., et al., "Extreme ultraviolet microexposures at the Advanced Light Source using the 0.3 numerical aperture micro-exposure tool optic," JVST B, 2004, **22**(6), http://goldberg.lbl.gov/pubs/index.php

[4] Naulleau, Patrick P., et al., "EUV microexposures at the ALS using the 0.3-NA MET projection optics," Proc. SPIE, 2005, **5751**, http://goldberg.lbl.gov/pubs/index.php

[5] Vukobratovich, Daniel and Richard, Ralph M. "Flexure mounts for high-resolution optical elements" SPIE Optomechanical and Electro-Optical Design of Industrial Systems, 1988, **959**

[6] Hale, Layton C., "Principles and Techniques for Designing Precision Machines," Ph.D. Thesis, MIT, 2/1999 (see Chapters 6 and 7) https://e-reports-ext.llnl.gov/pdf/235415.pdf

[7] Picomotor™ from New Focus http://www.newfocus.com

[8] Tajbakhsh, H., et al., "Three-Degree-of-Freedom Optic Mount for Extreme Ultraviolet Lithography," Proc. ASPE, 1998, **18** https://e-reports-ext.llnl.gov/pdf/235106.pdf

[9] Hale, Layton C., et al., "High–NA Camera for an EUVL Microstepper," Proc. ASPE, 2000, **22**, https://e-reports-ext.llnl.gov/pdf/239974.pdf

[10] Jensen, J. A. and Hale, L. C., "Application of Constrained-Layer Damping to a Precision Kinematic Coupling," Proc. IMAC-19, 2001 https://e-reports-ext.llnl.gov/pdf/242864.pdf

[11] Patterson, S. R., et al., "The Dimensional Stability Of Lightly-Loaded Epoxy Joints," Proc. ASPE, 1998, **18** https://e-reports-ext.llnl.gov/pdf/235105.pdf

[12] Sommargren, Phillion and Campbell, "Sub-nanometer interferometry for aspheric mirror fabrication," 9th International Conference on Production Engineering, 1999 https://e-reports-ext.llnl.gov/pdf/236193.pdf

[13] Sommargren, G. E., et al., "100-Picometer Interferometry for EUVL," Microlithography 2002, https://e-reports-ext.llnl.gov/pdf/241473.pdf

[14] Three Tooth Kinematic Coupling, U.S. Patent 6,065,898, 5/2000

FEEDFORWARD TUNING METHODS FOR WAFER SCANNING SYSTEMS

Hoday Stearns, Shuwen Yu, Sandipan Mishra, Masayoshi Tomizuka[1]
[1]**Department of Mechanical Engineering**
University of California Berkeley, Berkeley, California, 94720, USA

Photolithography is one of the central processes in semiconductor manufacturing. *Wafer Scanners* are optomechanical devices used for lithography. As photolithography technology becomes more sophisticated, better positioning accuracy is necessary for the wafer and reticle stages in wafer scanners. At the same time, in order to increase throughput, higher speeds of positioning are required. Hence, there is a growing need to introduce advanced control techniques for precision positioning of the wafer and reticle stages in wafer scanners.

Feedforward control has an important role in many industrial positioning systems. In conjunction with feedback control, feedforward control enables plants to achieve more accurate tracking of many motion trajectories than is possible with feedback control alone. Feedforward control allows compensation for errors arising from phase mismatch, in a sense giving the system a faster response to setpoint changes. Aditionally, when the same trajectory is to be executed multiple times, feedforward control may be used to compensate for repeated known disturbances. Due to these characteristics, feedforward control is often used in industrial applications today. While feedback control serves to improve robustness to uncertain and unforeseen disturbances, feedforward controllers are designed to incorporate *apriori* information about the disturbances and the trajectory to be tracked.

This paper presents a comparative study of three different methods of generating a feedforward control signal. We describe three particular methods of feedforward control, namely Iterative Learning Control, Iterative Feedback Control, and Adaptive Feedforward Control. Iterative learning control applies to repetitive processes and involves updating a control law based on data from previous runs of an experiment. Iterative feedback tuning is another iterative method that tries to minimize a cost function by tuning controller parameters. In Adaptive Feedforward Control, plant parameters are estimated in real-time and used to form a control input. These three methods of feedforward control are next implemented on a prototype single degree of freedom waferstage. Then the experimental results from the three methods are compared based on several metrics, such as peak error, 2-norm of error, settling time, and control effort. Finally, the results are discussed and interpretations of the findings are offered, including advantages and disadvantages on the three methods. The emphasis of this paper is the comparison of several feedforward control methods through the introduction of a set of metrics by which performance may be compared.

PROBLEM FORMULATION

This paper is concerned with the control of the system shown in Figure 1. The plant is a wafer stage moving along a linear track actuated by a linear permanent magnet motor with feedback information from a laser interferometer and position encoder. The stage is modeled as a single mass with damping

$$m\ddot{y} + b\dot{y} = ku + d \tag{1}$$

where y is the position of the stage, m is mass, b is the damping coefficient, u is the voltage applied to the motor actuating the stage, k is a amplifier constant, and d is external disturbances acting on the plant. Therefore the transfer function of the plant model is

$$P(s) = \frac{k}{ms^2 + bs}. \tag{2}$$

For evaluation of the feedforward control design techniques, we will set down a basic 2-DOF controller structure shown in Figure 1. The feedback controller C is fixed and designed apriori, considering the bandwidth requirement (PID control is used). The feedforward signal u_f is the design variable.

The process of interest is the scanning operation in a waferstage. A typical (single) scanning operation requires a trajectory shown in Fig 2. This

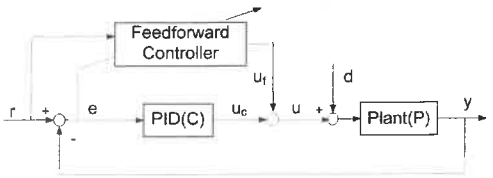

FIGURE 1. CONTROL SCHEME SETUP.

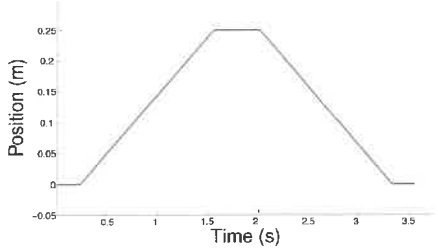

FIGURE 2. REFERENCE TRAJECTORY.

trajectory consists of two major phases (a) acceleration to a fixed velocity ν, (b) scanning at constant velocity ν.

One of the considerations when designing the feedforward signal u_f is the nature of the disturbance d. In a linear permanent magnet motor, the main sources of disturbance include nonlinear forces such as friction force, force ripple, and unmodeled uncertainties. We assume nonlinear friction force is negligible as the stage is supported by air bearings. This means force ripples become the dominant disturbance that causes the tracking error in the constant velocity phase. There has been significant research as well as industrial thrust on compensating the undesired disturbances. An accurate mathematical expression of force ripple [1] is too complicated to implement. Force ripples are not only position dependent but also current dependent [2]. Lee et. al. [3] pointed out that the amplitude of force ripple is highly dependent on position and velocity (which is proportional to the current). A reasonable approximation is suggested and validated in [4]:

$$F_{rip}(y) = u \sum_{k=1}^{M} A_k cos(k\frac{2\pi}{P}y) + B_k sin(k\frac{2\pi}{P}y) \quad (3)$$

Performance Metrics

The relative advantages and disadvantages of the three different methods will be compared based on the following metrics:

1. Peak error during constant velocity scan phase.

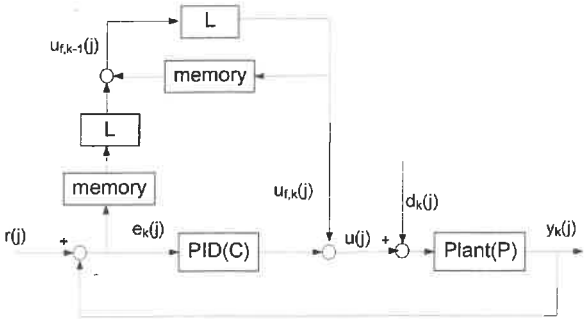

FIGURE 3. ILC CONTROL SCHEME.

2. Root mean squared error during constant velocity scan phase.
3. Peak position error during acceleration phases.
4. Control effort energy concentrated beyond bandwidth

$$E_f = \int_{\omega_B}^{\omega_{Nyq}} |U_f(j\omega)|^2 d\omega$$

5. Computational complexity.

ITERATIVE LEARNING CONTROL

Iterative Learning Control (ILC) is a feedforward control strategy used to improve performance of systems that operate repetitively over a fixed time interval. Based on information gathered about the process from previous iterations of the process, performance in the current cycle can be improved. ILC was originally developed for robot learning and training by Arimoto[5]. Since then it has found applications in many industrial processes[6]. ILC is especially attractive because of its simplicity of design, implementation and analysis. Since the scanning process is repetitive, the ideal feedforward signal can be generated through iterative refinement.

The ILC scheme for generating the feedforward signal is shown in Figure 3. From the figure, we have

$$y_k(j) = H_r(q)r(j) + H_{u_f}(q)u_{f,k}(j) \quad (4)$$

$$e_k(j) = r(j) - y_k(j) \quad (5)$$

$$H_r(z) = \frac{P(z)C(z)}{1+P(z)C(z)} \quad (6)$$

$$H_{u_f}(z) = \frac{P(z)}{1+P(z)C(z)} \quad (7)$$

The subscript k reflects the iteration number of the process. The goal of the ILC scheme is to obtain the ideal $u_f(j)$. For analysis of the general ILC scheme, we introduce a lifted formulation of

the ILC problem below [7]. Lifting refers to stacking up the various signals in a cycle into vectors of dimension $\Re^N$, where N is the period of the (discete) repetitive process. The advantage of lifting lies in the fact that a linear time varying (or time invariant) dynamic system can be converted into a static $N \times N$ matrix equation. Although the dimension of this matrix is large (typically orders can reach $N \approx 10000$), it is easy to design, analyze and categorize the behavior the lifted system from iteration to iteration. We can rewrite the above equations in lifted form by stacking all the signals into $N \times 1$ vectors [8]. Assuming zero initial conditions, we get the following lifted formulation of the repetitive system.

$$\mathbf{y}_k = T_r \mathbf{r} + T_{u_f} \mathbf{u}_f \quad (8)$$

$$\mathbf{e}_k = \mathbf{r} - \mathbf{y}_k \quad (9)$$

where T_r, T_{u_f} are Toeplitz matrices composed of the Markov parameters of $H_r(z)$ and $H_{u_f}(z)$ respectively[7].

In the general ILC design case, we have the feedforward control update law

$$\mathbf{u}_{f,k+1} = Q(\mathbf{u}_{f,k} + L\mathbf{e}_k) \quad (10)$$

The Q filter is used in order to separate out non-repetitive disturbances and improve robustness to model uncertainty. The ILC scheme is stable if $\rho\left(Q(I_N - LT_{u_f})\right) < 1$. The design of the learning matrices Q and L are based on robustness and convergence specifications for the system.

ITERATIVE CONTROLLER TUNING

Iterative Feedback Tuning (IFT) is a method of automatically tuning controller parameters iteratively so as to minimize a certain cost function [9], [10], [11]. Normally, such an optimization would require a complete model of the plant and a full-order controller. In IFT, the optimization is performed iteratively by using an estimate of the gradient of the cost function that is calculated based on data collected from experiment iterations. IFT has been applied to tune the controller of a wafer stage in [12]. Here we use an iterative controller tuning method to tune a fixed-structure feedforward controller for the wafer stage. Controller parameters are updated iteratively to minimize a quadratic function of tracking error. In addition, a fixed-structure feedforward controller for compensation of force ripple is also tuned.

IFT is applied to iteratively tune the feedforward controller of the wafer stage. The structure of the

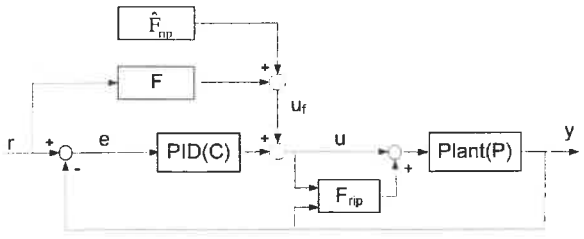

FIGURE 4. IFT CONTROL SCHEME.

feedforward control scheme is shown in Fig. 4. The feedforward controllers we wish to tune are represented by $F(s)$ and the feedforward force ripple compensator signal signal $u_f(t)$. $F(s)$ is the feedforward controller whose structure is the inverse of the plant model,

$$F(s) = \hat{\theta}_1 s^2 + \hat{\theta}_2 s \quad (11)$$

where ρ_1 is the parameter that corresponds to mass and ρ_2 corresponds to the damping coefficient.

In addition, we added a second feedforward control signal u_f to compensate for force ripple disturbance. Force ripple is modeled as in Eqn 3. We desire to cancel out the force ripple by additive feedforward control of the form

$$\hat{F}_{rip}(t) = k_c v(t)[\sum_{k=1}^{N} \hat{A}_k \sin(k\frac{2\pi}{p} r(t)) + \hat{B}_k \cos(k\frac{2\pi}{p} r(t)) + \hat{\gamma}_0 + \hat{\gamma}_1 r(t)] \quad (12)$$

where $r(t)$ is reference position, $v(t)$ is reference velocity, and k_c is a constant, and $\hat{A}_k$, $\hat{B}_k$, and $\hat{\gamma}_k$ are the parameters to be tuned. The reason for approximating $y(t)$ and $u(t)$ in equation by $r(t)$ and $k_c v(t)$ is so that the feedforward data u_f can be computed offline.

The objective of controller tuning is to find the values of the parameters $\hat{\theta}_1$, $\hat{\theta}_2$, $\hat{A}_k$, $\hat{B}_k$, and $\hat{\gamma}_k$ such that a cost function is minimized. The cost function we have chosen is

$$J(\hat{\theta}) = \int_0^{t_f} e(t)^2 dt \quad (13)$$

where $e(t) = r(t) - y(t)$ is the error, and $\hat{\theta} = [\hat{\theta}_1\ \hat{\theta}_2\ \hat{A}_k\ \hat{B}_k\hat{\gamma}_k]^T$ is a vector of controller parameters.

The values for the controller parameters are updated iteratively in a gradient-based search based

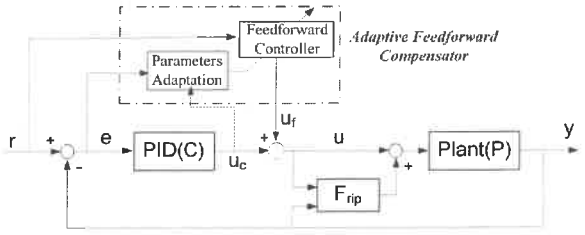

FIGURE 5. BLOCK DIAGRAM OF OVERALL CONTROL SCHEME.

on the error profile from the previous iteration. The update equation is

$$\hat{\theta}_{k+1} = \hat{\theta}_k - \gamma R^{-1} \left.\frac{\partial J}{\partial \hat{\theta}}\right|_{\hat{\theta}_k} \tag{14}$$

where $\hat{\theta}_k$ is the parameter estimate in the kth iteration, γ is a scalar parameter to control step size, R is a matrix to modify the search direction, and $\frac{\partial J}{\partial \theta}$ is the gradient of the cost function with respect to controller parameters evaluated at the present value of $\hat{\theta}$. The gradient $\frac{\partial J}{\partial \hat{\theta}}$ is estimated from data collected in experimental runs. The derivation of the formula for the gradient estimate can be found in [13].

ADAPTIVE FEEDFORWARD CONTROL

In this section, an adaptive feedforward controller for on-line force ripple estimation and compensation is described. Figure 5 shows the overall control structure, which consists of a feedback controller and an adaptive feedforward compensator. In the adaptive feedforward block, a parameter adaptation algorithm is used to estimate the unknown weighting parameters of force ripple and the feedforward controller is used to reduce the effects of the force ripple.

The adaptive algorithm for the feedforward controller is described in the following. First, a sliding surface is defined as

$$S = \dot{e} + \lambda e \tag{15}$$

where $e(t) = r(t) - y(t)$ is the tracking error, r and y represent the desired and measurement position, and λ is any positive gain which provides the stability of the sliding surface. By noting Eqn.(1) and differentiating Eqn.(15), we can get:

$$\dot{S} = \ddot{r} - \frac{1}{M}(ku - F_{rip}) + \lambda(\dot{r} - \dot{y}) \tag{16}$$

Here, the control input is expressed as $u = u_c + u_f + \nu$ where u_c represents the feedback control input, ν is synthesis control input, and u_f represents the feedforward control input. The aim of the feedback controller is to achieve good transient response and enhance robustness of the system. ν is set to $-\eta S$, so as to avoid chattering effects. The aim of the feedforward control input is to eliminate the nonlinear force ripple. Perfect compensation occurs when the feedforward input, u_f, is equal to actual force ripples. Therefore, we designed the feedforward input as:

$$u_f = \frac{1}{k} u \hat{\theta}^T \phi(r) \tag{17}$$

$\hat{\theta} = [\xi, \hat{A_1}, \hat{B_1}, ..., \hat{A_N}, \hat{B_N}]$, $\omega = \frac{2\pi}{P}$, and $\phi(r) = [1, \cos(\omega r), \sin(\omega r), ..., \cos(N\omega r), \sin(N\omega r)]$. The additional term, ξ, is utilized to eliminate the bias estimation of $\hat{\theta}$. The adaptation law is:

$$\dot{\hat{\theta}} = -\frac{1}{\rho} u_c \phi(y) S \tag{18}$$

where ρ is the parameter which is determined by the rate of convergence. For the digital implementation, the continuous adaptation law is approximated by discrete adaptation law.

COMPARISON OF FEEDFORWARD CONTROLLERS

The three different methods of feedforward control generation, ILC, IFT, and adaptive control, are compared in terms of the metrics described in the previous section. The results are compiled in Table 1. The error signals and control effort signals of the three methods are plotted and compared in figures 6, 7. The results shown for ILC are from after 9 cycles of learning, and the results for IFT are after 10 cycles. The adaptive control scheme is not an iterative scheme so the results shown are from a single independent run.

Upon examination of Table 1, it can be seen that ILC has the best performance in terms of metrics 1, 3, 4a, and 5. ILC was the most effective in eliminating error during the acceleration phase and also peak error during the constant velocity scan phase. However, ILC produces a control input signal that is the noisiest of the three methods, as can be seen from visual inspection of Figure 7. The input signal has the highest energy content beyond bandwidth (row 4b). However, the ILC scheme has the lowest computational complexity required per iteration out of the three methods. Further, ILC makes no assumptions about the structure of the controller, so is a very general

TABLE 1. COMPARISON OF FEEDFORWARD CONTROL METHODS

	ILC	IFT	Adaptive
1. Peak error during scan phase (m)	1.83×10^{-7}	5.25×10^{-7}	2.18×10^{-7}
2. RMS error during scan phase (m)	4.01×10^{-6}	9.10×10^{-6}	3.41×10^{-6}
3. Peak error (m)	2.92×10^{-7}	3.46×10^{-6}	1.12×10^{-6}
4a. Control effort energy beyond bandwidth (overall) (V^2)	3.89×10^{4}	4.32×10^{4}	4.78×10^{4}
4b. Control effort energy beyond bandwidth (ff only) (V^2)	1.03×10^{4}	6.36×10^{2}	7.74×10^{2}
5. Computational complexity (number of operations)†	$2NL$	$(20N + 210)L$	$40N$

† Computed in terms of number of scalar additions and multiplications. N = number of samples, L = number of iterations

method that can be applied in a wide variety of situations.

IFT produces a smooth control input signal (Figure 7). Of the three methods, the feedforward control input of IFT contains the lowest high frequency energy (row 4b) and avoids exciting high frequency resonances, which results in a low mean squared sensitivity value. However, it performed the poorest in terms of reducing peak error during scan phase, acceleration phase, and RMS error (rows 1,2,and 3). The IFT feedforward signal is overly simple and isn't effective in compensating error. In order to apply IFT, it is necessary to make assumptions about the plant structure and disturbance structure, and innaccurate modeling of both will degrade the potential performance of IFT. IFT performance may be improved by increasing the accuracy of modeling and complexity of the feedforward controller. In addition, IFT has higher computation complexity than ILC.

The adaptive algorithm achieved good performance in terms of reducing peak error and RMS error, and in fact achieved the best reduction of RMS error during the scan phase (row 2). The adaptive method is the most effective in eliminating error during the constant velocity scan phase arising from force ripple. As can be seen in Figure 7, the adaptive control input looks similar to the ILC input but is less noisy. Consequently, the control effort energy beyond bandwidth of the ff signal is lower than ILC (row 4b). Another advantage of the adaptive method is that high performance is achieved in only one run, instead of after multiple iterations needed in ILC and IFT.

CONCLUSIONS

Three different methods for generation of feedforward control inputs, ILC, IFT, and adaptive control, were presented. The performances of the three methods were evaluated based on a set of criteria that considered peak error, RMS error, sensitivity, peak control effort, control effort energy beyond bandwidth, and computational complexity. ILC has the least computational complexity of the three methods and was the most effective and reducing peak errors, but produced a noisy control signal and error. IFT performed the worst at reducing both peak error and RMS error, but produced a smooth signal with low high-frequency component. Adaptive control performed almost as well as ILC at reducing peak error and was the most effective at reducing RMS error during the constant velocity scan phase.

REFERENCES

[1] B Armstrong-Helouvery PD, de Wit CC. A survey of Models, Analysis Tools and Compensation Methods for the Control of Machines with Friction. In: Automatica. vol. 30; 1994. p. 1083–1138.

[2] Rohrig C, Jochheim A. Identification and Compensation of Force Ripple in Linear Permanent Magnet Motors. In: American Control Conference, 2007.. vol. 3. Arlington, VA, USA; 2001. p. 2161–2166.

[3] Tan HSN K K, Lee TH. Robust Adaptive Numerical Compensation for Friction and Force Ripple in Permanent-Magnet Linear Motors. In: IEEE Transactions on Magnetics. vol. 38; 2002. p. 221–228.

[4] Yu S, Mishra S, Tomizuka M. On-line Force Ripple Identification and Compensation in Precision Positioning of Wafer Stage. In: ASME International Mechanical Engineering Congress and Exposition, 2007. Seattle, WA, USA; 2007. .

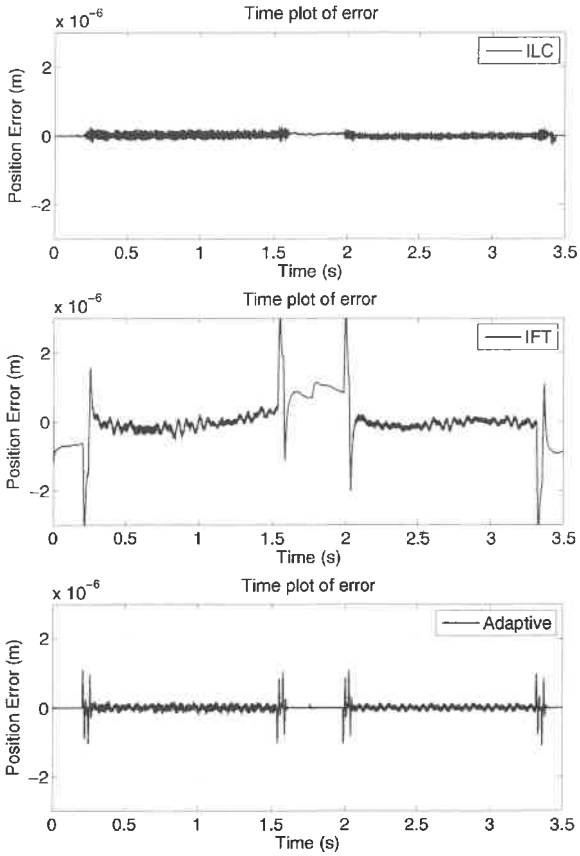

FIGURE 6. COMPARISON OF TRACKING ERROR.

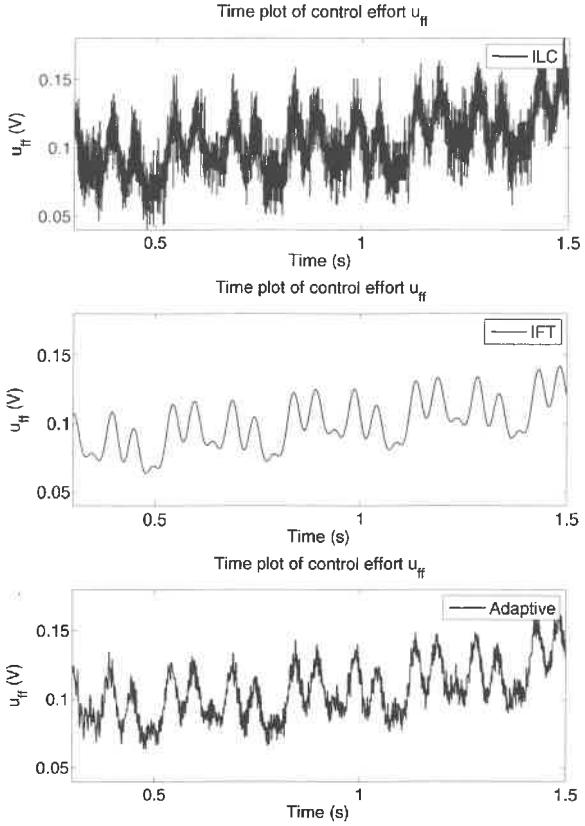

FIGURE 7. COMPARISON OF CONTROL EFFORT.

[5] Arimoto S, Kawamura S, Miyazaki F. Bettering operation of robots by learning. J of Robotic Systems. 1984;1(2):123–140.

[6] Bristow DA, Alleyne AG. A High Precision Motion Control System with Application to Microscale Robotic Deposition. IEEE Trans on Control Systems Technology. 2006;26(3):96–114.

[7] Gunnarsson S, Norrlof M. On the design of ILC algorithms using optimization. Automatica. 2001;37(1):2011–2016.

[8] Dijkstra BG, Bosgra OH. Extrapolation of Optimal Lifted System ILC Solution, with Application to a Waferstage. American Control Conference. 2002;p. 2595 – 2600.

[9] Hjalmarsson H, Gunnarsson S, Gevers M. A convergent iterative restricted complexity control design scheme. In: Decision and Control, 1994., Proceedings of the 33rd IEEE Conference on. vol. 2. Lake Buena Vista, FL; 1994. p. 1735–1740.

[10] Hjalmarsson H, Gevers M, Gunnarsson S, Lequin O. Iterative feedback tuning: theory and applications. IEEE Control Systems Magazine. 1998 Aug;18(4):26–41.

[11] Hjalmarsson H. Iterative feedback tuning-an overview. IntJAdaptControl Signal Process. 2002;16:373–395.

[12] van der Meulen S, Tousain R, Bosgra O. Fixed Structure Feedforward Controller Tuning Exploiting Iterative Trials, Applied to a High-Precision Electromechanical Servo System. In: American Control Conference, 2007. ACC '07. New York, NY, USA; 2007. p. 4033–4039.

[13] Stearns H, Mishra S, Tomizuka M. Iterative Tuning of Feedforward Controller with Force Ripple Compensation for Wafer Stage. In: 10th International Conference on Advanced Motion Control. Trento, Italy; 2008.

MOTION CONTROL FOR NANO LITHOGRAPHY

Shalom D. Ruben and Tsu-Chin Tsao
Mechanical and Aerospace Department
University of California, Los Angeles
Los Angeles, California

INTRODUCTION

This paper presents some motion control issues that we are addressing in developing a control system for a multi-degree-of-freedom stage designed for nano-imprint-lithography. We describe the motion control software and hardware configuration, and model the coordinate transformation among the spaces of sensors, stage position, and actuators. A characteristic problem that is common to many electric motor driven stages including the one we are working on is the excess number of motors and coils to the stage's kinematic degrees of freedom render a redundant system. To reduce thermal deformation of the work space by the heat generated by the motors, this redundancy is exploited. In minimizing the total electric power of the motors for a given force vector command from the servo controller we derive an interesting result that are general to common systems. Two formulations, one without and one with additional constraint for geometrically symmetric thermal deformation, for total motor heat minimization are considered. We will also present our initial PID servo control experimental result and discuss work in progress to further eliminate the servo errors in the PID loop.

PRECISION STAGE AND CONTROL INTEGRATION

High-precision motion control is a critical element of semiconductor lithography machines. While lithography typically involve planner motion, recent research in precision stages for lithography are designed for all six degrees of freedom mechanical mottion. Some recent designs (as in [1], [2], and [3]) use linear permanent magnet motors for actuation and interferometers and capacitance gauges as feedback. The stages are also levitated, with the help of air/fluid bearings, for non-contact motion by the linear motors using Halbach arrays [4]. In these referenced works, the two mappings from a desired forcevector to the motor forces and the desired motor(local) force vector, f, to the needed current vector, i, (commutation) are considered separately [5]. Optimization performed for each mapping, separately, does not necessarily represent the system optimization. A multi-degree-of-freedom similar to [5] is under development for nano-imprint lithography (see [6] for extensive design detail). Shown in figure, 1, the stage is in part a 3-DoF mask carrier (structural frame) actuated by piezo-electric actuators and a 6-DoF substrate carrier (platen) actuated by 4 Halbach linear motors. Each motor is capable of producing two orthogonal force. We will focus on the in-plane motion actuated by the Linear motors (x,y,θ_z). The integration of control for the platen is shown some detail in figure 2.

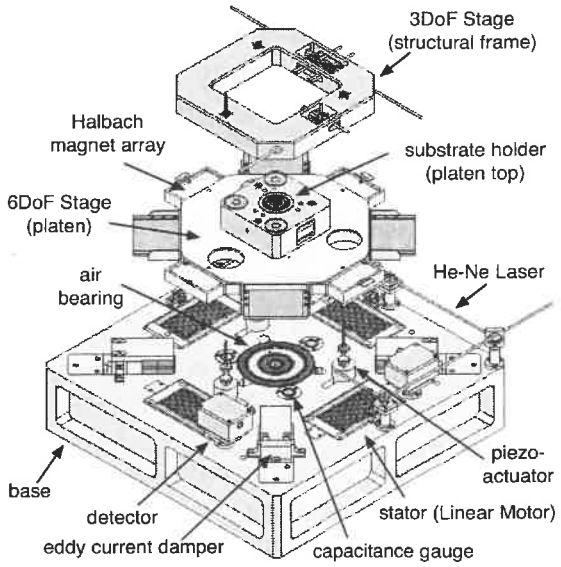

FIGURE 1. exploded view of MAPS stage

A UMAC industrial control system, by Delta Tau Data Systems, Inc, is integrated with the Multi-scale Alignment and Positiong Stage. This control system is composed of a PMAC2 controller and interfacing cards for I/0, A/D conversion, D/A conversion, and 4096X sin/cos quadrature encoder conversion. A PID control algorithm is being used for the initial integration of hardware and software. There is space on the controller for the user to write an advanced control algorithm, but is limited in memory and computational power for more sophisticated schemes, such as those men-

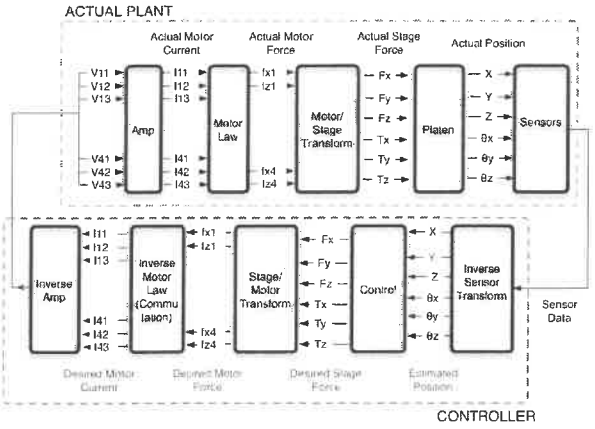

FIGURE 2. detailed block diagram of platen control

tioned in this paper. In the future, advanced control will be performed on the accompanying PC computer (running windows with a real-time kernel installed, such as INtime from TenAsys Corporation) and data will be read and written into dual-ported RAM to communicate with PMAC in synchronization with the PMAC servo cycle update rate. The PMAC can also perform commutation for brushless motors, but this feature can not be used for the Halbach motor. The commutation for the Halbach motor is user-written.

The platen's 3, 4-pass, interferometers sends a 158nm pitch sinusoidal quadrature signal to the controller through the sin/cos encoder conversion card. . A Sinusoidal signal can be sub-divided to get better resolution. the signals are, theoretically, subdivided by 4096. A tranformation on the sensors is performed ,by a user-written code , to convert from the sensors in to platen position. The command from the controller is sent to the user-written commutation. The commutation output is sent the D/A converters which send a desired voltage, proportional to current, to the amplifiers connected to all 12 coils.

DYNAMIC MODELING

After linearizing the platen model, by assuming that the rotation about each axis (θ_z, θ_x,θ_y) is small and can be used instead of Euler angles, we have a modeled plant G:

$$G: \quad \bar{M}\ddot{X} + \bar{B}\dot{X} + \bar{K}X = F$$

where the state vector X is equal to $[x\ y\ \theta_z\ z\ \theta_x\ \theta_y]^T$ and the global force vector F is defined as $[F_x\ F_y\ T_z\ F_z\ T_x\ T_y]^T$. The relationship between the local forces and the global forces can be seen, by figure 3, to be

$$F = Af$$

where f is defined as $[f_{x1}\ f_{x2}\ f_{x3}\ f_{x4}\ f_{z1}\ f_{z2}\ f_{z3}\ f_{z4}]^T$ and A is defined by:

$$A = \begin{bmatrix} 1 & 0 & -1 & 0 & 0 & 0 & 0 & 0 \\ 0 & 1 & 0 & -1 & 0 & 0 & 0 & 0 \\ R & R & R & R & 0 & 0 & 0 & 0 \\ 0 & 0 & 0 & 0 & 1 & 1 & 1 & 1 \\ 0 & 0 & 0 & 0 & -R & 0 & R & 0 \\ 0 & 0 & 0 & 0 & 0 & -R & 0 & R \end{bmatrix}$$

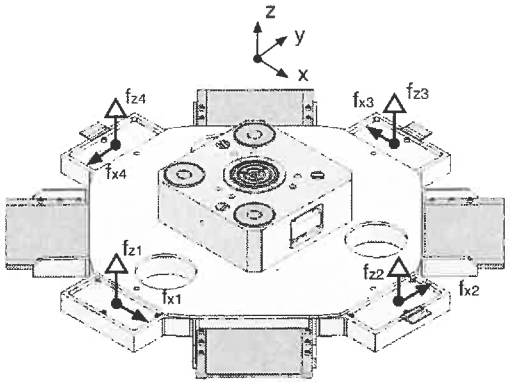

(a) isometric view

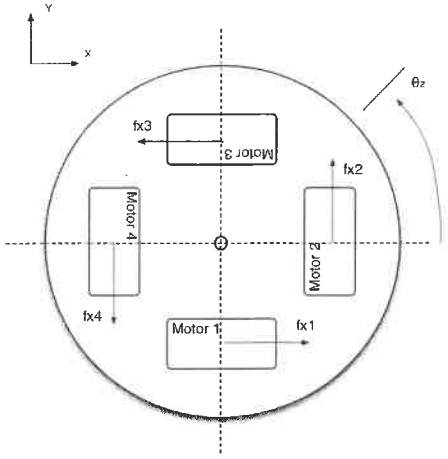

(b) top view

FIGURE 3. local forces acted on the platen

The current and local force relationship of the 3-phase Halbach motors is calculated by

$$f = Bi$$

where i is defined as $[i^1\ i^2\ i^3\ i^4]^T$ ($i^k = [i_{1k}\ i_{2k}\ i_{3k}]^T$), and B defines the four Halbach lin-

ear motors, each described by [5]:

$$f_{xk} = C^x_{1k} i_{1k} + C^x_{2k} i_{2k} + C^x_{3k} i_{3k}$$
$$f_{zk} = C^z_{1k} i_{1k} + C^z_{2k} i_{2k} + C^z_{3k} i_{3k}$$

or in vector form

$$f^k = \begin{bmatrix} f_{xk} \\ f_{zk} \end{bmatrix} = \begin{bmatrix} C^T_{xk} \\ C^T_{zk} \end{bmatrix} i^k$$

Where $C^x_{1k}(x_k) = a\cos(Kx_k + P)$, and $C^x_{2k}(x_k)$ and $C^x_{3k}(x_k)$ are shifted by $\frac{2\pi}{3}$. Also $C^z_{1k}(x_k) = a\cos(Kx_k + P + \frac{\pi}{2})$, and $C^z_{2k}(x_k)$ and $C^z_{3k}(x_k)$ are shifted by $\frac{2\pi}{3}$. Combining these two relationships, we have the relationship between the supplied current vector and the global force vector as

$$F = ABi$$

A controller C is designed so that the pair (G,C) is stable and meet performance requirements using feedback from the sensors. The sensor feedback must be transformed to state feedback. For the platen's in-plane position, the interferometers are measuring positions (y_1,y_2,x_3) on the faces of the platen top (see figure 4).

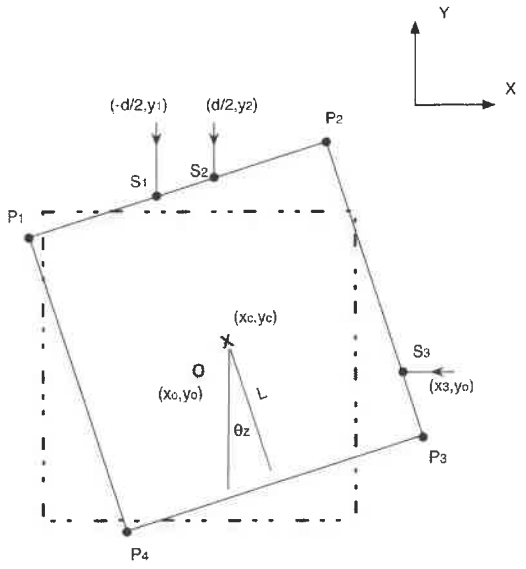

FIGURE 4. platen top and interferometer feedback (y_1,y_2,x_3)

It can be shown that the center of the platen can be easily calculated by knowing the point P_2 on the platen top and θ_z. The following equations relate the point P_2 and θ_z to the sensor feedback.

$$\theta_z = \tan^{-1}\left(\frac{\Delta}{d}\right)$$
$$P_{2y} = \frac{y_1 + \frac{x_3\Delta}{d} + \frac{\Delta}{2}}{\left(1 + \frac{\Delta^2}{d^2}\right)};$$
$$P_{2x} = x_3 - \frac{P_{2y}\Delta}{d}$$

where $\Delta = y_2 - y_1$. For small angle, the following simplified equations can be used:

$$\theta_z = \frac{\Delta}{d}$$
$$x = x3 - L$$
$$y = \frac{y2 + y1}{2} - L$$

The command, from the controller, is a desired global force vector and must be mapped to a current vector to be supplied to the platen. We will define $\mathcal{T}$ as the mapping from i to F ($\mathcal{T} : i \mapsto F$) and $\mathcal{T}_{\text{inv}}$ as the mapping from F to i ($\mathcal{T}_{\text{inv}} : F \mapsto i$). The mapping $\mathcal{T}_{\text{inv}}$ is the "inverse" operation of $\mathcal{T}$ but not to be confused with a matrix inverse. The block diagram of the control system in these terms can be seen in figure 5 which is a simplified version of figure 2.

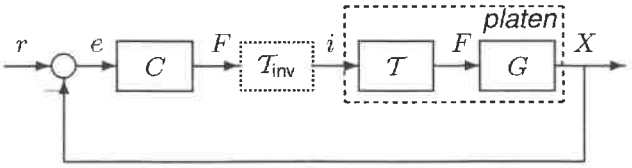

FIGURE 5. control loop with force/current tranformations

The mapping $\mathcal{T}$ has already been defined by $F = \mathcal{T}i = ABi$. And $\mathcal{T}_{\text{inv}}$ is the commutation and will be defined in the following section.

LINEAR MOTOR COMMUTATION

In this section we will show that the assumption of solving minimum power commutation for each motor ($\min ||i^k||^2$), independent of their relationship to the stage, will actually give the total minimum power ($\min ||i||^2$) is in general incorrect. Although, in the case that of using brushless permanent magnet motors as actuation, the

assumption is true (due to the structure of B). So the desire to minimize power, and thermal deformation, for systems using Linear motors, can be separated into a kinematic stage and an electromagnetic stage with out loss of the desired goal of minimizing total power. Also, we will propose a novel scheme to minimize thermal deformation by minimizing power subject to the constraints that there is heat symmetry about the center of the platen. Heat symmetry is attained by forcing all the motors to generate the same power ($||i^1||^2 = ||i^2||^2 = ||i^3||^2 = ||i^4||^2 = P$). This is possible, since a current can be supplied, and generate heat, to a linear motor without generating force (when i is in the null space of B). It turns out that, again due to the structure of B, this problem can also be solved by separating the problem into a kinematic stage and an electromagnetic stage. The important structure of B is that the square matrix BB^T turns out to be equal to a constant times the identity matrix ($= cI$)

Minimum Power

Given that the platen has 4 motors with 3 coils per motor, solving for the current that produces a desired force is an over-determined problem and has an infinite number of solutions. it is common to solve for the solution that gives minimim power ($\min ||i||^2$ s.t. $F = ABi$) since it is a closed-form solution and easily solved by the pseudo inverse, giving the current vector to be $i = (AB)^+F$. Where the solution, using the pseudo-inverse is well known to be equal to solving the following problem:

$$\begin{aligned} &\min ||i||^2 \\ &\text{subject to} \\ &F = ABi \end{aligned}$$

It is possible to attack this problem in two stages, a kinematic stage where you solve for the local force vector by $f = A^+F$ and a electro-magnetic stage, where you solve for the minimum power current vector by $i = B^+f$ giving us $i = B^+A^+F$. In general these two methods do not give the same solution since $(AB)^+ \neq B^+A^+$ [7]. In fact, the power solved by the one stage method is less than or equal, and therefore optimal, to the solution of the two stage method ($||(AB)^+F|| \leq ||B^+A^+F||$). This tells us that, in general, we must not separate the kinematic stage from the electro-magnetic stage if we want to minimize the power.

Due to the structure of the linear motors, the one stage solution is equal to the two stage solution ($||(AB)^+F|| = ||B^+A^+F||$). In can be shown that the methods are equal by shown that the following equation is true.

$$(AB)^+ = B^+A^+$$

The problem described above is a convex optimization problem defined by a quadratic cost function ($||i||^2$) subject to linear constraints ($F = ABi$).

Input: desired global force vector F

Stage 1.

Step 1: solve $f = A^+F$

Stage 2.

Step 1: solve $i = B^+f$

Output: current vector i

TABLE 1. Min Power Method

Heat Symmetry

We propose an adapted problem, by adding the constraints that each motor's power ($||i^k||^2$), separately, is equal to one another:

$$\begin{aligned} &\min ||i||^2 \\ &\text{subject to} \\ &F = ABi \\ &||i^k||^2 = \frac{P}{4}; \\ &k = \{1, 2, 3, 4\} \end{aligned}$$

This problem is motivated by the temperature gradient, and subsequent non-symmetric deformation of the platen, produced by the motors generating different power profiles. By each motor generating the same power we force heat symmetry on the platen and therefore symmetric deformation about the center of the platen. This problem is non-convex since the added quadratic equality constraints are non-convex [8].

The above stated problem is difficult to solve. We propose to solve this problem by a 2-stage method. We will introduce two different methods

to force heat symmetry by the motors and suggest that one the latter of these methods equal to the "exact" solution. The first method (a: see table 2) is to solve stage 1 and stage 2 as before, in the minimum power problem (see table 1) with added steps in stage 2. The first of these steps is to find the motor with the max power($P = \max_k(||i^k||)$ and then, using the current vector in the nullspace of each motor, increasing the current without changing the force. This is done until all the motor have the same power ($i_{1k}^2 + i_{2k}^2 + i_{3k}^2 = P$).

Given: desired global force vector F

Stage 1.

Step 1: solve $f = A^+F$

Stage 2.

Step 1: solve $i = B^+f$

Step 2: set $P = \max_k(||i^k||)$

Step 3: solve for i^k for each motor

$$f^k = \begin{bmatrix} C_{xk}^T \\ C_{zk}^T \end{bmatrix} i^k$$

$$P = (i^k)^T(i^k)$$
$$= i_{1k}^2 + i_{2k}^2 + i_{3k}^2$$

Output: current vector i

TABLE 2. Heat Symmetry Method (a)

The second method (b: see table 3) differs from the previous heat symmetric method (a) in stage 1. In stage 1 of this method, we are going to solve for the local force vector f that minimizes the maximum of the forces (actually the norm of the forces, $\min\max||f^k||^2$) rather than using the pseudo-inverse. Intuitively, since we are going to make the power of each motor the same, minimizing the total power would be equal to minimizing the power of just that one motor needing the greatest power. It can be shown, using the structure of linear motors, that the one motor needing the greatest power is also the one motor needing the greatest force (solved in stage 1).

The results of a simulated example, where the desired global forces are $F_x = 1$, $T_z = 1$, and all the rest are zero, are shown in table 4. It is

---

Given: desired global force vector F

Stage 1.

Step 1: solve convex problem for f

$\min(\max(||f^k||))$

subject to

$F = Af$

Stage 2.

Step 1: solve $i = B^+f$

Step 2: set $P = \max_k(||i^k||)$

Step 3: solve for i^k for each motor

$$f^k = \begin{bmatrix} C_{xk}^T \\ C_{zk}^T \end{bmatrix} i^k$$

$$P = (i^k)^T(i^k)$$
$$= i_{1k}^2 + i_{2k}^2 + i_{3k}^2$$

Output: current vector i

TABLE 3. Heat Symmetry Method (b)

interesting to notice that although the norm of the forces ($||f||^2$), solved in stage 1 of method (b), is greater than for method (a), the total power using method (b) is less than using method (a). A proof that the solution of method (b) is equal to the "exact" solution (P^*) is in progress.

Method	f_{x1}	f_{x2}	f_{x3}	f_{x4}	$\|\|f\|\|^2$	$\|\|i\|\|^2$
min P	1.5	1	.5	1	4.5	1.2
(a)	1.5	1	.5	1	4.5	2.4
(b)	1.25	1.25	.25	1.25	4.75	1.6

TABLE 4. Solving for i, by a given method, where $F_x = 1; T_z = 4R$

PRELIMINARY RESULTS

The minimum power commutation scheme has been implemented on the PMAC2 controller. Figure 6 shows the experimental results of a PID servo loop tracking trapezoidal profiles for each axis. Work is in progress to implement advanced control, such as iterative learning control [9], repetitive and adaptive control [11, 12] to further reduce the repeatable and non-repeatable errors.

ACKNOWLEDGEMENTS

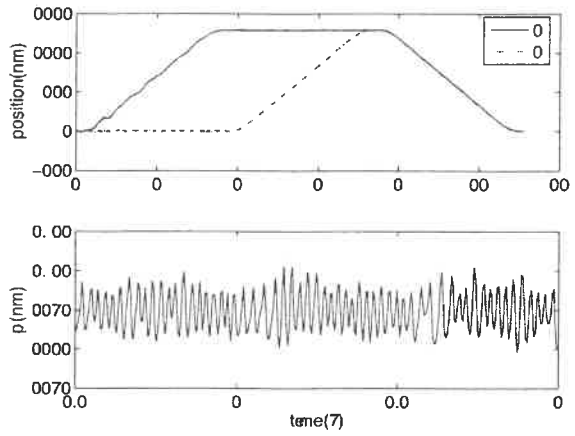

FIGURE 6. platen Trapezoidal trajectory under PID control

The authors would like to thank Prof. Robert Hocken, Ozkan Ozturk, and other members of the MAPS design team at UNC Charlotte for supporting the integration of the control system, and Delta Tau Data Systems, Inc., for donating the UMAC real-time control hardware and software. This work was supported in part by the National Science Foundation under grant no. DMI 0327077, Nanoscale Science and Engineering Center for Scalable and Integrated NAnomanufacturing (SINAM).

REFERENCES

[1] Ozturk O, Fesperman RR, Hocken RJ. Design of Multi-scale Alignment and Positioning System. In: Proceedings of euspen International Conference; 2008. .

[2] Holmes M, Hocken RJ, Trumper D. The long-range scanning stage: a novel platform for scanned-probe microscopy. Precision Engineering. 2000;24:191–209.

[3] Kim WJ, Hu T, Bhat ND. Design and Control of a 6-DOF High-Precision Integrated Positioner. In: Proceedings of the American Control Conference; 2004. .

[4] Trumper DL, Kim WJ, Williams ME. Design and Analysis Framework for Linear Permanent Magnet Machines. IEEE Transactions on Industry Applications. 1996;32(2):371–379.

[5] Holmes ML. Analysis and Design of a Long-Range Scanning Stage. University of North Carolina, Charlotte; 1998.

[6] Fesperman RR. Multiscale Alignment and Positioning System. University of North Carolina, Charlotte; 2007.

[7] Laub AJ. Matrix Analysis for Scientists and Engineers. SIAM; 2004.

[8] Boyd S, Vandenberghe L. Convex Optimization. Cambridge University Press; 2004.

[9] Mishra S, Coaplen J, Tomizuka M. Precision Positioning of Wafer Scanners: Segmented Iterative Learning Control for Nonrepetitive Disturbance. IEEE Control Systems Magazine. 2007 August;p. 20–25.

[10] Tomizuka M, Tsao TC, Chew KK. Analysis and Synthesis of Discrete-Time Repetitive Controllers. Journal of Dynamic Systems, Measurement, Control. 1989;111:353–358.

[11] Lin CY, Tsao TC. Nano-Precision Dynamic Motion Control. In: Proceedings of SPIE; 2007. .

[12] Lin CY, Tsao TC. adaptive repetitive control of piezoelectric actuators for nano-precision motion control. In: Proceedings of ASPE Annual Meeting; 2007. .

DAMPING AND HOMING IN A NANOIMPRINTING MACHINE

Ozkan Ozturk[1], John F. Brien[1], and Robert J. Hocken[1]
[1]Center for Precision Metrology,
University of North Carolina at Charlotte,
Charlotte, NC

ABSTRACT

MAPS is a low cost six degree of freedom precision positioning system with interchangeable modules designed and built for next generation lithography techniques such as Nano-scale Imprint Lithography (NIL) and Plasmonic Imaging Lithography (PIL). MAPS will also be capable of performing surface topography measurements by using an interchangeable Atomic Force Microscopy (AFM) module. The design of MAPS is discussed by Fesperman and Ozturk [1-3]. The moving platform of the stage (Platen) glides on a vacuum preloaded air bearing and translates laterally. Mechanical damping for the platen is obtained by four copper plates that are attached to the platen moving in a magnetic field causing eddy currents on the plates to create forces opposing to the motion. The displacement measurement of the platen is obtained by using double-pass heterodyne interferometers. Since laser displacement measurement interferometry is a relative measurement, optical density gradient scales are used as homing sensors for absolute positioning sensing. In this paper the eddy current dampers and the optical homing sensors of the MAPS will be discussed.

INTRODUCTION

Precision position stages require non-contact actuators and guideways in order to obtain higher accuracy and resolution. MAPS utilizes four Halbach linear motors to provide motion to the platen which glides on a vacuum preloaded air bearing in the lateral directions. Mechanical dampers are required to increase the performance of the system. A non-contact type damper is designed for MAPS by using the eddy current theory. Eddy currents are generated in a conductor by a moving or changing magnetic field, or by moving the conductor in a stationary magnetic field. Eddy currents are generated in the direction to oppose the effect of the magnetic field. Eddy currents have many applications areas such as generating electricity from movement, microphones, non-destructive testing, displacement sensors and mechanical braking. Mechanical dampers can be designed by using the eddy currents. Mechanical damping is always helpful to obtain better performance in precision positioning systems. There are several techniques to add damping to a system but eddy current damping was selected since it is non-contact and relatively clean.

Double-pass heterodyne interferometers with 0.15nm resolution are used to measure displacements of the platen along both x- and y-axes. Two interferometers are used for measuring displacements along the x-axis and rotations about the z-axis (yaw) and one interferometer is used for measuring displacements along y-axis. However, the displacement laser interferometer system can only provide relative feedback. Homing sensors are required to start and return the machine to its nominal position. Once the machine is returned to its home position, the reference coordinate system can be defined and all the axes can be reset to "0". This is important for phasing of the linear motors and for error mapping the machine. MAPS uses a unique method of determining the absolute position of the platen in X, Y and theta that also provides proportional position sensing adequate for servo use.

EDDY CURRENT DAMPING

MAPS utilizes four eddy current dampers located 90 degrees apart from each other at each corner of the stationary base structure.

Three L-brackets are used to locate the dampers and Belleville spring washers are used to adjust the tilt and therefore the gap between the copper plates and the magnets.

The magnet yoke is composed of a top plate, a bottom plate and a spacer. This made the assembly much easier than using a single monolithic yoke. The yoke components are made of mild steel (c1018). Totally eight magnets are used in one damper where four are attached to the bottom plate and the other four to the top plate (*FIGURE 1*).

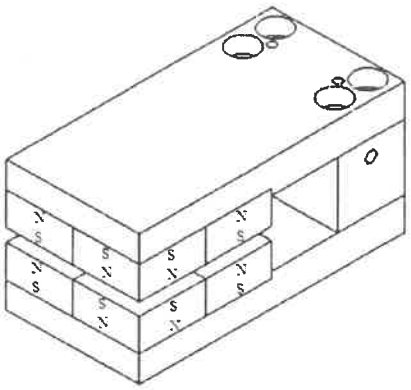

FIGURE 1. Eddy Current Damper Magnets

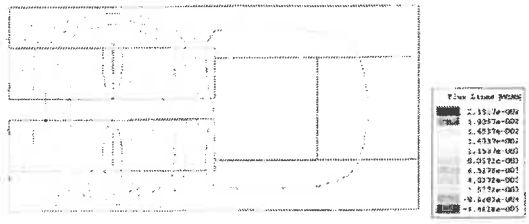

FIGURE 2. Flux Lines

Neodymium Iron Boron (NdFeB) magnets with flux density (Br) of 1.3 Tesla are used. Each magnet has the opposite polarization next to itself. Therefore magnetic flux is concentrated mostly in between the magnets (*FIGURE 2*) preventing the yoke being saturated and the generation of stray field around the damper. The stray fields can interfere with the magnetic field of the Halbach magnets arrays and can cause problems [4]. Although Br is specified as 1.3 Tesla for each individual magnet, the flux density between the magnets is expected to be different and was measured to be 0.95 Tesla [5]. Oxygen-free high conductivity copper plates are used as the conductive plates. Each copper plate is about 76 mm x 110 mm and has thickness of 3.5 mm. Four plates are attached to the platen 90 degrees apart from each other.

When copper plates move in the stationery magnetic field between the magnets, eddy currents are induced in the copper. The induced currents on the conductor plate create Lorentz forces impeding the motion. The formulations to calculate the damping coefficient and therefore the force are explained by Bae et al. [6] in detail.

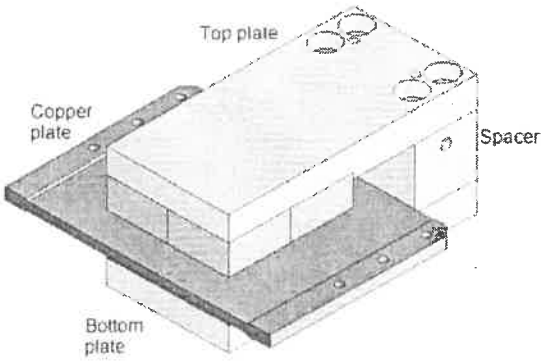

FIGURE 3. Eddy Current Damper

TABLE 1. Eddy current damper parameters

B	Magnetic field (T)	0.95
σ	Conductivity of copper (1/Ω.m)	6.00E+07
δ	Thickness of the copper plate (m)	3.5×10^{-3}
a	Width of the magnet array area (m)	50.8×10^{-3}
b	Height of the magnet array area (m)	50.8×10^{-3}
A	Pole projection area (m^2)	2581×10^{-6}

The damping coefficient for each damper can be calculated by using the formula

$$C_x = \sigma \delta B_z^2 A(\alpha_1 + \alpha_2)$$

where α_1 and α_2 are plate geometry related constants. The damping coefficient is calculated to be 216.4 per damper and 856.6 total. The total opposing force to the motion can be calculated with the formula

$$F = 856.6V$$

where F is in newtons and V is the copper plates speed in m/s.

The force prediction of the eddy current damper is compared with the actual measurement taken on the Moore Tool measuring machine (model no: 35-11-B03-2500-6350G). The results are as shown in the following table.

TABLE 1. Eddy current damper test results

Speed (m/s)	Predicted Force (N)	Measured Force (N)
0.00072	0.157	0.150
0.00036	0.078	0.070

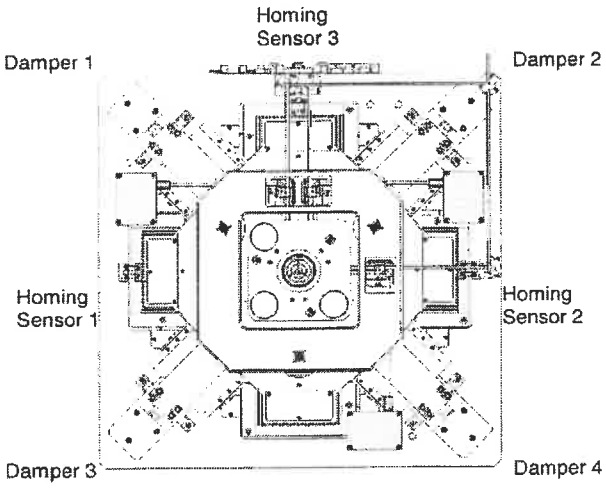

FIGURE 4. Eddy Current Damper and Homing sensor locations

HOMING

Three homing sensors are used in MAPS to home the stage in X, Y and θ_z. Two of the sensors are positioned across from each other along the x axis for the rotation about the z axis and the 3rd one is positioned along the y axis. The main elements of the sensors are optical elements with variably optical density. These elements are mounted on the platen on top of the Halbach magnet arrays. A special holder is designed to hold each sensor.

The optical density gradient scales are printed on a 5 mm by 12 mm clear Mylar by a commercial typesetter service. The scales are modeled using Autocad's shading tool. The scale is most transparent in the middle and most opaque at the outer edges along the length as seen in Figure 5.

Each homing sensor is composed of a scale and a pair of optical interrupters similar to the ones used in CDROM drives to detect the presence of a CD. The optical interrupters are spaced 6 mm apart and one half of the gradient passes through each interrupter. When the stage moves in one direction, one of the optical interrupters sees through the more transparent portion of the gradient while the other optical interrupter sees the more opaque portion of the gradient.

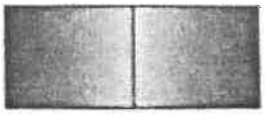

FIGURE 5. Optical density gradient scale

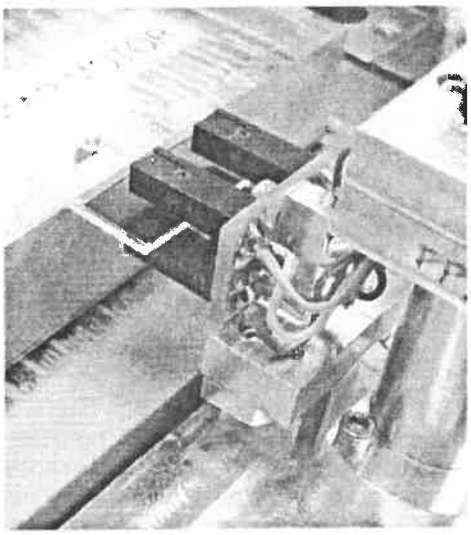

FIGURE 6. Homing Sensor

The IR phototransistor sections of the two optical interrupters are connected to a differential amplifier whose output voltage is a function of the light passing through the scale and thus the platen position. This voltage output is scaled for an output voltage of -10 volts DC for -5mm and +10 volts DC for +5mm. The midpoint output is 0 Volts.

The optical density gradient scales are mounted to the platen in such a way that during normal operation the X axis optical interrupters do not register motion in the Y direction and the Y axis optical interrupter does not register motion in the X direction.

The first step in the homing procedure is to rotate the platen so as to measure the same voltage from the two X axis optical interrupters. The second step is to move the stage in the Y direction until the output of the Y axis optical interrupter is 0 volts. The third step is to move the platen in the X direction until the X axis

optical interrupters output 0 volts. This puts the platen in home position for both X and Y axis as well as a θ_z of 0.

The performance of the homing sensors is measured by using the double-pass laser interferometers. The controller (using the lasers as the feedback sensors) of the system is turned on and the stage is commanded to go to the predefined home position (Position 1). Then the stage is commanded to travel to the numbered locations (2, 3, 4, and 5) shown in figure 7 respectively by returning back to the home position (Position 1) after each move.

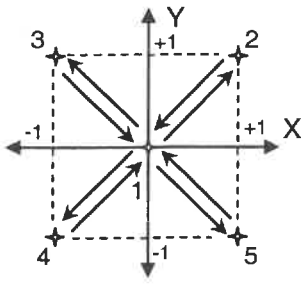

FIGURE 7. Homing Sensor Test Path

The results show that the homing sensors have ranges of ±4 μm repeatability in both X and Y axes. However the short term (10 minutes) drift of the stage due to the temperature variations in the lab is measured to be ± 6 μm.

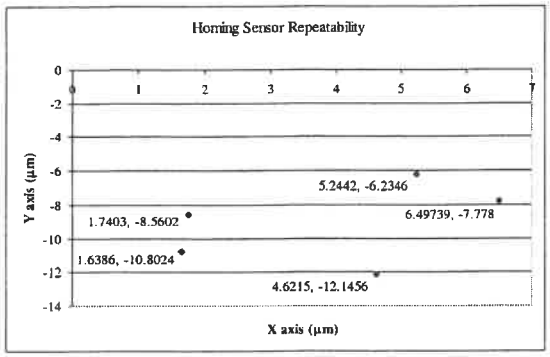

FIGURE 8. Homing Sensor Repeatability

CONCLUSION

The eddy current dampers provided the expected damping forces. They were designed to be simple and cheap. However some modifications could be done if they are to be designed again. Instead of using rectangular magnets, circular magnets could be used to reduce the edge effects. Since it is hard to find off the shelf circular magnets, the rectangular magnets were cheaper.

A special kind of homing sensors was designed and tested. The homing sensors are good enough to phase the linear motors and provide location for software correction. The gradation quality could be improved by using different techniques. Also a more robust and stable mounting technique could also be applied.

ACKNOWLEDGEMENTS

Authors would like to thank Dr. David L. Trumper of MIT and Fred Sommerhalter for their contribution in the design and assembly of the eddy current dampers, and Dr. T.C. Tsao and Shalom D. Ruben for providing the controller system for MAPS. The authors would also like to thanks UNC Charlotte Center for Precision Metrology and SINAM, an NSF Nanoscale Science and Engineering Center, for funding the project.

REFERENCES

[1] Fesperman RR, Design of Multi-scale Alignment and Positioning System, Ph.D. Disseration, UNC Charlotte, 2006

[2] Ozturk O, Design of Multi-scale Alignment and Positioning System II, Ph.D. Dissertation, UNC Charlotte, 2008

[3] Ozturk O, Fesperman RR, Hocken RJ. Design of Multi-scale Alignment and Positioning System, Proceedings of the euspen International Conference -Zurich- May 2008

[4] Private communication with Dr. David L. Trumper

[5] Reference and Design Manual, Dexter Magnetic Technologies

[6] Bae JS, Kwak MK, Inman DJ, Vibration suppression of a cantilever beam using eddy current damper, Journal of Sound and Vibration, 284 (2005) 805-824

PROVIDING PRECISION MECHATRONIC SOLUTIONS FOR THE CHALLENGES OF EUV-LITHOGRAPHY

Marcel Renkens, Rob Tabor, Theo Ruijl
Philips Applied Technologies
High Tech Campus 7, 5656AE Eindhoven,
The Netherlands
m.j.m.renkens@philips.com

CHALLENGES EUVL

EUV-Lithography (EUVL) is considered as the leading candidate to succeed 193nm-immersion lithography. Currently EUVL is expected to be inserted for volume production at the 32-nm node.

EUVL is bases on a wavelength of the light of 13.5 nm. Figure 1 shows schematic representtation of the 'optical system' of a EUVL tool.

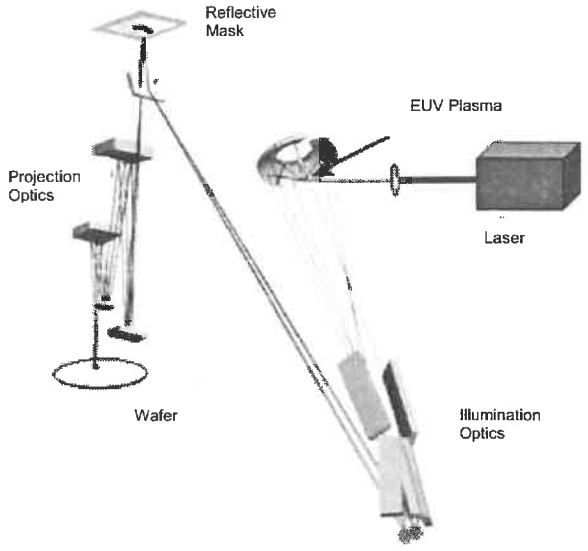

FIGURE 1. Schematic representation of a EUVL System (Courtesy EUV LLC)

The EUV light is produced by plasma. Currently two types of sources are considered: laser produced plasma (LPP) or discharge produced plasma (DPP). The emitted light of the plasma is (partly) collected by the collector optics and then shaped by the illuminator optics into a ring-shaped field on the reflective reticle. The projection optics produces a 4x reduction of the reticle image on the wafer

EUVL faces all common precision challenges related to sub-50nm lithography. One of the driving aspects in the design of sub-50nm lithography tools is the overlay performance of a few nanometers that has to be guaranteed. This asks for (sub)nanometer stage and metrology performance.

Furthermore the EUV technology puts several specific requirements on the design of these tools:

Vacuum

All materials are strongly absorbing at 13.5 nm. Since EUV light will also be absorbed in normal atmosphere, the system has to be operated in a vacuum environment. To limit the absorption to an acceptable level the air pressure within the system should be lower than 10^{-3} mbar, which can be characterized as 'medium vacuum'. However to avoid mirror degradation by oxidation or carbon growth the vacuum specification should be similar to a (ultra) high vacuum system. As a consequence the system should contain no or a minimum amount of high outgassing materials such as plastics, adhesives, lubricants etc. This will have a major impact on the design, realization and operation of a EUVL tool

Optics and Mask Heating

Optics and masks must be reflective and coated with a stack of multi-layers in order to provide sufficient reflection (60-70% per mirror). Consequently 30-40% of the EUV light will be absorbed at each mirror. The Projection optics will contain a minimum of 6 mirrors. Consequently the heat load on the mask will be significantly higher than for a 193nm system. For a production tool with a throughput of 150 300mm wafers per hour this leads to a heat absorption in the mask of at least 10W. To meet

the stringent overlay requirements, advanced thermal management strategies are required to control the thermal expansion of the mask. The required EUV power in the plasma of the source will be significantly higher than 1000W.

Optics Sensitivity

Reflective Optics (mirrors) are more sensitive to rotations of the optical elements than refractive optics (lenses). As a result, the internal vibrations of projection optics based on reflective elements should be about one order of magnitude lower than for a system bases on refractive elements. This requires a significant improvement of the vibration isolation system.

ENABLING EUVL

Within Philips Applied Technologies a number of technologies have been developed to enable EUVL.

Differentially pumped air bearing

Figure 2 shows a schematic representation of a differentially pumped air bearing. The small gap (app. 10 micrometer) that can be realized by an aerostatic bearing is used as a restriction for the incoming air. By applying one or more scavenging grooves (i.e. a groove connected to a vacuum pump), the remaining gas load on the system can be reduced to an acceptable level. Design rules have been developed to optimize the dimension of such a configuration.

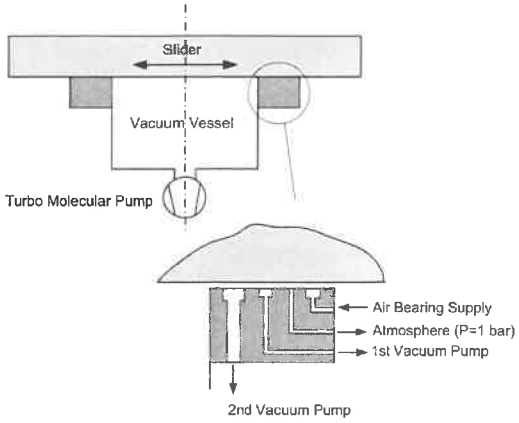

FIGURE 2. Schematic representation of a differentially pumped air bearing

A major advantage is the absence of mechanical contact. As a result no friction forces are observed, no particles are generated and no lubricants are needed. Besides, a motion within the vacuum chamber can be generated without having actuators and sensors in the vacuum chamber.

Several configurations have been designed and successfully tested for linear as well as rotational motions. This concept can be used for wafer stages, reticle stages, handler systems, etc.

Magnetically Levitated (Maglev) Stages

Conventional ball bearings show serious drawbacks for the application in EUVL systems: Without applying lubricants, the lifetime of these bearings is very limited. Besides, unwanted particles will be generated. These problems can be solved by applying magnetically levitated stages.

In the past decade Philips Applied Technologies has developed several 'long stroke' Maglev platforms. These platforms are based on linear as well as planar modules. A linear module features a relatively long in one direction combined with short strokes and rotations (order of millimeter/milliradian) in all other directions, with nanometer precision. The resulting system demonstrates six degrees of freedom. In a stacked configuration (e.g. H-drive) the linear modules can provide long stroke functionality in a plane. A planar Maglev module offers long stroke functionality in 2 linear directions and short stroke levitation in all other directions.

Three different Maglev technologies have been developed within Philips Applied Technologies, each of which has advantages for particular applications. These are:

1. Linear Maglev modules using variable reluctance actuators.
2. Linear Maglev technology using Lorentz actuators (so called 'NForcer Technology').
3. Planar Maglev technology using Lorentz actuators. This technology can be realized with moving coils as well as with moving magnets (so called 'inverted' planar motor)

Figure 3-left shows a demonstrator, fitted to a laser cutting machine using a XY motor with reluctance actuators. This motor uses a hybrid variable reluctance actuator consisting of an iron core, a permanent magnet and a current conducting coil (fig. 3-right).

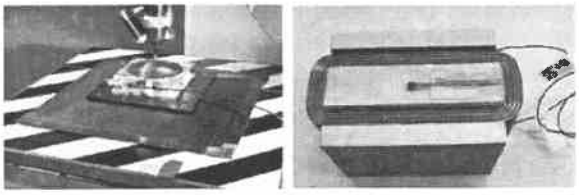

FIGURE 3. XY Maglev Stage based on linear Maglev modules using reluctance motors.

Philips Applied Technologies has patented the 'NForcer Technology'. This new innovation enables horizontally-mounted standard iron-less, multi-phase linear motors to generate lift as well as lateral motion. This can be realized by slightly re-positioning the components and driving them in an intelligent way. Consequently NForcer Technology also enables the production of precision magnetically levitated platforms with six axes of controlled motion (3-dimensional shifts and tilts) by using ordinary linear motors. Figure 5 shows a magnetically levitated platform movable in six degrees of freedom with nanometer accuracy.

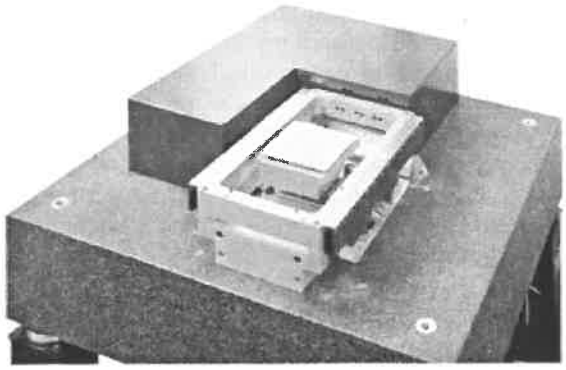

FIGURE 4. Magnetically levitated platform with nanometer accuracy based on 'NForcer Technology'

The use of 'NForcer technology' will reduce the number of motors and drive electronics, resulting in significantly lower equipment cost. By reducing the mass of moving parts, it will also allow designers to produce designs that achieve higher accelerations and operating speeds.

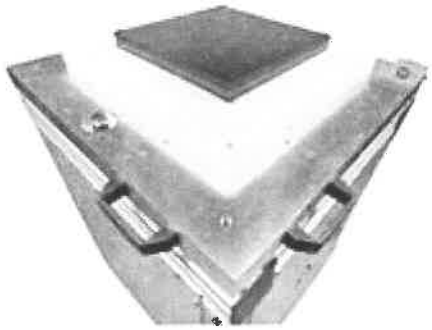

FIGURE 5. 'Inverted' Planar Maglev Motor using reluctance motors.

More recently, the inverted planar maglev technology has been developed (see figure 5). This is a unique development in maglev technology using Lorentz actuators to provide the motive force. The free-floating platform houses the permanent magnets (in a chess-board pattern where the "black" squares are "north", and the "white" squares are "south") while the fixed bed contains the coils. The force generated by the Lorentz actuators is related linearly to the flux carried by the coils.

The presented maglev stage configurations can all be realized in vacuum compatible versions.

Vibration Isolation System

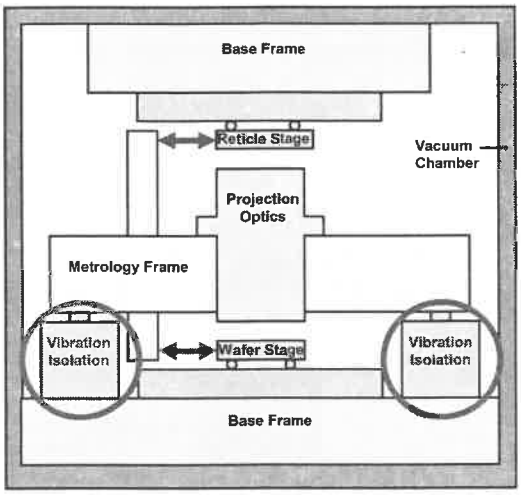

FIGURE 6. EUVL projection optics vibration isolation by vacuum compatible isolation systems.

One of the critical aspects of EUVL is the vibration isolation of the projection optics. Philips Applied Technologies has developed high performance vacuum compatible vibration isolation systems. These active vibration isolation systems offer sub-Hertz isolation combined with a very low internal noise level. Since these systems operate inside the vacuum system, all acoustic excitation of the isolated frames and/or projection optics can be eliminated. Acceleration levels have been demonstrated that meet the stringent EUVL requirements. Figure 6 shows a potential configuration for isolating the projection optics of a EUVL system.

CRITICAL DIMENSION CONTROL, OVERLAY, AND THROUGHPUT BUDGETS IN UV NANOIMPRINT STEPPER TECHNOLOGY

S.V. Sreenivasan[1, 2], P.D. Schumaker[2], B.J. Choi[2]

[1]Department of Mechanical Engineering
University of Texas at Austin
Austin, TX 78712, U.S.A.

[2]Molecular Imprints, Inc.
1807C, W. Braker Lane
Austin, TX 78758, U.S.A

ABSTRACT

Imprint lithography is known to possess remarkable patterning resolution down to sub-5nm, while simultaneously possessing the capability to pattern over large areas with long-range order. The ability to pattern materials at the nano-scale has the potential to enable a broad range of applications including CMOS IC fabrication, nanowire molecular memory, terabit density magnetic storage, photonic devices, and biomedical applications.

This paper focuses on manufacturing requirements for CMOS ICs and nanoelectronic devices, and provides a status of imprint lithography technology as related to these applications. The article includes a review of photon based lithography techniques, and proximity mechanical nanopatterning techniques including soft lithography and imprint lithography. Next, a UV nanoimprint process that is specifically suited for IC fabrication is discussed. This process is based on a drop-on-demand material dispense approach and it forms the basis for the UV imprint stepper technology. The article then provides a detailed discussion including a budget analysis of three lithographic metrics that are influenced by the tool design: Critical dimension (CD) control, overlay, and throughput. The article concludes with a gap analysis of the UV imprint stepper technology relative to sub-32nm IC fabrication requirements.

1. LITHOGRAPHIC REQUIREMENTS FOR CMOS IC AND NANOELECTRONICS:

The ability to pattern materials at the nano-scale over large areas is known to be valuable in variety of applications[1]. In CMOS IC fabrication, devices are being fabricated today at about 50nm half-pitch resolution. For CMOS memory and logic devices the patterning roadmap extends well below 15nm half pitch as published in the 2007 International Technology Roadmap for Semiconductors[2]. An example of a sub-40nm memory gate pattern is shown in Figure 1[3]. In the area of nanoelectronics, recent literature in nanowire molecular memory indicates that ultra-high density memory can be fabricated using patterning at the sub-20nm scale[4].

While several nanolithography techniques are reported in the literature, only a small percentage of them have the potential to be viable for volume manufacturing of ICs since the patterning approach has to satisfy the following attributes:

- ***Patterning of arbitrary patterns with varying pattern densities:*** Varying pattern densities are in general required for applications such as CMOS circuits (Figure 2). This places special challenges on imprint lithography as discussed later in this article.
- ***Long-range order in nano-structures:*** This includes CD control and image placement (location of the patterns with respect to an ideal grid). It is typically desirable that the CD control is ~ 10% of the feature size over the entire wafer and from wafer to wafer. Similarly, if the placement of the pattern is distorted significantly from an ideal grid, it can affect overlay of multiple lithography layers in CMOS ICs.
- ***Overlay:*** CMOS ICs and nanoelectronic devices require nano-scale overlay. The overlay requirement is typically < ¼ of the half-pitch for advanced memory applications.
- ***High throughput processes:*** This is critical for achieving acceptable data transfer rates in the manufacturing process to achieve cost-effective device manufacturing. The importance of patterned area and throughput relative to nanofabrication has been addressed in the literature[5]. Figure 3 is an adaptation of Figure 1 from reference[5] with current information provided for photolithography and imprint lithography.

- ***Substantially leverage existing technologies and infrastructure:*** It is very important that a new nanopatterning technology can be readily dropped into an existing process flow such that the new technology leverages most of the previous investment in manufacture of these devices; a new nanolithography technique should be able to "mix-and-match" with photolithography.
- ***Low process defectivity to achieve high overall product yield:*** It is important to ensure that the defect requirements of nano-scale devices are well understood and high device yields are achieved. Acceptable defect requirements vary for various ICc with logic devices being the most demanding.

2. NANO-PATTERNING OPTIONS:

Top down patterning with photolithography has been the workhorse of the semiconductor industry for over 30 years. In addition to it continued improvement in resolution, the appeal of photolithography has been its long-range order, precision overlay and its extremely high data transfer efficiency making it attractive in manufacturing of large-scale integrated devices. The leading edge photolithography solution is 193nm photolithography with water immersion (193nm-i) is expected to possess resolution down to about 45nm half-pitch beyond which double patterning techniques will be required. Double patterning will be expensive and put significant constraints on device designs essentially approaching repeating grating structures of a given pitch across an entire mask design. Critical layers for NAND Flash memory applications are conducive to such constrained designs and therefore, 193nm-i along with double patterning will likely allow sub-45nm half-pitch patterning for such memory devices. However, logic devices that have more complicated designs are expected to have significant challenges at half-pitch values of 45nm and below. Extreme Ultraviolet Lithography (EUVL) at 13.2nm (soft x-ray) wavelengths is being developed by the industry to provide patterning capability of arbitrary nanostructures. The EUVL technology has several challenges that need to be addressed including soft x-ray source power; a high-resolution photoresist with high sensitivity and low line edge roughness, tool complexity and cost, and a reflective mask blank infrastructure[6]. If these challenges are successfully overcome, EUVL is expected to be viable for sub-32nm half-pitch lithography for silicon ICs.

Imprint lithography has been known to possess sub-10nm replication resolution and an attractive cost structure based on the early results from reference[7] and sub-3nm resolution based on more recent results[8]. Historically, there have been legitimate concerns about its viability in manufacturing because of a lack of comprehensive development in areas such as long-range order, overlay, high throughput, and low defectivity. However, in recent years it is becoming evident that imprint lithography is maturing in its manufacturing attributes.

Early research related to imprint lithography (prior to reference[7]) includes micro-contact printing[9], wherein an "ink" adhering to the raised features of a polymer mold is transferred to a substrate using intimate contact of the soft mold and the substrate. This technique has been used very successfully for making micron and sub-micron scale printing. However, it does not possess the single-digit nanometer resolution of imprint processes that essentially molds a liquid to conform to the shape of the imprint mask. The first known attempt of using a nano-imprinting technique in a systematic way involved the use of a mold with recessed structures which was impressed onto a thermo plastic material, and with the combination of heat and pressure, the pattern in the mold was transferred to the thermo plastic material[7]. However, both the high temperature and pressure can induce technical difficulty associated with not only its low throughput due to high viscous flows, but also distortions causing overlay problems for fabrication of multi-layer circuits. The UV nano-imprint processes uses UV cross-linking chemicals as imprinting layers. The viscosity of the UV fluid can be tuned low enough so that the fluid filing can be accomplished in the absence of a high compressive pressure, which makes it a room temperature processing. This type of process has been implemented for both the step & repeat and whole wafer processes[10, 11, 12]. Depending on how the imprinting fluid is applied to the substrate, UV nanoimprint processes can be further divided into drop-on-demand dispense[11] and spin-on processes[13].

As illustrated in Figure 4, the Step and Flash Imprint Lithography (S-FIL™) process uses low viscosity UV imprint fluids where an array of small drops of the imprint fluids is dispensed in a drop-on-demand manner depending on the pattern density variations of

the imprint mask. The ability to handle arbitrary pattern densities is critical to silicon ICs a variety of applications. Also as indicated in the literature, use of spin-on material deposition can lead to non-uniform pressure distribution[14]. This can be further aggravated by the presence of pattern density variations[15]. The uniform low pressure, room temperature nature of S-FIL, and the transparent imprint masks make it particularly attractive for a high-resolution layer-to-layer alignment[16, 17]. Another aspect of S-FIL that assists in the alignment is the presence of a thin layer of low viscosity liquid between the imprint mask and substrate[17].

3. BUILDING BLOCKS FOR UV NANOIMPRINT LITHOGRAPHY

The three primary building blocks that contribute to a UV imprint lithography process are the (i) imprint masks, (ii) imprint materials, and (iii) imprint tools (see Figure 5). Imprint masks and materials are not discussed in any detail here as the focus of this article is tool technology. A discussion of imprint masks and materials is provided in reference[1].

3.1 UV Imprint Tools: Imprint tools based on drop-on-demand UV nanoimprinting are broadly divided into (i) Whole substrate tools for applications that do not require nano-resolution overlay (such as patterned media and photonic crystals for LEDs), and (ii) Steppers for applications requiring nano-resolution overlay and mix-and-match with photolithography (such as silicon ICs and thin film heads for magnetic storage) wherein the field size printing in one patterning step is the same as the industry standard advanced photolithography field size (26mm by 32mm). The basic drop-on-demand process shown in Figure 4 can be seamlessly integrated as part of a whole substrate tool or a stepper since in each case the material is dispensed only where needed just prior to the patterning step. This dispense approach not only allows drop tailoring based on mask pattern density variations, it also ensures that a stepper process does not require handling of wet, evaporative films as would be the case with a spin-on UV process. Figure 6 shows the schematic of a photolithography stepper and a UV imprint stepper based on drop dispense of the imprint material. The imprint tools include precision self-leveling flexure systems (Figure 6) to passively align the imprint mask and substrate to be substantially parallel during the imprint process[18] . In addition, by using a drop-dispense approach that can be tailored based on mask pattern variation, a highly uniform residual layer can be achieved. Here the residual layer in the underlying film of imprint material that is always present in the imprint process between the imprint mask and the substrate. This film needs to be thin and uniform for achieving a subsequent etch process that has a high degree of long-range uniformity (CD control).

In addition to the dispensing of the imprint fluid and the control of the residual layer, the stepper system has additional precision mechanical systems to achieve nano-resolution alignment and overlay. The alignment sub-system that aligns the imprint mask in x, y, and theta directions with respect to the wafer is based on field-to-field moiré detection alignment scheme developed originally for X-ray lithography[19] and subsequently adapted to UV imprint lithography[17]. In addition to the alignment, size (magnification) and shape (orthogonality and trapezoidal) corrections are required to perform nano-resolution overlay, particularly if mixing-and-matching to optical lithography. A precision mechanical deformation system that deforms the imprint mask has been developed and implemented as part of the stepper system[20, 17]. This allows the stepper to achieve sub-15nm ($\mu + 3\sigma$) overlay as discussed in Section 4.

4. STEPPER PERFORMANCE RESULTS

This section provides recent tool and process results for UV imprint stepper technology. The key performance metrics for IC fabrication include (i) resolution and CD control; (ii) alignment and overlay; (iii) throughput and cost considerations; and (iv) process defectivity. In this section the first three topics will be discussed in detail; process defectivity is weakly influenced by the tool design and therefore is not discussed here in any detail. Significant progress has been made in demonstrating feasibility of <1 def/cm^2 for UV imprint lithography and is discussed in the literature[21, 22].

4.1 Resolution, CD control and Line Edge Roughness: The resolution of the imprint lithography process is a direct function of the resolution of the imprint mask down to sub-3nm[8]. The imprinted CD control is also a direct function of the imprint mask fabrication process; imprinted CD is correlated with the imprint mask CD to well below 1nm 3σ fidelity[23, 24, 25]. This fidelity number may be currently limited by metrology and may well be substantially better.

If the imprint masks are obtained from commercially photomask houses such as DNP and Hoya that have well established e-beam, etch and metrology processes, good CD control over long-ranges has been obtained. Further, with optimized electron beam resists, low line edge roughness can be obtained in the imprint mask fabrication process (see Figures 7 and 8)[23, 26].

The total critical dimension uniformity (CDU_T) budget can be typically assumed to be 10% 3σ of the half-pitch of lithography[2]. In the imprint process, this CDU budget is allocated between the following:

- Mask CDU (CDU_M)
- Imprint process fidelity (CDU_I)
- Etch pattern transfer CDU (CDU_E)

$$CDU_T = \{(CDU_M)^2 + (CDU_I)^2 + (CDU_E)^2\}^{½}$$

For 32nm and 22nm half-pitch (HP) lithography, a reasonable CDU budget allocation would be as shown in Table 1 shown below:

Table 1: *CDU Budget Elements (in nm 3σ)*

HP	CDU_T	CDU_M	CDU_E	CDU_I
32nm	3.2nm	2.5nm	1.75nm	1nm
22nm	2.2nm	1.75nm	1nm	0.9nm

In the literature, CDU_M of about 3nm 3σ has been reported, and work is continuing to improve this to the levels shown in Table 1. Based on results to-date, the CDUI numbers in Table 1 are expected to be readily achievable. The CDU_E is the budget element that is most directly affected by the stepper performance, specifically the stepper's ability to control the residual layer, and it is discussed in detail next.

Figure 9 provides a comparison of the etch process for imprint and a typical advanced photolithography stack. Here CDU_E for imprint is defined as the uniformity while etching through the residual layer and the hardmask followed by a plasma ash process to remove the imprinted material. Figure 10 provides SEM span shots of 42nm half-pitch lines through the etch process steps and illustrates the ability to hold target CD through hardmask etch. Figure 11 provides a hypothetical relationship between CDU_E and residual layer thickness. Process A would be process that is unaffected by residual layer variations and would therefore make the tool performance requirements very relaxed. In practice, this is difficult to achieve and a more realistic process will have a small slope of about 0.2 to 0.25nm per nm as shown in Figure 12. This result is preliminary and further improvements will probably reduce this slope even further. However, for the purposes of this paper, it is assumed that a slope of ≤0.2nm per nm is reasonable to assume for the 32nm and 22nm half-pitch cases.

- ***Therefore, to achieve the CDU_E of < 1nm, 3σ (for 22nm half-pitch, see Table 1), the total residual layer variation should be <5nm, 3σ.***

Residual layer control is affected by a variety of factors including:

- ***Nano-scale orientation alignment errors between the imprint mask and the substrate***: This problem can be solved by using self-correcting precision flexures that react to asymmetric fluid pressure in the absence of proper alignment, see reference[18].
- ***Per-field flatness of wafers, imprint masks, and the corresponding chucks:*** Prime grade double side polished silicon wafers[27], 500nm flatness grade commercial 6025 mask blanks, and chuck flatness specification of 25nm TIR† within a field have been used to generate the data shown in the example below.
- ***Drop on demand resist distribution correlated with the mask pattern:*** The residual layer thickness can vary if the resist distribution is not correlated to the mask pattern density variations. As shown in Figure 13, a typical sub-32nm patterning mask requires a process with a mean residual layer of 15nm for proper etch transfer. Therefore, in the presence of pattern density variations within a field, resist dispense that is uncorrelated with the mask pattern will require the liquid to travel distances over millimeters in nano-scale channels. In practice this situation leads to very high localized pressures in the fluid causing wafer or mask deformations and local pockets of fluids with highly varying residual layers[15]. In this work, 6 picoliter drops are dispensed in correlation with the mask design leading to several thousand drops per 26mm by 32mm field. This process has been automated based on off-line volume computations using mask design information available in GDS-II format.

† Total indicated range

By incorporating the three factors presented above into the tool, a residual layer variation of <5nm, 3σ, was achieved over a 200mm wafer as shown in Figure 14. Similar variation has also been demonstrated for a high resolution film thickness measurement per field (>650 measurements within a field, see Figure 16 in reference[24]).

4.2 Alignment and Overlay: In this section alignment is defined as the accuracy with which an imprinted field can registered relative to a previously lithographed field at the four corners of the patterned fields. Overlay refers to the accuracy with which an imprinted field can be registered relative to the previous field at the four corners and several points (typically ~100) over a field. The standard field size chosen here is 26mm by 32mm.

The imprint stepper has three key sub-systems that contribute to alignment and overlay:

- ***Interferometric Moiré Alignment Technique (i-MAT):*** This is the approach used to obtain real-time relative overlay errors between points on the imprint mask and the corresponding points on the wafer. The imprint stepper described in this paper uses an i-MAT system that comprises of eight channels as shown in Figure 15. The moiré metrology approach presented here is adapted from a similar approach developed for x-ray lithography (see reference[19]). This approach can theoretically measure alignment errors at a single point down to well below 1nm.
- ***Magnification actuator system:*** This system has been previously described in the literature[17]. The system uses an array of actuators that are mounted around the imprint mask that allows for in-plane corrections including independent scale corrections in X and Y, orthogonality corrections, and to some extent higher order distortion corrections as discussed in[17]. This system works on the basis of imparting elastic deformations to fused silica over a small range of motion, for e.g. a few ppm of scale corrections.
- ***Wafer stage motion for rigid body corrections (X, Y, and Θ):*** The mask and the wafer are aligned by using an air bearing wafer stepper stage. This stage needs to hold position with very low noise to maximize overlay performance. As reported in reference[17], a lubricated alignment procedure has been developed that performs the alignment procedure at the end of step 2 of Figure 4. The low viscosity liquid resist, prior to UV curing, acts as a damping agent for any stage vibrations and it leads to good alignment provided that the stage possesses nanometer scale resolution.

The budget components of imprint-to-imprint overlay and imprint-to-photolithography overlay are provided in Figures 16 and 17 respectively. Here, matched machine overlay (MMO) refers to overlay results obtained by registering an imprint field to a previously imprinted and etched field, where both imprint steps are performed on the same imprint stepper. Further mix-and-match overlay (M&MO) refers to overlay results obtained by registering an imprint field to a previously patterned and etched field that was lithographed using a 193nm photolithography tool. Recent MMO and M&MO results obtained from the imprint stepper are presented in Table 2. Each data set was obtained from a 200mm wafer that contained 26 fields. For the alignment results only four overlay errors at the four corners were used, while for the overlay results 86 overlay errors were used per field for a total of 2,236 overlay error data per wafer. The results in Table 2 suggest that sub-15nm full-field overlay for imprint lithography registered to imprint lithography is possible. This result is consistent with results independently collected by Toshiba using a Molecular Imprints stepper[25]. Also, the results in Table 2 suggest that approximately 20nm full-field overlay for imprint lithography registered to 193nm photolithography is possible.

Table 2: *Alignment and overlay errors for the experiment described in Section 4.2 are listed below. All errors are in nm (mean+3σ)*

	X error	Y error
Alignment	5	6
MMO	11	15.5
M&MO	18	24

The M&MO result in Table 2 is consistent with the result independently obtained by IBM when they used a Molecular Imprints stepper to pattern a 30nm critical fin structure as part of a seven layer storage class memory device[26]. The other layers in the IBM device were fabricated using 193nm and 248nm photolithography tools. The IBM storage class device SEMs are shown in Figure 8.

A budget analysis of the Y error (15.5nm mean + 3σ) in the MMO data in Table 2 resulted in the following observations. The mean overlay error was found to be 2.1nm. The 13.4nm, 3σ error included the following. The alignment error was equal to 3.3nm, 3σ. This is equivalent to "D" in Figure 16. The uncorrectable distortions that repeated from field-to-field suggesting that it was mask related was found to be 8.8nm, 3s. This includes some combination of the component "G" in Figure 16 for the two layers. The uncorrectable random distortions were found to be 9.6nm, 3s. This includes some combination of E and F.

A similar budget analysis of imprint-to-photolithography M&MO is currently being undertaken.

4.3 Cost Considerations and Throughput:

The drop dispense UV imprint stepper has unique cost advantages. First, with respect to capital cost, the resulting tool (shown schematically in Figure 6) includes a self-contained material dispense module. In spin-on UV or thermal imprint processes, a separate spin coating tool is needed for material deposition and in photolithography as well as EUVL, a linked track is needed for resist coating, post exposure bake and for developing the resist. The elimination of the coater is significant capital cost saving for the drop dispense UV imprint stepper.

With respect to cost of consumables, the drop dispense approach has virtually no waste. It is estimated that the drop dispense approach will consume 1 to 0.1% of the volume that a spin coating process will consume since spin coating involves significant wastage. Since semiconductor applications require highly purified materials with ppb contamination levels, the cost of these materials is high and is generally proportional to the volume of the material used. Therefore, the drop dispense UV stepper is expected to have a much lower consumable cost.

The cost of the imprint stepper per wafer processed is a function of the imprint process throughput. A throughput target of 20 wafers per hour (WPH) which leads to a target of approximately 2,000 shots per hour (SPH) is chosen here. This is based on the fact that imprint tools are likely to be significantly lower in capital cost as compared to 193nm-i photolithography and EUV tools. A 20 WPH throughput is expected to result in imprint being lower than ½ the capital cost of 193-i double patterning in terms of throughput per tool cost. Based on this target, one shot has to be completed in about 1.6 seconds (see Table 3).

Table 3: *Field by field time budget for a throughput of 20wph (assuming 100 fields/300mm wafer; and a 20 second overhead for each wafer for loading, set-up and unloading)*

Field imprint steps	Time allocation
Stage move, fluid dispense	0.2 seconds
Imprint mask down	0.1 second
Alignment, fluid filling	1.0 seconds
UV cure	0.15 seconds
Separation	0.15 seconds
TOTAL	1.6 SECONDS

Of all the steps presented in Table3, only fluid filling is believed to be a fundamental technical risk as all the other steps can likely be achieved using extensions of known engineering approaches. A fluid filling goal of 1 second for a 26mm by 32mm field is therefore desired.

Fluid filling in a drop on demand UV imprint process is affected by various factors such as fluid viscosity, dispense drop resolution, control of fluid front dynamics, and targeting of drops correlated to the mask design. Also, sharp changes in pattern density in the mask design can cause regions where drop tailoring is sub-optimal due to limitations in drop resolution. Most acrylate based imprint fluids that have been used to-date have a viscosity in the range of 4-9cps[28]. There are vinyl ether materials that have much lower viscosity and if they can be integrated into the S-FIL process, they have the potential to enhance throughput significantly[29, 30]. The current tools use drops that are 6 picoliter in volume. In the future these drops will approach 1 picoliter that should assist in improving throughput. Figure 18 shows a fluid front where the drops are merging to form a contiguous film. It is important to control the geometry of approach between the mask and the wafer to ensure that the drops do not encapsulate large bubbles. This can negatively impact throughput. It is important that the drops merge laterally to form a contiguous film that has the correct volume distribution locally to fill the varying patterns in the mask.

In this article two different mask designs are presented (i) Highly varying pattern density; and (ii) Slowly varying pattern density. It can be seen from Table 4 that if the process is not performed properly, the case of highly varying pattern density can have very slow filling that is

more than 10X worse than the optimal case. In summary, by using design-based drop targeting and fluid front control, a fluid filling time that is 4X higher than the targeted value for silicon ICs has been achieved. Continued improvements in material viscosity, drop volume resolution and drop pattern placement optimization is expected to help achieve 1 second fill time for mask patterns with highly varying densities.

Table 4: *Fluid filling time in seconds for two types of mask patterns demonstrating that the use of mask design-driven (GDS-II based) drop dispense and the use of fluid front control leads to the best results.*

	No fluid front control		Fluid front control	
Drop Pattern	Grid	GDS-II Based	Grid	GDS-II Based
Mask Design 1: High Pattern Density Variance	>40	25	30	4
Mask Design 2: Low Pattern Density Variance	30	15	10	3

5. SUMMARY AND FUTURE DIRECTIONS

Drop dispense based UV nanoimprint lithography has evolved over the last few years from being a research curiosity to becoming a serious candidate for volume manufacturing of silicon semiconductor devices, particularly non-volatile memory and novel nano-scale memory architectures.

This article has provided a review of UV nanoimprint stepper technology with a particular emphasis on CD control, overlay and throughput status of these steppers. It has been shown that the stepper technology can achieve the CD control budget for imprinted features down to 22nm half-pitch. Continued progress in imprint mask technology is required to achieve a total CDU budget of 2.2 nm, 3σ. The matched machine overlay has been demonstrated down to 15.5nm, mean + 3σ. At the 32nm and 22nm half-pitch, this number needs to approach 7nm and 5nm respectively. A budget analysis has been presented for overlay and continued progress in mask distortions and temperature control in the tool is needed to achieve progress in overlay. With respect to cost, it has been pointed out that the drop dispense UV stepper avoids the capital cost of a coater and has significantly lower material consumable costs. Finally, with respect to imprint stepper throughput, an improvement of about 4X in fluid filling time is required to achieve the target throughput of 20 WPH. Key areas of improvement that will lead to improved fluid filling speeds have been presented.

ACKNOWLEDGEMENTS:
This work was partially funded by DARPA Contract No. N66001-02-C-8011, NIST Advanced Technology Program Contract No. 70NANB4H3012, and DoD Contract No. N66001-06-C-2003.

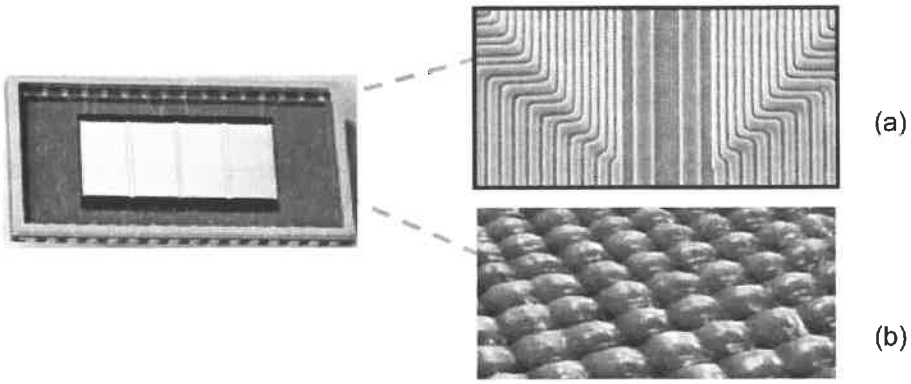

Figure 1: *A representative semiconductor device that requires nanolithography is an ultra-high density memory device. Figure 3 (a) shows a 38nm half-pitch gate layer pattern for a flash memory device[3], and Figure 3(b) shows a 17nm half-pitch molecular cross-bar memory device[4].*

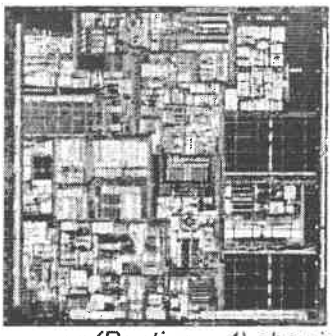

Figure 2: *Intel Norwood processor (Pentium - 4) showing pattern density variations*

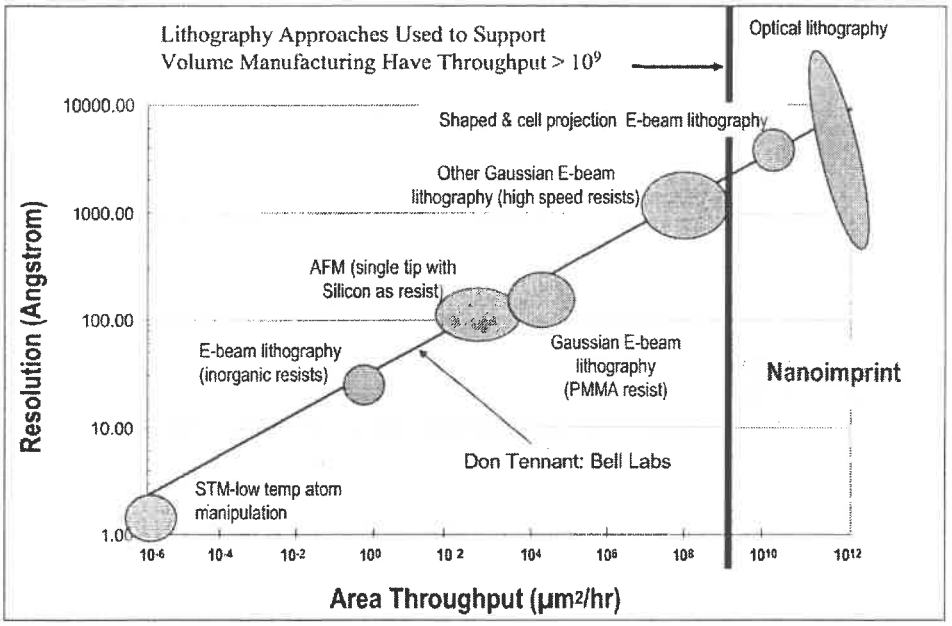

Figure 3*: Importance of lithographic throughput for volume manufacturing, adapted from reference*[5]

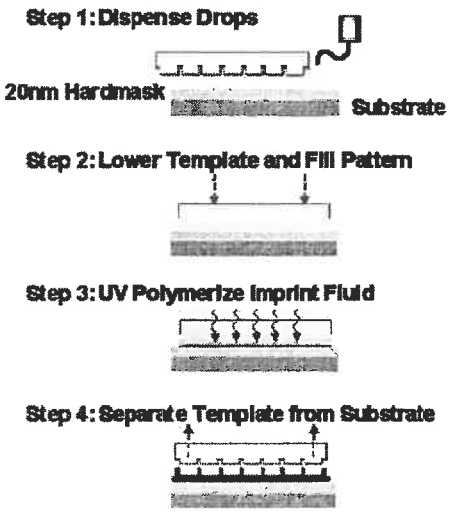
Step 1: Dispense Drops
20nm Hardmask
Substrate
Step 2: Lower Template and Fill Pattern
Step 3: UV Polymerize Imprint Fluid
Step 4: Separate Template from Substrate

Figure 4: *Step and Flash Imprint Lithography (S-FIL) is a Drop-on-Demand UV Imprint Process*

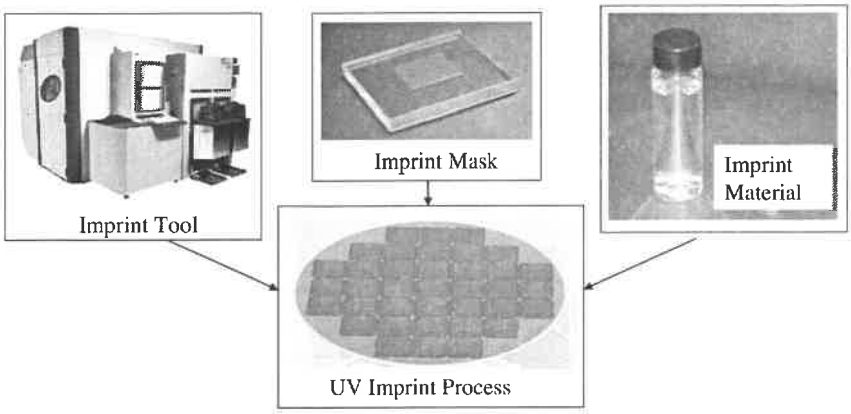

Figure 5: *Building Blocks of the UV Imprint Process: Tool, Mask and Material*

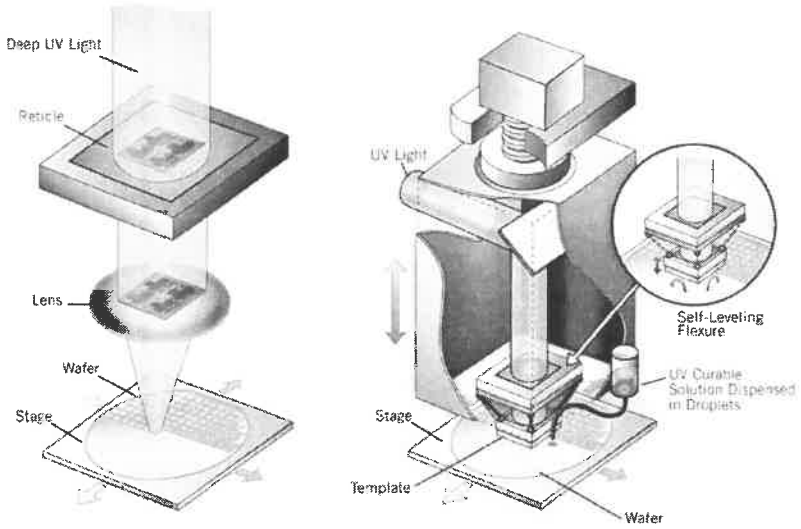

Figure 6: *A schematic of an optical lithography stepper (left) and a UV nanoimprint lithography stepper (right) based on the process of Figure 4*

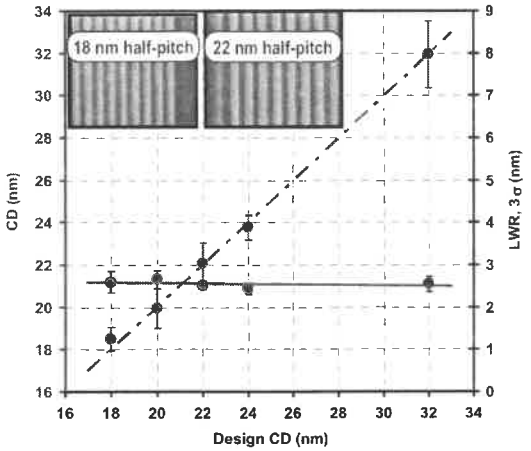

Figure 7: *A fixed line width roughness of ~ 2.5nm (3σ) is observed for patterns varying from 18nm half-pitch to 32nm half-pitch*[23].

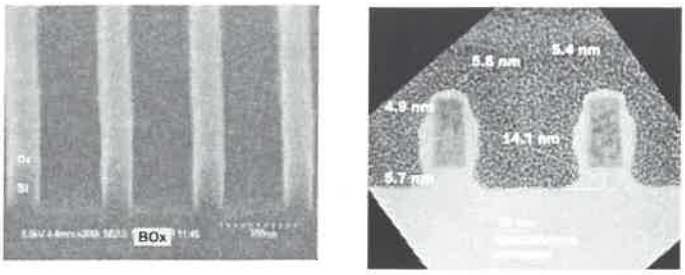

Figure 8: *Cross section views of experimental device fabricated using imprint lithography by IBM[26]. The left micrograph shows 27nm silicon fins, imprinted and etched (with very low line edge roughness); and the right micrograph shows the cross section of completed device.*

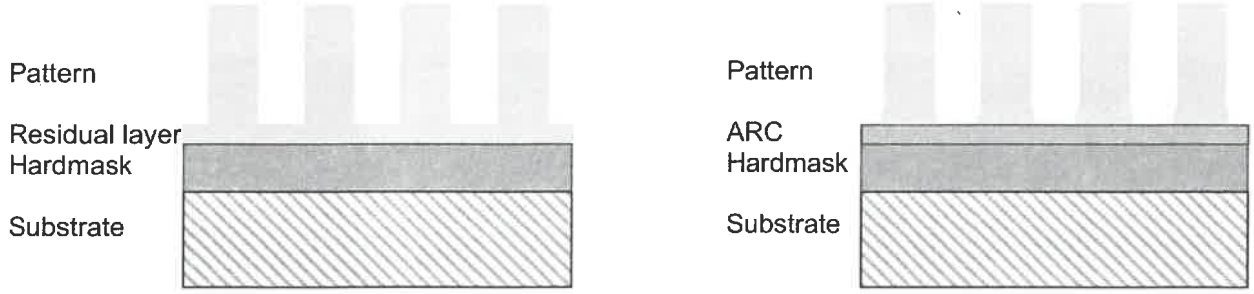

Figure 9: *The imprint stack (left) includes a small residual layer above the hardmask layer and the optical lithography stack (right) typically includes an antireflective coating (ARC) layer and some resist footing[24].*

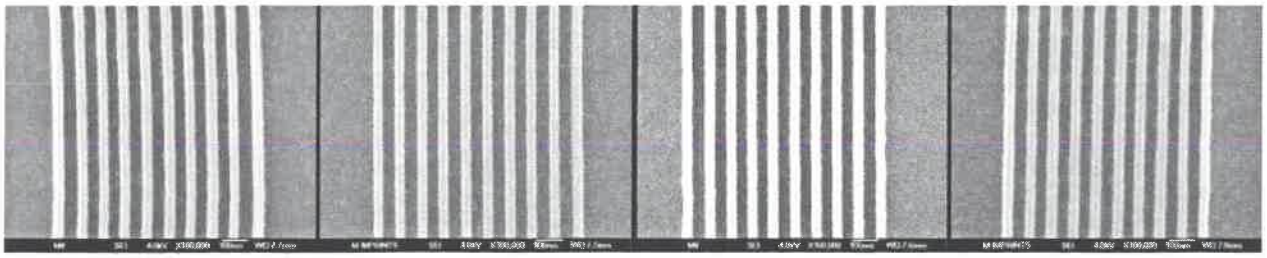

At imprint	After descum	After hardmask etch	After resist strip
CD = 36.2 nm	CD = 34.6 nm	CD = 34.7 nm	CD = 36.7 nm
LWR = 2.9 nm, 3 σ	LWR = 2.5 nm, 3 σ	LWR = 2.8 nm, 3 σ	LWR = 2.9 nm, 3 σ

Figure10: *Top-down SEM micrographs of 42 nm half-pitch lines at etch process step. The critical dimension was maintained at ~35 nm throughout the process. Line width roughness (LWR) was also monitored and remained reasonably constant matching the LWR at imprint.*

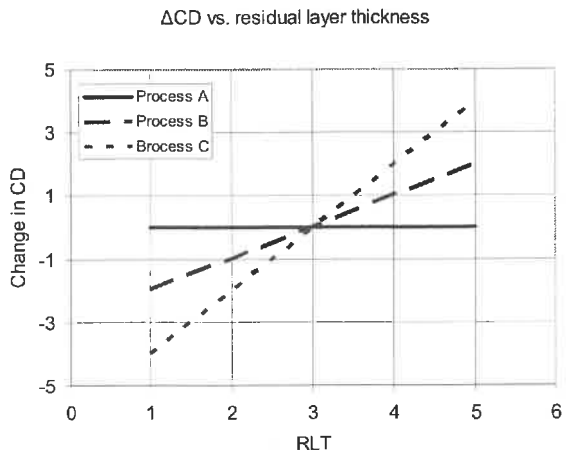

Figure 11: Hypothetical relationship between residual layer thickness (RLT) and CD change through an etch process.

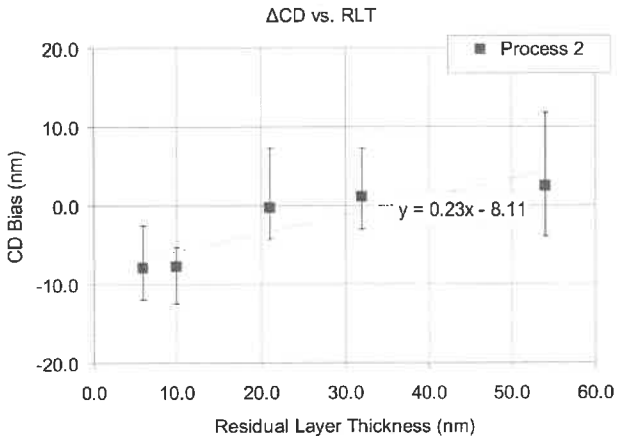

Figure 12: Change in CD as a function of residual layer thickness for an actual imprint etch process[24].

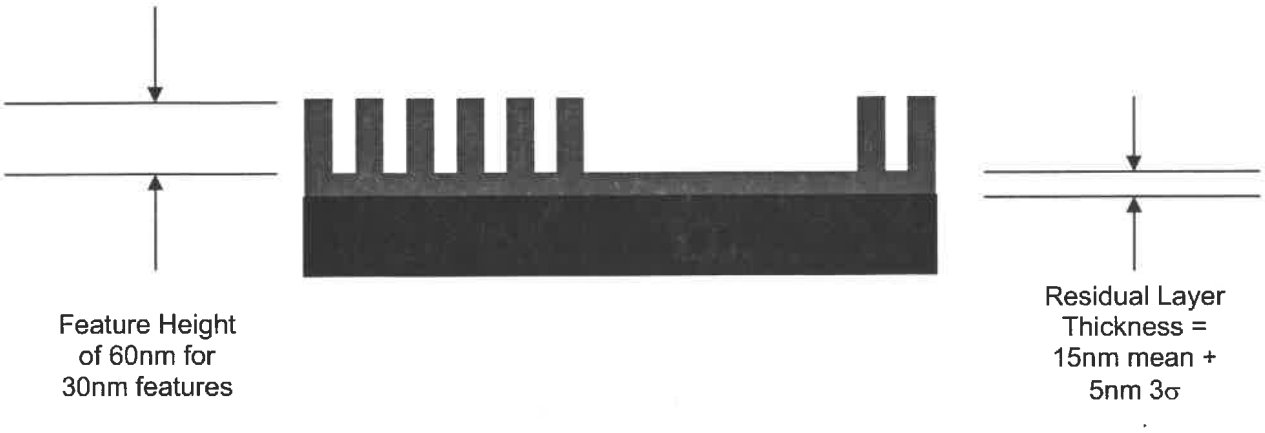

Figure 13(a)

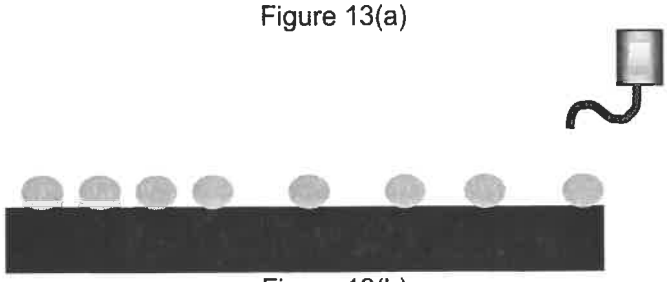

Figure 13(b)

Figure 13: A pattern of 30nm half-pitch and aspect ratio of 2:1 is shown in Figure 13(a). A residual layer thickness of 15nm mean is assumed here based on reference[24]. Figure 13(b) qualitatively illustrates the need for non-uniform resist dispense to correlate the pattern density variation shown in Figure 13(a).

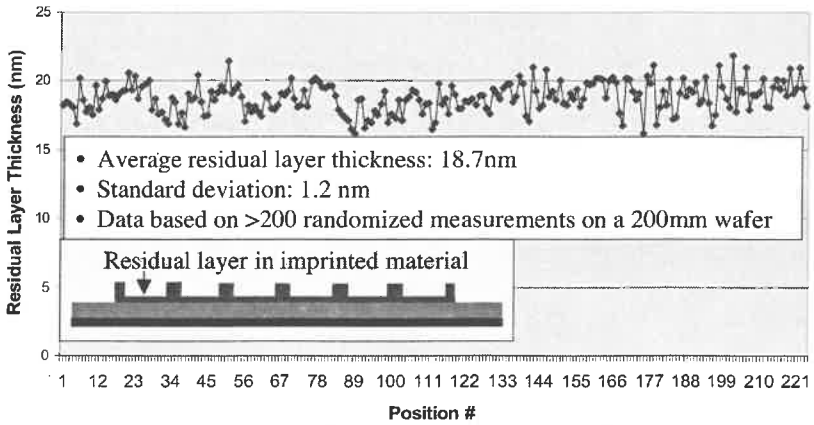
Residual Layer Thickness (nm)
25
20
15
10
5
0
• Average residual layer thickness: 18.7nm
• Standard deviation: 1.2 nm
• Data based on >200 randomized measurements on a 200mm wafer
Residual layer in imprinted material
1 12 23 34 45 56 67 78 89 100 111 122 133 144 155 166 177 188 199 210 221
Position #

Figure 14: Sub-5nm, 3σ, variation in residual layer of sub-20nm mean thickness

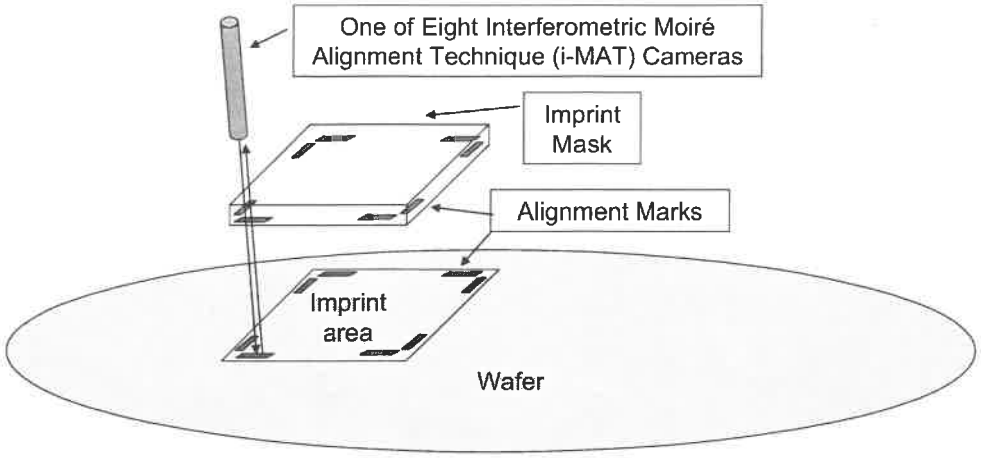

Figure 15: The alignment scheme discussed in this article uses inteferometric moiré alignment technique (i-MAT) that is adapted from the x-ray lithography literature (reference[19]). The figure illustrates a field-to-field alignment approach based on eight alignment cameras and eight sets of moiré alignment marks on the imprint mask and wafer.

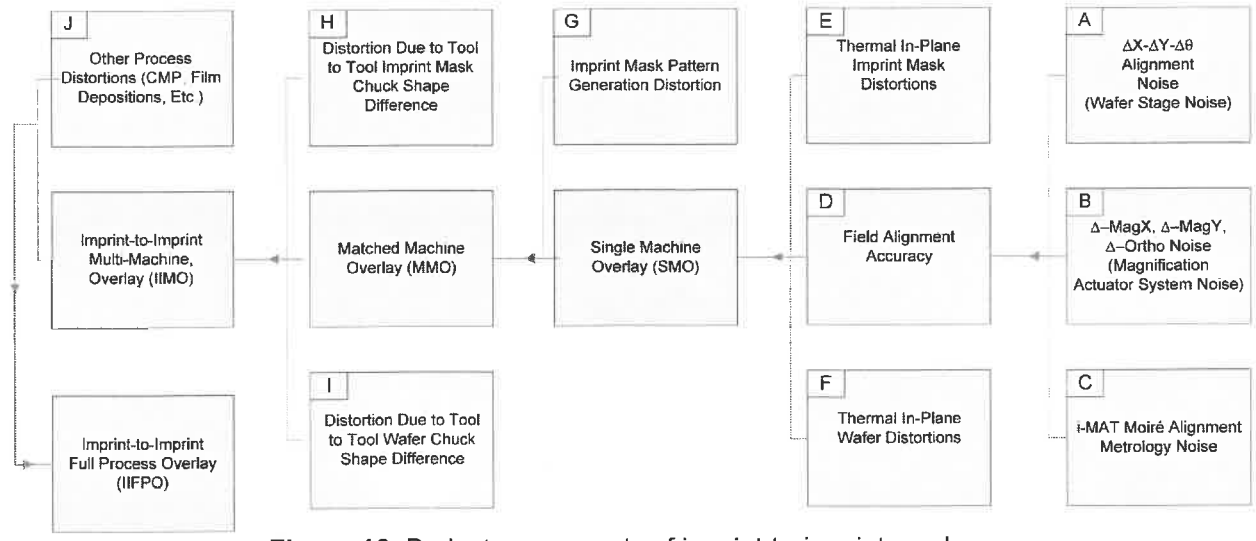

Figure 16: Budget components of imprint-to-imprint overlay.

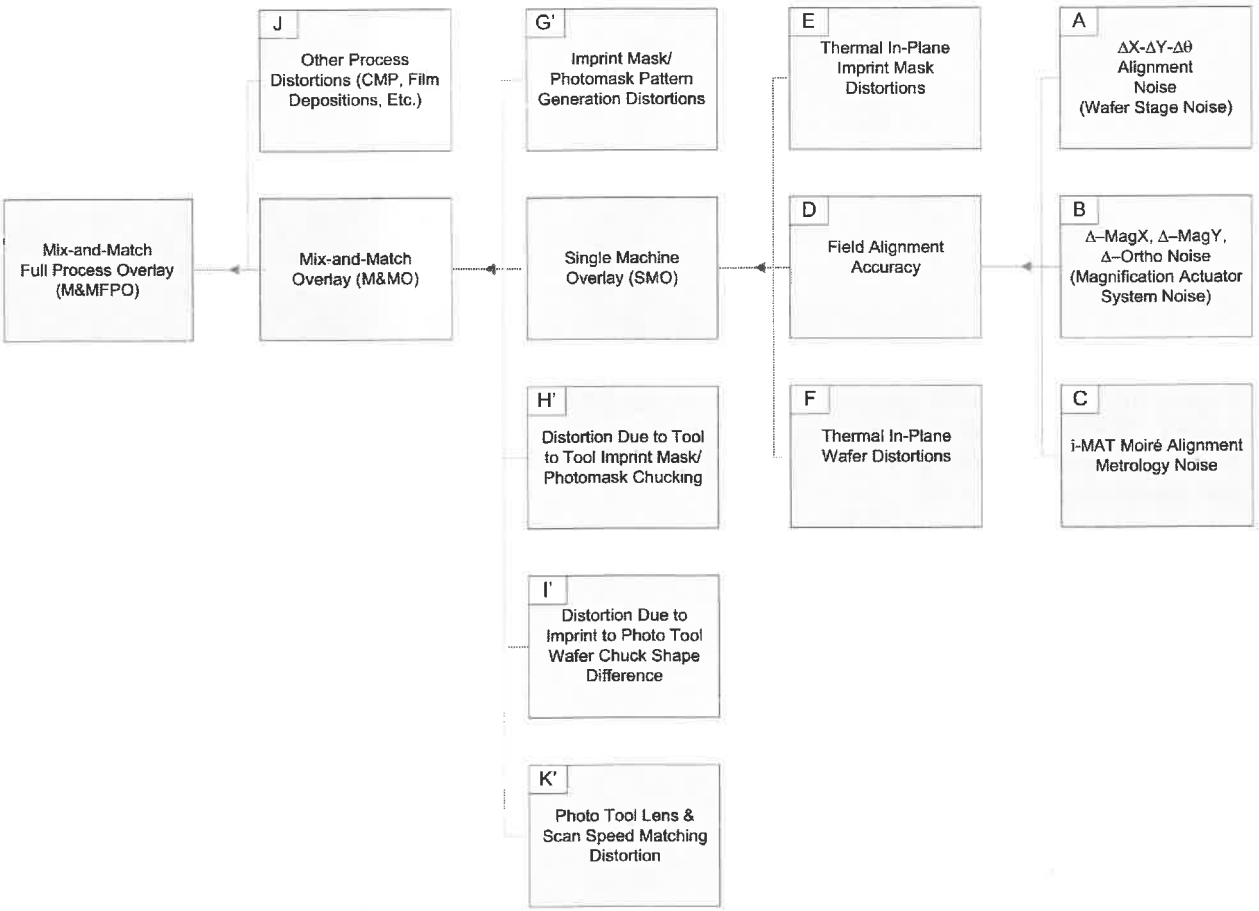

Figure 17: Budget components of imprint-to-photolithography overlay

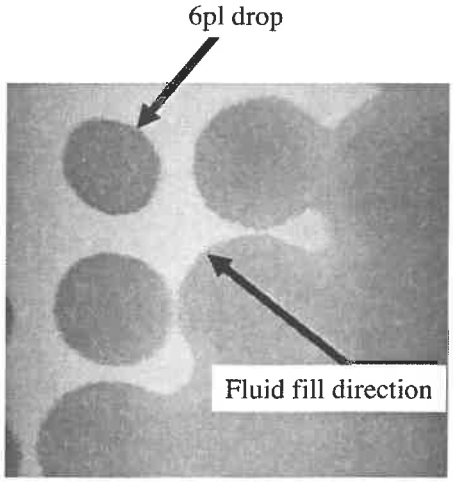

Figure 18: Control of fluid front to avoid trapping of large bubbles between the discrete drops

REFERENCES

[1] Sreenivasan, S.V., "Nano-Scale Manufacturing Enabled by Imprint Lithography," *MRS Bulletin*, Sept. 2008 (To Appear)

[2] http://www.itrs.net/

[3] Kim, K.T., et al., "Full-field imprinting of sub-40-nm patterns," Proceedings of SPIE Advanced Lithography, Emerging Lithography Technologies, 2008, In Press.

[4] Chen, Y. et al., "Nanoscale molecular-switch crossbar circuits," Nanotechnology, 2003, 14, p. 462.

[5] Christie R. K. Marrian, C.R.K, Tennant, D.M., "Nanofabrication," J. Vac. Sci. Tech. A, 2003, 21(5): p. S207.

[6] Mori, I., et al., Keynote Speaker, "Selete's EUV program: progress and challenges," Proceedings of SPIE Advanced Lithography, Emerging Lithography Technologies, 2008, In Press.

[7] Chou, S.Y., Krauss, P.R., Renstrom, P.J., "Nanoimprint lithography," J. Vac. Sci. Tech. B, 1996. 14(6): p. 4129.

[8] F. Hua, Y. Sun, A. Gaur, M. A. Meitl, L. Bilhaut, L. Rotkina, J. Wang, P. Geil, M. Shim, J. A. Rogers, and A. Shim, "Polymer imprint lithography with molecular-scale resolution," Nano Lett. 4(12), 2467–2471 (2004).

[9] Xia, Y. and G.M. Whitesides, Soft Lithography. Angew. Chem. Int. Ed. Engl., 1998. 37: p. 550.

[10] Colburn, M., et al., Step and Flash Imprint Lithography for sub-100nm Patterning. Proc. SPIE: Emerging Lithographic Technologies IV, 2000. 3997: p. 453.

[11] Resnick, D.J., Sreenivasan, S.V., Willson, C.G., "Step & flash imprint lithography," Mats. Today 8(2), p. 34, 2005.

[12] Resnick, D.J., et al., "High Volume Full-Wafer Step and Flash Imprint Lithography," Solid State Technology, February 2007.

[13] Otto, M., et al, "Reproducibility and homogeneity in step and repeat UV-nanoimprint lithography," Microelectronic Engineering, Volume 73-74 , Issue 1, June 2004.

[14] Deguchi, K., Takeuchi, N., Shimizu, A., "Evaluation of Pressure Uniformity Using a Pressure-Sensitive Film and Calculation of Wafer Distortions Caused by Mold Press in Imprint Lithography," Japan. J. Appl. Phys. Vol. 41, Part 1, No. 6B, June 2002, p. 4178.

[15] Sirotkin, V. et al., "Coarse-grain method for modeling of stamp and substrate deformation in nanoimprint," Microelectronic Engineering, 84 (2007), p.868.

[16] Sreenivasan, S.V. et al., "Status of the UV nanoimprint stepper technology for silicon IC fabrication," Proceedings of SPIE Advanced Lithography, Emerging Lithography Technologies, 2008, In Press.

[17] Choi, B.J. et al., "Distortion and overlay performance of UV step and repeat imprint lithography," Microelectronic Engineering, 2004 V78-79, p633, January 2005.

[18] B. J. Choi, S. Johnson, M. Colburn, S.V. Sreenivasan, C. G. Willson, "Design of Orientation Stages for Step and Flash Imprint Lithography," Journal of Int. Societies for Precision Engineering and Nanotechnology, Volume 25, No. 3, pp. 192-199, July, 2001.

[19] Moon, E.E., Lee, J., Everett, P., Smith, H. I., "Application of interferometric broadband imaging alignment on an experimental x-ray stepper," Journal of Vacuum Science & Technology B: Microelectronics and Nanometer Structures, November 1998, 16(6), p. 3631.

[20] Cherala, A., et al., "An Apparatus for Varying the Dimensions of a Substrate During Nano-Scale Manufacturing," US Patent No. 7,170,589.

[21] McMackin, I., et al., "Patterned Wafer Defect Density Analysis of Step and Flash Imprint Lithography," J. Vac. Sci. Technol. B 26(1), Jan/Feb 2008, p. 51.

[22] McMackin, I., et al., "High-resolution defect inspection of step and fl ash imprint lithography for the 32-nm node and beyond," Proceedings of SPIE Advanced Lithography, Emerging Lithography Technologies, 2008, In Press.

[23] Schmid, G. et al., "Minimizing line width roughness for 22nm node patterning with step and flash imprint lithography," Proceedings of SPIE Advanced Lithography, Emerging Lithography Technologies, 2008, In Press.

[24] Brooks, C.B., LaBrake, D.L., and Khusnatdinov, N., "Etching of 42-nm and 32-nm half-pitch features patterned using step and flash imprint lithography," Proceedings of SPIE Advanced Lithography, Emerging Lithography Technologies, 2008, In Press.

[25] Yoneda, I. et al., "Study of nanoimprint lithography for applications toward 22-nm node CMOS devices," Proceedings of SPIE Advanced Lithography, Emerging Lithography Technologies, 2008, In Press.

[26] Hart, M.W., "Step and flash imprint lithography for storage-class memory," EIPBN Presentation, May 2007, Denver, CO, USA.

[27] http://www.memc.com/

[28] Xu, F. et al., "Development of Imprint Materials for the Step and Flash Imprint Lithography Process," SPIE Microlithography, Emerging Lithography Technologies, Santa Clara, CA, March 2004.

[29] E. K. Kim, N. A. Stacey, B. J. Smith, M. D. Dickey, S. C. Johnson, B. C. Trinque, C. G. Willson, J. Vac. Sci. Technol. B 22(1), Jan/Feb 2004, p. 131.

[30] Houle, F.A. et al., "Chemical and mechanical properties of UV-cured nanoimprint resists," Proceedings of SPIE Advanced Lithography, Emerging Lithography Technologies, 2008, In Press.

OVERCOMING OVERLAY CHALLENGES IN NANOIMPRINT BY WAFER/MASK BENDING

Robert Walmsley,[1*] Wei Wu,[1] William M. Tong, [1,2] Jonathan Bartman,[2] Yufeng Chen,[2] Zhaoning Yu,[1] Duncan Stewart,[1] Inkyu Park,[1] Carl Picciotto,[3] Jun Gao, [3] R. Stanley Williams[1]

[1] Quantum Science Research, HP Labs, Hewlett-Packard Co., Palo Alto, CA 94304 USA

[2]Technology Development Operations, Hewlett-Packard Co., Corvallis, OR 97330 USA

[3] HTL, HP Labs, Hewlett-Packard Co., Palo Alto, CA 94304 USA

INTRODUCTION

Nanoimprint lithography (NIL)[1] is an alternative to traditional photolithography offering a potentially lower cost path down the resolution curve. We have employed NIL to fabricate crossbar structures with half-pitch down to 17 nm.[2] Although NIL's resolution has exceeded that of photolithography, overlay remains substantially inferior. Traditionally, improvement in overlay has required expensive improvements in the thermal and mechanical stability of the system. NIL adds the additional burden of requiring a final mechanical displacement in order to transfer the pattern. Reducing the thermal/mechanical path length between mask and wafer patterns is key to improving overlay without incurring an unacceptable cost increase. To this end, we have developed a novel approach that isolates the final aligned mechanical system to essentially include only the mask and wafer. Standoff features on mask or wafer isolate regions on mask and wafer that can deformed by controlling differential pressures across both mask and wafer. Advantages include: (1) minimized loss of alignment during imprint process, (2) improved stability in aligned state resulting from reduction in thermal/mechanical path length, (3) elimination of backside pattern distortions that result from hard-tool pressure non-uniformities, (4) initial contact is at pattern center and spreads preventing trapped air.

In principle, the approach is extensible to multi-die step-and-repeat printing, however, the prototype system to be discussed allows for only a single imprint field of up to 25x25 mm on center of a 100 mm diameter wafer. The imprint mask size in this case is 127x127 mm. Two optical methods for achieving substantially sub-wavelength overlay precision, nDSE[4] (nanoscale Displacement Sensing and Estimation) and Morie patterns, will be discussed. The imprint system uses a UV-curable NIL process with double layer spin-coated resists.[3]

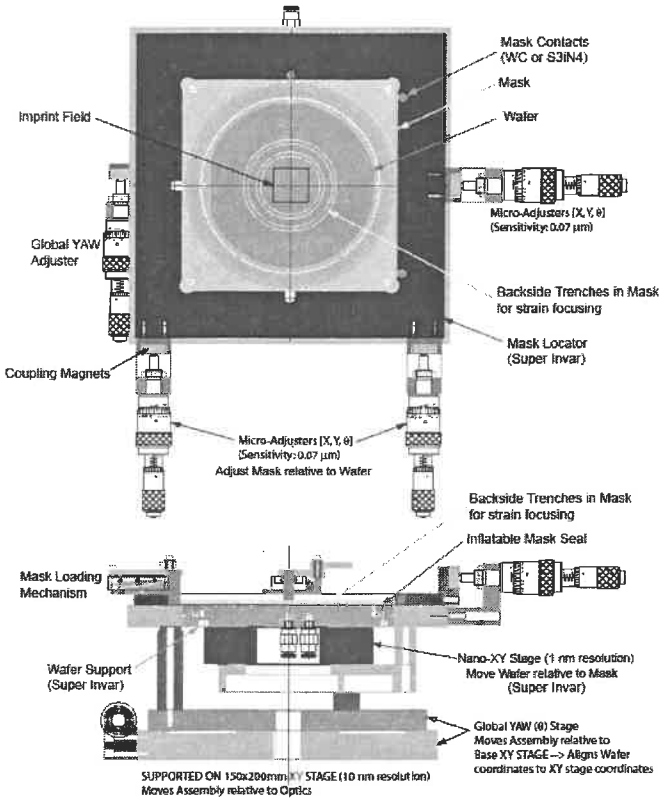
Mask Contacts (WC or S3iN4)
Mask
Wafer
Imprint Field
Micro-Adjusters [X, Y, θ] (Sensitivity: 0.07 μm)
Global YAW Adjuster
Backside Trenches in Mask for strain focusing
Mask Locator (Super Invar)
Coupling Magnets
Micro-Adjusters [X, Y, θ] (Sensitivity: 0.07 μm) Adjust Mask relative to Wafer
Backside Trenches in Mask for strain focusing
Inflatable Mask Seal
Mask Loading Mechanism
Nano-XY Stage (1 nm resolution) Move Wafer relative to Mask (Super Invar)
Wafer Support (Super Invar)
Global YAW (θ) Stage Moves Assembly relative to Base XY STAGE --> Aligns Wafer coordinates to XY stage coordinates
SUPPORTED ON 150x200mm XY STAGE (10 nm resolution) Moves Assembly relative to Optics

FIGURE 1. Plan and section views of Nano-Imprint Module.

THE IMPRINT MODULE

Plan and section views of the imprint module are shown in FIG. 1. This sub-assembly sits on top of an Aerotech XY(150x200 mm) airbearing stage assembly supported on an air-isolated granite surface plate as shown if FIG. 2. An optics system (no details shown) is supported on

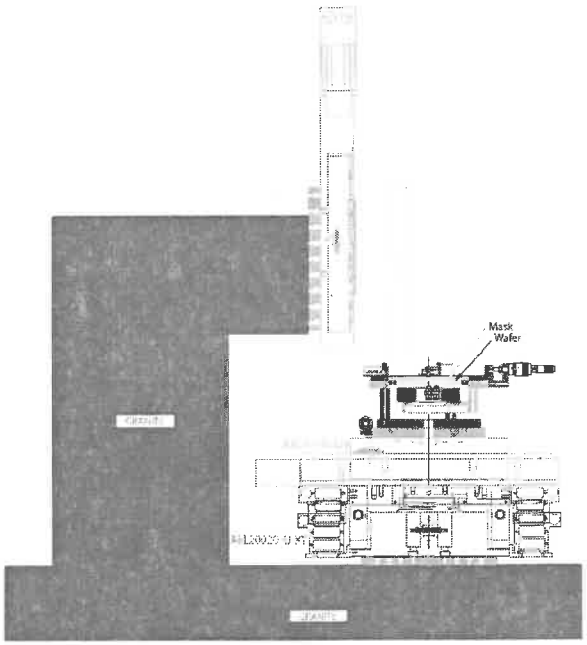

FIGURE 2. Side view of Imprint System including Imprint Module, Aerotech XY Stages, granite support structure, Optics sub-assembly (no details) and Optics Z

an Aerotech stage attached to a granite nose piece. The XY stages allow rapid and accurate translation between widely separated alignment fields as well as allowing for quantification of initial misalignment during the first stages of the alignment process. Final alignment and imprint mechanisms are all contained within the imprint module. Wafer and mask contain multiple alignment marks divided into wafer level and field level marks. Alignment steps are as follows:

1. Adjust Global Yaw (Θ_G) to align wafer coordinate system to XY stage coordinate system using wafer level marks.
2. Align Mask to Wafer using wafer level marks by adjusting local X,Y and Θ_L using Micro-Adjusters. Local Θ_L is fixed at this point (i.e., Mask Locator is vacuum restrained).
3. Initial Nano-XY alignment to field level marks by moving wafer using Nano-XY stage. Misalignment determined by sub-wavelength optical method (e.g., nDSE or Morie)
4. Engage Mask Seal and Load Mask by reducing pressure between Mask and Wafer. Perform final Nano-XY alignment. Iteration between steps 3 and 4 may be required.
5. Perform imprint cycle as shown in Fig. 3. Alignment shift can be tracked during imprint using nDSE. If alignment within specification, UV expose resist and disengage Mask and Wafer.

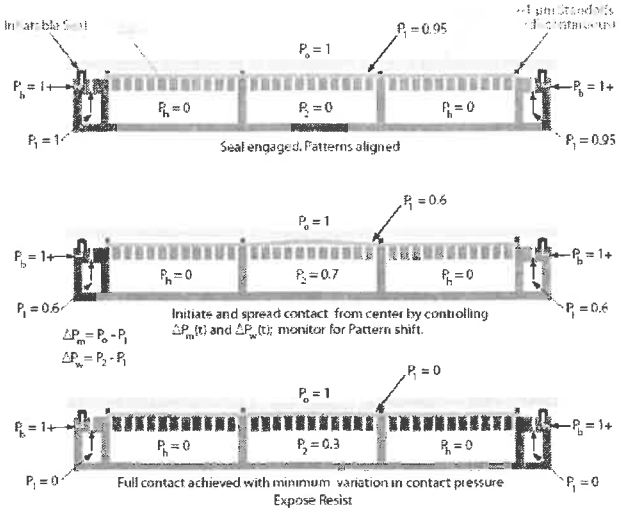
Seal engaged. Patterns aligned
Initiate and spread contact from center by controlling
monitor for Pattern shift.
Full contact achieved with minimum variation in contact pressure
Expose Resist

FIGURE 3. Illustration of Imprint Process. Control parameters are P_h, P_1, P_2 and P_b. Final P_2 pressure is selected to minimize strain-induced field distortion of imprint pattern

THE IMPRINT PROCESS

The imprint process shown in FIG. 3 is illustrative only. The top figure assumes nano-alignment has been achieved, that the seal is engaged and a small mask/wafer preload ($P_1 < 1$ atm) is in force. The programmatic control parameters are the differential pressures across mask, $\Delta P_m = P_o - P_1$, and across wafer, $\Delta P_w = P_2 - P_1$. These parameters are computer controlled to follow a specified time-pressure profile. Optical alignment measurement may be performed continuously or at designated points during this process. When full aligned contact has been achieved, UV exposure cures the resist and the wafer and mask are disengaged.

At the start of the imprint process, the thermal-mechanical path connecting mask and wafer patterns should include only mask, standoff-contacts, and wafer. For the current system, this is imperfectly true, as a result of the Nano-XY stage and inflatable seal. A future design aims at reducing external coupling further. Even if decoupling is effectively achieved, differential imprint field distortion resulting from thermal and mechanical strains must be accounted for.

IMPRINT FIELD DISTORTION

Assuming imprint masks are mastered at a standard metrology temperature of 20°C, precision of transferred patterns is compromised if imprint temperature deviates from the master reference temperature unless CTE (Coefficient of Thermal Expansion) of mask and wafer are equal. Additionally, differential CTE between mask and wafer introduce overlay error unless all imprint operations are performed at the same temperature. For quartz masks, differential CTE is approximately 2 ppm/°C resulting in a aggregate pattern mismatch of 50 nm over a 25 mm field for 1° C difference between any two imprint operations . Using masks with a closer CTE match to silicon can reduce this problem to acceptable levels, however, temperature control will be a necessary part of any imprint machine capable of nanometer overlay since temperature uniformity is also required.

A second contribution to imprint field distortion is produced by differential interfacial strains between mask and wafer during imprint. Even a perfectly uniform compressive load will produce differential strain between mask and wafer as a result of differences in Modulus and Poisson's ratio. For the imprint process proposed, deformation strain fields within mask and wafer will produce non-uniform interfacial strain and therefore some degree of distortion of the imprinted pattern. An example of this is shown in Figure 4 where a uniform quartz mask plate is pressure deformed into contact with a wafer resting on an infinitely stiff platen. In this case boundary conditions maintain a flat interface and only the mask moves. Contact pressure is shown in Figure 5.

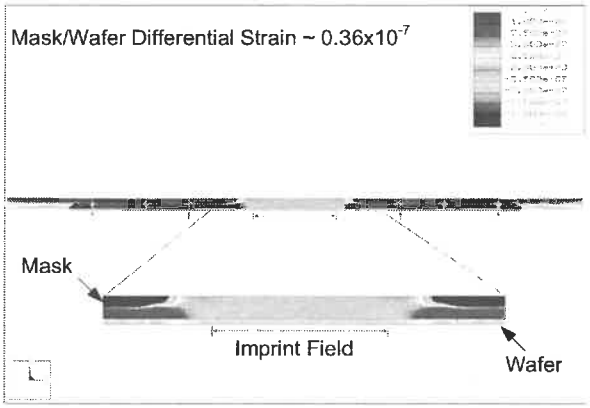

FIGURE 4. Radial Strain in Mask and Wafer resulting from 1 atm differential pressure, ΔP_w. Wafer bottom surface is constrained in Z

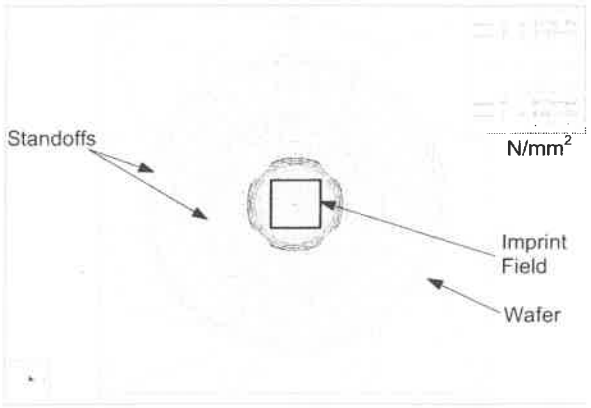

FIGURE 5. Contact Pressure between Mask and Wafer resulting from 1 atm differential pressure, ΔP_w. Wafer bottom surface is constrained in Z. Two Standoff rings provide 1 μm Mask-to-Wafer initial separation. Additional Standoff features may be added to reduce distortion outside imprint zone. (PTC Mechanica)

If pressure is applied to the backside of the wafer within the inner standoff radius, both Wafer and Mask will displace toward each other reducing uniform radial strain differences, but increasing interfacial strain that results from the curvature of the contacting surfaces. Strain focusing cuts made to the backside of the Wafer can reduce this curvature thereby reducing interfacial strain during imprint. For the Mask/Wafer combination analyzed, total differential interfacial strain across the imprint field can reduced to less than 0.2 microstrain (10^{-6}). Maximum pattern shift over the 25 mm field will therefore be less than 5 nm. Assuming similar strain-induced field distortion is present during each imprint operation, common mode rejection will reduce pattern shift further.

Sub Optical-Resolution Alignment

Nanometer-scale overlay requires an alignment metric with resolution substantially below optical resolution limits. Methods for achieving this include the nDSE technique developed by Gao et.al.[4] as well as techniques using Morie patterns resulting from beats between repetitive patterns of lines with a small pitch difference. The nDSE method has demonstrated 5 nm resolution in pattern shift as can be seen in Figure 6. Improved optical axis stability is expected to improve on this performance. A

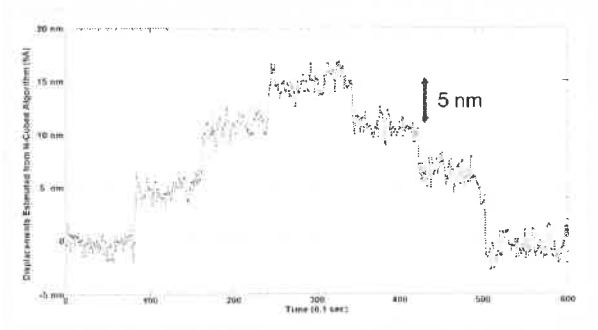

FIGURE 6. Sensitivity of nDSE technique to pattern shift.

major contributor to optical axis instability is the result of thermally-driven motion of imager relative to the optical axis. This is a camera performance metric not typically specified by manufacturers, but is of special concern for nano-scale optical techniques. All optical components within the optical system including illumination are subject to stringent stability requirements.

Acknowledgements:
This work was supported in part by DARPA.

QUESTIONS
Please direct any questions to Robert G. Walmsley. His contact information is listed below.

- Telephone: (650) 857-2397
- Facsimile: (650) 813-3312
- Email: bob.walmsley@hp.com

REFERENCES
[1] S. Y. Chou, P. R. Krauss, and P. J. Renstrom, Journal of Vacuum Science & Technology B **14**, p4129 (1996).
[2] G.-Y. Jung, E. Johnston-Halperin, W. Wu, Z. Yu, S.-Y. Wang, W. M. Tong, Z. Li, J. E. Green, B. A. Sheriff, A. Boukai, Y. Bunimovich, J. R. Heath, and R. S. Williams, Nano Letters **6**, p351 (2006).
[3] W. Wu, G.-Y. Jung, D. L. Olynick, J. Straznicky, Z. Li, X. Li, D. A. A. Ohlberg, Y. Chen, S.-Y. Wang, J. A. Liddle, W. M. Tong, and R. S. Williams, Applied Physics A: Materials Science and Processing **80**, p1173 (2005).
[4] J. Gao, C. Picciotto and W. Jackson, App. Phys. A: Materials Science & Processing, **80**, n6, p1265 (2005).

CONTROLLING IMAGE PLACEMENT ERRORS DURING THE FABRICATION OF EUVL MASKS

Roxann L. Engelstad, Venkata Siva R. Battula, Pradeep Vukkadala, Andrew R. Mikkelson, Madhura Nataraju, and Kevin T. Turner
Computational Mechanics Center (UW-CMC)
University of Wisconsin – Madison
Madison, WI USA

ABSTRACT

With the stringent requirements on image placement (IP) errors in the sub-50-nm regime, all sources of mask distortion during fabrication and usage must be minimized or corrected. For extreme ultraviolet lithography, the nonflatness of the mask is critical as well, due to the nontelecentric illumination during exposure. This paper outlines a procedure to predict the IP errors induced on the mask during the fabrication processing, e-beam tool chucking, and exposure tool chucking. Finite element (FE) models are used to simulate the out-of-plane and in-plane distortions induced during each processing step. The FE results are compiled to produce a "Correction Table" that can be implemented during e-beam writing to compensate for these distortions and significantly increase IP accuracy.

INTRODUCTION

The tolerance on image placement (IP) errors is becoming increasingly severe as lithography technology drives the minimum integrated-circuit feature size below 50 nm. According to the International Technology Roadmap for Semiconductors, meeting the requirements for critical dimensions (CD) and overlay at the lower nodes may be one of the most difficult technical challenges in lithography. The goal of this research is to investigate the IP errors induced during mask fabrication and usage for one of the leading NGL candidates – extreme ultraviolet lithography (EUVL). The basic concept is that if repeatable IP errors (due to fabrication and usage) can be predicted to a reasonable accuracy, it may be possible to correct for these errors when the mask is initially patterned in the e-beam writer. This paper describes the finite element (FE) models that have been developed to simulate the response of the EUVL mask during the fabrication process, as well as when it is chucked in both the e-beam and exposure tools. The FE predictions of the mask response are then used to determine the "Correction Table" to be implemented when e-beam patterning is performed.

A schematic of a simplified fabrication process flow is shown in Fig. 1. For modeling purposes, the individual processing steps are grouped by load steps that are used in the FE simulations. The first step is the deposition of the multilayer stack, absorber stack, photoresist, and backside layer. Typical values for the thicknesses and stresses of these layers are listed in Table I. Load Step 2 is the mechanical mounting of the mask in the e-beam tool for patterning. The development of the resist, etching of the absorber, and removal of the resist have all been grouped into Load Step 3. Finally, the mask is electrostatically chucked in the exposure tool at Load Step 4.

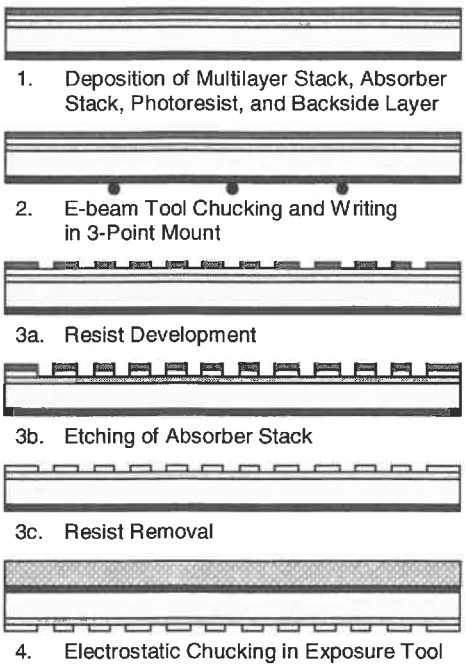
1. Deposition of Multilayer Stack, Absorber Stack, Photoresist, and Backside Layer
2. E-beam Tool Chucking and Writing in 3-Point Mount
3a. Resist Development
3b. Etching of Absorber Stack
3c. Resist Removal
4. Electrostatic Chucking in Exposure Tool

FIGURE 1. Simplified EUVL mask fabrication process flow.

TABLE 1. Typical EUVL mask fabrication parameters.

Layer	Thickness (nm)	Stress (MPa)
Multilayer Stack	280	400 (Compressive)
Absorber Stack	70	100
Photoresist	250	10
Backside Layer	63	150

DESCRIPTION OF EXAMPLE CASE

Full 3-D FE models have been developed to predict the response of the EUVL mask under the load steps given in the simplified fabrication process flow. The mask substrate was low-thermal expansion material (LTEM) with the standard size of 152 mm × 152 mm × 6.35 mm; here the Quality Area is defined as the central square region with side dimensions of 142 mm. The flatness of the EUVL mask is a key issue to minimize IP errors due to the nontelecentric illumination during exposure. SEMI Standard P37 [1] specifies the flatness of the frontside, backside, and thickness variation of the substrate in terms of the class of substrate. In essence, the Quality Area must be flat to within 30 nm to 100 nm peak-to-valley (p-v) for these classes.

As an example case, an interferometric measurement from an actual LTEM substrate was used to represent the nonflatness of the surfaces that result from the polishing procedures. Figure 2(a) shows the interferometric data displayed in 2-D and 3-D plots for the frontside surface of the reticle. The nonflatness is 50 nm p-v over the entire area. For this example case, the backside surface was assumed to have the same shape, but opposite sign, as shown in Fig. 2(b). Thus, the thickness variation was easily calculated by subtracting the backside flatness data from the frontside flatness data. The thickness variation, which has a maximum value of 100 nm, is shown in a 2-D contour plot in Fig. 3.

To input the initial nonflatness of the substrate into the FE structural models, the interferometric data were fitted with an 8 × 8 matrix of Legendre polynomials. Legendre polynomials have been identified as effective means to represent experimentally measured EUVL substrate surface shapes.

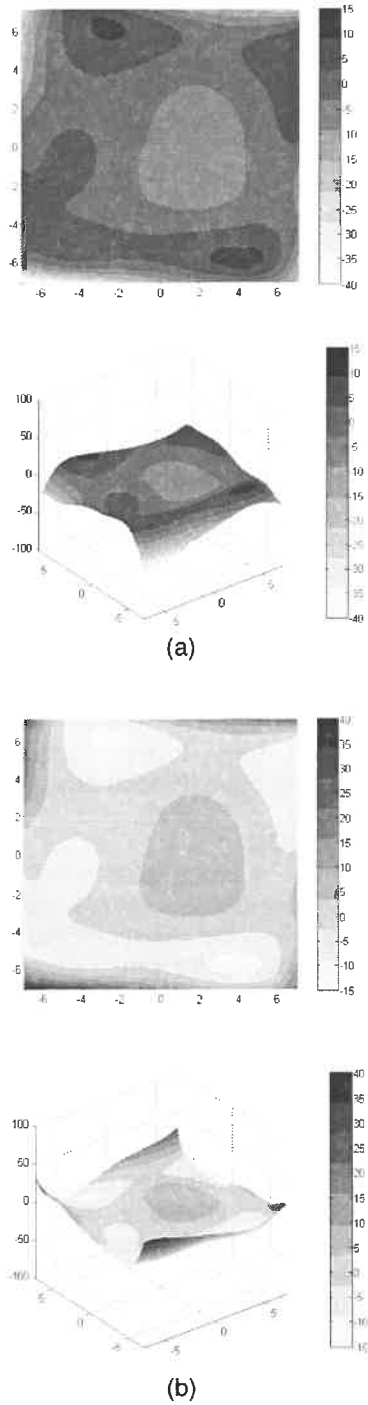

(a)

(b)

FIGURE 2. Nonflatness assumed for the EUVL mask substrate due to polishing procedures (shown in 2-D and 3-D plots). (a) Frontside surface (p-v = 50 nm) and (b) backside surface (p-v = 50 nm).

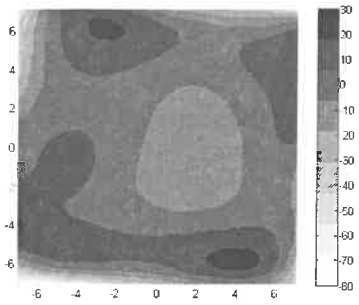

FIGURE 3. Thickness variation of the EUVL mask substrate (maximum = 100 nm).

The FE models can also be used to simulate the effects of stress nonuniformities that may be present in the thin film stacks. For the example case here, all the thin films were uniform with the thicknesses and stresses as given in Table I, except for the multilayer stack. It was assumed that the multilayer had a compressive stress of 450 MPa on one half of the substrate with the other half at a compressive stress of 350 MPa (as shown in Fig. 4). This is a worst case scenario that is used for illustration purposes only.

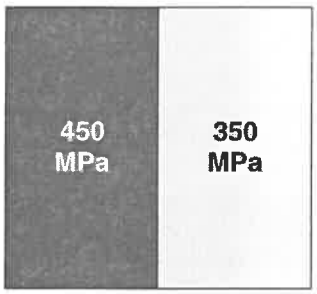

FIGURE 4. Stress nonuniformity assumed in multilayer stack. Compressive stresses are 450 MPa and 350 MPa for dark and light gray area, respectively.

SIMULATING THIN FILM DEPOSITION (LOAD STEP 1)

After generating the FE model of the EUVL substrate with the frontside and backside nonflatness, the deposition of the nonuniform stressed layers is simulated. Figure 5 shows the out-of-plane distortion (OPD) of the reticle displayed in 3-D and 2-D contour plots. The maximum bow of the reticle is 1310 nm p-v; the convex shape is consistent with that fact that the net stresses are compressive. The nonuniform stress distribution causes a bowed shape that is not truly spherical, as shown in the 2-D contours of Fig. 5(b). It is not necessary to calculate in-plane distortions (IPD) at this load step.

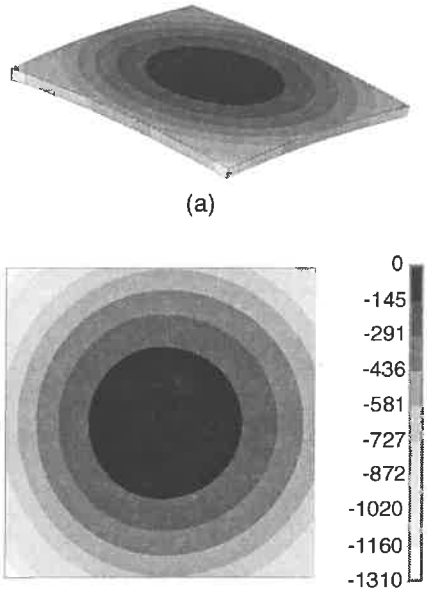

FIGURE 5. FE simulation of thin film deposition (Load Step 1). OPD contours of the entire reticle illustrating the resulting bow of 1310 nm (p-v) in (a) 3-D and (b) 2-D plots.

SIMULATING E-BEAM TOOL CHUCKING (LOAD STEP 2)

The SEMI Standards Committee originally recommended the development of an electrostatic chuck for use in the e-beam tool (SEMI P40) [2]. However, the industry prefers to retain the use of a three-point mount during patterning. Figure 6 shows a schematic of a typical three-point mount; support conditions consistent with this mount are included in the FE model.

Load Step 2 of the FE simulation predicts the response of the reticle when it is positioned in the three-point mount under gravitational loading. Consequently, the FE results for this load step include the initial nonflatness of the substrate and the nonuniform stress distribution, as well as the gravitational distortions. Figure 7(a) illustrates the OPD contours in 3-D, where the initial bow of 1310 nm has now increased to 1421 nm due to the effects of gravity. The corresponding IPD plot of the frontside surface is shown in Fig. 7(b); the value of the maximum IPD is 114 nm. The location of the mounting supports is indicated on the figures.

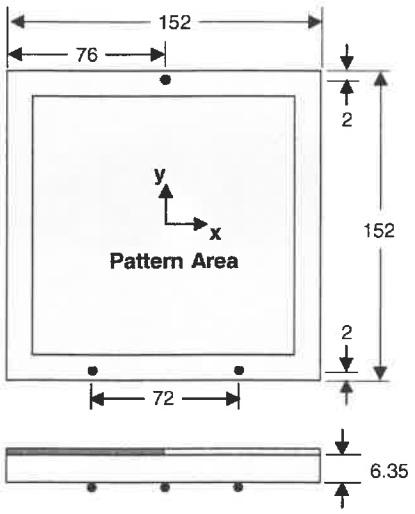

FIGURE 6. Schematic of the three-point mount in the e-beam tool (units in mm).

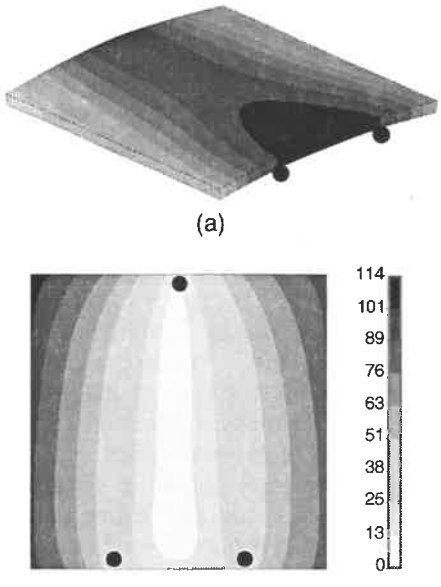

FIGURE 7. FE simulation of e-beam tool chucking (Load Step 2). (a) OPD plot of entire reticle (1421 nm p-v) and (b) IPD plot of reticle frontside surface (maximum = 114 nm).

The IPD results shown in Fig. 7(b) are repeatable distortions that must be compensated for during patterning. It should be noted that this IPD map does not contain the thermomechanical distortions due to the actual e-beam writing. FE models to predict the thermomechanical response of the reticle during e-beam exposure have been developed in previous research conducted at the UW-CMC [3]. If patterning distortions are found to be repeatable and significant, they can be vectorially added to IPD in Fig. 7(b).

SIMULATING THIN FILM ETCHING AND DEVELOPING (LOAD STEP 3)

In the Example Case, Load Step 3 includes the development of the resist, the etching of the absorber stack, and the removal of the resist. Previous analyses at the UW-CMC have shown that the change in OPD and IPD due to these processing steps is roughly 3 nm. However, if the fabrication process included the etching of the multilayer stack, FE simulations should be performed to identify the corresponding change in OPD and IPD. In fact, pattern-specific distortions can be predicted via the use of equivalent modeling techniques and submodeling procedures.

SIMULATING EXPOSURE TOOL CHUCKING (LOAD STEP 4)

It has been proposed to use a "pin-type" electrostatic chuck (e-chuck) in the exposure tool to ensure the mask is flattened and to minimize the effects of particles. Specifications on the e-chuck are given in SEMI P40, the EUVL Mask Chucking Standard: stiffness ≥ 30 kN-m, clamping pressure = 15±1.5 kPa, and nonflatness limited to ~ 50 nm (p-v). Full 3-D FE structural models have been developed to simulate the response of the EUVL mask during electrostatic chucking. The model capabilities include: nonflatness of the chuck, gap-dependent pressures, contact friction, chuck stiffness, and any support constraints. Consequently, the FE simulations are able to predict the final shape of both the frontside and backside of the reticle, the deformation of the chuck, and the remaining gap at the interface.

Electrostatic chucking of the mask was simulated using the interferometric measurements from an actual chuck, where the nonflatness was 263 nm p-v. Since this chuck was not within the SEMI P40 specifications, the magnitude of the nonflatness was scaled down to 50 nm p-v (as shown in Fig. 8). A clamping pressure of 15 kPa was used, the coefficient of friction was assumed to be relatively small, and the chuck was relatively stiff so chuck deformation was negligible.

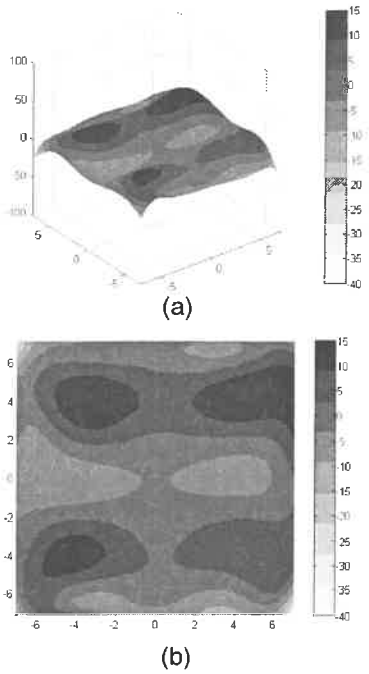

FIGURE 8. Interferometric measurement of the electrostatic chuck surface scaled down to a nonflatness of 50 nm p-v shown in (a) 3-D and (b) 2-D plots.

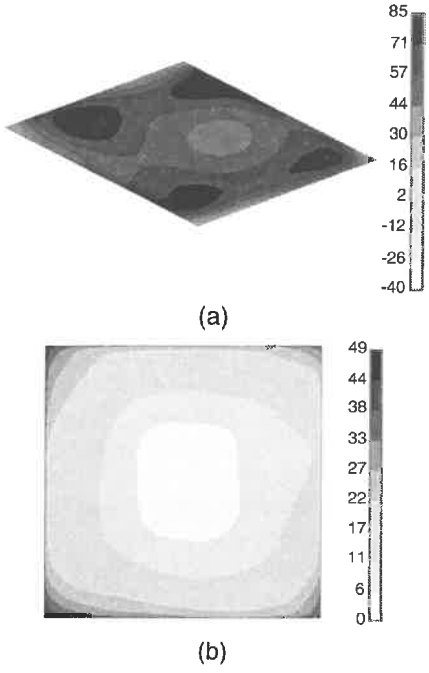

FIGURE 9. FE simulation of exposure tool chucking (a) 3-D OPD plot of reticle frontside surface (125 nm p-v) and (b) 2-D IPD plot of reticle frontside surface (maximum = 49 nm).

Figure 9 shows the final OPD and IPD of the reticle frontside surface after e-chucking. Here the maximum OPD was 125 nm, and the corresponding IPD had a maximum value of 49 nm.

During the FE simulations of the EUV mask fabrication and chucking, the maximum OPD and IPD from the distortion maps are tracked as a function of the process step (or FE load step). For example, Fig. 10(a) illustrates the effects of employing a three-point mount instead of an electrostatic pin chuck during e-beam patterning. The effects are even more dramatic when considering the maximum IPD, which is shown in Fig. 10 (b). Pattern transfer IPD is defined as the vectorial difference between the IPD field during e-beam chucking and the IPD field during exposure chucking. If an electrostatic pin chuck could be used for both e-beam writing and exposure scanning, the maximum distortion would be only a few nanometers. However, when the three-point mount is used in the e-beam tool, the final pattern transfer IPD has a maximum value of 72 nm, as shown in Fig. 10(b). Again, the pattern transfer IPD is repeatable and must be corrected during e-beam patterning.

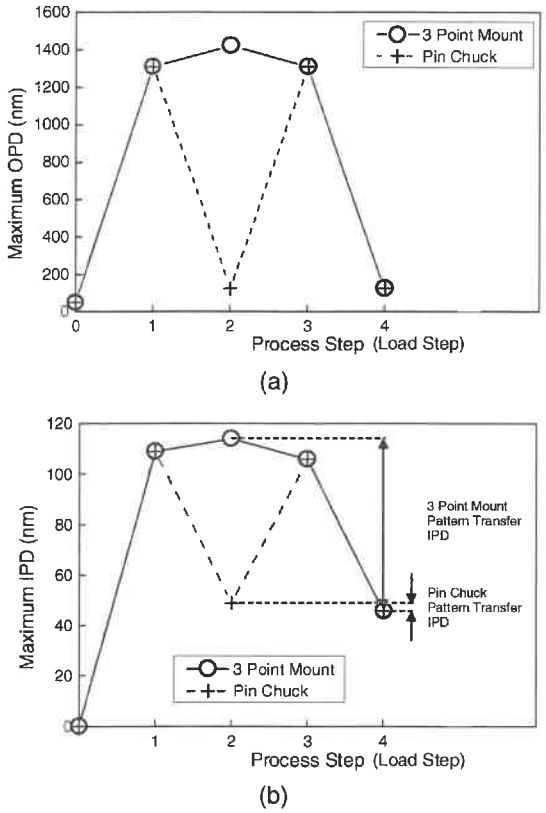

FIGURE 10. Maximum (a) OPD and (b) IPD as a function of the individual processing steps.

To calculate the final Correction Table, it is necessary to consider the IP error at the wafer level. Because the exposure tool uses nontelecentric illumination, both the pattern transfer IPD and the OPD of the reticle after e-chucking will contribute to the total IP error at the wafer. These error components are expressed in Eqs. (1) and (2). Here the magnification factor (M) is 4 and the angle of incidence (β) is 6º. Consequently, the total IP error at the wafer is the vector addition of these two components. Figure 11 shows the final IPD map that must be compensated for during e-beam patterning. To accommodate the e-beam tool software, the FE code would produce these results in tabular form as needed. The tabular data from this map (multiplied by the magnification factor) constitutes the Correction Table.

$$(IP\ Error)_{IPD} = \frac{Pattern\ Transfer\ IPD}{M} \quad (1)$$

$$(IP\ Error)_{OPD} = \frac{OPD \times \tan\beta}{M} \quad (2)$$

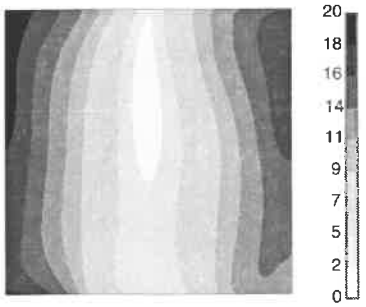

FIGURE 11. Final IP error at the wafer level for x-direction scanning (maximum = 20 nm).

SUMMARY AND CONCLUSIONS

FE simulations were used to identify the response of the EUVL mask during fabrication processes and chucking. To replicate the fabrication process flow, structural FE models simulated the deposition and etching of the various thin film layers. OPD and IPD were tracked as a function of the various processing steps. Both the initial nonflatness of the mask and the nonuniform stress distribution in the multilayer were included in the numerical simulations. The final mask configuration after processing was predicted as a function of the material properties and the inherent thin film stresses and thicknesses.

Chucking of the EUVL mask was considered separately, as the e-beam writer consists of a three-point mount, and the exposure tool utilizes an electrostatic pin chuck. FE models were first used to predict the distortions of the reticle in the three-point mount under gravitational loading. The electrostatic chucking simulations included the nonflatness of the EUVL reticle, gap-dependent pressures, and contact friction. The final OPD map of the frontside surface was modified to account for telecentric effects, then combined with the pattern transfer IPD map to obtain the Correction Table. An experimental program has been initiated with SEMATECH to verify and benchmark the FE modeling procedures associated with the individual load steps.

It should be noted that the Correction Table could also be modified to include thermomechanical distortions during scanning exposure. Previous research at the UW-CMC has shown that the magnitudes of the thermomechanical distortions are highly dependent on the contact conductance and the coefficient of friction between the reticle and the e-chuck. When more data becomes available on these specific parameters, the corresponding OPD and IPD will be included in the Correction Table as well.

ACKNOWLEDGMENTS

This research was supported in part by SEMATECH, the Intel Corporation, and the Semiconductor Research Corporation (SRC). Computer support was provided by the Intel Corporation and Microsoft.

REFERENCES

[1] SEMI P37-1102, SEMI Standard Specification for Extreme Ultraviolet Lithography Mask Substrates.

[2] SEMI P40-1103, SEMI Standard Specification for Mounting Requirements and Alignment Reference Locations for Extreme Ultraviolet Lithography Masks.

[3] Sohn J, Engelstad R, Lovell E. Predicting Pattern-Specific Distortions Induced during Optical Mask Patterning," Journal of Vacuum Science and Technology B. 2001; 19: 2626-2630.

ANALYSIS OF COULOMB AND JOHNSEN-RAHBEK ELECTROSTATIC CHUCK PERFORMANCE FOR EUV LITHOGRAPHY

Michael R. Sogard[1], Andrew R. Mikkelson[2], Madhura Nataraju[3], Kevin T. Turner[2], and Roxann L. Engelstad[2]
[1]Nikon Research Corporation of America
Belmont, CA 94002
[2]Computational Mechanics Center
University of Wisconsin – Madison
Madison, WI 53706-
[3]Intel Corporation
Santa Clara, CA 95054

INTRODUCTION

The imaging system in extreme ultraviolet lithography (EUVL) incorporates a reflective mask that is subjected to non-telecentric illumination during exposure. As a result, any nonflatness (i.e., variation of the height) of the pattern surface results in image placement errors on the device wafer. For this reason, it is imperative that the frontside and backside of the reticle, as well as the electrostatic chuck (ESC), be exceptionally flat to meet the critical dimension control and overlay budget requirements. The EUVL Mask Standard, SEMI P37, specifies that the substrate surface nonflatness not exceed 100 nm peak-to-valley (*p-v*) [1]. SEMI P40, the EUVL Mask Chucking Standard, requires the chucking surface nonflatness to be less than 50 nm *p-v* [2]. Consequently, EUVL depends upon the capability of an ESC to reduce the final mask nonflatness; the successful implementation of EUVL requires this flattening capability be characterized, predicted, and well-understood.

An ESC clamps a substrate to a dielectric chuck surface by electrostatic force. Two types of electrostatic chucks are the Coulomb and Johnsen-Rahbek (J-R) [3,4]. These are distinguished by the characteristics of their dielectrics and the resulting mechanism of clamping force generation. The Coulomb chuck functions like a conventional dielectric capacitor. The J-R dielectric has a large but finite resistance, so a current flows through it and the substrate when the surfaces are in contact and voltage is applied. Charge accumulates at the interface between substrate and dielectric. Since the thickness of the interface region is related to surface roughness, the charge separation is typically quite small, and strong electrostatic forces can be generated.

COULOMB STYLE CHUCK

For a monopolar Coulomb chuck, the electrostatic pressure, P, is given by:

$$P = \frac{\varepsilon_o V_o^2 K^2}{2\left(t_D + K\delta\right)^2}, \qquad (1)$$

where V_o is the applied voltage, K is the relative permittivity of the dielectric, ε_o is the permittivity of free space (8.85×10^{-12} F/m), t_D is the dielectric thickness, and δ is the total gap between the backside of the mask and the dielectric surface. For a given magnitude of applied voltage, the pressure generated by a monopolar chuck is four times larger than that from a bipolar chuck. Only monopolar chucks are examined in this paper.

A characteristic of the Coulomb chuck is that clamping pressure exists everywhere between the reticle and chuck. Typical values for t_D in a Coulomb chuck are 100-200 μm and the $K\delta$ term in the denominator of the pressure equation is often an order of magnitude smaller than t_D. Thus, the clamping force is virtually unaffected in the presence of non-flat substrates or entrapped particles (considering relatively small gaps), as illustrated in Fig. 1.

JOHNSEN-RAHBEK STYLE CHUCK

Details of the clamping characteristics of a J-R chuck are illustrated in Fig. 2(a). When voltage is applied, charge accumulates along the rough chuck-substrate interface, or contact layer. This layer has a thickness t_{CL} which is related to surface roughness, as illustrated in the figure. The properties of the chuck also depend on the resistances of the bulk dielectric (R_V) and the

contact layer (R_{CL}). In addition to the attractive force generated in the contact layer, a conventional Coulomb chuck force is also generated between the substrate and the chuck electrode.

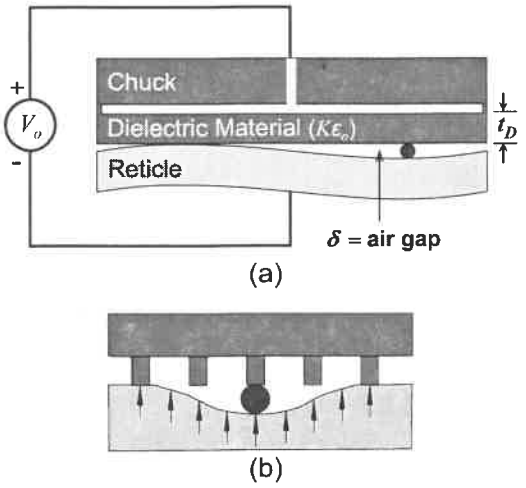

FIGURE 1. (a) Characteristics of a Coulomb chuck and (b) corresponding pressure distribution with an entrapped particle.

While the details of the accumulated charge in the contact layer are quite complicated, a phenomenological model of the J-R chuck force mechanism can be created by treating the contact layer as a small air gap capacitor, of thickness t_{CL}. The amount of charge deposited at the contact layer (or equivalently the voltage drop) can be related to the relative values of R_V and R_{CL}, which function as a resistive divider. This results in the following expression for the clamping pressure, P:

$$P = P_{COUL} + P_{JR} \tag{2}$$

where,

$$P_{COUL} = \frac{\varepsilon_0 V_0^2}{2}\left(\frac{K}{t_D + K(\delta + t_{CL})}\right)^2 \tag{3}$$

and

$$P_{JR} = \frac{\alpha \varepsilon_0 V_0^2}{2}\left(\frac{(R_{CL}/R_V)}{t_{CL}\{1+(R_{CL}/R_V)\}}\right)^2 \tag{4}$$

The parameter α is an empirical factor representing the effect of a nonuniform charge distribution on the interface, and δ is now the physical gap between the reticle and dielectric layer. In practice R_V and R_{CL} can be measured; t_{CL} can then be obtained from a measurement of pressure at a given voltage.

The first term in the expression arises from the conventional Coulomb force between the chuck electrode and the substrate. The second term arises from the J-R effect. Typically $t_D >> t_{CL}$, so the Coulomb term is negligible compared to the J-R term. The empirical factor α represents the effect of the non-uniform distribution of charge on the interface surfaces. Here a value of 2.5 was assumed [5].

The J-R force depends on electrical contact between the chuck and substrate. This leads to distinctly different behavior from that of the Coulomb chuck when nonflat substrates or particles are present, as illustrated in Fig. 2(b). No clamping force is generated in the non-contacting regions. This brings into question the effectiveness of the J-R chuck for high flatness requirement applications, and is a major motivation for the present study.

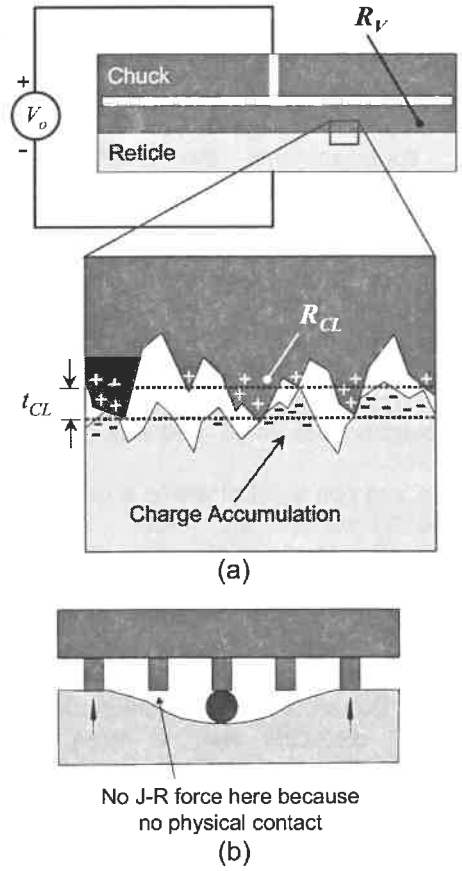

FIGURE 2. (a) Characteristics of a J-R chuck and (b) corresponding pressure distribution with an entrapped particle.

Finite element (FE) analyses have been used to investigate the J-R performance for nonflat substrates. However, the contact requirement for J-R force generation causes a problem, because of the finite mesh of the model. Therefore, for computational convenience a finite range is assumed for the J-R force. The finite range is introduced into Eq. (4) by redefining the constant α as a gap dependent function, which decreases from 2.5 at zero gap to zero at a gap of 30 nm. While this finite range is introduced to facilitate convergence within the FE model, short range forces, such as van der Waals ($\propto 1 / gap^3$) and Casimir ($\propto 1 / gap^4$) exist over a comparable distance [6] and would be included in a more complete theory.

FINITE ELEMENT MODEL

In order to predict the clamping ability of Coulomb and J-R electrostatic chucks, full three-dimensional FE models were developed. Parameters were chosen to be representative for each style of chuck and the initial nonflatness of both surfaces of the reticle and of the pin surface of the chuck were based on interferometric measurements of actual chucks and reticles to provide a realistic and impartial comparison [7].

The pin chuck was modeled to have a 12 × 12 array of square pins, each having a side length of 2.5 mm and a height of 10 μm. The pin pitch was 12.67 mm and the coverage was 4%. The pin region was 142 mm^2 corresponding to the reticle quality area. The chuck was assumed to have an elastic modulus of 380 GPa and a Poisson's ratio of 0.24, which is typical for ceramic materials used in electrostatic chucks. A total thickness of 22.5 mm was used for the body of the chuck, which included a 150 μm thick dielectric for the Coulomb chuck and 2.0 mm thick dielectric for the J-R chuck.

Separate models were developed for each style of chuck and each model included the local gap-dependent pressure. All gravitational effects were ignored, and the coefficient of friction was assumed to be 0.2. The simulations were then used to predict the final flatness of the reticle patterned and backside surfaces, the final bow (or flatness) of the chuck, the final gap between the reticle and chuck, and also the pressure distribution on the backside surface of the reticle or the pressure distribution on the pins.

For each model it was assumed that the relative dielectric constant was 10. The model of the Coulomb chuck utilized an applied voltage range of 365 to 895 V, which corresponds to an average pressure (with complete chucking) of 1.0 to 6.0 kPa. The J-R model assumed a contact layer thickness of 1.0 μm and the voltage was varied from 284 to 696 V, which produces an average pressure of 1.0 to 6.0 kPa.

Results from the FE simulations are shown in Fig. 3. The remaining gap for an average pressure of 1.0 kPa is shown in Figs. 3(a) and (b) from the Coulomb and J-R models, respectively. In both cases the maximum gap is around 20 nm. For this example case, the models predict that an average pressure of 1.0 kPa is sufficient to reduce the gap from an initial value of 1.0 μm down to approximately 20 nm. At an average pressure of 6.0 kPa, the remaining gap is predicted to be negligible.

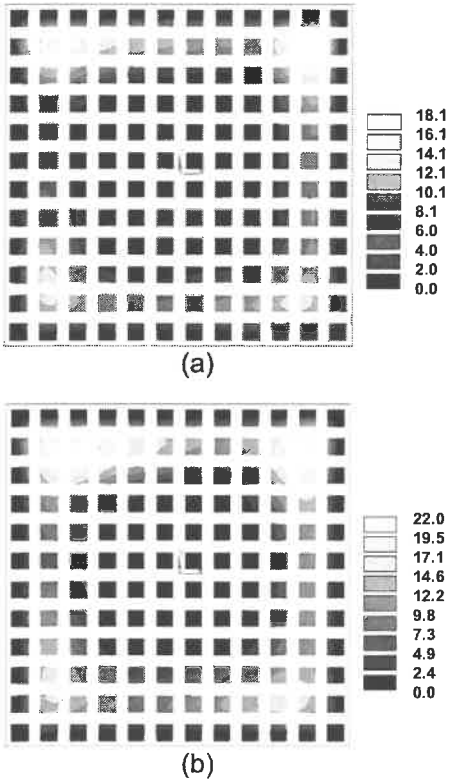

FIGURE 3. Residual gap at 1 kPa average pressure for (a) the Coulomb chuck and (b) the J-R chuck. Note that the size of pin areas are exaggerated for display purposes.

Figures 4(a) and (b) show the final pattern surface shape of the reticle at an average pressure of 6.0 kPa; the shapes are very similar.

For these plots the applied voltage for the Coulomb and J-R cases was 895 V and 696 V, respectively. The *p-v* value for these surfaces is approximately 90 nm, and the *p-v* value within the quality area for both is just under 80 nm. Since the models predicted almost complete chucking at 1.0 kPa, the pattern surface flatness of the reticles did not change significantly between an applied average pressure of 1.0 and 6.0 kPa.

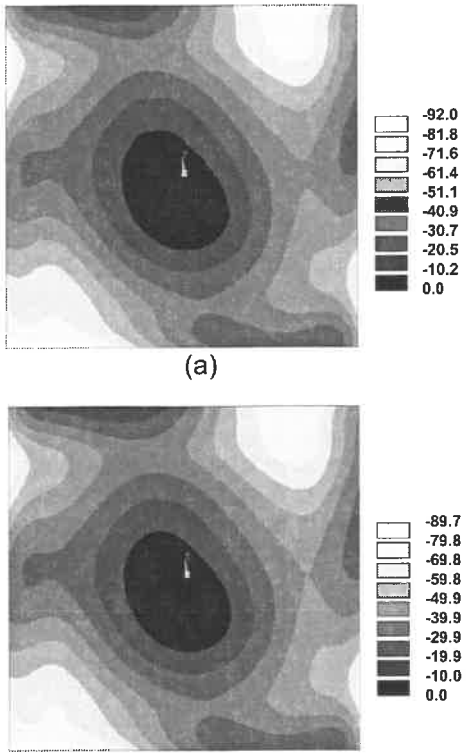

FIGURE 4. Reticle pattern surface after chucking with an average pressure of 6.0 kPa on a (a) Coulomb chuck and (b) J-R chuck. Both scales are in nanometers.

The final flatness of the backside (or chucking surface) of the reticle is shown in Figs. 5(a) and (b) for the Coulomb and J-R models, respectively, for an average pressure of 6.0 kPa. Both models predict the backside surface to have a *p-v* of about 90 nm and a *p-v* value of approximately 50 nm within the quality area. The overall shape of the contours of these plots are quite similar; however, the local distortion at or between the pins is much more apparent in the Coulomb case.

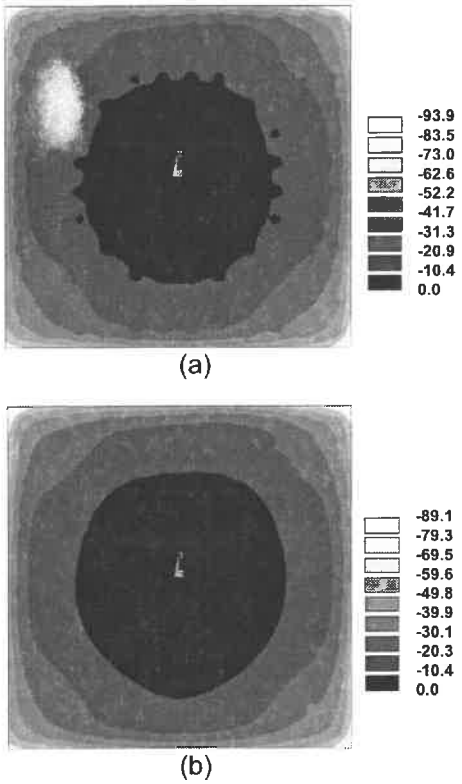

FIGURE 5. Reticle backside surface after chucking with an average pressure of 6.0 kPa on a (a) Coulomb chuck and (b) J-R chuck. Both scales are in nanometers.

Figure 6 is a plot of the remaining gap as a function of average pressure. The Coulomb chuck results in smaller gaps at lower pressure and the J-R chuck provides slightly smaller gaps at larger average pressures. Even though the Coulomb and J-R chucks have drastically different pressure dependence on gap, both are able to completely flatten the reticle against the chuck.

SUMMARY AND CONCLUSIONS

The governing pressure equations for Coulomb and J-R chucks were presented, and for the nominal parameters used, the J-R chuck was capable of producing significantly higher pressures for the same applied voltage in the contact (pin) regions. Due to the J-R chuck dependence on contact to initiate charge accumulation, the J-R chuck pressure is spatially nonuniform and restricted to the contacting regions. However, due to the Coulomb chuck having a spatially uniform pressure distribution, it could cause some reticle distortion between pins. A desirable attribute of a Coulomb chuck is that the pressure is not

highly dependent on gap and therefore would not change appreciably due to the presence of a particle. If relatively tall pins are required to minimize particle effects, the force in a Coulomb chuck could be significantly reduced while the pressure in a J-R chuck would change a negligible amount. However, what still needs to be determined is how a J-R chuck will perform with a particle between a pin and the backside of the reticle. Additionally, in-plane distortion of the reticle surface was not included in this study.

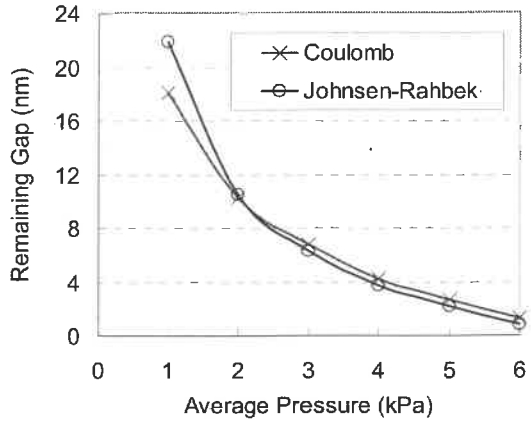

FIGURE 6. Summary of the gap as a function of average pressure.

The FE simulations indicated that for the example case considered, average pressure was a good predictor of final gap and flatness regardless of the chuck type. Both styles of chucks were able to pull the nonflat reticle to complete contact with the nonflat chuck with reasonable average chucking pressures.

ACKNOWLEDGMENTS

This research has been funded by Nikon, SEMATECH, Intel, and the Semiconductor Research Corporation. Computer support was provided by the Intel Corporation and Microsoft.

REFERENCES

[1] SEMI P37-1102, SEMI Standard Specification for Extreme Ultraviolet Lithography Mask Substrates.

[2] SEMI P40-1103, SEMI Standard Specification for Mounting Requirements and Alignment Reference Locations for Extreme Ultraviolet Lithography Masks.

[3] Hartsough L. Electrostatic Wafer Holding. Solid State Technology. 1993; 35: 87-90.

[4] Wright D, Chen L, Federlin P, Forbes K. Manufacturing Issues of Electrostatic Chucks. Journal of Vacuum Science and Technology B. 1995; 13: 1910-1916.

[5] Watanabe T, Kitabayashi T, Nakayama C. Japanese Journal of Applied Physics. 1993; 32: 864-871.

[6] Chan H, Aksyuk V, Kleiman R, Bishop D, Capasso F. Quantum Mechanical Actuation of Microelectromechanical Systems by the Casimir Force. Science. 2001; 291: 1941-1944.

[7] Sogard M, Mikkelson A, Nataraju M, Turner K, Engelstad R. Journal of Vacuum Science and Technology B. 2007; 25: 2155-2161.

CHUCK INDUCED DEFORMATIONS IN EUV MASK SUBSTRATE METROLOGY

Chris Evans, Bruce Truax and Craig Smith
Zygo Corporation
Middlefield, CT, USA

INTRODUCTION

Specifications for photomask blanks for extreme ultraviolet lithography (eg SEMI spec P37-1102 [1]) call for flatness and thickness variations as low as 30 nm peak to valley. These photomask blanks are ~ 150 mm square and 6.25 mm thin, frequently made from fused silica or other low expansion materials. The area of the mask reserved for handling is limited to a narrow band, typically less than 5 mm wide outside a defined "*quality area*". The flatness specifications apply to an "unconstrained" substrate; hence the metrology must be performed either:

- Using a chuck that introduces deformations which can be absorbed in the measurement uncertainty budget (a few nm (k=1)); or
- With subtraction of the chuck induced deformations, which must therefore be repeatable and amenable to validation.

We have adopted the second option in a metrology tool for automated measurement of masks. After a brief description of the salient features of the tool, we describe a method for separating chuck induced errors from mask blank flatness.

RETICLE FLATNESS METROLOGY TOOL

Figure 1 is an overview of the tool. The optical system comprises a 100 mm nominal aperture laser Fiaeau interferometer which feeds an in-line 100-225 mm beam expander. Standard 300 mm transmission and return flats (TF, RF) are in custom, ISO Class 1 clean room compatible mounts on a Z-axis rail to allow cavity length to be adjusted as required. The optical axis of the system is tilted 2 degrees from horizontal.

Reticles to be measured are removed from the SMIF pod by the robot and placed, horizontally, on the reticle frame. The frame rotates and then slides between the TF and RF so that the surfaces of the reticle are normal to the optical axis. In this configuration, a transparent reticle gives multiple interference patterns. The interferometer light source is tuned over a range of 150 GHz and, through implementation of Fourier Transform Phase Shifting Interferometry[2] (FTPSI), the instrument reports a number of parameters including surface flatnesses, wedge, index, homogeneity, thickness variation, and slopes. The dominant, time invariant sources of uncertainty in the flatness measurements are the calibrations of the TF and RF and the chuck induced deformations.

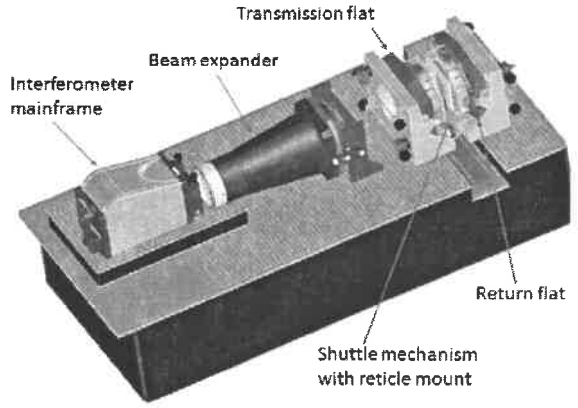

FIGURE 1: Overview of metrology tool (top) and close up (lower) showing the robot loading a reticle blank

TF AND RF CALIBRATION

The TF and RF are calibrated using an N-position areal 3-flat test[3,4]. A third kinematically mounted flat, capable of rotation about its optical axis, can be used as either the TF or RF. The calibration is performed *in-situ* to

eliminate uncertainties associated with remounting the flats.

A simple, routine, sanity check of the calibration is to sum the calibration files for the TF and RF and subtract from an independent measurement of the cavity. Figure 2 shows the results of one such test, clearly characterized by a L-R flip error leading to LR anti-symmetry in the (very small) difference.

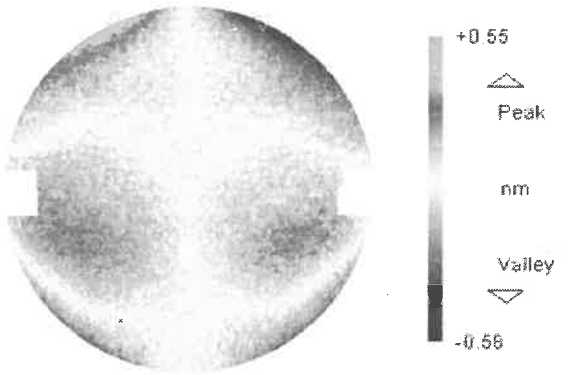

FIGURE 2: Calibration check; difference is 1.1 nm PV, 0.14 nm rms

RETICLE FEA

In the measurement position, the reticle is supported on two points located on the edge of reticle (and in front of the center of gravity) and on 3 points outside the quality area on the back. There is an additional location on one of the vertical edges (Figure 3) to maintain a repeatable mounting location. The predicted deformations are symmetric, and show very little difference between "front" and "back" surfaces (Figure 4).

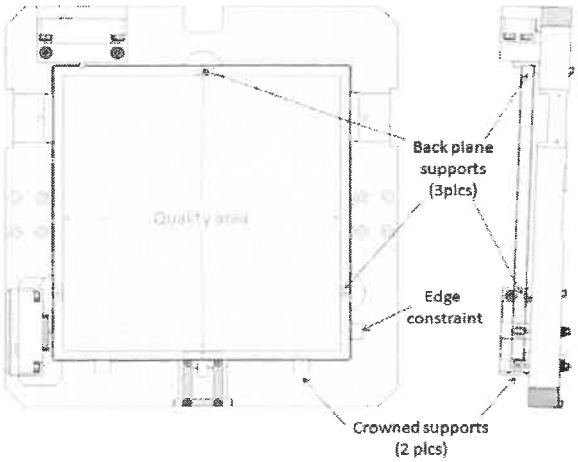

FIGURE 3: Reticle frame (chuck) showing constraint locations

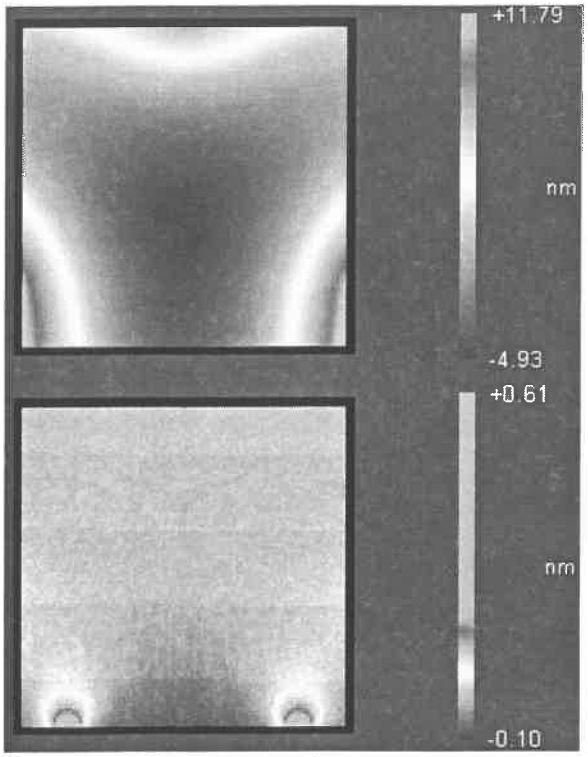

FIGURE 4: Predicted (16.7 nm PV) chuck induced deformations over the test aperture (top) and the difference (lower) between predicted deformations of front and back surfaces (0.7 nm PV).

The problem with simply subtracting the predicted deformations arises from the part aspect ratio (~25:1) and the support locations. Small differences between the modeled and actual contact conditions result in differences in deformation that exceed the target measurement uncertainty.

MEASUREMENT OF DEFORMATIONS

An obvious approach to separating chuck induced deformations from the real part surface is to invoke the same kind of algorithms that were used to calibrate the TF and RF. Lindquist et al[5] considered chuck induced deformation in the measurement of reticles using an Abramson interferometer. They use three measurements of the reticle at 0, 90° and 180 ° – plus matrix flips and rotations in the manner of Ai et al[6]. This process has different error propagation than a four position test[3], but the same blindness to rotationally invariant terms and to terms that are harmonic in $4k\theta$, where k is a positive integer.

Clearly, we can make 4 measurements of the reticle in a conventional 2 surface Fizeau

geometry, rotating 90° between measurements. The average of these four measurements contains the chuck-induced error (or at least the repeatable portion thereof), plus any rotationally invariant and 4kθ flatness errors in the reticle.

It may be reasonable to argue that a 3 point chuck (plus edge supports) is unlikely to produce a 4θ term in the part; it is less easy to argue that no quadratic term (or any other term symmetric about the center of the part) can be produced.

Using FTPSI, we measure independently the cavity between the TF and the first surface of the reticle and between the second surface of the reticle and the RF. Now, consider the case where two measurements are made with the reticle reversed (about a line perpendicular to the optical axis) – as shown very schematically in Figure 5. As measured in the two cavities, the sign of the figure error of the reticle does not change (for the sign convention that the OPD increases for decreasing gap between the "reference" surface and the reticle surface). The chuck induced deformations, however, have opposite signs in the two cavities. Hence – in 2 dimensions -- this looks like a classic reversal[7]; in practice, the reticle coordinates are flipped about either X or Y. As implemented in the tool at Zygo, the flip is about the Y axis.

The TF and RF are calibrated separately. We assume:

- The chuck design provides repeatable locations and forces;
- The reticle is symmetric (in terms of mechanical properties) about the optical axis; and
- The measured surface error of a reticle is well described as a linear superposition of its "freeform" shape and the chuck induced form errors.

Now we can perform the four position test as discussed above and get an estimate (*E*1) from the TF/reticle cavity of the chuck induced deformations:

$$E1 = \frac{1}{4}\left[\left(TF + P_0\right) + \left(TF + P_{90}\right) + \left(TF + P_{180}\right) + \left(TF + P_{270}\right)\right] - TF_{cal}$$

$$E1 = PRI + P4k\theta(x, y) + chuck$$

where *P* refers to the reticle (part). After reversing the reticle we get a second estimate (*E*2) from the reticle/RF cavity:

$$E2 = \frac{1}{4}\left[\left(RF + P_0'\right) + \left(RF + P_{90}'\right) + \left(RF + P_{180}'\right) + \left(RF + P_{270}'\right)\right] - RF_{cal}$$

where the prime ' indicates the flip. Hence:

$$E2 = PRI + P4k\theta(x, -y) - chuck$$

The chuck induced errors change sign because of the sign convention used. The half the difference ((E1-E2)/2) gives the chuck induced error including only those 4kθ terms in the reticle which are not symmetric about the flip-axis:

$$\frac{E1 - E2}{2} = chuck + \frac{P4k\theta_{odd}(x, y) - P4k\theta_{odd}(x, -y)}{2}$$

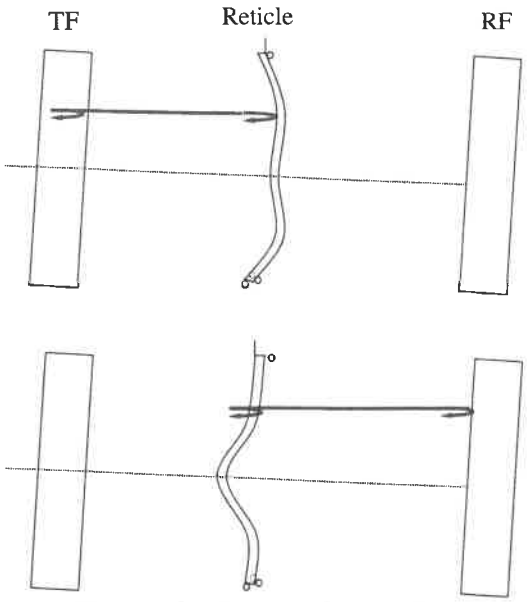

FIGURE 5: Schematic of the reversal showing a reticle with a quadratic error with higher order chuck induced errors superimposed.

An alternate algorithm (derived from [3]) rotates the data sets back to their original orientation, averages, and then subtracts from data taken at the original orientation. This has the effect of setting the $4k\theta_{odd}$ term in the estimate of the chuck error to zero. In practice, the asymmetric $4k\theta_{odd}$ terms are negligible

RESULTS

Figure 6 shows the measured "quality" area from two surfaces of a reticle. Figures 7 and 8 show two evaluations of the chuck induced deformations made using two different reticles with significantly different surface shapes. The rms of the difference between these maps is 1.02 nm. Differences between repeated maps of

the chuck induced deformations made using the same reticle are within 0.4 nm rms.

Figure 9 shows the difference between the predicted and the measured chuck induced deformations based on the average of 4 evaluations using 2 different reticles. We fit the data of Figure 9 to a quadratic (2nd order Legendre polynomial) which we used to correct the predicted chuck induced errors. The unfit residual from this procedure is 0.5 nm rms and is easily identified as arising from shearing the high slopes at the edge of the reticles used.

SANITY CHECKS?

Procedures involving manipulating multiple data sets to generate correction files always carry with them the risk of, for example, a sign error which results in highly repeatable but biased results. In this case, there are two simple sanity checks.

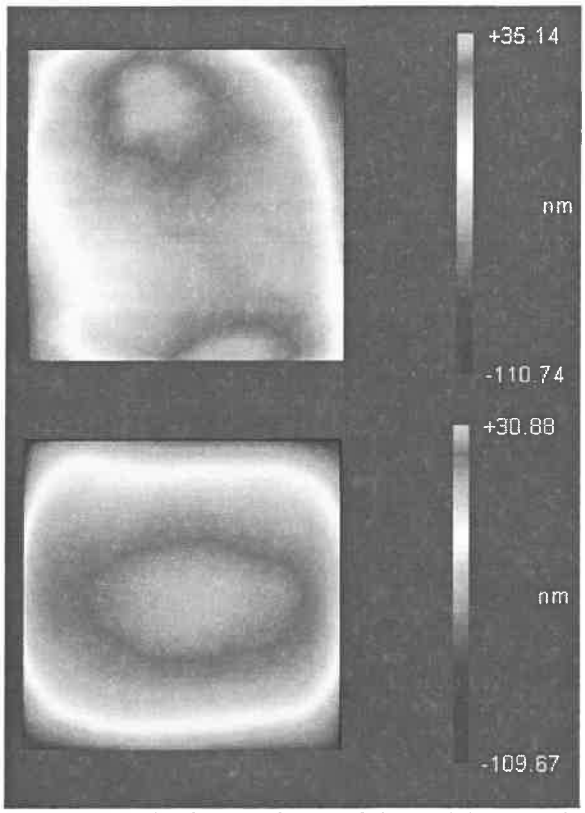

FIGURE 6: Surfaces of one of the reticles used in evaluating the chuck induced deformations

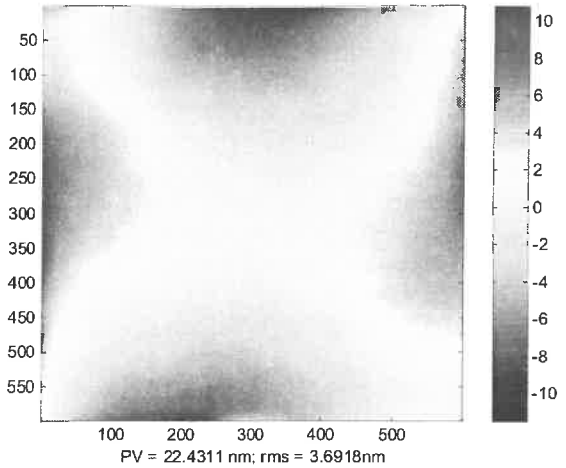

FIGURE 7: Estimated chuck induced deformations

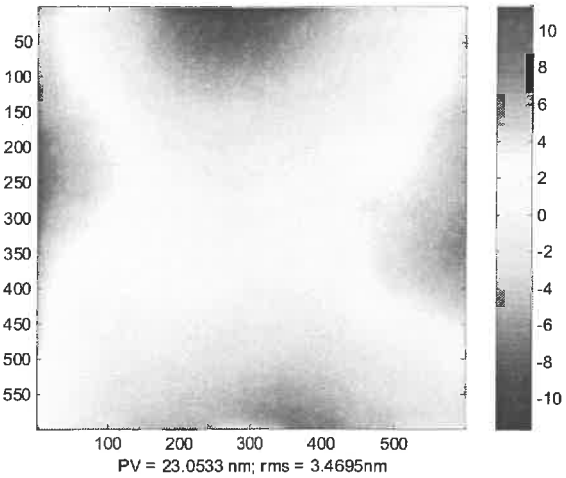

FIGURE 8: Estimated chuck induced deformations

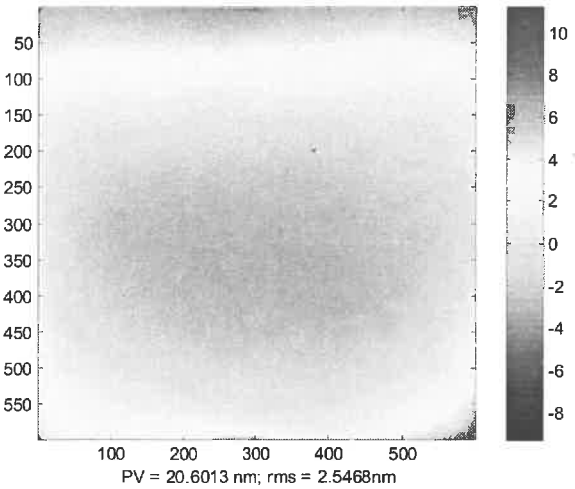

FIGURE 9: Difference between measured and modeled chuck induced deformations

First, if all the calibrations are correct, a simple flip test (where the part is measured sequentially with respect to the TF and RF) should give the same result. Figure 10 shows the standard deviation (pixel by pixel) for 8 such flip tests taken after the tool was installed at the customer's site. The consequence of the high velocity downward air flow in the test cavity is all too apparent. Despite this, the mean of the standard deviation map is 1.03 nm

A second, somewhat fortuitous, sanity check is the measurement of a reticle with surface flatness errors of the same order of magnitude as the chuck induced errors (Figure 11). Clearly, there is no suggestion in this data of the characteristic shape of the modeled chuck induced deformations or of the experimentally derived correction to it.

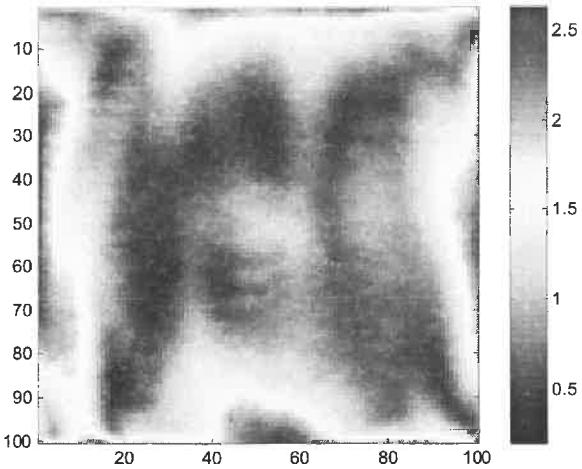

FIGURE 10: Standard deviation map for 8 sets of flip test measurements (mean =1.03 nm)

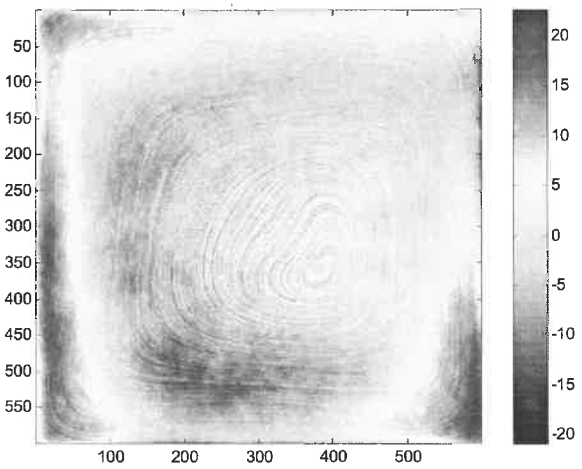

FIGURE: 11 Measurement of a reticle with small low spatial frequency surface form errors

CONCLUDING REMARKS

The specifications for the flatness metrology tool briefly described in this paper included a requirement that no contact be made with either surface of the reticle within the "quality area". One design goal was that the chuck induced deformations be highly repeatable, so that they could be subtracted from the raw measurement result.

This paper has presented a simple procedure for separation of the chuck induced errors from the "freestanding" surface flatness errors. The measurements confirm that small differences between the assumed and actual contact conditions lead to large differences between modeled and measured chuck deformations. These improved assessments of the chuck induced deformations were necessary to meet the target uncertainty in measuring reticle flatness (as specified in[1]) less than 12 nm (k=2).

REFERENCES

[1] SEMI P37-1102, Specification for Extreme Ultraviolet Lithography Mask Substrates, September 2002

[2] Deck L.L. Absolute distance measurements using FTPSI with a widely tunable IR laser Proceedings of SPIE, Volume 4778, 2002, pages 218-226.

[3] Evans C.J., Kestner R.N. Test optics error removal. Applied Optics, 1996, Vol 35, No 7, p1015

[4] Evans C. J. Comment on the paper "Interferometric testing of optical surfaces: absolute measurements of flatness", Optical Engineering, 1998, Vol 37, p1880

[5] Lindquist D., et al "High resolution tool for measuring photomask flatness", Proc. SPIE, 2003, Vol 5130, p528

[6] see , for example, Ai C. and Wyant J. C. "Modified three flat method using odd and even functions" Optical Fabrication and Testing Workshop proceedings (1992) or Parks R. E. et al "Pixel–based absolute topography test for three flats" Applied Optics, Vol 37 (1998) No, 25 pp5951-6

[7] Evans C. J., Hocken R.J., Estler W. T. Self-calibration, reversal, redundancy, error separation and "absolute testing". Annals of the CIRP, 1996, Vol 45/2, p617

DISPLACEMENT MEASUREMENT INTERFEROMETER ERROR CORRECTION TECHNIQUES

Stephen L. Mielke[1], Frank C. Demarest[1]
[1]Precision Positioning Solutions
Zygo Corporation
Middlefield, CT, USA

INTRODUCTION

Heterodyne displacement measurement interferometers (DMIs) have been a standard tool for motion control feedback in the semiconductor industry for over 20 years. In this paper we discuss DMI error sources that become significant when nanometer-level accuracy is required, and error correction techniques that can be used to mitigate them when implementing DMIs for motion control feedback. In particular, we discuss cyclic errors, mirror mapping, and data age uncertainty.

CYCLIC ERRORS

A heterodyne DMI beam has two orthogonal, linearly polarized components, separated by a split frequency f_R. In ZYGO's products $f_R =$ 20 MHz. The principle of operation is that one polarization is sent to a stage mirror, while the other polarization does not travel out of the interferometer. The polarization travelling to the stage mirror obtains a Doppler shift $f_D = 4v/\lambda$ for a double-pass interferometer configuration, a stage mirror moving with velocity v, and a laser wavelength λ. The two polarizations are then mixed to obtain a beat frequency $B = f_R + f_D$. The phase of B relative to f_R is used to calculate displacement. The typical optic used to separate the polarizations is a polarizing beam splitter (PBS) cube.

In a real system the two polarizations and frequencies can get mixed unintentionally through several factors, including

- Non-orthogonality of the polarizations
- Having a component of the wrong frequency in either polarization
- Misalignment between the axes of polarization and the PBS cube
- Imperfect anti-reflection coatings on the optics

The unintentional mixing results in cyclic errors, which get their name from the periodic variation of the amplitude of the error as a function of stage mirror displacement. The amplitude of cyclic errors can be several nanometers. Since the amount of stray light changes with stage mirror displacement and angle, in order for cyclic error compensation to be effective it must take place in real time.

The two largest contributors to cyclic error are easy to understand conceptually. The first, which we call $C0$, results from neither polarization going to the stage mirror. In this case, the beat frequency $B = f_R$ regardless of the stage mirror velocity. The second, which we call CN, results from the two polarizations each going to the wrong place: the polarization (and frequency) intended to travel to the stage mirror stays in the interferometer, while the polarization (and frequency) intended to stay in the interferometer travels to the stage mirror. When these two polarizations mix, the result is a beat frequency $B = f_R - f_D$. We summarize these frequencies in Table 1.

TABLE 1. Frequencies of the largest cyclic errors. B is the beat frequency; f_{CE} is the observed frequency of the cyclic error.

Signal	B	Offset from f_R	f_{CE}
Measurement	$f_R + f_D$	f_D	-
$C0$	f_R	0	f_D
CN	$f_R - f_D$	$-f_D$	$2f_D$

TABLE 2. Observed cyclic error frequency f_{CE} examples for various stage mirror velocities.

Stage Mirror Velocity (mm/s)	$C0$ F_{CE}		CN F_{CE}	
0.001	6.3	Hz	12.6	Hz
50	316	kHz	631	kHz
200	1.3	MHz	2.5	MHz

ZYGO has implemented cyclic error compensation (CEC) on our ZMI 4100 series measurement boards. The principle of operation follows. The measurement board receives the

beat frequency B and the reference frequency f_R. The beat frequency is band pass filtered, digitized, and then run through a discrete Fourier transform (DFT). At this point CEC is applied to the complex output of the DFT. The complex amplitude of the desired measurement signal and the two cyclic error signals are calculated. From these, compensation signals are generated for the cyclic errors. The compensation signals are subtracted from the DFT output. The compensated measurement signal then undergoes a coordinate rotation to calculate the position and velocity of the stage mirror. Since CEC operates on the complex amplitude of the measurement signal before coordinate rotation, it is able to provide highly effective compensation for cyclic errors in real time. ZYGO's measurements show that CEC reduces $C0$ and CN by more than a factor of 10.

MIRROR MAPPING

Displacement measurement interferometers use plane mirrors mounted on the moving stage to detect motion. The stage mirrors can be a source of error in semiconductor equipment since even high-quality stage mirrors with flatness of $\lambda/20$ (at $\lambda = 633$ nm) have surface figure errors of 32 nm. White light interferometers may be used to map the surface figure of stage mirrors, but the large size of white light interferometers typically necessitates off-line mirror mapping. In this case, any surface figure changes during the mirror mounting process will not be recorded.

ZYGO has developed an in-situ mirror mapping and error correction (MMEC) algorithm based on multiple-axis interferometers. The interferometer configuration uses a single primary beam and three secondary beams. With this design, calculating a first difference parameter (FDP), the difference in measured displacement between two axes, we eliminate contributions from overall stage displacement and from the primary beam, leaving only the difference in measured displacement between the two secondary beams. Calculating a second difference parameter (SDP), the difference between two FDPs, eliminates contributions from stage angle. By using the SDP, ZYGO's mirror mapping algorithm does not require accurate knowledge of the stage mirror displacement or orientation to map the mirror surface.

Results from the MMEC algorithms are shown in Figures 1 and 2. Figure 1 shows a simulated mirror surface with peak-to-valley figure error of 30 nm. MMEC was applied to the mirror shape. The resulting calculated mirror shape was subtracted from the original. Figure 2 shows the residual error after subtraction of the calculated shape. The residual error is less than 0.3 nm peak-to-valley, with $\sigma = 0.049$ nm.

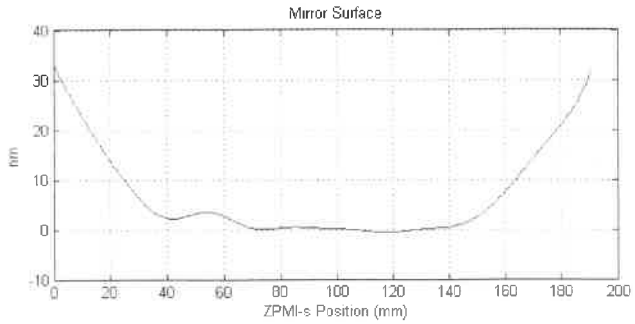

FIGURE 1. Mirror error before compensation.

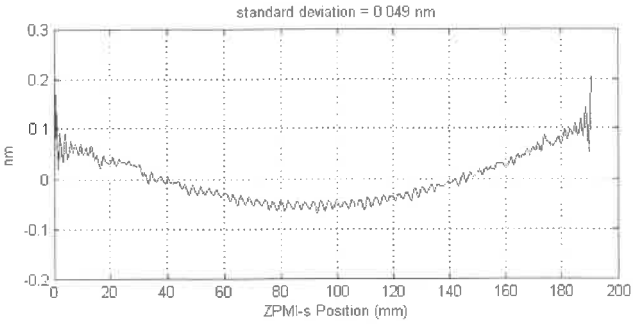

FIGURE 2. Residual error after compensation.

DATA AGE UNCERTAINTY

To control precision motion accurately it is necessary to provide not only position data but also time data: when the measured object is at a particular location. Data age is the time difference between when the stage mirror is measured and when the user control system gets the position information. Data age uncertainty is the maximum variation in the data age between axes in a multi-axis system. Data age uncertainty is due primarily to process variations in the electronics and differences in optical and electrical path lengths.

To minimize data age uncertainty, multiple measurement boards are synchronized in two ways. The measurement board phase meters are synchronized by a reference signal passed from board to board through a reference tree. The measurement output is synchronized by

latching all axes on all measurement boards with the same backplane signal.

There are several contributors that must be properly accounted for in order to minimize data age uncertainty. For each measurement channel, the following must be considered:

- Data processing time for that channel
- Reference tree and reference cable delays from board to board
- Fiber optic cable delays

Data age compensation can be made by combining previously measured delays and cable lengths, or through direct measurements of the absolute phase of the measurement signal.

Data Age by Calculation

Each aspect of data age may be measured individually, and then combined to form an overall data age compensation for the system.

Data Processing Time

The approximate data processing time for ZYGO measurement boards is 1 µs (2 µs with CEC active). During the measurement board acceptance testing prior to shipment, ZYGO measures the data processing time for each measurement channel. That time is compared to a standard data processing time for the particular family of measurement boards. For each axis, the difference between the standard time and the actual time for that axis is stored in EEPROM.

Reference Tree Delays

For each measurement board, the electrical reference tree output delays are also measured and stored in EEPROM. From the electrical reference output, a calibrated cable is used to transmit the electrical signal to the next measurement board. The reference cable delay is typically measured when the cable is manufactured, and printed on the cable.

Fiber Optic Cable Delays

There is also a propagation delay for light travelling to the measurement boards through fiber optic cables from each interferometer. The fiber delay F is given by $F = Ln/c$, where L is the length of the fiber optic cable, n = 1.46 is the index of refraction of the fiber core, and c is the speed of light. The calculation for this delay may also include the distance from the interferometer to the stage mirror at the stage mirror's closest point of travel. For a double-pass interferometer, this delay is given by D/c, where D is the distance from the fiber end face to the PBS cube, plus twice the distance from the PBS cube to the stage mirror.

Compensating for the Total Delay

The total delay for each axis is the sum of the measurement channel data processing time, fiber optic cable delay, and one or more electrical reference tree output delays and cable lengths. The axis with the maximum delay is assigned a data age adjust value of zero. The other axes are assigned a data age adjust value which is the difference between the maximum delay and the delay for that particular axis. In this manner, each axis is assigned a delay that brings it in line with every other measurement channel.

During data collection, the fiber optic reference signal goes to the first board in the electrical reference tree. That board also generates the clock signal for all other boards to latch data.

Using this technique, we achieve a data age uncertainty of ± 1 ns for up to three reference jumper cables. Since each measurement board has two electrical reference outputs, this allows us to have ± 1 ns data age uncertainty for up to 60 measurement channels.

In-System Data Age Compensation

It is also possible to determine the correct data age adjustment in an assembled system by measuring the absolute phase of a measurement signal. The absolute phase register samples the phase value when the position value is updated. Making a direct measurement of the phase reduces data age uncertainty by eliminating the accumulation of uncertainties that occurs when calculating the total data age from multiple components in the system.

The data age for each channel is measured using a null interferometer consisting of a neutral density filter in front of a fiber optic pickup with no additional interferometer or stage mirror. The measurement axis is reset, and the absolute phase recorded. For each axis, an average of approximately 100 measurements is needed to determine the average absolute phase. The data age for each channel is computed from the absolute phase. The resulting compensation for each channel is calculated as described above,

by assigning the channel with the longest data age a compensation value of zero. The other axes are assigned a data age adjust value which is the difference between the maximum delay and the delay for that particular axis.

SUMMARY

We have described error correction techniques for three significant sources of measurement error in displacement measurement interferometry. Cyclic error compensation reduces the two most significant contributors to cyclic error by more than a factor of ten. Mirror mapping reduces mirror figure error to less than 1 nm. Data age compensation allows up to 60 measurement channels to be used with ± 1 ns data age uncertainty. Each of these error reduction techniques significantly increases the accuracy of measurements made with displacement measurement interferometry.

DESIGN OF AN INTERFEROMETER FOR EUV INTERFERENCE LITHOGRAPHY AT THE NIST SURF III SYNCHROTRON

Kenan Cole[1], R. Ryan Vallance[1], Thomas Lucatorto[2]
[1]Precision Systems Laboratory, The George Washington University
Washington, D.C. USA
[2]Electron and Optical Physics Division, NIST
Gaithersburg, MD USA

INTRODUCTION

The National Institute of Standards and Technology (NIST) and The George Washington University (GWU) are collaborating to develop an Extreme Ultra-Violet Interference Lithography (EUV-IL) [1, 2, 3, 4] system at NIST's SURF III synchrotron source. The EUV-IL system will employ a cascaded arrangement of diffractive gratings suited to producing patterns with half-pitches as fine as 20 nm over millimeter-sized fields. Two cascaded gratings, G1 and G2, are arranged in the interferometer as shown in Fig. 1 so that G1 splits the EUV beam and G2 recombines the two legs to produce interference fringes on the surface of a resist film. The exposure time is expected to be several minutes, and the interferometer must remain stable to a few nanometers in the lateral directions during this period.

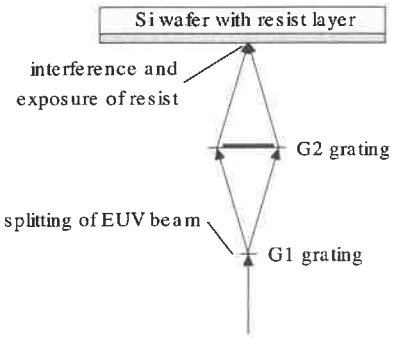

FIGURE 1. Cascaded arrangement of diffractive gratings for EUV-IL

CONCEPTUAL DESIGN

The prototype interferometer pictured in Fig. 2 was designed to be thermally stable, vacuum compatible, and provide nanometer adjustments of the focal plane. Three capacitive displacement sensors track variation in the focus distance and parallelism between the two gratings and wafer. The parallelism between the locked G1 and G2 gratings and the wafer is manually adjustable with fine-pitch screws and a kinematic tip-tilt stage that has its center-of-rotation set at the exposure point on the wafer. The focus is adjusted with a nano positioning system that allows for more than 10 micrometers of focus adjustment with near-nanometer resolution. By combining the capacitive displacement sensors and the nano positioning system in a low-bandwidth control loop, we will actively compensate for thermal drift in the focus (distance between the G2 grating and the resist surface).

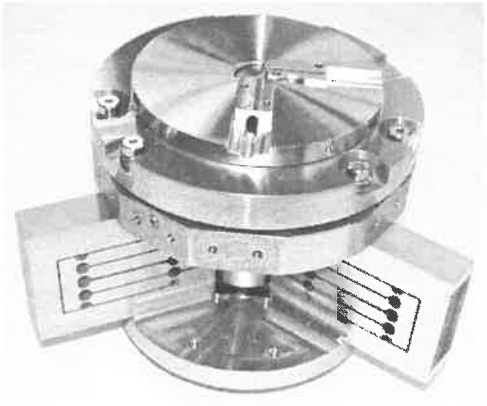

FIGURE 2. Prototype interferometer

Two key components in EUV-IL are the gratings and the wafer. The gratings will be fixed to opposing sides of an invar cylinder as shown in Fig. 3(a). The length of the cylinder sets the separation distance between the G1 and G2 gratings, and the distance between G2 and the wafer surface should be identical if the fringe pattern is to be focused. The G2-to-wafer distance is adjustable using the nanopositioning system described in the next section. The silicon wafer is held to the bottom surface of a rigid plate with the thin resist layer facing down as shown in Fig. 3(b). The wafer is held on the plate by a clamp with an open channel that allows for the exposure across the diameter of the wafer. The next-generation interferometer will allow for exposures over large areas of the wafer.

Accurately setting and maintaining the parallelism between the G2 grating and the wafer and the focus distance is crucial to obtaining successful exposures. The depth-of-focus is expected to be about 1 micrometer, but this must account for error in the focus distance and non-parallelism errors across the width of the exposure area. The nano positioning system should achieve at least ten nanometer resolution, and a resolution of about 0.4 milliradians is expected for the parallelism adjustment. If this is achieved, then exposure areas might exceed 2 millimeters in width.

Variation in relative position (focus) and parallelism (tip-tilt) of the gratings with respect to the wafer is measured by three capacitive displacement sensors (Lion Precision*, Model C3-D) with a sensitivity of 0.5 μm/V and 0.4 nm resolution. As seen in Fig. 4(a), the three sensors are arranged at 120° increments around the optical axis and at a radial distance of 40.4 mm from the optical axis. All three sensors target the surface of the wafer.

The focus distance (between G2 and the wafer) is set in the prototype interferometer with the flexure-guided nanopositioning stage illustrated in Fig. 4. Three parallel compound flexures [5] are arranged at 120° increments about the optical axis of the interferometer. This arrangement provides thermal symmetry, sets the center-of-stiffness on the optical axis, provides for accurate linear translations, and yields high off-axis stiffness. The three flexures are fixed to a top plate and a base plate that serve as mechanical ground for the interferometer. The translating links of the flexures are connected with a cylindrical tube that distributes the actuation equally to each flexure.

A piezo actuator (Piezomechanik*, HPSt 150/20-15/12), with the properties listed in Tbl. 1, generates the displacement and force applied to the three compound flexures. Displacement of the piezo actuator is controlled by applying a 0 to

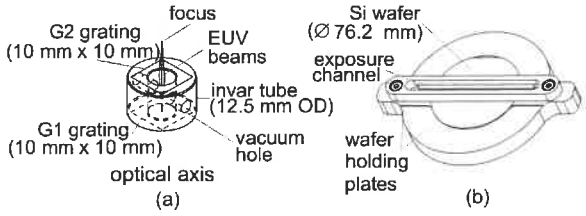

FIGURE 3. (a) grating holder (b) wafer holder

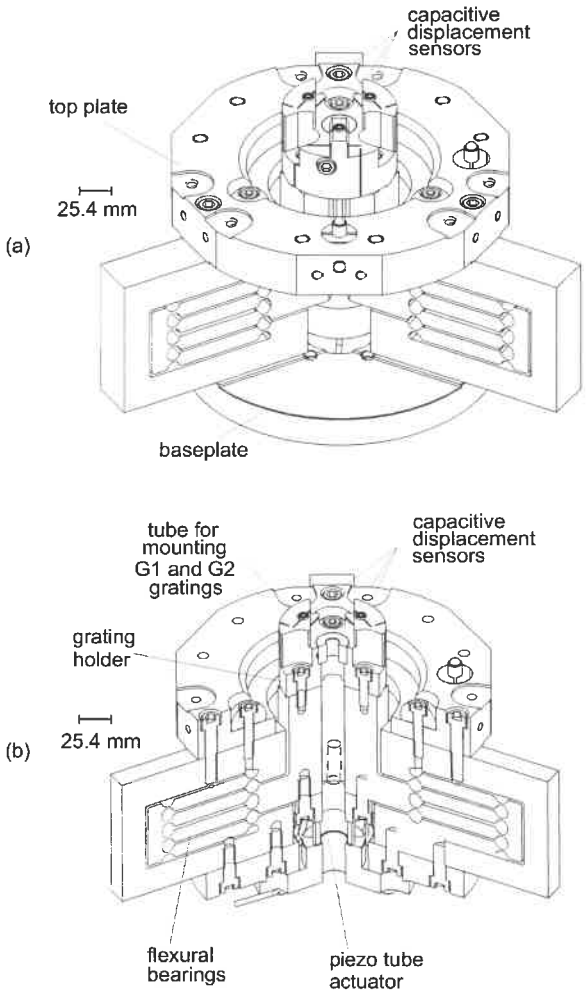

FIGURE 4. Isometric view of nanopositioning system for adjusting focus (a) isometric view and (b) cutaway view revealing piezoelectric actuator and grating holder

150 V analog voltage from a piezo amplifier (Thor Labs*, MDT693). Eventually this displacement will be controlled by a closed-loop feedback system to maintain constant distance between G2 and the wafer and thereby correct for thermal drift in the focus, but all of the tests reported in this paper were conducted in an open-loop mode using a 0 - 10V command into the piezo amplifier.

The parallelism between the gratings and wafer must also be set accurately using the tip-tilt stage illustrated in Fig. 5. The center-of-rotation for the tip-tilt stage is coincident with the focus point on the surface of the wafer so that parallelism can be adjusted with minimal influence on the focus of the interferometer. The tip-tilt stage consists

TABLE 1. Properties of piezoelectric actuator

Outer diameter	20	mm
Inner diameter	15	mm
Height	13.5	mm
Stroke (0 to 150 V)	12	μm
Stiffness	450	N/μm
Blocking force	8000	N

of a kinematic arrangement of a hardened 440C stainless steel spherical segment with diameter of 101.6 mm that is pressed onto the tip-tilt plate. The spherical segment slides on three aluminum 19.05 mm diameter tip-tilt bearing balls that are fixed to the top plate of the interferometer. The contact lines between the three tip-tilt balls and the spherical segment intersect at the focus point on the wafer surface. The tip-tilt plate is preloaded towards the top plate to maintain contact between the spherical segment and the three tip-tilt balls using a pattern of six stacks of belleville springs arranged around the perimeter of the interferometer.

Two fine-pitch adjustment screws (Thor Labs*, 1/4-100) are arranged 90° apart, and they rotate within phosphor bronze nuts that are pressed into the top plate. The screws push against the flat ends of two sapphire rods that are pressed into the tip-tilt plate. This arrangement allows the tip-tilt orientation to be manually adjusted with a resolution of about 0.4 milliradians. Once the parallelism is set (using an optical interferometer at NIST), a set-screw clamps the fine pitch screws and holds their position. Figure 5(b) shows the position of the tip-tilt plate when assembled and preloaded to the top plate.

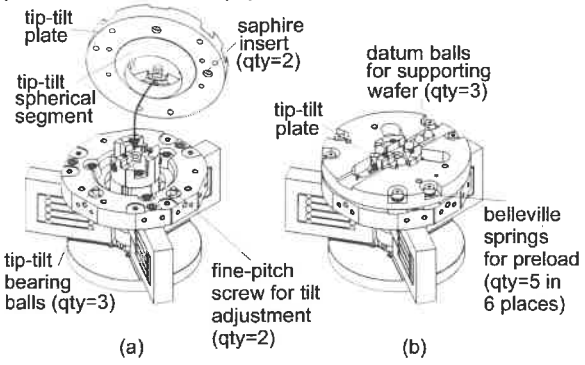

FIGURE 5. Isometric view of tip-tilt stage (a) tip-tilt plate removed and (b) tip-tilt plate preloaded to top plate

The wafer and its support plate (Fig. 3(b)) rests on three 9.53 mm balls mounted on the top surface of the tip-tilt plate. Therefore, adjustment of the the tip-tilt plate's orientation sets the parallelism between the gratings and the wafer. This is displayed in Fig. 6(a). An additional motor (New Focus*, Picomotor) indexes the wafer to new positions for multiple exposures. Figure 6(b) shows the completely assembled interferometer ready for exposure.

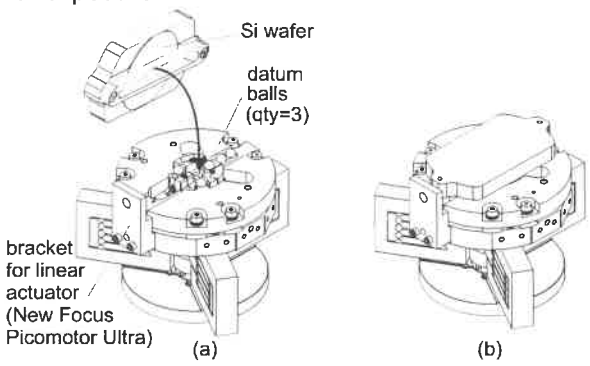

FIGURE 6. Assembly of the wafer onto the interferometer (a) wafer holder removed (b) wafer holder in place, full assembly

DESIGN OF NANO POSITIONING SYSTEM

Each flexure is made of invar, which has a modulus of elasticity E of 130 GPa and a yield strength S_y of 260 MPa. To maintain a factor-of-safety $N = 3$, the maximum von Mises stress σ within the flexure under maximum displacement is limited to 86.7 MPa.

As shown in Eq. 1, the maximum displacement δ_{max} is the sum of the preload distance p and the stroke s. The stroke s is to be around 15 micrometers, and the preload should be set within about +/- 2.5% of the target value. This can easily be achieved with a dial indicator that is graduated in 19.7 μm (0.0005 inch) increments if the preload distance is about 228 μm (0.009 inches). Therefore, the flexure is designed for a maximum displacement of about $\delta_{max} = 244$ micrometers.

$$\delta_{max} = s + p \tag{1}$$

The preload force should be at least equal to the maximum inertial force that arises during maximum accelerations. The preload force F_p is then approximately the product of the moving mass m and the maximum acceleration a_{max} that occurs during periodic motion with frequency f and amplitude $s/2$, which gives the expression in Eq. 2. If the moving mass is about 0.31 kg and the maximum frequency is about 850 Hz, then the preload

force should be about 66 N.

$$F_p = ma_{max} = 2\pi^2 msf^2 \quad (2)$$

The equivalent stiffness of the three flexures k_{eq} is given by the ratio of the preload force and the preload displacement. This ratio, given in Eq. 3, yields an equivalent stiffness k_{eq} of 289 N/mm or about 97 N/mm for a single flexure.

$$k_{eq} = \frac{F_p}{p} \quad (3)$$

Assuming small rotation angles θ at the flexure's pivots, the displacement δ of the flexures is approximated by Eq. 4, where L is the distance between pivots. The other critical dimensions in the flexure are the thickness b, the thickness t of the web in the pivot, and the radius R of the pivot. All of these dimensions are identified in Fig. 7.

$$\delta = 2\theta L \quad (4)$$

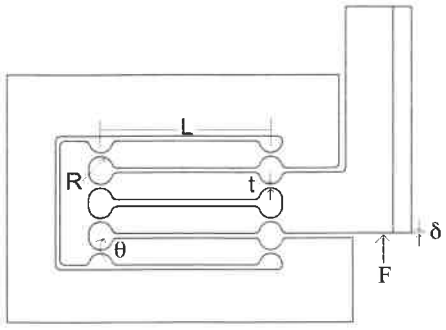

FIGURE 7. Dimensions of compound flexure with semicircular pivots. Force F produces displacement δ.

Values for the dimensions of the flexure were determined by considering two constraints, one based on the stress in the pivot and another based on the stiffness. Equating the potential energy of an equivalent system of stiffness k_{eq} with the potential energy of the 24 pivots acting in parallel gives the relationship in Eq. 5 for k_{eq} in terms of the torsional stiffness k_t of an individual pivot. Paros and Weisbord [6] provided the expression in Eq. 7 for the torsional stiffness k_t of a semicircular pivot.

$$\frac{1}{2}k_{eq}\delta^2 = 24(\frac{1}{2}k_t\theta^2) \quad (5)$$

$$k_{eq} = 6k_t/L^2 \quad (6)$$

$$k_t = \frac{2Ebt^{5/2}}{9\pi R^{1/2}} \quad (7)$$

The maximum stress, which will occur at the center of the pivot's web, must be less than $S_y/N =$ 83.7 MPa. The maximum stress σ is given by Eq. 8 where K_t is the stress concentration factor and M_{max} is the maximum moment at the pivot for δ_{max} given by Eq. 9.

$$\sigma = \frac{6K_tM_{max}}{bt^2} \quad (8)$$

$$M_{max} = k_t\theta_{max} = k_t\left(\frac{\delta_{max}}{2L}\right) \quad (9)$$

Smith et al. [7] gave the approximation in Eq. 10 for the stress concentration factor K_t in terms of the dimensions of a semi-circular pivot.

$$K_t = \left(1 + \frac{t}{2R}\right)^{9/20} \quad (10)$$

Equation 8 can be solved for L after substituting expressions from Eqs. 9 and 10, and the result is given in Eq. 11. This expression for L is then used in Eq. 6 to relate t and R as shown in Eq. 12. After selecting a value of R, Eq. 12 can be solved to find a value of t, and then the corresponding value of L is found with Eq. 11.

$$L = \frac{2E\delta_{max}N}{3\pi S_y}(1 + \frac{t}{2R})^{9/20}(\frac{t}{R})^{1/2} \quad (11)$$

$$(1+\frac{t}{2R})^{9/20}t^{-3/2}R^{-1/2} - \frac{3\pi bS_y^2}{E\delta_{max}^2N^2k_{eq}} = 0 \quad (12)$$

The results of the analysis are presented in Fig. 8. The radius R and the thickness t are independent design variables, and each curve represents a different value for the width b. Points along the curve correspond with values of L that satisfy the constraints on stress and stiffness. We chose the dimensions identified by the asterisk and listed in Tbl. 2 for their reasonable compromise in size, off-axis stiffness, and manufacturability.

TABLE 2. Dimensions of flexures

b	=	21.000 mm
t	=	0.975 mm
R	=	3.175 mm
L	=	45.834 mm

A flexure with the dimensions listed in Tbl. 2 was also evaluated with finite element analysis. The flexure was analyzed using a plane-stress 2D model, and the maximum force per flexure of 11.2 N was applied. The stress and displacement values agreed with the analytical values to within 10%. The stiffness of the manufactured prototype flexure was also measured experimentally, and its stiffness agreed within 5% of the analytical value.

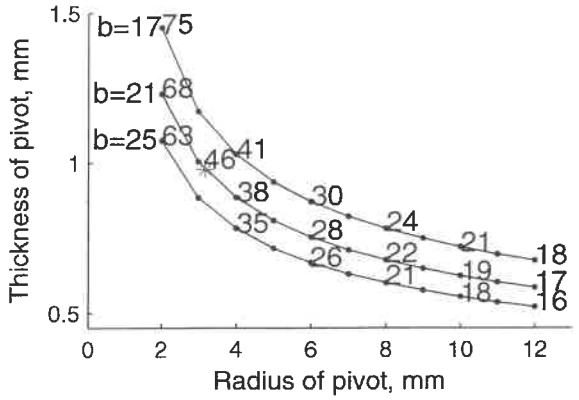

FIGURE 8. Dimensions of flexure that satisfy stress and stiffness constraints

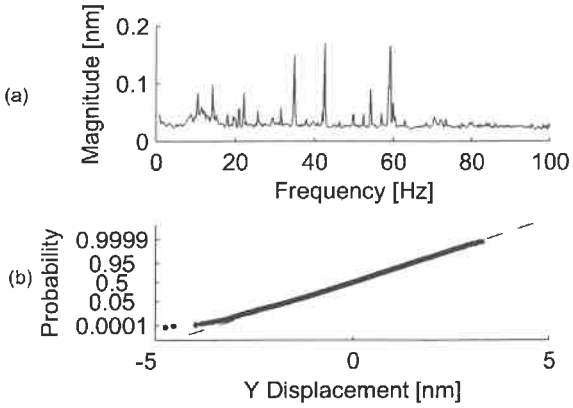

FIGURE 10. Random y-direction displacements (a) displacement spectrum and (b) probability plot

PRELIMINARY TESTING OF PROTOTYPE

Displacements in the z-direction (focus) and y-direction were measured with capacitive displacement sensors (Lion Precision*, Models C1-C and C4-E) having sensitivities of 2.54 μm/V and 1.25 μm/V, respectively. The analog outputs from the capacitive displacement sensors were low-pass filtered at 100 Hz and measured with a 16-bit A/D converter (Iotech* DAQ2000) with a sampling frequency of $f_s = 200$ Hz. Measurements were made under three conditions to evaluate the level of random motion (vibration and motion due to electrical noise): 1) only the DAQ system, 2) the DAQ system and 0 V applied to the PZT, and 3) the DAQ system and 150 V applied to the PZT. Figures 9 and 10 show plots of the displacement spectrum and a Gaussian probability plot for the z and y directions.

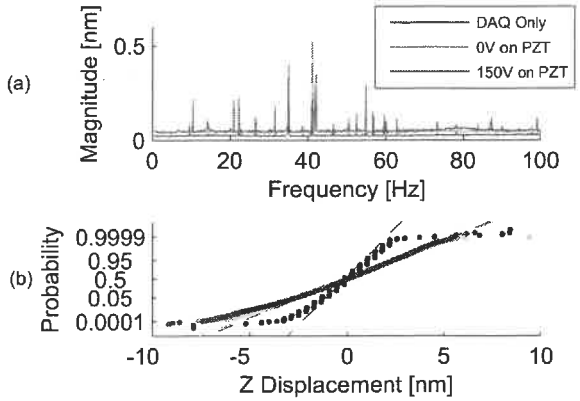

FIGURE 9. Random z-direction displacements (a) displacement spectrum and (b) probability plot

Motion of the nanopositioning stage was evaluated with sine-wave and square-wave commands into the piezo amplifier. The response due to sinusoidal commands is shown in Fig. 11 for four different amplitudes of voltage commands. The magnitude of the hysteresis and the sensitivity (nominal slope) increases slightly as the amplitude of the command is increased, but these effects will be of little concern when the nanopositioning system operates with closed-loop control. The response due to square-wave commands is shown in Fig. 12. Despite the noise in the current DAQ system, step sizes down to 10 nm were clearly achieved.

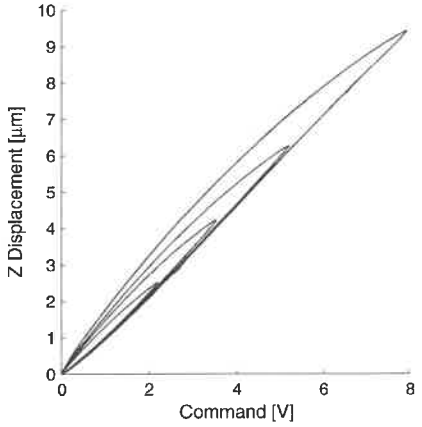

FIGURE 11. Hysteresis and increasing sensitivity of piezo actuator

Thermal drift of the interferometer was also evaluated over a period of 16.5 hours, and the relative motion in the z and y directions between the wafer and gratings is shown in Fig. 13. The peak-to-valley drift was around 1.5 μm in the z-direction and around 0.4 μm in the y-direction. The ambient temperature in the room was 26.0°C

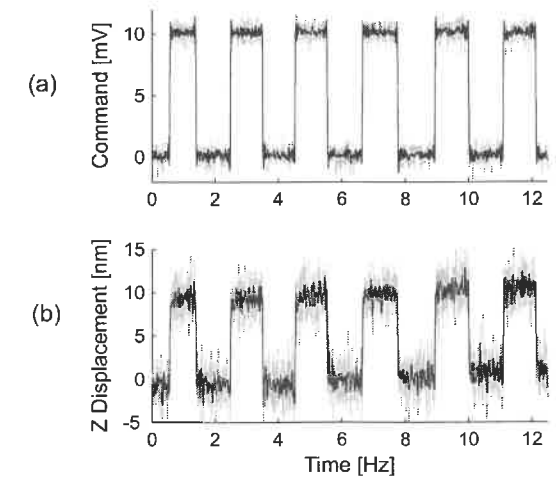

FIGURE 12. Steps of 10nm (a) command voltage (b) measured displacment response

+/- 0.5°C. Since the interfereometer will operate in high vacuum, this experiment will be repeated again inside the vacuum chamber where it will not be subject to ambient convection.

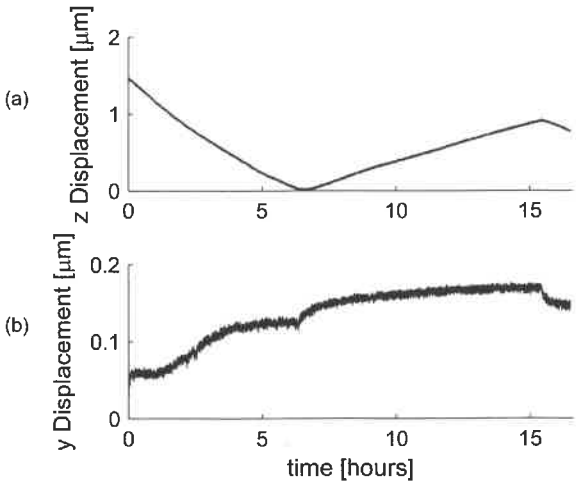

FIGURE 13. Thermal drift over 16.5 hours (a) z-direction displacement (b) y-direction displacment

CONCLUSION

The EUV-IL interferometer shows great promise for producing patterns on the order of a 20 nm half-pitch. The focus adjustment system provides nearly nanometer resolution, and the tip-tilt stage provides sub-milliradian parallelism adjustments without disturbing the focus. Based on the initial tests for motion, random vibrations, and thermal drift, the interferometer performs very well.

ACKNOWLEDGEMENTS

This work was partially supported by Kenan Cole's Presidential Administrative Fellowship from the George Washington University. The authors also acknowledge Duane Enderle at NIST for constructing the prototype parts.

REFERENCES

[1] M. Wei, D. T. Attwood, T. K. Gustafson, and E. H. Anderson. patterning a 50-nm period grating using soft x-ray spatial frequency multiplication. *J. Vac. Sci. Technol. B.*, 12:3648–3652, 1994.

[2] M. L. Schattenburg, C. Chen, P. N. Everett, J. Ferrera, P. Konkola, and H. I. Smith. Sub-100 nm metrology using interferometrically produced fiducials. *J. Vac. Sci. Technol. B.*, 17:2692–2697, 1999.

[3] H. H. Solak, D. He, W. Li, and F. Cerrina. Nanolithography using extreme ultraviolet lithography interferometry: 19 nm lines and spaces. *J. Vac. Sci. Technol. B.*, 17:3052–3057, 1999.

[4] A. Isoyan, Y.-C. Cheng, F. Jiang, J. Wallace, and F. Cerrina. Progress in extreme ultraviolet interferometric and holographic lithography. *J. Vac. Sci. Technol. B.*, 25:2145–2150, 2007.

[5] S. T. Smith. *Flexures: Elements of Elastic Mechanisms.* CRC Press, 2000.

[6] J. M. Paros and L. Weisbord. How to design flexural hinges. *Machine Design*, pages 151–156, November 1965.

[7] S. T. Smith, V. G. Badami, J. S. Dale, and Y. Xu. Elliptic flexure hinges. *Review of Scientific Instruments*, 68(3):1474–1483, March 1997.

*Mention of the product name is for experimental completeness only and does not constitute an endorsement of the product by any agency of the U.S. Government or by GWU.

ELECTRON BEAM PATTERN GENERATION SYSTEM DESIGN

John G. Hartley
[1]**College of Nanoscale Science and Engineering**
State University of New York at Albany
Albany, NY USA

INTRODUCTION

Electron beam pattern generators (EBPG's) are the tool of choice for advanced reticle patterning and device prototyping. For over a decade it has been necessary for the designers of such machines to concern themselves with details that potentially contribute to the final performance of the system at levels of only a few nanometers or less. Not everything that potentially contributes to the final accuracy of target image placement is well understood at this level. When such "known unknowns" are encountered during the design process, the system designer has several choices: 1) Initiate a research project to accurately understand the phenomena in question, 2) Implement new engineering approaches to the design which avoids the questionable area, or 3) Proceed cautiously into the unknown, guided by a mixture of hope and intuition. None of these approaches is ideal. Initiating a research project in the course of an engineering design project can play havoc with budget and schedule. Alternative approaches may work fine but usually come at the expense of performance against some other metric. Hope and experience may lead a team down a path where potentially serious problems are not uncovered until late in the build cycle with serious financial and schedule impact.

Here we examine a model error budget for a hypothetical e-beam pattern generator in some detail. Perhaps the best way to avoid the three design traps highlighted above is to identify problem areas sufficiently far in advance that research projects become independent of the system design schedule.

GENERIC EBPG SYSTEM MODEL

Figure 1 illustrates the system layout of a generic EBPG. Many of the system elements have direct analogs in optical lithography but with significant variations in detail. The most important detail is the use of an electron beam as the vehicle for transfer of the pattern information to the substrate.

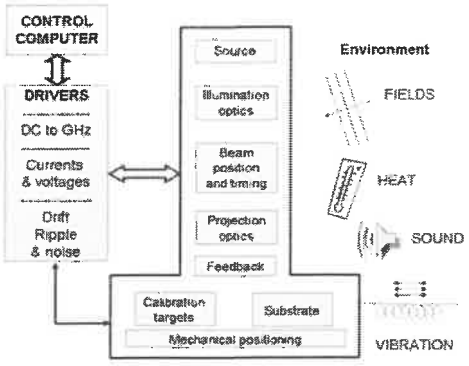

FIGURE 1. Generic layout of a typical EBPG illustrating the main components and some of the known detractors to system performance.

The trajectory of an electron is easily modified by electric and magnetic fields. This feature is what permits the degree of control required for imaging and software controlled pattern formation. The downside is that the same electrons can see their trajectories perturbed by uncontrolled excursions from an ideal case and in high current systems by each other.

Electronic Errors

The factors in an EBPG error budget which are well defined consist of the systems response to the presence of voltage and current excursions in the drive electronics as shown in Figure 1. At each point in the electron optical path where an excursion may be injected a transfer function to the substrate may be defined to assess the impact on the trajectories termination point. The resultant errors are vector summed for drift, ripple and quantization while noise errors are vector summed in quadrature. While ripple is generally interpreted to mean the line frequency and its harmonics, it is generalized here to include any disturbance with a stable and unique spectral signature. The summation is performed at each frequency under the assumption that all ripple error components contribute in phase. Dependent upon the specific location of the error

source the effect may manifest itself in the printed image in a variety of ways resulting in a single error source contributing to multiple components of the error budget.

Correction Errors

Within an electron optical system there may exist a variety of mechanical alignment errors between the optical elements and the nominal optical path. It is a common practice to introduce alignment deflectors whose function is to ensure that the beam passes through the optic axis of each lens. Each such alignment deflector has a penalty however, as it functions as another channel for introducing noise into the system. In some cases, a mechanical alignment scheme may be preferable.

Corrections are also introduced that improve the electron optical performance of the system. As the beam is deflected off axis its nominal focus and stigmation in the image plane vary as a function of beam position. Coils that cancel these effects out are typically included in the column along with drive electronics that are subject to the same issues previously mentioned. More sophisticated correction elements are possible as well to correct a variety of aberrations, each with their own associated electronic driver packages and corresponding impact on placement and imaging performance limits. As with optical lithography tools, an e-beam system needs to be aware of the location of the writing plane and adjust its focus for optimal imaging.

Correctly setting the nominal values for all of the different drive circuits in an electron optical system requires accurate calibration methods. A feedback element is illustrated in Figure 1. which represents the various detectors throughout the column which sense the response of the beam to a variety of controlled inputs. As with the drivers, the circuits that comprise the feedback loop introduce errors as well with an associated component in the overall error budget.

Dynamic Errors and Throughput

Dynamic errors in EBPG systems arise from the necessity of steering the electron beam across the substrate to form the pattern. Figure 2. shows an example of the deflection hierarchy found in a typical EBPG. A substrate is anchored to a stage which is mechanically driven over a range large enough to span the largest substrates to be exposed. The exact stage coordinates are fed back to the deflection electronics that drive the field and sub-field deflectors and enable the EBPG to match the coordinate system on the substrate. The beam dwells at a fixed location for a predetermined time interval to expose the resist and then steps to the next location. The time required for the beam to settle to its desired location forms a significant fraction of the patterning time in when writing dense patterns.

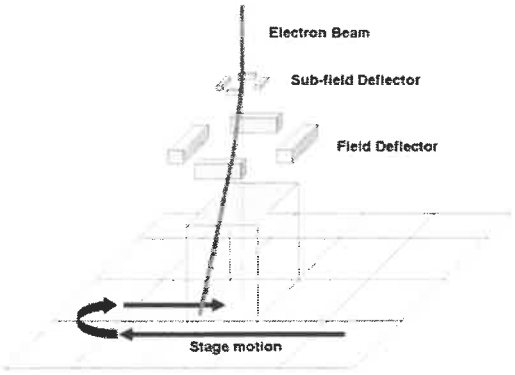

FIGURE 2. Typical EBPG deflection hierarchy with 3 levels of motion. Fields are on the order of a few mm and stitched together to form chips.

Many of the subsystem specifications are determined by the goal of achieving the target performance while maximizing throughput. Performance and speed requirements generally work against each other as increased speed generally translates into increased bandwidth and therefore increased noise. Figure 2. illustrates one method of achieving high bandwidth through the use of staged deflections. In each instance, the range is reduced and the bandwidth increased while maintaining a signal to noise ratio consistent with subnanometer accuracy. Another way of improving throughput while maintaining accuracy is through the use of a parallel architecture.

Not all dynamic errors involve a tradeoff with throughput. A class of errors exist which are referred to as history or pattern dependent errors. A simple example occurs in the situation where a pattern requires a large number of shapes to be patterned near the corner of the deflection field. To reach the corner of the field, the drive electronics must remain in a high power configuration for an extended period of time. If the waste heat generated in this state is

not adequately removed or corrected via feedback channel, a shift in the nominal operating point may be observed.

Two categories of dynamic error that are unique to the EBPG environment are eddy currents and charging. Eddy currents can occur whenever a time varying magnetic field operates in the vicinity of bulk conductors or conversely, whenever a bulk conductor moves in the presence of a static magnetic field. Eddy currents decay in complex ways depending upon the geometry and material properties of the conductor. If the time constant of the decay is on the same order as the deflection stepping time the effects can accumulate into a significant source of error. Charging can manifest itself in a variety of ways with trapped charge on the substrate being a major concern. Insulating surfaces, intentional or otherwise within line of sight to the electron beam can accumulate charge as well with complicated time dependencies.

EBPG systems are also subject to proximity effects which are superficially similar to the optical proximity effects found in photon based exposure tools. The underlying physical mechanism differs significantly however since the proximity effect in EBPG systems is due to electron scattering. The basic principles involved are fairly well understood with the main challenge concerned with the development of efficient algorithms that produce results with the required accuracy in a cost effective manner.

Dose control is another essential element to patterning at the nanometer scale. The arrival of a single electron in a square nanometer is the equivalent of a dose of $16uC/cm^2$. In order to avoid shot noise issues it is necessary to work with low resist sensitivities (high numbers) while maintaining tight control over exposure time and beam current.

Environmental Errors

Figure 1 lists four environmental factors which may have a negative impact on the overall EBPG performance. Optical tools are largely immune to environmental E&M fields but have similar issues with thermal, acoustic and mechanical disturbances. There are three primary means by which an EBPG system is isolated from the effects of stray E&M fields. The first is distance whereby external sources of E&M interference are kept physically remote from the EBPG. The second method is to introduce passive shielding that shunts the fields away from the electron beam. The final line of defense is to introduce active field cancellation where Helmholtz coils are driven to null out any fields detected in proximity to the EBPG column. It is important to remember that each of these approaches are to some degree frequency dependent and the potential to adversely influence the beam is present up to times scales on the order of the shot time.

Optical Aberrations

Electron optical lenses are generally considered terrible by light optic standards. To compensate in part, exposure fields and numerical aperture are held to very small values relative to those found in light optics. Working in favor of EBPG optics is the short effective wavelengths available at high accelerating voltages. One effect which degrades the performance of electron optics that has no direct counterpart in light optics is the Coulomb effect where a beam diverges due to the mutual repulsion between the electrons. This tends to play an important role in high throughput systems where a high beam current is desirable to reduce the shot time per flash. If the current in the column varies on a per flash basis such as seen in the current generation of shaped beam commercial mask writers significant focus shift may occur on a per flash basis. Many of the effects of lens aberration are correctable in an EBPG system due to the deep level of intrinsic numerical control. The minimum achievable resolution undeflected, however, sets the floor for the best possible imaging performance

Other Errors

Error sources that are common across both electron and photon based pattern generators are not considered explicitly in this discussion. Examples include acceleration induced slips and distortions of the stage and substrate. Other contributors are various vibration driven bending modes that may be specific to a given EBPG design but are amenable to the same methods applied in optical system.

NANOMETER SCALE EFFECTS

As should be evident from the preceding discussion, an EBPG has many sources of potential error that need to be captured and understood. Special attention needs to be paid

to errors that are vector summed as the potential exists for the errors to combine in a fashion that quickly overwhelms an error budget. Wherever possible, the EBPG system should be designed in such a way as to ensure that vector errors cancel by design to gain additional margins. Drift errors are correctable in principle by calibration. The magnitude of the acceptable error and the drift rate determine the frequency of need for recalibration. If the required frequency of recalibration is small compared to the time required to complete an exposure then drift correction may be expected to play a significant role in the throughput model.

Several of the items discussed above have the potential to contribute significantly to the error budget and are not well understood. This should not be interpreted as to a lack of understanding of the fundamental underlying physics but rather the complex environment in which it must be applied. The most complex effects to work with are those that have a time dependent component such as charging, eddy currents and heating. Each of them has seen activity at a variety of levels that seek to mitigate the effects.

Eddy currents [1][2] can be avoided entirely through the use of purely electrostatic optics in the vicinity of conducting elements. The penalty associated with this approach is a higher level of aberrations for an equivalent field size when compared to magnetic systems and the need to work with relatively high voltages and slew rates. When magnetic systems are used it is possible to shield bulk conductors from time dependent fields through the judicious use of ferrite and the replacement of bulk conductors with insulating material coated with thin layers of a conductor to avoid charge accumulation on surfaces exposed to the electron beam. Compensation strategies have also been developed with varying degrees of success.

Substrate charging has been addressed by a number of researchers [3] with techniques ranging from application of conductive discharge layers to sophisticated models that predict the dynamical charge accumulation and seek to apply corrections at exposure time. Whether the accuracy is sufficient for sub-nanometer residual error is to be determined.

Thermal effects receive a high degree of attention with liquid cooling of EBPG system components being fairly common. The effects of the heat load introduced into the substrate during patterning are fairly well understood but the application to actual pattern writing with sub-nanometer accuracy remains to be demonstrated.

One common problem with all 3 of these issues for a model based correction strategy is the necessity of accurately understanding the system timing. If a system has events that are reactive, system timing may not be identical between otherwise identical pattern exposures. If the model based correction is not capable of reacting in real-time to these events the accuracy may be compromised.

SUMMARY

The full parameter space for the error budget of an EBPG system is complex. While many of the contributors are well understood, there are several items whose detailed contribution depends upon a detailed history of the system prior to exposing an individual flash. In order to better predict the degree to which these effects contribute to the overall system accuracy at the design phase, more accurate system modeling tools are required to capture all of the underlying physics.

REFERENCES

[1] Takahashi Y, Yamada A, Oae Y, Yasuda H. and Kawashima K. Electron beam lithography system with new correction techniques. J. Vac. Sci. Technol. B: Microelectronics and Nanometer Structures -- November 1992 -- Volume 10, Issue 6, pp. 2794-2798

[2] Pfeiffer HC, and Sturans MA. Compensated magnetic deflection coil for electron beam lithography system, US Patent 4,251,728

[3] Benjamin Alles B, Cotte E, Simeona B, and Wandel T. Modeling the Work Piece Charging During e-Beam Lithography, SPIE Microlithography, in press.

[4] Babin S, Gaevski ME, and Konnikov SG. Measurement and simulation of temperature dynamics under electron beam J. Vac. Sci. Technol. B 19(1), Jan/Feb 2001 pp153-158

SYSTEM DESIGN BASED ON "DYNAMIC ERROR BUDGETING"

Jan van Eijk[1], Dave Trumper[2], and Leon Jabben[3]
[1]Technical University Delft / MICE bv
Delft, The Netherlands
[2]Massachusetts Institute of Technology
Cambridge, Massachusetts, USA
[3]Vision Dynamics
Eindhoven, The Netherlands

SUMMARY

During the design of Precision Systems the influence of many different disturbances on the performance must be taken into account. Static Metrology Budgets and Thermal Budgets are examples of such budgets. In systems where dynamic and stochastic disturbances occur a good method to predict the combined influences on the final performance is most valuable.

Such disturbances can originate from sources in different domains. Major examples are floor vibrations, sensor and amplifier noise, discretisation effects and acoustic disturbances. In "Dynamic Error Budgeting" a rigorous method to evaluate these influences is used. The method yield quantitative predictions of the influence of individual sources. The distribution of the influence over the frequency domain is easily described and this leads to effective approaches to improve the design.

The framework is also very well suited to guide the design of "optimal" controllers based on the H2 method.

The application will be illustrated in the design of the rotor for Optical Disc Mastering developed at the Delft University of Technology. This work forms the basis for a full day tutorial organized at the EUSPEN annual meeting in May 2008 in Zurich, Switzerland.

NANOTUBE MICRO-OPTO-MECHANICAL SYSTEMS

B. Panchapakesan
Delaware MEMS and Nanotech Laboratory,
University of Delaware, Newark, DE 19716, USA
(Tel: 001-302-831-4062; Email: baloo@ece.udel.edu)

INTRODUCTION

Materials that can reversibly change their physical properties upon application of external stimulus are used as sensors and actuators in many applications such as robotics, switches, prosthetic devices, micro-mechanical and microfluidic devices and various sensor applications. The best-known materials used today for actuation are piezoelectrics, electrostrictive materials, conducting polymers and shape memory alloys (SMA) [1]. However, electrostrictive materials are limited by the high driving voltages and low work density per cycle; Faradaic processes involving ionic diffusion encountered in conducting polymers present limitations on the actuation rate and cycle life in this actuation material [2]; SMA based actuation has been widely used in many applications and can be configured to give high strain capabilities; however, a cyclic mechanical deformation mechanism is needed for repeatable operation. It must be appreciated that all the above actuation technologies have already been successfully employed in a wide variety of practical applications, giving that different actuation materials match certain application requirements while their drawbacks are not a critical issue in such an application. However, most of them are not suitable in fabricating low cost, high performance miniature actuators for future nanotechnology, bio-nanotechnology and biomedical applications, where batch fabrication capability, scalability into nanoscales, ease of operation, remote controllability and high performance are all critical issues. Also, as devices become smaller (μm–nm), electrical connections are often complicated, requiring additional wiring circuits on different length scale.

Carbon nanotubes (CNT) and CNT/Pt hybrid nanowires have been recently proposed as new classes of actuator materials that require only small voltages for actuation compared to piezoelectric and ferroelectric materials [2, 3]. However, current applications of these nanomaterials for mechanical energy conversion are based solely on electrochemical and electromechanical processes that require the use of electrolytes or external electronics, respectively, for their operation and thus are not capable of operating in a massively parallel fashion and in a remotely controlled environment. While CNTs have been shown to have better electromechanical properties than many known materials, there have been no reports on the use of the actuation properties of CNT with MEMS devices that shows simplicity of integration and achieves similar or better performance compared to their electrostatic MEMS counterparts. The lack of precise patterning of carbon nanotube films have been a major stumbling block for practical realization of micro-devices. The lack of proper integration techniques of nanotubes with MEMS and CMOS processes make devices based solely on carbon nanotubes elusive.

Compared to electromechanical transduction, photomechanical actuation offers an alternative way to couple energy into actuator structures and brings distinctive advantages such as wireless actuation, remote controllability, electrical– mechanical decoupling, low noise, easier scaling down and elimination of electrical circuits. Unfortunately, few material systems have been shown to exhibit photomechanical actuation properties and are often not compatible with CMOS processing techniques. Recently carbon nanotubes have demonstrated to undergo photo-mechanical actuation both in primitive and when mixed with polymers [4, 5] thereby opening a new area in photomechanical actuation.

By developing a new carbon nanotube patterning technique that is CMOS compatible [6], we have demonstrated in this paper that complex microsystems could be carved out of carbon nanotubes using simple film formation, film transfer, photo-lithography and reactive ion etching. We have demonstrated several microsystems including a micro-gripper, micro-mirrors and micro-cantilevers [7, 8]. By utilizing the photomechanical actuation, the devices exhibited multiple functionalities of both structural materials and actuation mechanisms and no electrical circuits were used for driving or energy conversion. Compared to electrostatic MEMS devices, nanotube MOMS devices

showed better performance in terms of displacement, energy consumed, and useful work output. Further, the use of photons makes the possibility of controlling the devices remotely with out the need for electrical circuits. Since the power consumed is three orders of magnitude smaller than most MEMS electrically driven devices, no amplification is necessary and even a remote source of light may enable photomechanical actuation thereby opening the possibilities of deep space exploration using nanotube MOMS.

EXPERIMENT

Single wall carbon nanotubes were first dispersed in isopropyl alcohol to 0.1 mg/ml by ultrasonication and was vacuum filtered through mixed cellulose ester (MCE) filter to produce nanotube films. The nanotube film with the filter was then directly bonded to the silicon substrate and annealed at 75C for 20 min ensured the bonding of nanotube films on the silicon substrate. The same procedure can be used to bond nanotube films onto silicon dioxide and wide variety of substrates. Nanotube films of thicknesses between 40 nm to 800 nm were fabricated for subsequent processing into devices. Figure 1 shows the nanotube films and their partial transparency. With thickness less than 200 nm the films show high degree of transparency. Photolithography was employed to define patterns followed by oxygen plasma etching. At power of 200 W, bias power of 100 W and oxygen flow rate of 50 sccm, a film etch rate of 4 nm/sec was obtained. The method that is shown here offers several advantages compared to other patterning techniques: 1) uniformity of nanotube films, 2) low processing temperatures, 3) high feature resolutions, 4) sharp patterns (Fig.2) around edges, (5) compatible with MEMS/CMOS processes.

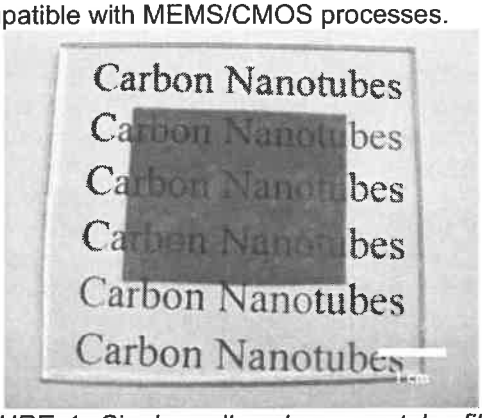

FIGURE 1: Single wall carbon nanotube film ~ 200 nm thickness showing high degree of transparency.

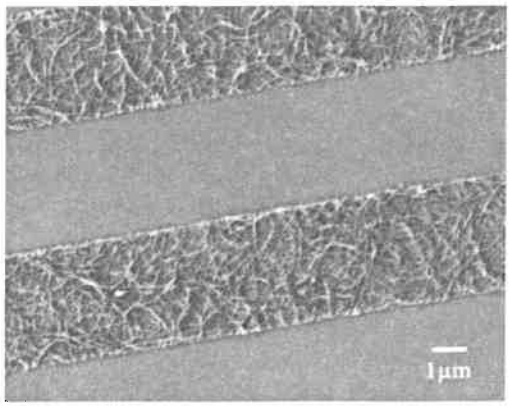

FIGURE 2: Etching of single wall carbon nanotube patterns showing precise features in a oxygen plasma etching.

The excellent processing of nanotube films by oxygen plasma offers the potential for several applications. Figure 3 shows the arrays of cantilever actuators that were fabricated using this technique. On incidence of infra-red light, these cantilevers showed eye observable actuation [5]. For a 30 μm x 300 μm x 7 μm cantilever, a linear displacement of ~23 μm at 170 mW of laser power was observed (Fig.4). Most electrically driven actuators need anywhere between 5-100V for actuation. The presented optically driven actuators need much lower energy and also have no electrical connections thereby enabling remote actuators on the micron to nanometer scale. Figure 5 shows the SEM image of a micro-gripper using the same principle for remote manipulation of micro-objects. Figure 6 shows the sequence in the remote manipulation of polystyrene microspheres in air. When infrared laser light of ~550 mW is directed to the actuating arms, the gripper tips open to 20 μm, resulting in 16.5 μm displacement of the actuator. The photomechanical actuation of the actuating arms causes the elongation of this arm and a length difference between the actuating arm and the supporting arm, resulting in the gripper opening. We have reported that a released CNT/SU8 cantilever exhibits a '*Z*' direction displacement normal to the cantilever surface under light illumination [6]. However, the '*Z*' direction actuation is not suitable for the integration of the actuation mechanism with surface micro-machined structures. By employing an 'actuating arm and supporting arm' double arm structure, the photomechanical actuation can be transferred into the horizontal '*X–Y* ' plane as

shown by the gripper example, which brings more compatibility of this photomechanical actuation with surface micro-machined structures. Theoretically, many electrically driven MEMS structures that involve movable structures such as micro-motors, micro-gears, micro-stages and micromirrors can be implemented using this nanotube photomechanical actuation principle without requiring electrostatic actuators. The advantages of this actuation principle are the ease and simplicity of implementation, low power of operation, capable of working in liquid, air and vacuum environments.

Figure 7 shows the image of fully suspended micro-mirrors with serpentine actuators made of nanotubes. These mirrors can obtain the same performance as electrically driven MEMS micro-mirrors (Fig.7) and consume only 300 μW-1.3 mW of power. When 830nm (~35mW) laser pulses of 50% duty cycle at 0.6Hz was used to actuate the left serpentine actuator in Figure 7, a downward motion was addressed at point "A", being at the same side as the actuation light spot, while an upward motion was addressed at point "B", being at the opposite side as the actuation light spot. The two traces of the mirrors plotted in Figure 8 correspond to the rotation signals recorded from point "A" and "B", respectively. Thus, a "counter clockwise" rotation of the micromirror was achieved in response to light. The photomechanical actuation of carbon nanotube/SU8 structure created a downward bending of the actuator under illumination. The operation mechanisms of the CNT-MOM mirrors involve light induced electrostatic, elastic, photomechanical effects and local thermal confinement in the nanotube/polymer structures. Opto-thermal effects of the structure also contribute to the total actuation. From previous works conducted on macro-size samples, the thermal effects was estimated to be smaller than 25% of the total actuation (rotational angles of 0.5°), showing that it is the competing mechanisms between elastic, electrostatic, photomechanical and opto-thermal effects that causes the actuation. The photomechanical actuation of left serpentine actuator in Figure 7 resulted in "counter clockwise" rotation. Similarly, a "clockwise" rotation of the mirror would result if the actuation light spot is located on the right serpentine actuator in Figure 3(a). In Figure 8, the bi-directional rotation of the mirror set the mirror travel range as +/-2.4°. Taking the laser intensity and the small area (~36000μm^2) of the actuator into account, the driving photonic energy was calculated to be 1.3mW in order to obtain this operation range. Such micromirrors are capable of exhibiting comparable rotational range as the electrically driven micromirror, however, only driven by light. This shows the benefits of optically powered CNT-MOMS, which may hold promise in the both future MEMS and MOMS, and CNT based applications. Low power optical sources well focused into small spots would be enough for mirror operation. Structural optimization of the micromirror will further help to reduce the required light power. Figure 9 shows the rotation angles of this micromirror as a function of laser powers at 830nm. While the upper curve represented the rotational signal recorded from the opposite side "point B" of the mirror to the actuator in force, the lower curve was that from the same side "point A" of the mirror as the working actuator. Nearly linear response was acquired from both of the testing positions "A" and "B", in agreement with the optical responses of macro carbon nanotube based optical actuator [8]. A large angular rotation of ~7.2° was obtained from the MOM mirror when the laser output power is set to 130mW (~4.7mW for driving the single mirror). The large rotation angle acquired is partially due to the serpentine design of the actuator, which served to elongate the effective actuator length to ~1200μm.

Operation speed of MOMS is a critical issue in many potential applications. The frequency response of the micromirror was also tested and was shown in Figure 5. A monotone decrease of the rotational displacements was witnessed with the increase of laser pulse frequency at 276mW. Noticeably, a large rotation angle of ~19° was recorded at operation frequencies of 4Hz, corresponding to power consumption of ~10 mW for a single mirror operation. Although operated in air, the micromirror is capable of rotation upto ~130Hz with observable rotation angles (0.03°), which is acceptable for low speed applications such as sensors.

The All these demonstrations clearly indicate nanotube-MOMS can be developed that consumes fraction of the energy and achieves similar/better performance compared and offers remote control compared to MEMS based electrical systems. The mechanism of actuation is due to the physical interlinks between elastic, optical, electrostatic, thermal and polaronic effects in nanotubes [5].

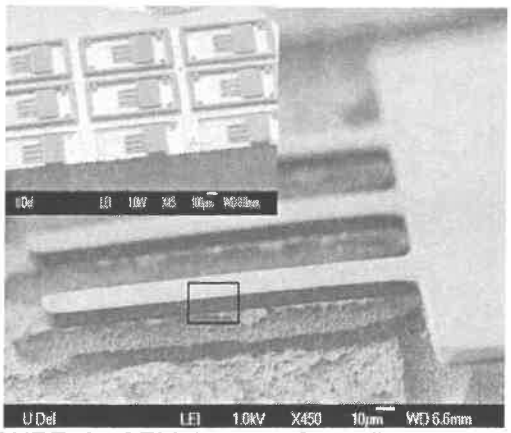

FIGURE 3: SEM image of cantilever actuator made from nanotube/SU8 polymer, Inset: arrays of the cantilever structure that was released.

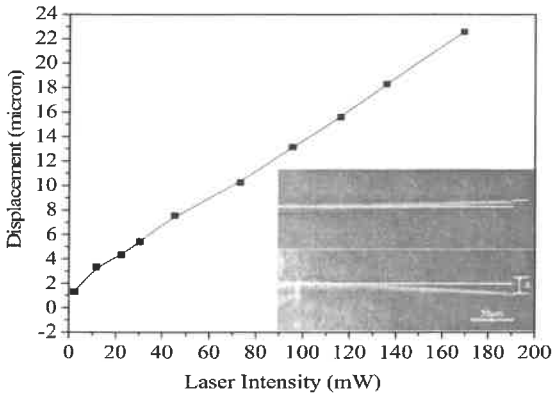

FIGURE 4: Displacement versus laser intensity for cantilever actuator, inset: shows the differences in actuation during light off and on. Straight lines were drawn for eye guidance

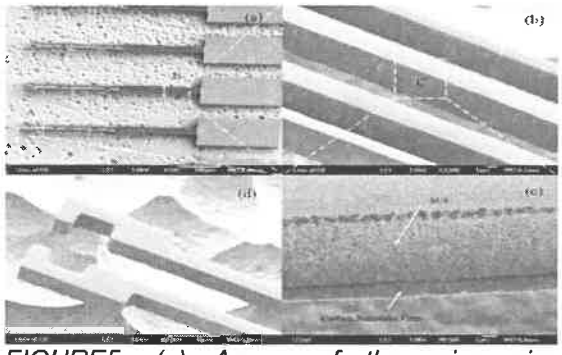

FIGURE5: (a) Arrays of the micro-gripper released after nanotube patterning and XeF2 release, (b) SEM image of lines of SU8/nanotube patterns, (c) SEM image of the opening of the gripper, (d) SEM image of a single line showing SU8 on top and nanotube film on bottom.

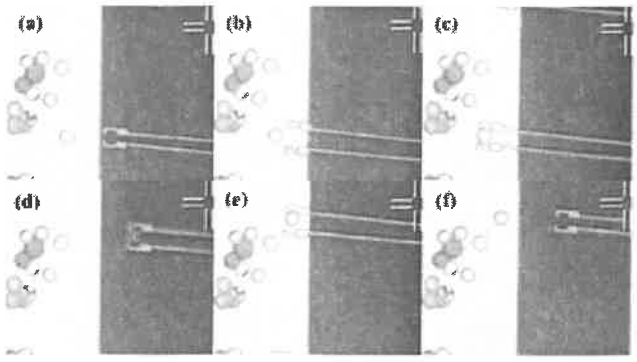

FIGURE 6: Sequence of CNT-MOMS gripper manipulating polystyrene micro-spheres in air. Arrays of such grippers can manipulate many microspheres/cells simultaneously using one light source.

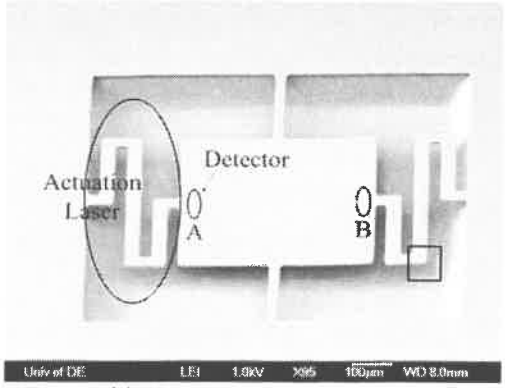

FIGURE 7: SEM image of a micro-mirror formed using nanotube patterning technique. The nanotubes are patterned on the actuator arms. Gold is deposited to form the mirror surface.

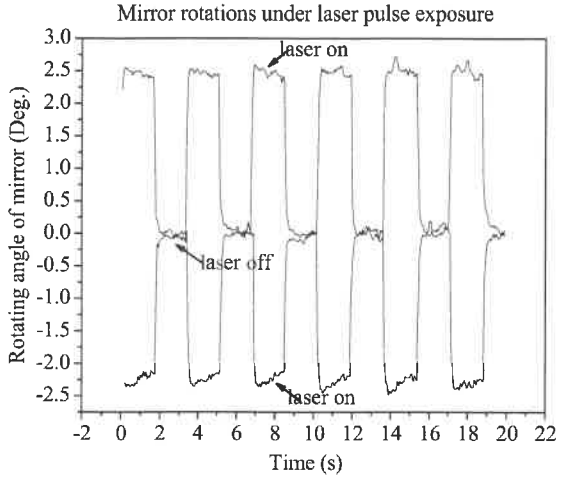

FIGURE 8: Micromirror rotation recorded from both sides (A and B) of the mirror. Laser pulse is ~35mW at 830nm.

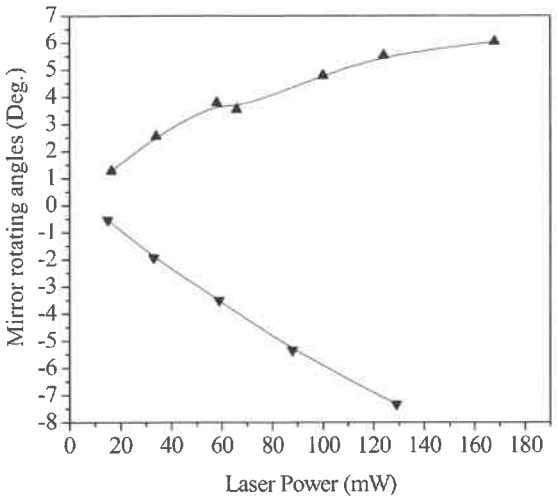

FIGURE 9. Mirror rotational displacements as a function of laser power at 830nm when position detector is on both sides (A and B) of the mirror.

CONCLUSIONS

We have reported the first application of SWNT based micro-opto-mechanical systems. By using nanotube film formation, film bonding, photolithography and reactive ion etching, complex micromechanisms were fabricated including micro-cantilevers, micro-grippers and micro-mirrors. The MOMS devices outperformed electrically driven MEMS systems in several ways including low power consumption (240 μW), remote controllability, efficient energy transduction, useful optical to mechanical work output, reversible actuation, batch fabrication, out of plane actuation and stability. The MOMS grippers were demonstrated for micro-manipulation. The mechanism of actuation is due to physical interlinks between optical, electrostatic, elastic and thermal effects in carbon nanotubes. MOMS could find use in nanorobotics, sensors, micro-surgery, biomedical nanotechnology and deep space exploration.

ACKNOWLDEGEMENTS

Funding for this research was partially supported by the NSF CAREER Award, ECS: 0546328 for Balaji Panchapakesan.

REFERENCES

[1.] G.T. Kovacs, Micromachined Transducers Sourcebook, Mc Graw Hill, New York, 1998.

[2.] R.H. Baughman, Carbon nanotube actuators, Science 1999; 284 1340.

[3.] S.Lu and B. Panchapakesan, Hybrid Pt/SWNT nanowire actuators: metallic artificial muscles, Nanotechnology, 2006; 17, 888.

[4.] S.V. Ahir and E.M. Terentjev, Photomechanical actuation of carbon nanotubes, Nature Materials 2005; 4 491.

[5.] S. Lu and B. Panchapakesan, Optically Driven Nanotube Actuators, Nanotechnology 2005; 16, 2548.

[6.] S.Lu and B. Panchapakesan, Nanotube microoptomechanical actuators, Applied Physics Letters, 2006; 88 253107.

[7.] S. Lu and B. Panchapakesan, Nanotube Micro-Opto-Mechanical Systems, Nanotechnology 2006; 18 (6), 065501.

[8.] S.Lu and B. Panchapakesan, All Optical Micro-Mirrors from Nanotube MOMS with Wavelength Selectivity, Journal of Micro-Electro-Mechanical Systems, 2007; 16(6) 1515-1523.

FROM DESPERATE TO DISPARATE: BROAD ARRAY OF CENTIMETER TRAVEL, PICOMETER RESOLUTION, HIGH STIFFNESS PIEZOMECHANISMS SUDDENLY ENABLES A WEALTH OF NEXT-GENERATION TOOLS

Scott C. Jordan
PI (Physik Instrumente) L.P.
San Jose, California, USA

INTRODUCTION

Application requirements of next-generation lithographies, microscopies and scanned-probe metrologies ε placing seemingly-conflicting demands on structural and motion subassemblies for semiconductor manufacturing. In the general problem, position must be controlled in more degrees of freedom with higher dynamic and static accuracy, yet faster throughputs and larger travels are necessary to meet financial metrics. These conflicting requirements have, until recently, had no solution; Moore's Law seemed to be demanding technologies which did not exist. Application examples abound:

- Optic assemblies of escalating sophistication require multiple axes of nano-precision alignment yet must remain aligned for months of 'round the clock usage.
- Emerging nanoimprint methodologies demand exquisite positioning and trajectory control yet must retain alignment integrity under significant physical and thermal stresses.
- AFMs and similar process- and quality-monitoring scanned-probe microscopes must process larger areas faster--needs for up to 1mm square have emerged--yet their scans must never deviate from nanometer-scale planarity since this forms the datum plane.

The Traditional Solution

When precision is needed, piezoelectric actuation is the default choice. Similarly, when high force or high dynamics is required, piezoelectric actuation represents the gold-standard. But the examples noted above illustrate several conflicting physical demands for which piezo positioning approaches present no obvious solution. For example, conventional piezo actuators offer limited travel. Fortunately, effective flexure lever-amplification approaches have been devised over many years which provide travels to several hundred microns. Unfortunately, the stiffness of lever mechanisms diminishes as the square of the lever ratio. So, demands for longer travels with faster actuation or higher holding force are at cross-purposes. Similarly, needs for larger-area processing in (for example) an AFM conflict with needs for tighter nanoscale planarity in obvious ways. Furthermore, at some point the granularity of the driving DAC will begin to be seen in unacceptably coarse positioning resolution.

Now, a Wealth of Solutions

Fortunately, a confluence of radical new approaches has breathed new capability into the nanopositioning world. Some of these represent significant incremental advancement of essentially traditional piezoelectrically-actuated mechanisms; others represent significant forks in the road of positioning technology.

BACKGROUND: PIEZO ACTUATION

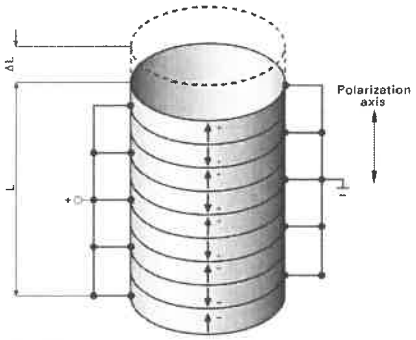

FIGURE 1. Piezoelectric nanopositioning actuators are stacked slices of piezo ceramic separated by electrodes.

Piezoelectric ceramics are sophisticated, layered structures of specialized ceramic and electrodes (FIGURE 1), electrically and conceptually similar to some types of capacitors. These actuators exhibit a quasi-linear dimensional change with applied voltage. The electric field causes ionic translation in the ceramic lattice (FIGURE 2).

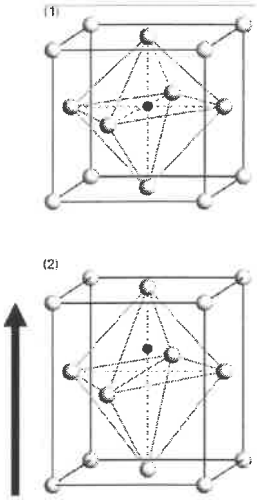

FIGURE 2. Bulk material expansion of piezo materials occurs when a voltage is applied, causing ionic translation in the ceramic lattice.

Piezo actuators can be designed to actuate longitudinally or laterally in shear mode. Piezo actuators' nonlinearity, asymptotic approach to settled position and hysteretic behaviors are routinely eliminated by integrating servo control based on position feedback (FIGURE 3). For typical piezo materials, the maximum strain ($\Delta L/L$) is about 0.1%. This and other characteristics are subjects of intensive development. Novel architectural advancements have provided increased dynamical capabilities as well while enhancing these actuators' already-impressive reliability (FIGURE 4).

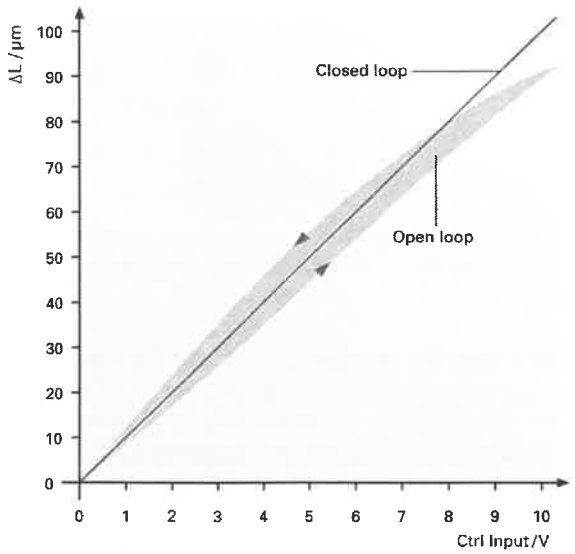

FIGURE 3. Piezo expansion is more-or-less linearly related to applied voltage.

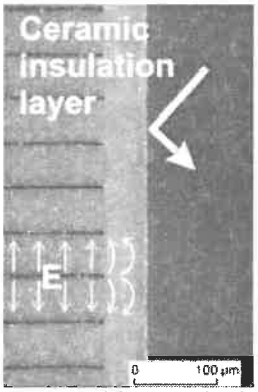

FIGURE 4. Recent architectural advances include this PICMA actuator's ceramic insulation, which enhances its dynamical characteristics along with providing orders of magnitude improved humidity resistance.

NANOMETERS OVER MILLIMETERS

Recent years have seen the introduction of piezo-driven nanomechanisms integrating actuators such as we've described, driving novel flexure amplification subsystems which provide unprecedented workpiece travels of up to 2mm. This addresses the mechanical needs for some larger-area processes but presents new controls challenges.

Ordinarily, the necessarily lower resonant frequency of highly-leveraged nanomechanisms (cf.
EQUATION ***1***) limit the bandwidth and thus the tracking performance of traditional servo-control techniques.

$$C_n = \frac{C_{Piezo}}{r^2} \quad \text{r : lever amplification ratio}$$

EQUATION 1. Lever amplification for longer travels impacts mechanical stiffness.

This is now addressed by novel controls technologies. Digital Dynamic Linearization™, a non-traditional algorithm integrated into the latest digital nanopositioning controls, virtually eliminates following errors in repetitive motion patterns and scanning of these long-travel nanomechanisms. The controller integrates the algorithm into the metrology and servo logic; this optimizes the internal command generated for a repetitive waveform according to the error signal detected with the internal sensor. A brief (typically <1 second) auto-optimization is commanded by the user (or a reload of previously-

saved optimizations) when application changes occur. After this, following errors are reduced to approximately the noise level of the system (FIGURE 5).

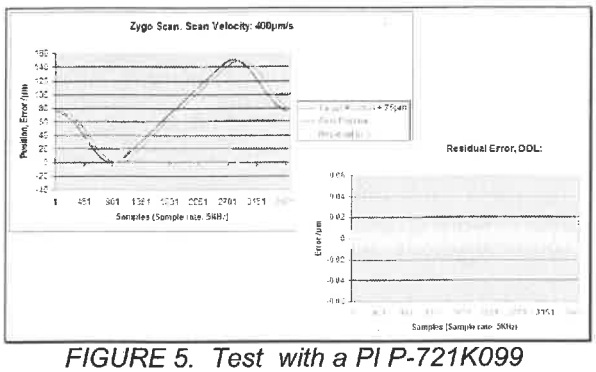

FIGURE 5. Test with a PI P-721K099 nanopositioner with and without DDL, as visualized with a Zygo ZMI-2000 laser interferometer. In this fast-waveform test, the following error is reduced from up to 10µm to 15nm or less—an improvement of three orders of magnitude.

This capability is supported by internal waveform generators and software drivers including COM objects, DLLs and LabVIEW libraries.

Eliminating the Travel/ Resolution Trade-Off

Recall FIGURE 3 shows piezo actuation is roughly proportional to applied voltage, typically generated by a digital-to-analog converter (DAC) driving an amplifier. The number of addressable positions for a piezo mechanism is 2^{bits} – reflecting the bit-width of the DAC's digital input. Traditionally, the resolution of the nanopositioner can be no better than its travel divided by this number. With today's unprecedentedly long-travel flexure nanopositioners, achieving tight resolution goals requires higher and higher DAC bitness.

Until recently, a DAC's limitations were permanent characteristics of the specific chip chosen by the designer. OEM engineers designing their own controls might choose a 20- or 24-bit DAC for their custom circuit design, but care must be taken, as such DACs can present drift issues, noise or other drawbacks. Sometimes a new design is not economically practical, necessitating use of lower-bitness legacy DACs, yet end-user demands for higher resolution persist.

The recently-introduced, patented HyperBit™ technology[1] leverages the under-utilized time-domain capability of DACs, converting it into many additional bits of physical positioning resolution (FIGURE 6). HyperBit™ employs modulation of the least-significant bit(s) of a DAC to accomplish this (EQUATION 2). For example, the LSB can be dithered using pulse-width modulation at a high rate. The result is higher positioning resolution without tradeoffs.

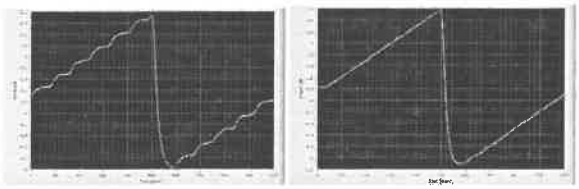

FIGURE 6. Fine actuation of a long-travel flexure nanopositioner, per laser vibrometer, showing DAC granularity (left) vs. superior resolution (right) with HyperBit™.

$$Bits(effective) \rightarrow Bits(DAC) \square \log_2\left(\frac{DAC\_rate}{PWM\_freq}\right)$$

EQUATION 2. Rule of thumb for resolution enhancement

NANOMETERS OVER CENTIMETERS

To address applications with longer travel needs than can be met via mechanical amplification of piezo stack actuators, engineers have developed an array of new technologies based on novel configurations and actuation modes of piezo ceramics.

Resonant Piezomotors

Piezo ceramic plates can be configured so that high-frequency excitation drives one or more resonant modes in the material, conferring a micon-scale oscillatory motion to a friction tip at an antinode (FIGURE 7). The friction tip can then be preloaded against a guided workpiece, driving long-travel motion with behavior somewhat similar to that of DC servomotors.

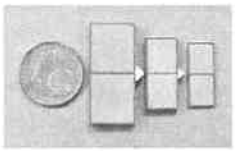

FIGURE 7. Piezo slabs, when configured and resonated according to patented principles, can confer a motive force to a workpiece.

A wide assortment of linear- and rotary-motion configurations have been commercialized, both open- and closed-loop. By eliminating lead-

[1] US Pat. #6,950,050, foreign Patents pending.

screws and their inertia and associated linkages and structures, such mechanisms can be very compact and responsive. For example, the linear stage shown in FIGURE 8 provides 19mm of travel at up to 500mm/sec and 10gee acceleration with an 0.1μm resolution, non-contacting linear encoder, all in a package 35mm square.

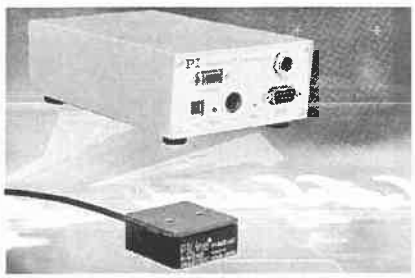

FIGURE 8. Compact piezomotor stage with 500mm/sec speed, 0.1um resolution.

In-position stability is superior to conventional DC servomotors since the actuator acts as a brake when quiescent. Magnetic fieldlessness, vacuum-compatibility, long life and other signature advantages of piezo actuation also apply. In addition, an entirely new automatic and adaptive digital control technology for resonant piezomotors was introduced at SEMICON 2007; this provides highly robust and consistent servocontrol in applications with varying loads and dynamics, such as in handling and shuttling applications, with exceptional tracking performance.

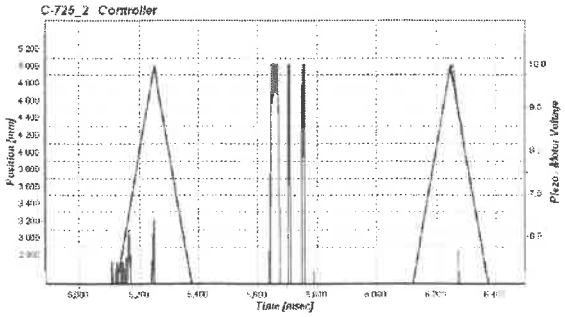

FIGURE 9. New adaptive controller accommodates dynamical changes. In this close-up of a motion test of stage in FIGURE 8, blue trace: commanded triangle-wave motion; red: actual position; green: motor command. At about the midpoint in the graph, a 750g load was affixed to the stage. The subsequent tracking demonstrates robust adaptability.

Piezo Walking Drives

By combining piezo elements acting in longitudinal and transverse directions, the fundamental actuation unit for a walking actuator is composed. These elements can be compressed against a longitudinal rod to confer motion. One familiar progenitor of this family of mechanisms was the Burleigh Inchworm. More recently-developed mechanisms offer high stiffness and holding force (FIGURE 10) and are optimized for reliability in applications requiring long-term position hold while providing centimeters of travel with picometer-class resolution.

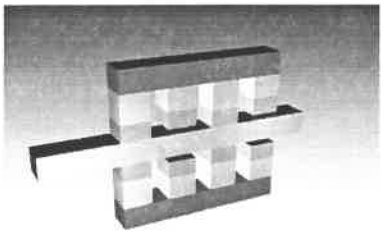

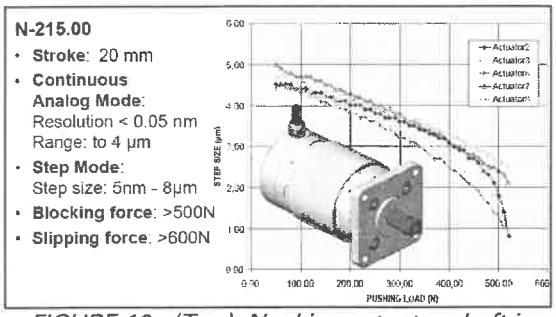

FIGURE 10. (Top) NexLine actuator shaft is clamped and translated by array of walking elements composed of both longitudinal and transverse (strain) PZT elements, combining cm travel with pm resolution. (Bottom) Packaged actuator exhibits high stiffness and actuation force.

FIGURE 11. High-stiffness, fieldless 6-degree-of-freedom hexapod utilizing actuators from FIGURE 10

An even newer solution uses cost-effective bender-type piezo elements rather than the built-up units at the heart of FIGURE 10's design. Size and cost are substantially reduced; power-off stiffness is still remarkable, with 10N holding force. This design also provides centimeters of travel range and picometer-class resolution.

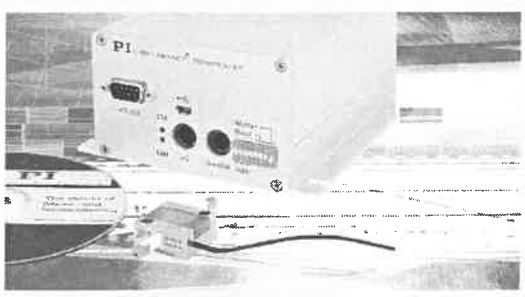

FIGURE 12. Optimized for next-generation micro-lithography alignment and positioning, NexAct actuator provides 10N power-off holding force and smooth coarse/fine motion over centimeters with picometer-class resolution in compact, cost-effective format.

In the case of both FIGURE 10's and FIGURE 12's mechanisms, motion is achieved in two modes: a long-travel stepping mode, and a fine-motion analog mode in which the actuator elements are sheared but not stepped.

Hybrid Motorized/Piezo Mechanisms

While the mechanisms discussed so far can displace magnetic motors, piezo actuation can also be combined with them for coarse/fine motion. Traditional "stacked" coarse and fine mechanisms operate independently; the piezo mechanism greatly improves the minimal incremental motion capability of the system, but the overall repeatability is be no better than the motorized stage alone (FIGURE 13a).

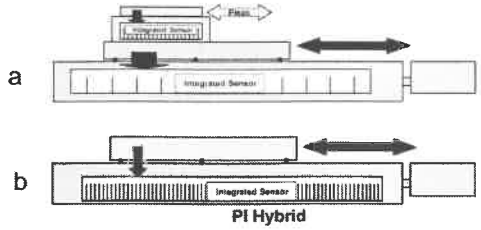

FIGURE 13. (a) A piezo stage stacked on top of a motorized stage improves resolution but not repeatability. (b) Ultra-resolution encoder with advanced controls allows both stages to be coordinated to provide nm-scale resolution and repeatability over many mm.

The advent of linear encoders with nm-scale resolution has allowed construction of hybrid mechanisms where both the coarse and fine mechanisms use the same feedback sensor (Figure 10b). Coordinated by advanced controls, this hybrid provides piezo-class repeatability and fast dynamics over many cm of travel.

NM FLATNESS OVER MM

So far we have discussed the challenges—and solutions—for providing "piezo-class" in-line performance over the increasing travel ranges demanded by today's production-economic prerogatives. Similar challenges exist in scanning applications. In many advanced metrology applications such as profilometry and AFMs, the XY trajectory of the piezo scanner forms the datum plane for the measurement. As travel demands increase into the millimeter range, the nm-scale flatness of the stage trajectory must be maintained— obviously a difficult proposition to achieve using conventional mechanical approaches based on laborious tweaking.

A new approach, on which patents are pending, leverages one or more linearized high-bandwidth Z-axis actuators of travel sufficient to accommodate the native out-of-plane-motion (OOPM) of the uncompensated scanner mechanism. Tradenamed PicoPlane™, a fast active compensation operates to correct the mechanism's native OOPM. Importantly, the compensation may be refined in-situ by scanning a reference flat while observing Z motion through real-time external metrology, such as the AFM tool's own probe.

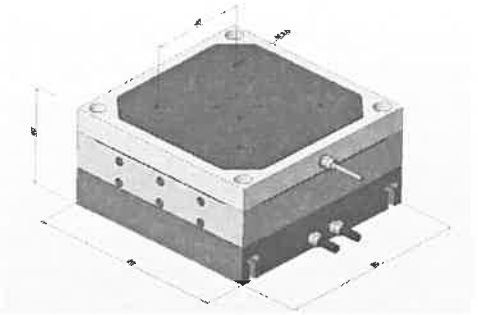

FIGURE 14. Catalog 800x800μm XY nanopositioning scanning stage with active PicoPlane™ Z compensation. The stage travel is sufficient to profile meso-scale microelectronic and biological specimens with <1-2nm planarity.

The resulting data is then used automatically by the stage's digital controller to flatten the stage's motion.

Results

FIGURE 15 illustrates the effectiveness of the technique over an 800x800μm scan, providing OOPM of a degree unachievable by previous volume-manufactured nanopositioning scanners with a fraction of the travel range.

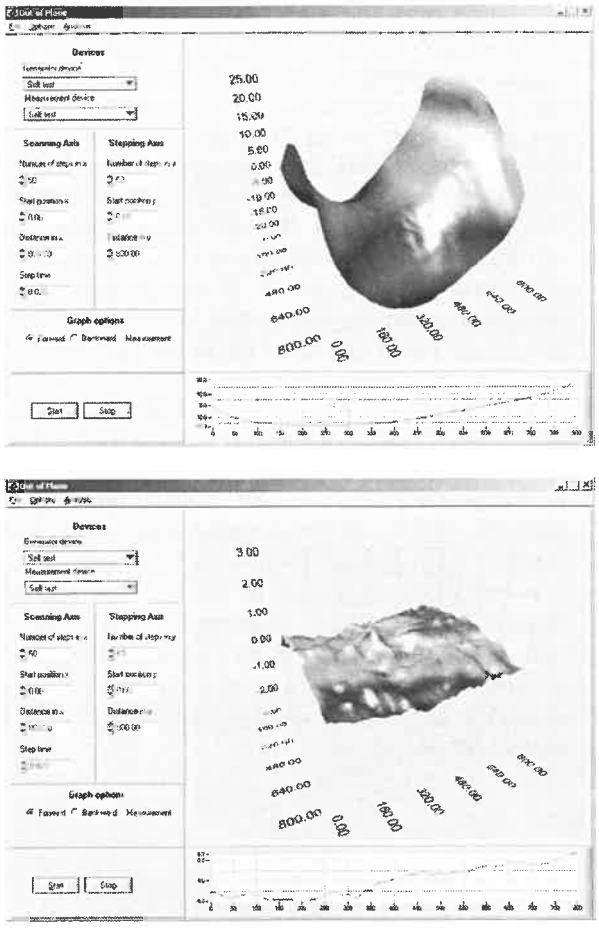

FIGURE 15. (Top) XY trajectory of uncompensated stage with stressed loading. (Bottom) PicoPlane™ compensation provides nm planarity over 800x800μm scan.

CONCLUSION

The field of piezo motion control has expanded rapidly in recent years, with a wealth of new concepts introduced or under active exploration, all aimed at eliminating piezos' former travel limitations while preserving their unmatched resolution, responsiveness and throughput capabilities. Consequently, not only is piezo actuation increasingly suitable for applications formerly addressable only by magnetic motors, but significant benefits accrue in terms of size, speed, fieldlessness, reliability, vacuum compatibility, resolution, dynamics and reliability. These in turn are enablers for significant advances in existing and new applications.

REFERENCES

[1] S. Jordan, S. Chen, M. Culpepper, "Positioning Resolution Enhancement of MEMS and Piezo Nanopositioners," *Proceedings of the 4th International Symposium on Nanomanufacturing*, pp. 166-170, 2005, Cambridge, Massachusetts, USA

[2] P. Pertsch, S. Richter, D. Kopsch, N. Kraemer, J. Pogodzik, E. Hennig, "Reliability of Piezoelectric Multilayer Actuators," *ACTUATOR 2006*, Bremen, Germany, pp. 527-529

[3] R. Gloess, "Nanometer Precise Hybrid Actuator in Positioning Mechanism with Long Travel Range," *ACTUATOR 2006*, Bremen, Germany, pp. 668-671

[4] K. Spanner, S. Vorndran, "Advances in Piezo-Nanopositioning Technology," *Proceedings of the IEEE/ASME International Conference on Advanced Intelligent Mechatronics*, 2003, Kobe, Japan

[5] S. Jordan, H. Marth, "Novel High-Bandwidth Active Parasitic Motion Compensation for Sub-nm Planarity in AFM and Profiler Applications", *Proceedings of the ASPE*, 2007, Dallas, Texas

Author Index

Barnola, Sébastien 10
Bartman, Jonathan 93
Battula, Venkata Siva R. 97
Binnard, Michael 10
Brien, John F. 70
Butler, Hans 7
Chen, Yufeng 93
Choi, B. J. 78
Choi, Young-Man 31
Cole, Kenan 117
Demarest, Frank C. 113
Engelstad, Roxann L. 97, 103
Evans, Chris J. 108
Gao, Jun 93
Gaugiran, Stéphanie 10
Glöss, Rainer 48
Guilmeau, Isabelle 10
Gweon, Dae-Gab 31
Hale, Layton C. 52
Hartley, John G. 123
Hazelton, Andrew J. 10
Hirukawa, Shigeru 10
Hocken, Robert J. 70
Hwang, Donghyun. 39
Ishikawa, Jun 10
Jabben, Leon 127
Jeong, Jaehwa 31
Jordan, Scott C. 133
Kim, Dong-Min. 31
Kim, Ho-Sang. 39
Kim, Jin-Young. 39
Kim, Wan Soo 35
Kluk, Daniel J. 19
Lapeyre, Celine 10
Lee, Moon-Goo 39
Lee, Sun-Kyu. 35
Lercel, Michael 3
Lucatorto, Thomas. 117
Ludwick, Stephen J. 44
Magome, Nobutaka 10
McCallum, Martin 10
Mielke, Stephen L. 113
Mikkelson, Andrew R. 97, 103
Mishra, Sandipan. 58
Nataraju, Madhura. 97, 103
Norg, Meindert L.. 25
Ozturk, Ozkan 70
Panchapakesan, Balaji 128
Park, Inkyu 93
Picciotto, Carl 93
Renkens, Marcel J. M. 74
Ruben, Shalom 64
Ruijl, Theo A. M.. 74
Schumaker, P. D. 78
Smith, Craig. 108
Sogard, Michael R. 103
Sreenivasan, S. V. 78
Stearns, Hoday 58
Stewart, Duncan 93
Tabor, Rob 74
Taylor, John S. 52
Tomizuka, Masayoshi 58
Tong, William M. 93
Tousain, Rob 25
Traux, Bruce 108
Trumper, David L. 19, 127
Tsao, Tsu-Chin 64
Turner, Kevin T. 97, 103
Vallance, R. Ryan 117
van Eijk, Jan * 16, 25, 127
Vukkudala, Pradeep 97
Wakamoto, Shinji. 10
Walmsley, Robert G. 93
Williams, R. Stanley. 93
Wu, Wei 93
Yu, Shuwen 58
Yu, Zhaoning 93
Yun, Cheol Ho 35

* No extended abstract available at press time

ASPE 2008 Sustaining Corporate Sponsors

3M Company
St. Paul, MN 55144
Phone: (651) 737-3790
www.mmm.com

ADCOLE Corporation
669 Forest Street
Marlborough, MA 01752
Phone: (508) 485-9100
Fax: (508) 481-6142
www.adcole.com

Aerotech, Inc.
101 Zeta Drive
Pittsburgh, PA 15238-2897
Phone: (412) 963-7470
Fax: (412) 963-7459
www.aerotech.com

Ametek Precitech, Inc.
44 Blackbrook Road
Keene, NH 03431
Tel: (603) 357-2511
Fax: (603) 358-6174
www.precitech.com

Center for Precision Metrology
University of North Carolina-Charlotte
9201 University Blvd.
Charlotte, NC 28223
Phone: (704)-687-8499
www.cpm.uncc.edu

Chardon Tool
115 Parker Court
Chardon, OH 44024
Phone: (440) 286-6440
Fax: (440) 286-7165
www.ChardonTool.com

Corning Tropel Corporation
60 O'Connor Road
Fairport, NY 14450
Phone: (585) 388-3500
Toll-free: (888) 4-TROPEL
www.tropel.com

Equilibria
472 Amherst Street
Unit 25
Nashua, NH 03063
Phone: (603) 880-7722
www.eqlib.com

Fabreeka International, Inc.
P.O. Box 210
1023 Turnpike Street
Stoughton, MA 02072
Phone: (781) 341-3655
Toll-free: (800)-322-7352
www.fabreeka.com

Lion Precision
563 Shoreview Park Road
St. Paul, MN 55126-7014
(651) 484-6544
(651) 484-6824
www.lionprecision.com

ASPE 2008 Sustaining Corporate Sponsors

Mitutoyo America Corporation*
945 Corporate Boulevard
Aurora, IL 60504-9102
Phone: (630) 723-3619
Fax: (630) 978-6471
www.mitutoyo.com

Moore Tool Company, Inc.
800 Union Avenue
Bridgeport, CT 06607-0088
Phone: (203) 366-3224
Fax: (203) 366-5694
www.mooretool.com

New Way Precision, Inc.
4009-I Market Street
Aston, PA 19014
Phone: (610) 494-6700
Fax: (610) 494-0911
Toll-Free: (800) 394-1046
www.newwaybearings.com

Philips Applied Technologies
1140 Ringwood Court
MS16
San Jose, CA 95131-1706
Phone: (408) 991-2261
www.apptech.philips.com

Professional Instruments Company
7800 Powell Road
Hopkins, MN 55343
Phone: (952) 933-1222
Fax: (952) 933-3315
www.airbearings.com

Queensgate Instruments, Ltd.
Woodland Road
Torquay Devon TQ2 7AY
United Kingdom
Phone: 44-1803-407710
Fax: 44-1803-4076
www.nanopositioning.com

StarragHeckert, Incorporated
Skyport Business Park
2379 Progress Drive
Hebron, KY 41048
Phone: 859-534-5201
Fax: 859-534-5212
www.starragheckertus.com

Trust Automation, Inc.
143 Suburban Road
San Luis Obispo, CA 93401
Phone: (805) 544-0761
Fax: (805) 544-4621
www.trustautomation.com

Zygo Corporation
Laurel Brook Road
Middlefield, CT 06455-0448
Phone: (860) 347-8506
Fax: (860) 347-8372
Toll-free: (800) ZYGO-NOW
www.zygo.com

ASPE 2008 Corporate Sponsors

Contour Fine Tooling, Inc.
Marlborough, NH 03455
Contact: Jeffrey Tomlin
(603) 876-4908

Corning Inc.
Corning, NY 14831
Contact: John Thomas
(607) 974-3842

Cranfield Precision,
Div. of Landis Lund
Division of Cinetic Landis Grinding, Ltd.
Cranfield, Bedford MK43 OJR, U.K.
Contact: Edric M. E. Brown
+44-1234-754222

euspe*n*
Cranfield University
Cranfield, Bedford, MK43 OAL, U.K.
+44-1234-754024

Nano Corporation
Tokyo 144-0042, Japan
Contact: Akira Hayashi
+81-3-5735-6631

Reflexite Precision Technology Ctr.
200 Park Centre Drive
West Henrietta, NY 14586
Contact: Mr. Steven M. Scott
(585) 272-0290

Seagate Technology
Scotts Valley, CA 95066
Contact: Robert M. Pelstring
(831) 439-3697

Singulus Mastering, B. V.
5657 EN Eindhoven, The Netherlands
Contact: Guido Dalessi
+31-40-7501-400

Taylor Hobson, Ltd.
Leicester LE4 9JQ, UK
Contact: Daniel I. Mansfield
+44-116-2763771, Ext. 2126

Veeco
Tucson, AZ 85706-7123
Contact: Geoffrey Anderson
(520) 741-1044